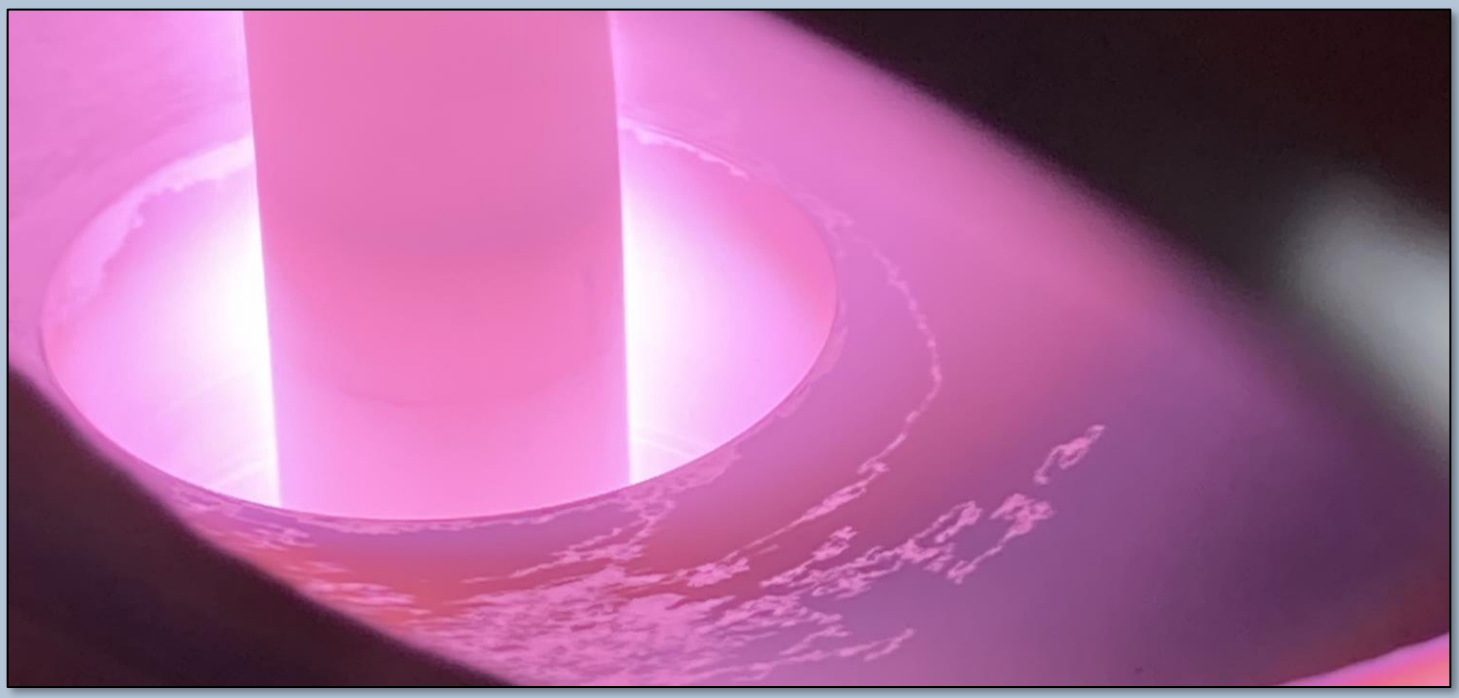

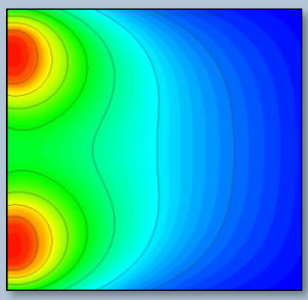

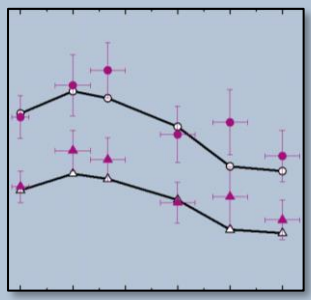

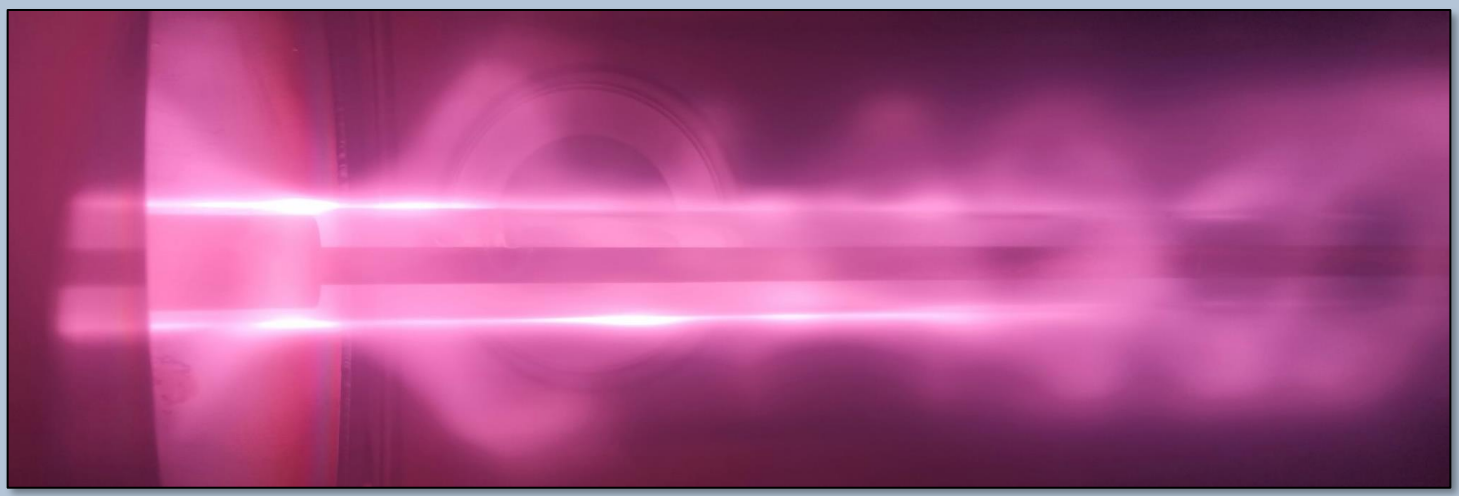

Yannick Kathage

Characterization of plasma-driven permeation for the development of a hydrogen selective vacuum pump

Charakterisierung plasma-getriebener Permeation zur Entwicklung einer wasserstoffselektiven Vakuumpumpe

Characterization of plasma-driven permeation for the development of a hydrogen-selective vacuum pump

Zur Erlangung des akademischen Grades eines

DOKTORS DER INGENIEURWISSENSCHAFTEN (Dr.-Ing.)

von der KIT-Fakultät für Maschinenbau des
Karlsruher Instituts für Technologie (KIT)
genehmigte

DISSERTATION

Von

M. Sc. Yannick Kathage

Tag der mündlichen Prüfung:	23.07.2024
Hauptreferent:	apl. Prof. Dr. rer. nat. Sven Ulrich
Korreferent:	Prof. Dr.-Ing. Daniel Banuti

Kurzfassung

In thermonuklearen Fusionsreaktoren werden die beiden Wasserstoffisotope Deuterium und Tritium unter Energiefreisetzung zur Kernfusion gebracht. Der Verwendung von Tritium stehen globale Knappheit, die Radioaktivität des Isotops und die Eignung für den Einsatz in Kernwaffen gegenüber, welche mit strengen Lizensierungsauflagen durch Regulatoren einhergeht. Um den Betrieb zukünftiger Fusionsreaktoren zu gewährleisten, wird das Konzept des „Direct Internal Recycling“ vorgeschlagen. Es basiert auf der Separation großer Mengen fusionsfähigen Brennstoffs bei niedrigen Drücken früh im Aufbereitsprozess des Abgasstroms. Der Effekt der Superpermeation durch Metallfolien kann diese Anforderungen erfüllen. Diese Arbeit befasst sich mit der Entwicklung eines darauf beruhenden technischen Prozesses in der sogenannten Metallfolienpumpe.

Superpermeation kann mit einem kalten Plasma getrieben werden, welches Wasserstoffteilchen die nötige Energie zur Permeation durch dünne Metallfolien zuführt. Um die Operation einer Metallfolienpumpe quantifizieren zu können, wird in dieser Arbeit das Plasma mittels einer auf einem Fluidansatz beruhenden Plasmasimulation charakterisiert. Als Grundlage zur Verwendung der daraus abgeleiteten Daten dient eine experimentelle Validierung des Modells, die mittels optischer Emissionsspektroskopie mit einem Aktinometrie Ansatz erfolgt. Im Rahmen dieser wird die Konzentration atomaren Wasserstoffs in räumlicher Abhängigkeit im Plasma und unter Variation der Operationsparameter Druck und Leistung des Plasmas variiert. Um die Ergebnisse der Plasmasimulation in einer anknüpfenden Teilchentransportsimulation zu applizieren, wird ein Parameter extrahiert, welcher eine Anregungswahrscheinlichkeit für die Energetisierung eines Teilchens beim Auftreffen auf die Plasmaquelle darstellt. Die Teilchentransportsimulation basiert auf einem Monte Carlo Ansatz, in dem konkrete Oberflächeninteraktionen mit Wahrscheinlichkeiten beschrieben werden. Im experimentellen Teil der Arbeit werden parametrische Studien des Permeationsflusses durchgeführt, welche weitere Daten für die Vakuumsimulation liefern.

Drei verschiedene Konzepte zum Aufbau einer Metallfolienpumpe werden in der Vakuumsimulation unter Variation der wichtigsten Parameter miteinander verglichen, wobei besonderer Fokus auf den Leitwert, das Saugvermögen und die Separationseffizienz gelegt wird. Für das vielversprechendste Design werden weitere Rechnungen durchgeführt, welche die Zusammenhänge zwischen Sauggeschwindigkeit, Separationseffizienz und den Dimensionen der Pumpe evaluieren. Ein Konzept einer solchen neuartigen Pumpe, welches alle ausgearbeiteten Anforderungen erfüllt, wird empfohlen.

Abstract

In thermonuclear fusion reactors, the two hydrogen isotopes deuterium and tritium are merged in an exothermic fusion reaction. The use of tritium comes with the isotopes' global scarcity, radioactivity and its applicability for use in nuclear weapons, which is accompanied by strict licensing imposed by regulators. To ensure the operation of future fusion reactors, the concept of "Direct Internal Recycling" is proposed. It is based on the separation of large quantities of fusionable fuel at low pressures early in the exhaust recycling process. The effect of superpermeation through metal foils can fulfill these requirements. This work deals with the development of a superpermeation based technical process in the so-called metal foil pump.

Superpermeation can be driven by a cold plasma that provides hydrogen particles with the energy required to permeate through thin metal foils. As part of the quantification of the operation of a metal foil pump, the plasma is characterized by means of a plasma simulation based on a fluid approach. The model is experimentally validated using optical emission spectroscopy with an actinometry ansatz. A spatial resolution of the atomic hydrogen concentration with varying operational parameters of pressure and plasma power is given. A parameter, which represents an excitation probability for the energization of a particle when it hits the plasma source, is extracted from the results of the plasma simulation for application in a subsequent particle transport simulation. The latter is based on a Monte Carlo approach in which surface interactions are specified by probabilities. In the experimental part of this work, parametric studies of the permeation flux are carried out to provide further data for the particle transport simulation.

Three concepts for the design of a metal foil pump are compared with the particle transport simulation by varying the most important parameters, with a particular focus on the conductance, pumping speed and separation efficiency. For the most promising design, further calculations are carried out to evaluate the correlation of pumping speed, separation efficiency and the dimensions of the pump. A metal foil pump concept that meets all the requirements is recommended.

Inhalt

Symbols and Abbreviations

Symbols and Constants

Symbol	Description	Unit
A	Surface area or cross-section	(m^2)
A_{ij}	Einstein coefficient for radiative decay from i to j	(s^{-1})
B	Magnetic flux density	(T)
b_{min}	Minimum impact parameter	(m)
C	Conductance	($m^3\ s^{-1}$)
c	Speed of light (= $2.998 \cdot 10^8$)	($m\ s^{-1}$)
c_H	Concentration of atomic hydrogen	(m^{-3})
$c_{m,i}$	Molar concentration of species i	($mol\ m^{-3}$)
D	Electric displacement field	($A\ s\ m^{-2}$)
D_e	Electron diffusivity	($m^2\ s^{-1}$)
D_ε	Electron energy diffusivity	($m^2\ s^{-1}$)
D_{ij}	Binary Maxwell-Stefan diffusivity for components i, j	($m^2\ s^{-1}$)
D_{mfp}	Diameter of a MFP module	(m)
d_{kin}	Kinetic diameter	(m)
E_{kin}	Kinetic energy	(J)
E	Energy	(J)
$\vec{E}$	Electric field	($V\ m^{-1}$)
E_a	Activation energy	($J\ mol^{-1}$)
E_d	Activation energy for diffusion	($J\ mol^{-1}$)
E_p	Maximum amplitude of electric field	($V\ m^{-1}$)
e	Elementary charge (= $1.602 \cdot 10^{-19}$)	(C)
$\vec{F}$	Force	(N)
$\vec{F}_c$	Centripetal force	(N)
$\vec{F}_L$	Lorentz force	(N)
F_{opt}	Correction term considering optical factors	(-)
f	Distribution function	(-)
G_e	Source term for electron production	($m^{-3}\ s^{-1}$)
g	Ratio of two feed flows at certain valve position	(-)
H	Magnetic field	($A\ m^{-1}$)
h	Planck's constant (= $6.626 \cdot 10^{-34}$)	(J s)
I	Current	(A)
I_i	Optical emission intensity of species i	(-)
J	Throughput	($Pa\ m^3\ s^{-1}$)
J_{emiss}	Emission flow leaving the foil surface on one side	($Pa\ m^3\ s^{-1}$)
$J_{M,j}$	Diffusive molar flux	($mol\ m^{-2}\ s^{-1}$)
J_{ori}	Throughput through an orifice	($Pa\ m^3\ s^{-1}$)

J_p	Plasma current density	(A m^{-2})
j_{perm}	Permeation flux	(Pa m^3 m^{-2} s^{-1})
j_i	Diffusive flux vector	(kg m^{-2} s^{-1})
K	Solubility	(s $m^{-2.5}$ $kg^{-0.5}$)
K_λ	Optical device response at certain wavelength λ	(-)
k	Correction factor for the actinometry calculation	(-)
k_B	Boltzmann constant (= $1.381 \cdot 10^{-23}$)	(J K^{-1})
$k_{R,i}$	Reaction rate of species i	(m^{-3} s^{-1})
$k_{r,i}$	Reaction rate of species i	(m^3 s^{-1})
k_{rec}	Surface recombination rate factor	(m^4 mol^{-1} s^{-1})
k_{surf}	Surface reaction rate	(mol m^{-2} s^{-1})
k_0	Wave number	(m^{-1})
Kn	Knudsen number, indicates the flow regime	(-)
L_e	Loss term for electrons	(m^{-3} s^{-1})
l	Length	(m)
M_i	Molar mass of species i	(kg mol^{-1})
m	Mass	(kg)
m_e	Electron mass (= $9.109 \cdot 10^{-31}$)	(kg)
N_A	Avogadro constant (= $6.022 \cdot 10^{23}$)	(mol^{-1})
$\dot{N}$	Molar flow	(mol s^{-1})
$\dot{n}$	Particle flux density	(m^{-2} s^{-1})
n	Particle number density	(m^{-3})
$n_{e,c}$	Electron cut-off density	(m^{-3})
P	Product of separation efficiency and pumping speed	(m^3 s^{-1})
P_e	Power transfer to electron fluid	(J m^{-3} s^{-1})
p	Pressure	(Pa)
p_e	Pressure tensor	(Pa)
p_t	Pressure downstream turbomolecular pump	(Pa)
Q_r	Correction term considering all quenching reactions	(-)
q	Charge	(C)
R	Universal gas constant (= 8.314)	(J mol^{-1} K^{-1})
R_Ω	Electrical resistance	(S^{-1})
r	Radius	(m)
S	Volumetric flow or pumping speed	(m^3 s^{-1})
S_{en}	Gain or loss of energy due to inelastic collisions	(eV m^{-3} s^{-1})
S_{eff}	Effective pumping speed	(m^3 s^{-1})
$S_{p,i}$	Pumping speed of a pump for gas-species i	(m^3 s^{-1})
s	Separation ratio of Direct Internal Recycling	(-)
T	Temperature	(K)
T_d	Temperature in the downstream chamber	(K)
T_e	Electron energy	(eV)

t	Time	s or min
U	Voltage	(V)
U_p	Plasma potential	(V)
U_f	Floating potential	(V)
u	Bulk velocity	(m s^{-1})
$\dot{V}$	Volumetric flow	(m^3 s^{-1})
$V_{D,i}$	Multicomponent diffusion velocity	(m s^{-1})
$\bar{v}$	Mean or thermal velocity	(m s^{-1})
w_i	Mass fraction	(-)
y	Molar fraction	(-)
Z	Kinetic gas theory coefficient	(mol s kg^{-1} m^{-1})
Z_i	Charge number	(-)
z	Axial position	(m)
α	Sticking coefficient	(-)
α_m^*	Pre-factor for Arrhenius function	(-)
Γ_e	Electron flux	(m^{-2} s^{-1})
Γ_ε	Electron energy flux	(eV m^{-2} s^{-1})
Γ_{mig}	Ion migration flux close to wall	(kg m^{-2} s^{-1})
Γ_t	Thermionic electron emission flux	(m^{-2} s^{-1})
γ_e	Electron reflection probability	(-)
γ_b	Secondary electron emission probability	(-)
γ_s	Sticking coefficient	(-)
δ	Stoichiometric factor	(-)
ε	Electron mean energy	(eV)
ε_f	Foil surface asymmetry factor	(-)
ε_s	Mean energy of secondary electron	(eV)
ε_t	Mean energy of electrons emitted by thermal emission	(eV)
ε_0	Permittivity of free space (= $8.854 \cdot 10^{12}$)	(A s V^{-1} m^{-1})
ε_r	Relative permittivity	(-)
ϵ	Electron energy	(eV)
ς_{mag}	Degree of magnetization	(-)
η	Orifice transmission probability	(-)
θ	Surface coverage with impurity	(-)
λ	Wavelength	(m)
λ_D	Debye-length	(m)
λ_{mfp}	Mean free path	(m)
μ	Mobility	(m^2 V^{-1} s^{-1})
μ_i	Chemical potential	(J m^{-3})
μ_r	Relative permeability	(-)
ν	Wave frequency	(s^{-1})
ν_m	Collision frequency for momentum transfer	(s^{-1})

ν_{en}	Electron-neutral collision frequency	(s^{-1})
ξ	Absorption probability of suprathermal hydrogen	(-)
ρ	Density	(kg m^{-3})
σ	Collisional cross-section	(m^2)
σ_{DC}	Direct current electrical conductivity	(S m^{-1})
σ_p	Plasma electrical conductivity	(S m^{-1})
σ_{rou}	Surface roughness	(-)
σ_s	Surface charge density	(C m^{-2})
τ	Angle of velocity and electric field	(°)
φ	Excitation probability on plasma source	(-)
χ	Permeation probability	(-)
ψ	Capture coefficient	(-)
ψ_x	Phase angle of electromagnetic wave	(°)
ω_g	Gyrofrequency	(s^{-1})
ω_{pe}	Plasma frequency	(s^{-1})

Subscripts

	Description
$\square_a$	Atomic
$\square_{abs}$	Absorption
$\square_c$	Characteristic
$\square_{coll}$	Collision
$\square_{des}$	Desorption
$\square_e$	Electron
$\square_{en}$	Electron-neutral
$\square_\varepsilon$	Electron-energy
$\square_g$	Gas
$\square_H$	Atomic hydrogen
$\square_{id}$	Ideal
$\square_{imp}$	Impinging
$\square_{in}$	Incoming
$\square_{ion}$	Ionic
$\square_l$	At location l
$\square_M$	Maxwell
$\square_m$	Molecular hydrogen
$\square_{perm}$	Permeation
$\square_r$	Reaction
$\square_{rec}$	Recombination
$\square_{rem}$	Reemission
$\square_{tot}$	Total
$\square_{x,y,z}$	Into x-, y-, z-direction
$\square_0$	At location 0
$\hat{\square}$	Complex amplitude

Abbreviations

Abbreviation	Description
AES	Auger electron spectroscopy
BB	Breeding blanket; part of a nuclear fusion reactor
CANDU	Canada Deuterium Uranium reactors; capable of producing tritium
CARS	coherent anti-Stokes Raman scattering; type of spectroscopy
DIR	Direct Internal Recycling; novel fuel cycle architecture
DSCM	Direct simulation Monte Carlo; an approach to transition flow calculations
ECR	Electron-cyclotron-resonance
EDX	Energy-dispersive X-ray diffraction spectroscopy
EEDF	Electron energy distribution function
ER	Eley-Rideal mechanism; type of recombination of atomic species
EU-DEMO	Demonstration power plant; Successive to ITER, a nuclear fusion reactor
FMF	Free molecular flow
GDP	Gas-driven Permeation
HERMESplus	Hydrogen experiment for research on metal foils and superpermeability – plasma utilization setup
ITER	Nuclear fusion research reactor; latin for “The Way”
INTL	Inner tritium plant loop
KALPUREX	Karlsruhe liquid metal based pumping process for fusion reactor exhaust gases
LES	Linear equation system
LH	Langmuir-Hinshelwood mechanism; type of recombination of atomic species
MFC	Mass flow controller
MFP	Metal foil pump
MSC	Multi-stage cryopump
OES	Optical emission spectroscopy
OUTL	Outer tritium plant loop
PDP	Plasma-driven permeation
REMPI	Resonance-enhanced multiphoton ionization; type of spectroscopy
SEM	Scanning electron microscopy
SEY	Secondary electron yield
TALIF	Two-photon absorption laser induced fluorescence; type of spectroscopy
TPMC	Test particle Monte Carlo; an approach to free molecular flow calculations
VUVAS	Vacuum ultraviolet absorption spectroscopy
XRD	X-ray diffraction spectroscopy
XRF	X-ray fluorescence spectroscopy

Vorwort / Preface

Schon von klein auf haben mich die Geheimnisse der Physik, insbesondere die des Kosmos und der kleinsten Teilchen, fasziniert. Diese Leidenschaft bewegte mich auch dazu, meine Arbeit dem Forschungsfeld der Kernfusion zu widmen und für die Möglichkeit dazu bin ich sehr dankbar. Dieser Dank gilt vor allem Personen, die diese Arbeit ermöglicht oder direkt unterstützt haben.

Allen voran danke ich meinem ursprünglichen Hauptreferenten, Professor Dr.-Ing. Robert Stieglitz, welcher diese Arbeit bis unmittelbar vor ihrer Fertigstellung betreute. Sein breites Fachwissen und sein Scharfsinn fürs Detail bereicherten diese Arbeit enorm. Mit ihm verlor die Forschung einen ausgezeichneten Wissenschaftler und Doktorvater. Ebenso bin ich Professor Dr. Sven Ulrich zu großem Dank verpflichtet, welcher als Hauptreferent den Abschluss dieser Arbeit ermöglichte. Außerdem möchte ich Professor Dr.-Ing. Daniel Banuti für die Übernahme des Korreferats danken.

Einen besonderen Dank möchte ich Dr.-Ing. Christian Day aussprechen. Als Leiter meiner Arbeitsgruppe am Institut für Technische Physik (ITEP) prägte er meine Arbeitsweise immens und schuf die Rahmenbedingungen für diese Arbeit. Ebenfalls gilt ein großer Dank meiner Arbeitsgruppe am ITEP. Insbesondere Martin Jäger, aber auch Alan Kumb, Thomas Johann, Jürgen Weinhold, Peter Pfeil, Jürgen Jung und Hartmut Stump halfen mir regelmäßig, die Forschungsanlage funktionstüchtig zu halten, waren maßgeblich für ihr Errichten zuständig und ermöglichten auch in schwierigen Zeiten das Leben mit Humor einfacher zu machen. Ralf Müller möchte ich danken, stets mit Schnelligkeit und eigenen Ideen aus meinen Skizzen wertvolle technische Zeichnungen gefertigt und die Zusammenarbeit mit der Werkstatt geleitet zu haben. Ein großer Dank gilt auch meinen Kollegen Stefan Hanke, Dr.-Ing. Thomas Giegerich und Dr. Xueli Luo für die enge Zusammenarbeit im Projekt und hilfreiche sowie spannende Diskussionsrunden. Gleicher Dank gilt Volker Hauer, Dr. Stylianos Varoutis, Katharina Battes und Juri Igitkhanov, an die ich mich immer wenden konnte, wenn ich fachkundigen Ratschlag brauchte.

Diese Arbeit wurde außerdem sehr durch meine Doktoranden-Kollegen geprägt, für deren Expertise und Inspiration ich unheimlich dankbar bin. Allen voran ist hier Alejandro Vázquez Cortés zu nennen, mit dem ich über Jahre an der gleichen Forschungsanlage auf das gleiche Ziel hinarbeitete und viele Ideen in fachlichen Diskursen austauschte. Aber auch Tim Teichmann, Jonas Schwenzer und Annika Uihlein lieferten stets wertvolle Anregungen und verstanden immer, Arbeitsalltag und Spaß unter einen Hut zu bringen. Einen sehr starken Einfluss auf die Entwicklung meines Fachwissens hatte auch Dr. Andrei Busnyuk, der mich vor allem zu Beginn meiner Arbeit an seinen umfangreichen Erfahrungen in unserem gemeinsamen Forschungsthema teilhaben ließ. Außerdem möchte ich mich bei meinen Kollegen an der Universität Stuttgart, Dr. Stefan Merli, Dr.-Ing. Andreas Schulz und Dr.-Ing. Matthias Walker bedanken, von denen ich über die Jahre der Kooperation viel lernen konnte und bei Besuchen an der Stuttgarter Forschungsanlage immer herzlich aufgenommen wurde.

Ein großer Dank gilt auch all meinen Freunden – und meiner Freundin Joana für ihren Optimismus und emotionalen Rückhalt. Zuletzt danke ich meiner Familie und insbesondere meinen Eltern. Auf jedem meiner Wege erhielt ich die Ermutigung, das zu tun, was mir Spaß bereitet und obwohl sie nicht beide den Abschluss dieser Arbeit erleben können, wusste ich jederzeit um ihre bedingungslose Unterstützung.

1 The fuel cycle of a thermonuclear fusion power plant

Ever since the rise of industrialization, economic growth and prosperity of modern civilizations have been dependent on a reliable supply of energy. The fossil fuels coal, oil and gas were the most important resources for power generation until the mid of the 20th century, when the understanding of nuclear fission made major progress, which allowed its employment in nuclear power plants for production of electricity with high low resource intensity and high power output. Starting in the 1980s, concerns for the safety of nuclear power plants as well as the prospect of possible depletion and environmental impact of fossil fuels motivated the development of power plants based on renewable energies. However, the lack of suitable energy storage systems to cover periods without sufficient wind and solar power are, to this day, a crucial weakness of renewables. Nuclear fission, on the other hand, currently presents the backbone of some countries' electrical grids, but long-time storage of radioactive waste and the high cost of its recycling remain a drawback. One very strong benefit of nuclear fission, however, is CO_2-neutrality – a characteristic shared with nuclear fusion, which at the same time does not come with the risk of runaway chain reactions and produces no radioactive waste in the fusion reaction except for irradiated reactor materials.

Research on the role of thermonuclear fusion as a process that powers stars [1-3] led to its appreciation for large-scale power supply and the first efforts to harness it in a technical application [4]. Since then, this has proven to be a major technological challenge. In the first two decades of the 21st century, a continuous, worldwide focus of efforts to develop alternatives to fossil fuels [5] [6] has been accompanied by public funding of fusion research. Nuclear fusion is only possible in extreme conditions as, for example, given in the core of stars. It is the merger of two atomic nuclei into a heavier one under the release or uptake of energy, based on the mass of the nuclei. During most of their lifetime, stars like the sun will burn hydrogen to form helium via one of several fusion processes like the proton-proton chain reaction [3]. The mass of the product helium is smaller than the combined mass of all initial participants of the reaction, yielding a mass defect. This mass is not lost but instead irradiated as electromagnetic energy, neutrinos and/or transformed to kinetic energy of the particles that participate in the reaction. Assuming no motion of the mass, the transfer of mass to energy is described by the famous equation

$$E = mc^2, \tag{1.1}$$

published by Albert Einstein [7], who derived that mass m and energy E are equivalents. In this equation, c is the speed of light. Fusion is only exothermic for reactions that produce elements with a smaller proton number than iron. Elements with more protons have endothermic fusion reactions, meaning they liberate energy when split into lighter elements. The energy required to bind a nucleon to the core of an atom can be plotted for all the scientifically proven isotopes as it is shown in Figure 1.1 [8].

For fusion to happen, the energy potential of the electromagnetic force, which leads to the repelling of approaching positively-charged nuclei, has to be overcome by the kinetic energy of the two colliding nuclei. This requires extremely high particle velocities, i.e. temperatures. The probability of a fusion reaction is commonly expressed as a cross-section, which depends on the particles' kinetic energies. Fortunately, an effect called quantum tunneling allows particles to overcome a potential energy barrier caused by the Coulomb repulsion despite having insufficient energy to surpass it according to classical mechanics. This is accounted for in the shown fusion cross-sections in Figure 1.2 [9]. It shows the relationship of cross-section over the center of mass kinetic energy for a few of the most-prominent fusion reactions for a thermonuclear fusion reactor [10-14]. The fusion cross-section of two hydrogen-1 nuclei does not appear in this graph because it is too small. It is approximately 24 orders of magnitude smaller than that of the deuterium (D) and tritium (T) reaction, which translates into a too low power density for operation of a fusion reactor.

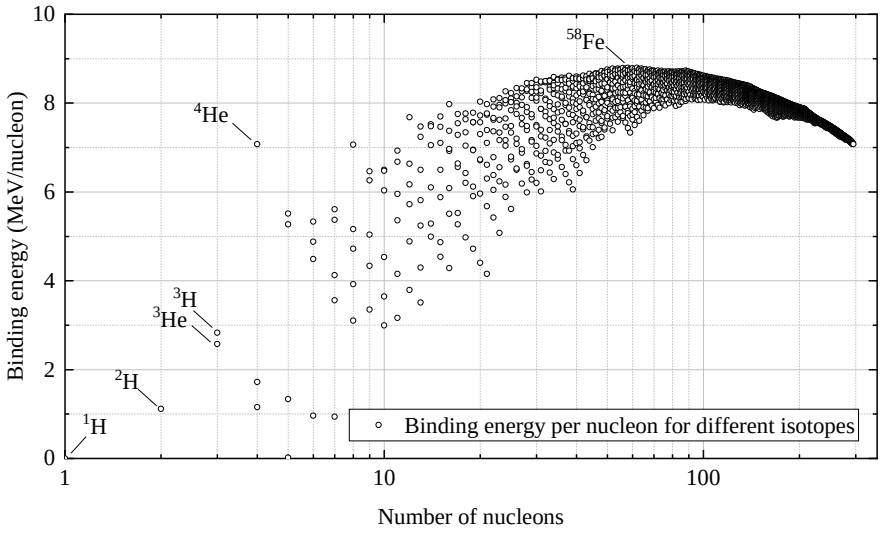

Figure 1.1: Binding energy per nucleon for all known isotopes [8].

Due to its large reaction rate and feasibility at relatively low temperatures, the DT fusion reaction

$$^{2}_{1}H + ^{3}_{1}H \rightarrow n + ^{4}_{2}He + 17.6\,MeV. \qquad (1.2)$$

is currently considered the best candidate for a thermonuclear fusion reactor. The excess energy is carried away as kinetic energy by the two reaction products. While deuterium is quite abundant as it accounts for 0.015 % of the hydrogen in seawater [15], tritium is scarce. Its only natural occurrence on earth is due to the splitting of upper atmosphere nitrogen atoms by cosmic radiation [16] and it is continuously lost to radioactive decay with a half-life time of 12.3 years. This also compromises artificially produced reserves from Canadian Deuterium Uranium (CANDU) reactors, which generate ~ 2 kg per year [17] at the current reactor portfolio. While some countries might have military stockpiles, the global civil tritium inventory available for fusion research is in the range of several tens of kg [18]. The European Union's project EU-DEMO (short for demonstration power plant) should demonstrate that the operation of a nuclear fusion power plant with net electricity production is possible. Until the commissioning of EU-DEMO, the existing tritium reserves will be further depleted by decay and consumption in other fusion research reactors, highlighting the importance of tritium management in EU-DEMO and introducing low tritium inventories as one of the major design drivers [19]. A key characteristic of EU-DEMO will be its tritium self-sufficiency by means explained in section 1.1.

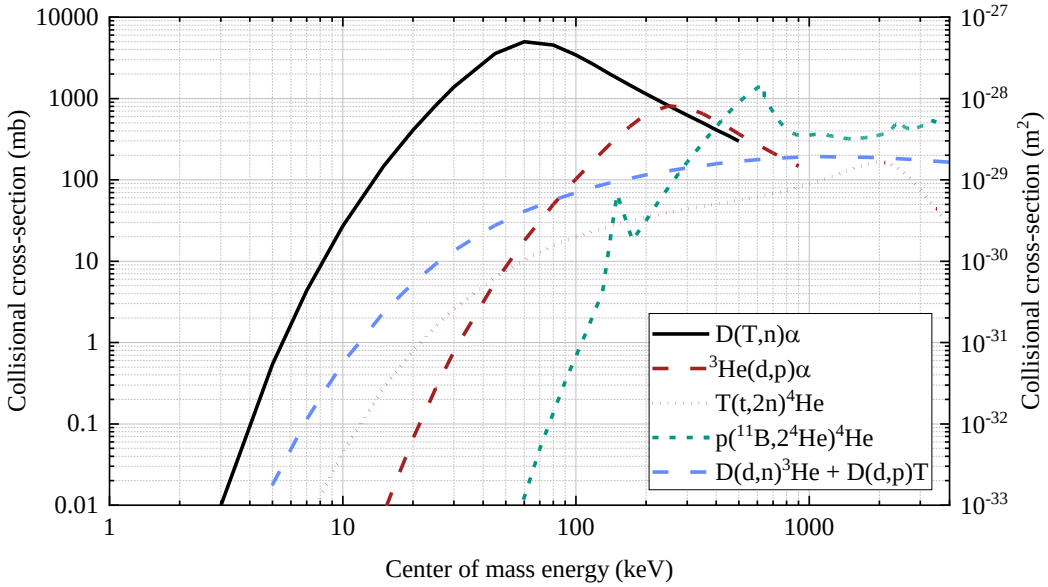

Figure 1.2: Collisional cross-sections for some fusion reaction candidates in a fusion reactor [10-14].

1.1 The technological realization of thermonuclear fusion

The previously mentioned high temperatures required for the onset of fusion in a gas lead to its ionization, forming plasma, to which the abundance of free charges, electrons and ions, is characteristic. This grants plasma the property of electrical conductivity and allows manipulation of its density and positioning with magnetic fields. Thus, enabling the confinement of the hot fusion plasma in a magnetic bottle to avoid interactions with the plasma-facing walls, is a key aspect. Currently, there are two major concepts for providing a magnetic encagement of a technical realization of a thermonuclear fusion reactor. Those concepts lead to individual reactor designs called Tokamak and Stellarator. At this point in time, the fusion community regards the Tokamak, due to its simplicity, as the more promising candidate for the first demonstrational fusion power plant. Therefore, an explanation of the Stellarator concept is neglected in this work and mentions of the reactor plasma chamber, also termed torus, refer to the Tokamak concept. Nevertheless, research done in the scope of this work can be applied in the fuel cycle of a Stellarator design as well.

As sketched in Figure 1.3, a Tokamak features a set of toroidal and poloidal field coils and a central solenoid to generate its magnetic field. The necessary high magnetic flux densities are reached by driving extremely large currents through the coils, which require them to be superconducting and, thus, operated at cryogenic temperatures. For better isolation from the reactor heat and shielding of fast neutrons that are created in the core plasma, the coils are located outside of the vacuum vessel. The central solenoid is used to drive an inductive current in the plasma to heat and confine it. As the continuously increased central solenoid current reaches its upper limit, the plasma is extinguished. This necessitates a pulsed operation of the machine. In the period between the pulses, also referred to as dwell time, the magnetic systems are re-loaded.

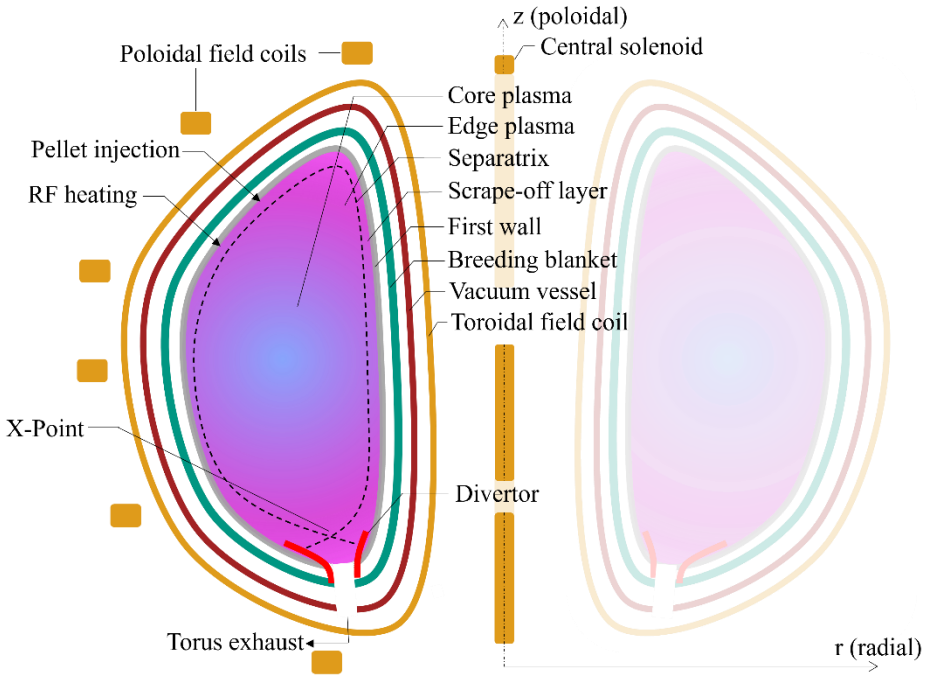

Figure 1.3: Cross-section of a Tokamak.

In a Tokamak, deuterium and tritium are introduced into a donut-shaped plasma vessel and heated in order for fusion to set in. This is done through either resistive heating by inducing a current, heating with electromagnetic waves that accelerate free charges in the plasma or neutral beam injection, which is based on the acceleration of hydrogen ions in a static electric field and their neutralization before injection into the plasma [12]. Playing an important role in the collisionality of the plasma, gas density and pressure in a tokamak are orders of magnitude below atmospheric values.

The fast neutrons originating from the fusion reaction are unaffected by the magnetic field and carry their kinetic energy to the surrounding installations of the reactor. After penetrating the first wall, the majority of neutrons deposit their energy in the breeding blanket (BB), which is responsible for the production of tritium, heat extraction, protection of the coil systems from the fast neutrons and cooling of the first wall [19]. The first wall, made of solid tungsten plates, is supposed to protect the BB from high heat fluxes. Made from the same material, the divertor is an arrangement of targets with the main duty to withstand extremely high power densities and to neutralize the torus gases for pumping. In this way, helium is removed from the vessel downstream the divertor. The high heat load is produced by fast plasma particles. Those drift from the core towards the scrape-off layer, the region between the wall and separatrix, which is the boundary between open and closed field lines. From there, the charged particles are transported to the divertor along the separatrix. It forms a strike-point on the divertor, yielding heat loads of up to 10 MW/m² in normal operation during burn for the currently pursued plasma scenario of EU-DEMO, which features a "single-null" (X-Point) configuration with a divertor at the bottom of the machine [20]. To cool and neutralize the particles before impingement, noble gases are buffered in, which are essential to stay below the thermal limits but also act as an additional burden as the gas has to be evacuated together with the exhaust gas from the plasma.

The second fusion product, a helium-4 core, is subjected to the magnetic field due to its charge. Its kinetic energy dissipates in collisions in the core plasma, effectively heating the fuel. In theory, such heating can be used to sustain the plasma temperature when a certain fusion rate is attained and no further external heating is needed to allow for steady plasma burn. However, fusion of the fuel leads to dilution of the plasma core with non-reactants, which reduces the fusion rate and causes larger power losses from the core plasma due to *bremsstrahlung*. *Bremsstrahlung* is the emission of electromagnetic radiation, which occurs from electron deceleration in the vicinity of the electric field of ions. The higher the charge number of the ion, the larger the *bremsstrahlung* losses. Any element with a higher nucleus charge number than hydrogen in the core plasma, hence, leads to substantially increased thermal losses from the core towards the walls.

A constant pumping on the torus chamber is required to remove the fusion product helium-4 and keep its concentration in the plasma core below a certain limit of a few percent [21]. In the process of helium pumping, fuel is also removed. The fuel concentration in the core is balanced by injection of frozen high-velocity fuel pellets, of which, however, only a fraction reach the core. The purity of the pellets is of paramount importance to reduce bremsstrahlung losses. However, recently there have also been considerations of admixing certain noble gases to the pellets to enhance plasma performance [22], which could lighten constraints on other impurities in the pellets. In ramp-up and ramp-down, fueling takes place via injecting gas from the boundary of the vessel, which is also used to improve radiative cooling and surface protection at the plasma edge and divertor during burn. A fuel excess at the plasma edge is also required to provide plasma stability. During dwell, the vessel is continuously evacuated with the main throughput coming from hydrogen outgassing of the walls. The fuel cycle is the architecture of the technologies used for the treatment and recycling of the processed gases.

1.2 Fuel cycle and fuel separation

Pumping on the torus and fueling to substitute the losses of fuel in the core plasma is essential. A mixture of gases is removed at the divertor, which can also be interpreted as the starting point of the fuel cycle, of which a simplified scheme is given in Figure 1.4. The main components of the reactor exhaust are the two fuel constituents, D and T, some residual protium (H), helium ash from the burning plasma (He) and plasma enhancement gases (PEGs), which typically are argon (Ar) and xenon (Xe) at the current EU-DEMO baseline scenario and neon (Ne) is also a possible candidate [23]. The high value, scarcity and biological hazard of T necessitates to design a closed-loop fuel cycle. The recycling of the torus exhaust is performed via the so-called inner tritium plant loop (INTL). The INTL's main duties

can be summarized as the removal of impurities (PEGs, He and H), isotope separation & rebalancing and tritium storage, handling and fueling.

For EU-DEMO, the fuel cycle is utilizing a smart architecture, supplementing the INTL by a Direct Internal Recycling (DIR) loop. The DIR concept is based on a simple principle: Most of the tritium is to be handled in fast processes with low residence times, while the flows through sophisticated recycling stages with long residence times are reduced. A realization of this concept is given by the KALPUREX-process (Karlsruhe liquid metal based pumping process for fusion reactor exhaust gases), which employs a main torus pumping system based on pumps using liquid metals, namely mercury (Hg) as working fluid [24]. It is tritium-compatible due to the negligibly low retention of T in Hg. A Hg vapor diffusion pump is used as high vacuum pump and the backing pump is a liquid ring pump operated with Hg. An essential part of the DIR concept is a fuel-selective bypass to the tritium plant. It creates the DIR loop, which should recycle ~ 80% of the total hydrogen throughput of the reactor in a single process step, greatly reducing the average recycling time [25] while still accounting for the vitally important duties of the fuel cycle [26]. This asks for a technology capable of separating large throughputs of hydrogen at the given conditions close to the torus (see the highlighted box in Figure 1.4). In KALPUREX, this role is fulfilled by a so-called metal foil pump (MFP) that uses an effect called superpermeability. At this point in time, the effect has been researched for some decades but no technological application has arisen, giving the MFP a low technology readiness level and the motivation to this work.

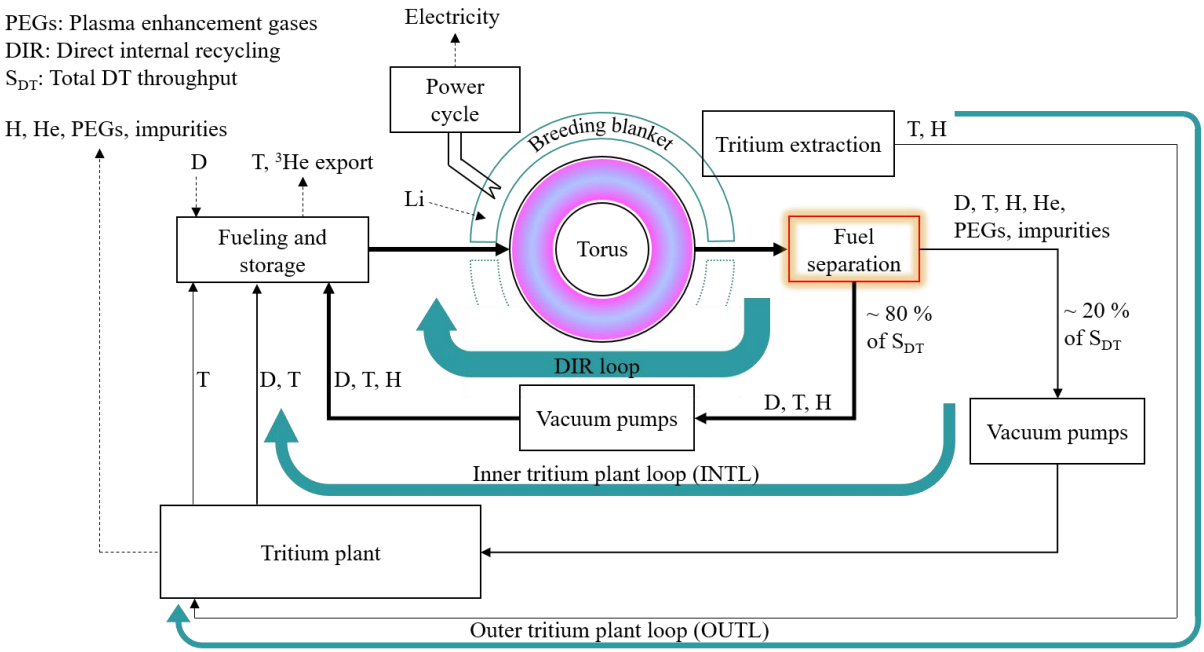

Figure 1.4: Schematic flowchart of the fuel cycle of a demonstration fusion power plant.

In the breeding blanket, fast neutrons from the fusion reaction deposit their energy and generate heat, which powers a Rankine cycle and produces electricity. The BB is also responsible for the breeding of tritium, which happens through interactions of neutrons with Lithium [27]. In the outer tritium plant loop (OUTL), the BB coolant is purified and bred tritium extracted from the blanket. The amount of tritium produced over the amount consumed is described by the tritium-breeding ratio [28]. This ratio is bound to vary during the operation of a reactor such as EU-DEMO and may be adapted to the global requirements of fusion. While still accounting for unpreventable losses like radioactive decay and absorption by reactor materials, the produced tritium should also satisfy the plant's self-sufficiency and be used to supply the start-up inventory of future fusion devices [29]. Once removed from the BB and isolated in pure form in the fuel cycle, the tritium can be stored in thermal release getter beds and delivered to fueling systems with deuterium to produce pellets via cryogenic extrusion.

1.3 Requirements for fuel separation

The task to be fulfilled is the separation of an ideally ultra pure and large fraction of hydrogen from the torus exhaust in the low pressure regime in the sub-divertor region. As of right now, too many uncertainties concerning the fueling in DEMO exist to give a specific requirement on the accepted purity of the separated stream, but requirements are expected to become very demanding [30]. The recycled flow corresponds to the total machine throughput, which is in the range of 265 – 430 Pa m^3 s^{-1} according to the EU-DEMO operation baseline scenarios [23]. Simulations have shown that separating ~ 80 % of the hydrogen from this flow yields sufficiently high tritium conversion rates [31] and is, therefore, identified as a requirement of the technology. During the burn-phase of the plasma, the range of possible pressures in the pump duct varies between 0.1 – 10 Pa with D, T, He, Ar, H and Xe being the main gas species present [23]. The fuel separation of choice should be able to operate with the specified gases in the noted pressure regime.

During dwell, the vessel is evacuated until the pressure drops to ~ 0.5 mPa [23]. Throughputs are certainly significantly lower at this point in operation, mainly coming from outgassing from the walls but no reliable data on the throughput at this point of operation is available. Its not essential to perform fuel separation during dwell but it can be regarded as beneficial if its possible. Evacuation of the vessel down to 0.5 mPa is performed by the secondary pumping system, consisting of the linear diffusion and liquid ring pumps. The performance of those pumps depends strongly on the conductance of the whole system from divertor to the inlet of the linear diffusion pump. The fuel separation stage is the only major component in this flow area and, therefore, has a significant impact on the conductance. For the pumping system to fulfil its duty, attention has to be paid to the system's conductance in the design phase. Preliminary calculations [32] of the rough pumping system stress the requirement of a high conductance of the pump duct as a whole, which necessitates separating the fuel close to the torus. This does not only impose geometrical constraints on the technology but also limits connections to auxiliary systems. In the current design, the MFP pump cask measures approximately 2.4 x 2.1 x 2.3 m (width x height (h) x depth (d)) and is highlighted in red with a shade in the CAD drawing in Figure 1.5 (a). The width is not displayed and represents the depth of the cask in the sketch. At the starting point of this work, up to 16 pump ducts are available for installation of the fuel separation stages [33].

A strong magnetic field of the closeby superconducting coils is present in the pump duct. A detailed analysis of this magnetic field during the start of flattop of the EU-DEMO baseline scenario 2017 shows magnetic flux densities of up to 1.5 T in the pump duct section of interest and strong inhomogeneity and curvature of the localized magnetic field lines. Figure 1.5 (b) features a map of the total magnetic flux density, which is composed of the radial, axial and toroidal components. The latter has low contribution and the strongest magnetic fields are pointed in radial and axial direction, depending on the position inside the duct. Major effects of such a strong magnetic field are forces on current-carrying conductors, ferromagnetic materials and effects on the ignition and behavior of plasma. In transient operation, a fast change in magnetic field strength can also induce large electric fields and currents in conductors. As a final point for the list of requirements, tritium compatibility is pointed out to be of paramount importance, which means that the technology of choice has to operate without organic hydrocarbon components, such as oil, other lubricants and viton gaskets. All requirements the fuel separation technology has to fulfil are listed in Table 1.1.

In the preliminary design phase of DEMO, two technologies are considered for fuel separation: A metal foil pump (MFP) and a multi-stage cryopump (MSC). Sketches of the technologies are shown in Figure 1.6 A and 1.6 B. The MFP exploits a phenomenon termed superpermeability. It requires a source of atomic hydrogen at appropriate energy and a thin metal foil of specific material and condition, as will be explained in section 2. For the production of atomic hydrogen, incandescent filaments as well as different types of plasma sources have been experimentally researched.

Table 1.1: Requirements on the fuel separation in the DIR of EU-DEMO.

Nr.	Description
1	Recycle a throughput of 265 – 430 Pa m^3 s^{-1}
2	Separate 80 % of the hydrogen in the throughput (~ DIR-ratio of 80 %)
3	Operate at pressures between 0.1 and 10 Pa
4	Provide high purity of hydrogen in the separated stream
5	Tolerate impurity (5 vol-% He, 2.5 vol-% Ar, 0.05 vol-% Xe)
6	Fit in the foreseen space in the DEMO pump duct (16 ducts with 2.4 x 2.1 x 2.3 m)
7	Provide a conductance as high as possible
8	Operate under the influence of a strong, inhomogeneous magnetic field

The use of filaments exhibits downsides concerning lifetime and pressure range, which are not featured by plasma sources, for which experience and availability from industry are strong advocates.Pumping of hydrogen through superpermeable foils has already been demonstrated at large fluxes and over long periods of time by different groups [34] [35]. In theory, it is able to separate hydrogen from other gases very sharply [31]. However, it has also been shown that superpermeability can be sensitive to the surface condition of the foil [36], which limits the MFP's resistance to surface alternations caused by impurities or sputtering.

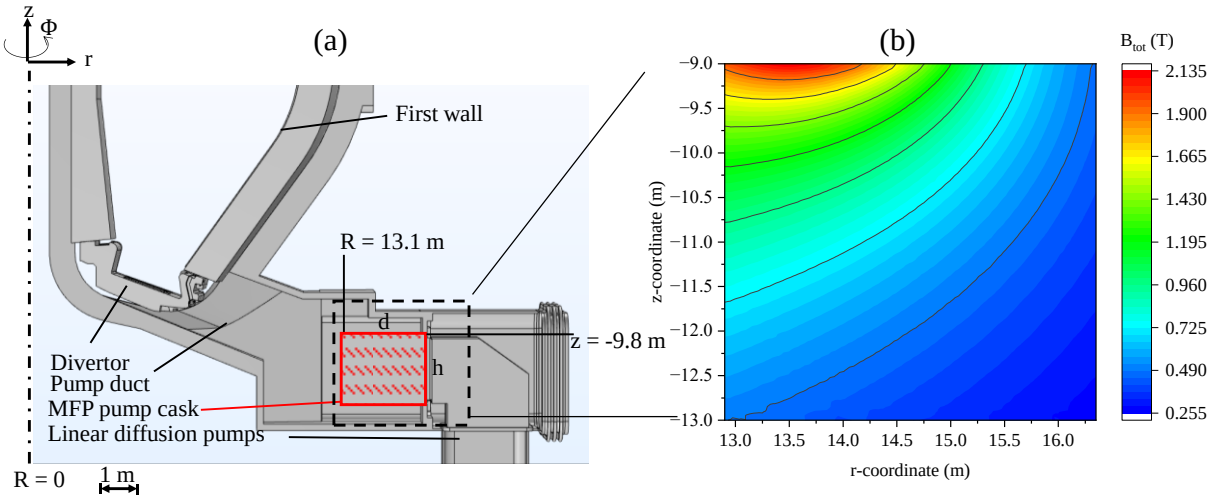

Figure 1.5: Pump duct of EU-DEMO pre-conceptual design with foreseen cask for a metal foil pump, rough pumping and total magnetic flux density map during the start of flattop of the EU-DEMO baseline scenario 2017.

The MSC builds on a solid history of cryopump application in fusion and in general. It is imagined as a sequence of three chambers, which are filled with cryogenically cooled panels and separable from each other via gate valves. Upon entering the pump, the gas passes an 80 K baffle that serves as a first condensation stage for heavy gases and impurities. In the first vessel, the temperature of the cryopanel is kept at 20-30 K for condensation of PEGs [33]. In the second vessel, hydrogen is captured on the sorbent material at 10-20 K and in the third vessel, the helium ash sublimates at the lowest temperature of 4.5 K [37]. Upon saturation of the surface, the chambers are isolated from each other via gate valves and the sorbent material is regenerated by heating. The released gas from the 2nd chamber has a high content of hydrogen and is transported to matter injection systems by rough pumps. However, some impurity gases in the form of He or PEGs will be present in the regenerated gas stream, which is inherent to the pump's design. At this point in time, it is not clear if the purity delivered by the MSC is acceptable or if additional purification, i.e., by permeators, is required [23]. Another uncertainty of this technology is the design of the big gate valves, which is complicated by their movement in the magnetic field without means of lubrication due to the need to be tritium-compatible and little space to operate in.

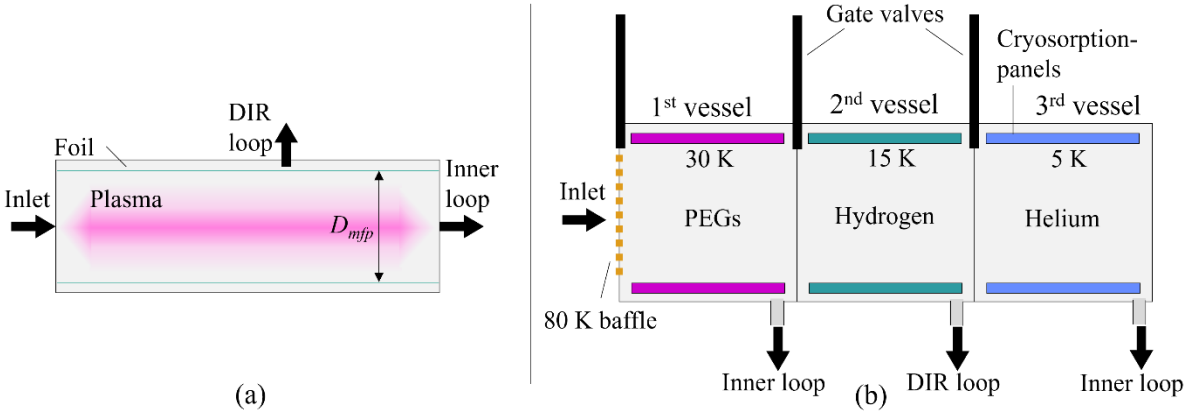

Figure 1.6: Fuel separation concepts for Direct Internal Recycling: (a) a metal foil pump consisting of a cylindrical plasma in the center with a surrounding metal foil and (b) a multi-stage cryopump with separable chambers for sorption of the different gas species.

Its continuous operation mode, significantly lower tritium inventories, no need for cryogenic infrastructure, lower power consumption and a high purity DIR stream are the main benefits of the MFP over the MSC, making it the more elegant and desirable solution. Prospects of space consumption also favor the MFP over the MSC. This is faced by the lower technology readiness level, making the MFP also the riskier candidate. This work aims at progressing the MFP's readiness in a structured approach. Knowing the magnitude of the recycled flows, the pressure regime as well as the space for installation of the technology allows designing a MFP, which is able to fulfil the requirements of throughput and separation in the given environment.

1.4 Objectives and structure of work

This work focuses on the development of a conceptual design of a metal foil pump (MFP), which allows the realization of the DIR concept for a demonstrational fusion power plant. Such development builds on existing knowledge on the MFP and expands it towards an application by use of experiment and simulation. A model is created that allows parametric testing of different MFP geometries and predicting their performance in view of a scale-up for power plant application.

In line with the above-mentioned objectives, the present work is structured as follows.

The present section introduced the concept of Direct Internal Recycling with the possible realization in the KALPUREX process. The requirements of a fuel separation technology are formulated and two options, the metal foil pump and the cryopump, are presented.

Section 2 explains the basic physics of "Superpermeation in a metal foil pump". This chapter gives the baseline for the direction, in which the research of the second main component of a metal foil pump, a plasma source, is tailored.

The ensuing section 3, "Plasma in plasma-driven permeation applications" is aimed towards giving an understanding of plasmas and the processes that take place in plasma and potentially affect superpermeation. An analysis of the suitability of different plasma sources for application in a MFP in EU-DEMO is presented.

A "Verification & validation strategy towards a closed MFP design" is lined out in section 4. It delineates the development plan that has been followed to advance the technological readiness level of a MFP and produce a simulation and experiment based model that allows scaling and predicting the performance of a MFP.

Section 5, "Simulation of microwave generated hydrogen plasma in a MFP", explains the modelling of a hydrogen plasma with a fluid approach and appropriate choice of boundary conditions.

The most important results of parametric studies are presented, focusing on the production of atomic hydrogen, which is condensed into a single excitation probability by simplification of the plasma simulation.

In section 6, “Hydrogen plasma experiment and diagnostics”, the experimental facility HERMES*plus* is introduced and the experimental methodology is explained. The experimental method for validation of the plasma simulation, actinometry with optical emission spectroscopy, is introduced and its validity is demonstrated.

In sectin 7, “Parametric studies of plasma and metal foil operation”, results of the atomic hydrogen density measurement are presented and compared to the simulation results. The sensitivity of the plasma-driven permeation process to various operation parameters such as plasma power, pressure, foil temperature and noble gas presence is shown with respect to a detailed analysis of the metal foil condition in the experiments.

The “Integral performance assessment of a power plant MFP” is done in section 8 using a Test Particle Monte Carlo approach. For three designs, developed in this work, each with their individual combination of plasma sources and metal foils, pumping speed and separation ratio are evaluated using the free molecular flow code ProVac3D. Based on findings in sensitivity studies of the operational parameters and characteristic dimensions of the designs on one side, and by considering the requirements lined out in section 1.3 on the other side, a recommendation for the design in EU-DEMO is given.

An outlook and a summary are given in section 9.

2 Superpermeation in a metal foil pump

Superpermeation, which is the working principle behind a metal foil pump (MFP), shares some features with the process employed in classical permeators, such as the high permeation selectivity for hydrogen, yielding an output with high purity. But there are also important differences between the two technologies. In classical permeators, the permeation is driven by concentration gradients, which translates into poor performances in terms of fluxes at the low pressure range the MFP is expected to work in. Instead, superpermeation utilizes an energy gradient from the hydrogen upstream of a metal foil to downstream to drive a permeation flux through it. This also allows for compression against pressure gradients, which is unfeasible with classical permators. Superpermeability can be defined by an orders of magnitude larger probability for particles to permeate through a foil than in the case of regular concentration driven or also called gas-driven permeation (GDP) [38]. In this section, the background and physics of the process of superpermeation are introduced, the key component for the generation of the energy gradient is described and the possible effects of this component on the metal foil surface are presented.

2.1 Gas-driven permeation and superpermeability

Before adressing superpermeation, the sketch in Figure 2.1 is used to describe the classical permeation of hydrogen. Approaching a metal lattice (grey dots in the Figure), hydrogen (blue, shaded dots) in the form of a molecule can dissociate after interacting with the metal surface and be adsorbed on it in atomic form. An exposed metal surface can act as a catalyst by lending to the incoming hydrogen one of its free electrons to fill its outer electron shell, greatly increasing the likelihood of successful absorption into the metal. This process happens at so-called surface sites. The energy necessary for the dissociation of the hydrogen molecule can be supplied as thermal energy by the surface or be carried as kinetic or potential energy by the molecule itself. Inside of the metal lattice, the hydrogen moves via the interstitial sites and can reach the downstream surface by a random walk process that is known as diffusion. There, to complete the permeation process, the diffused particle can recombine with another hydrogen atom and be released into the gas phase again. The interaction with the bare metal surface is crucial to this type of permeation as it enables the dissociative absorption in the first place.

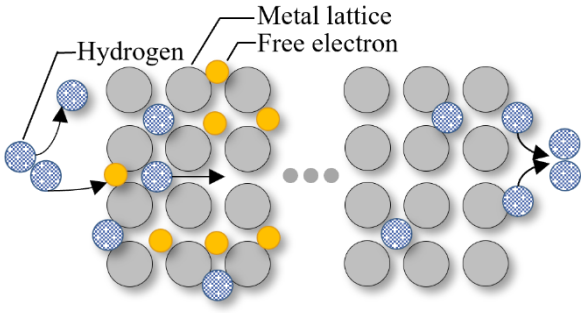

Figure 2.1: Sketch of hydrogen (blue, shaded dots) permeation through a metallic (grey dots) membrane upon catalytic dissociation of the hydrogen using the metal's free electrons (yellow dots).

Superpermeation, however, is based on the presence of an energetic permeation barrier, usually caused by a non-metallic impurity (such as oxygen, carbon or sulphur) [38-40] on the surface of the metal, typically in a mono-atomic layer as depicted in the red, striped dots in the sketch in Figure 2.2. Such a layer inhibits the interaction of the hydrogen with the free electrons of the metal, greatly reducing dissociative absorption. The energy barrier means that the required absorption energy is elevated in absence of the metal's catalytic role. If the hydrogen arrives at the surface already carrying the energy required for absorption, e.g. in atomic form, it can be absorbed into the metal despite the surface barrier with higher probability than molecules [40]. In literature, this state of hydrogen is typically referred to

as suprathermal as the hydrogen particles that are absorbed in this way are not in thermal equilibrium with the gas in front of the foil. The key to superpermeation is introducing a source of suprathermal, e.g. atomic hydrogen only at the upstream side of the foil. While this increases the absorption flux on this side of the foil by orders of magnitude, the absorption flux on the downstream side remains unchanged. As the membrane fills up with hydrogen, reemission fluxes towards both sides of the foil are established based on the ratio of the surface energy barriers. A higher upstream barrier than downstream indicates a favorable asymmetry in the energy barrier and allows for higher permeation probabilities as long as the suprathermal hydrogen can still be absorbed. In the case of symmetric surface barriers, half of the implanted flux can be considered to permeate through a thin foil.

Some metals naturally form such impurity monolayers and, thereby, produce high absorption barriers to hydrogen like the group 5 metals Nb [41], V [35] and Ta [38], which have been researched for application of superpermeation extensively. Other materials that have peaked the interest of researchers for this application are Pd [42-44], Mo [45], Ni [46] and Fe as well as coated Fe foils [47] [48]. Reviewing the data on different materials for application of superpermeation, no consistency in ranking the candidate materials corresponding to their suitability emerges. According to theoretical considerations, however, the group 5 metals, especially Nb and V, are the most promising materials due to their low energy diffusion barrier within the bulk but generally high surface barriers due to the naturally present non-metallic impurity layers [35].

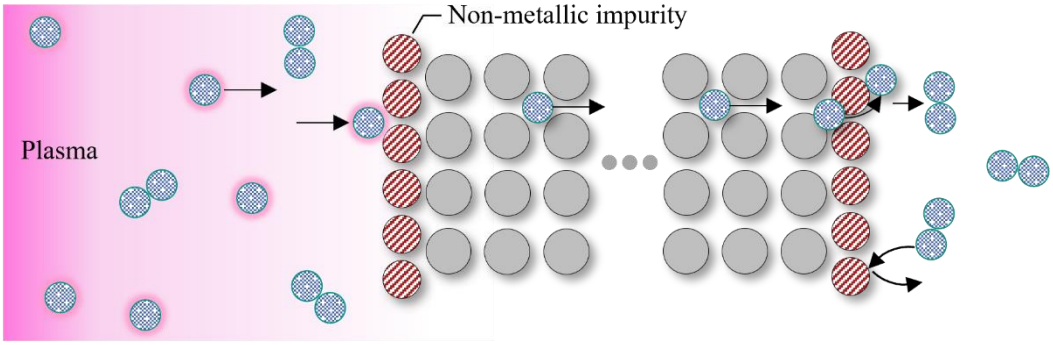

Figure 2.2: Sketch of plasma-driven permeation of hydrogen (blue, shaded dots) through a metal (grey dots) with non-metallic impurity monolayer (red, striped dots) on its surface.

Three different types of permeation have to be distinguished. Exposing a thin, heated group 5 metal foil to hydrogen without any previous energization of the hydrogen typically leads to the production of a permeation flux driven by a pressure gradient. Vacancies in the impurity layer create active centers of absorption, where the hydrogen molecules can dissociate despite the presence of an impurity layer [40] [49]. This permeation is referred to as gas-driven permeation (GDP) and the probability of molecular hydrogen to dissociatively absorb is called molecular sticking coefficient. The other two permeation processes emerge from the supply of suprathermal hydrogen. The first uses incandescent filaments, which dissociate hydrogen that impinges on their surface [50] [51], mainly producing atomic species, thus leading to atomic-driven permeation (ADP). The second is plasma-driven permeation (PDP), which is caused by plasma and, hence, also associated with ion supply. All three of these permeation phenomena are hydrogen-selective [31].

2.2 Sources of suprathermal hydrogen

Incandescent filaments have been used in superpermeability studies for the supply of suprathermal hydrogen extensively [40] [52] [53] even though their use has several limitations. First, the pressure range of applicability is limited to the sub-Pa regime due to a decrease in atomization efficiency with pressure [31] [51]. Although no exact values for the sub-divertor pressures are known at this point in time, the conceptual design of a MFP has to account for reliable operation up to 10 Pa, far exceeding

the range in which filament use is reasonable. Furthermore, filaments are operated at high temperatures (~ 2000 K) and, thus, suffer from reliability issues. Previous proposals of metal foil pumps for use in a fusion reactor built on incandescent filaments as source of suprathermal hydrogen and were not continued further [54]. For the stated reasons, they will also not be discussed further in this work as a possible solution for the supply of suprathermal particles in a metal foil pump.

Plasma is an alternative source of suprathermal hydrogen. Industrial plasma sources can excite large quantities of gas particles in a given volume and provide them with the required energy to overcome the surface barrier. Obtaining steady-state PDP operation, however, is challenging due to the typical formation of a plasma sheath in front of the metal foil, which leads to an acceleration of ions towards the surface with the potential to cause sputtering damage or introduce surface defects, which increase local recombination rates of hydrogen [55].

The requirements put on the plasma source of a MFP are not met by all types of plasma sources. Especially the issue of scalability for handling of large throughputs emerges as challenging. The search for such a plasma source has to consider industrial availability, which usally comes with a better understanding of the operation of the plasma.

2.3 Sensitivities of plasma-driven permeation

While there is a broad variety of plasma sources available, only a few types have been studied for their interaction with superpermeable membranes. Those varied in pressure ranges, power densities and electron temperatures – all of which are important parameters to influence the possible effect of plasma particles on the surface of the metal foil and the permeation fluxes. In [34], an array of metal filaments was biased against the surrounding vessel by several tens of V in order to operate a multicusp plasma that achieved long-term (300 h) steady-state PDP within a pressure range of 0.13 to 4 Pa and substantial permeation fluxes of 10^{17} H cm^{-2} s^{-1}. The electron energy in this setup was assumed to be below 1 eV [35]. The observations show the great potential of PDP with this kind of plasma source, which, on the other hand, is somewhat limited in its scalability. Another candidate plasma source concept features electron-cyclotron-resonance (ECR) heating of electrons by combination of microwaves and magnetic fields. Those plasmas can typically operate to pressures below 0.1 Pa and achieve high electron energies of up to 5 eV [56] [57]. A third type of plasma source features a hot-cathode duopigatrone and a penning cell placed in transverse electric and magnetic fields to produce electron densities of up to 10^{16} m^{-3} and electron energies of a few eV [49]. Ion beams with higher particle energies (> 1 keV) have also been studied but typically showed worse performance [58], which can mainly be attributed to the destruction of the upstream surface impurity layer. Glow [59] and radiofrequency (RF) discharges [60] [61] have also seen some application in superpermeability experiments but have not been imagined in designs of a metal foil pump thus far either.

Considering the use of a component employing PDP based superpermeation for unburnt fuel separation inside the pump duct of a fusion reactor, the necessity of using the available space efficiently becomes clear. This motivates finding a plasma source that produces large enough densities of suprathermal particles and is capable of providing sufficiently high flows, without negatively impacting the metal foil surface condition in the long run. From the available literature, only little general conclusions on the performance of the different kinds of plasma sources can be drawn. It can be stated that reports on PDP have been limited to pressures below 4 Pa. Lower pressures are typically associated with higher electron energies, increased production of suprathermal particles and less effective heating of the gas particles. As some publications on PDP stress, achieving stability of the foil condition is not always trivial [36] [62]. Specifically high energies of particles impacting on the upstream surface of the foil can negatively impact the performance. In cold plasma, such particles typically origin from acceleration in a plasma sheath in front of the foil or by application of a potential bias on the foil. While high electron energies increase production rates of suprathermal particles, they can also be the cause of

damage to the foil by forming larger sheath potentials as will be explained in section 3.3 in detail or by producing larger quantities of fast neutrals in dissociative reactions. Subsequently, finding a balance between sufficient power density and plasma volume for production of plenty suprathermal particles and long-term steady state operation emerges as a major challenge in the selection process of a suitable plasma source. Developing a design of a metal foil pump includes integration of such a plasma source technology with a metal foil that utilizes the plasma particles efficiently.

The characteristics of the plasma source employed in a PDP process only represent one link in the chain. The other major factor to account for is the condition of the superpermeable foil and how it capitalizes on the suprathermal particles supplied by the plasma source. In the following, the relationship between the actually permeating flux and the flux of incoming suprathermal particles is explained and the sensitivities of the foil lined out. Considering a supplied flux of suprathermal particles onto a metal foil $j_{in,0}$, the upstream absorption flux of suprathermal particles

$$j_{abs,0} = j_{in,0}\xi, \tag{2.1}$$

depends on the suprathermal particle's probability for absorption ξ. The index 0 denotes the upstream surface of the foil while l is used further below to refer to the downstream surface.

In the case of dissociative absorption of molecules, the situation is quite different. This process depends on the availability of active centers for thermal absorption [35], which can be expressed through the degree of surface coverage θ of an agent inhibiting absorption site formation, such as an impurity monolayer. Unlike the absorption of suprathermal particles, it is temperature dependent and described by an Arrhenius' relation

$$j_{m,abs,0} = j_{m,in,0}\alpha_{m,0} = j_{m,in,0}\alpha_m^*(1-\theta)exp\left(\frac{-2E_a}{RT}\right), \tag{2.2}$$

in which $j_{m,in,0}$ is the incoming flux of molecules to the upstream surface and $\alpha_{m,0}$ is the upstream molecular sticking coefficient which follows an Arrhenius function with the pre-factor α_m^*, the surface coverage θ, the universal gas constant R and the activation energy for absorption into the metal E_a. This activation energy can be different on each side of the foil, causing different sticking coefficients and surface asymmetry. Peters [31] introduces an asymmetry factor ε_f as the ratio of upstream to downstream product of surface roughness factor σ_{rou} and recombination rate factor k_{rec}

$$\varepsilon_f = \frac{\sigma_{rou,0}k_{rec,0}}{\sigma_{rou,l}k_{rec,l}}. \tag{2.3}$$

The surface roughness factor itself is the ratio of real surface to the expected one if it is perfectly flat. Especially under plasma exposure, this variable has been shown to deviate from 1 due to the creation of surface defects. Peters has shown that the solubility of the metal K as described in Sievert's law by the ratio of the molar concentration of hydrogen in the metal c_H to the square-root of the hydrogen partial pressure p in the gas-phase

$$K = \frac{c_H}{\sqrt{p}}, \tag{2.4}$$

has a simple relationship with the recombination rate factor and the molecular sticking coefficient

$$k_{rec} = \frac{\alpha_m Z}{K^2}, \tag{2.5}$$

through the kinetic gas theory coefficient Z

$$Z = \left(2\pi m_i k_B T_g\right)^{-0.5} \cdot N_A^{-1}, \tag{2.6}$$

in the case of local equilibrium, when the solubility can be described just from surface processes. N_A is Avogadro's constant. In eq. (2.6), m_i denotes the mass of element i in kg, k_B is Boltzmann's constant and T_g the gas temperature in K.

The details of the permeation behavior can be derived on the basis of the H-metal energy diagram. Such a diagram is specific to the metal and its surface condition. The phenomenon of interest is the permeation of H through a metal with a self-replenishing non-metallic monolayer and exothermic absorption such as Nb or V as this is the system to be employed in a MFP. The corresponding diagram is depicted in Figure 2.3. In the H-metal system, let a ground-state hydrogen molecule in the gas-phase infinitely far from the metal surface have an energy of E = 0 per definition. When physisorbed on the surface, the hydrogen is energetically in the valley left of location (a). By supply of the energy portion E_{a1}, it can be dissociated to overcome the energy barrier (a). This energy can be supplied by a heated foil. Each of the two hydrogen atoms of the molecule end up at a surface-absorbed state with E_{a2} (b) that is stable. More energy has to be supplied to move the hydrogen from there. The presence of a non-metallic impurity monolayer on the surface causes high activation barriers to the movement of the hydrogen from the subsurface to surface sites and vice versa. Those barriers are described by E_{a3} (c) and they lead to the condition of strong internal reflection [49] [63]. Once absorbed, a hydrogen atom diffuses back and forth through the metallic bulk before reemission, either upstream or downstream. This behaviour causes a smoothening of the hydrogen concentration throughout the bulk and justifies the assumption of a homogeneous concentration c_H along the foil thickness. Under ambient conditions, the non-metallic impurity can take the form of a "thick" oxide layer but if the metal is heated, the oxygen solubility increases and it is dissolved into the bulk, while a stable monolayer remains, giving rise to superpermeability. The diffusion energy E_d is supplied to the H atom by lattice vibrations (i.e. temperature) as it moves along the grain boundaries. The impingement of an atomic H from the gas phase is also depicted in the diagram with it being unaffected by the molecular adsorption barrier (a), and directly overcoming the surface barrier (b), yielding the subsequent absorption into the subsurface, from where it can diffuse towards the downstream surface.

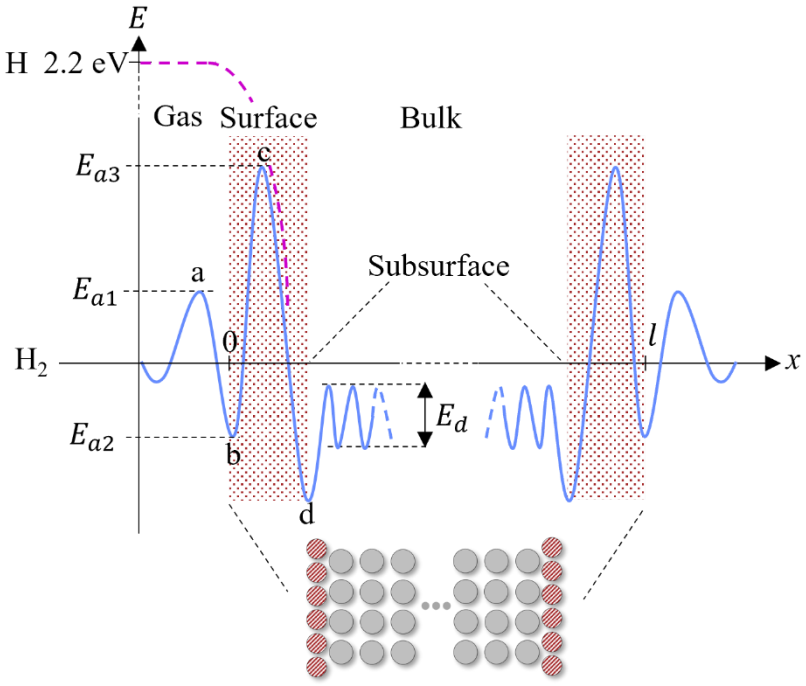

Figure 2.3: Energy diagram for the hydrogen-metal surface interaction in the case of a group 5 metal with non-metallic impurity monolayer on the surface.

Neglecting absorption on the downstream surface is reasonable if the pressure there leads only to fluxes in the backstream direction orders of magnitude below the suprathermal absorption flux $j_{abs,0}$. In this case, the permeation flux j_p during PDP equals the release flux on the downstream surface based on the balance of incident flux and reemission flux upstream $j_{rem,l}$

$$j_{perm} = j_{rem,l} = \sigma_{rou,l} k_{rec,l} c_H^2 = j_{in,0}\xi - \sigma_{rou,0} k_{rec,0} c_H^2. \tag{2.7}$$

Eq. (2.7) assumes a homogeneous concentration of hydrogen c_H throughout the whole thickness of the foil, which is fulfilled for a strictly surface limited operation regime. Rearranging eq. (2.7) to $j_{in,0}$ is useful to express the permeation probability χ

$$\chi = \frac{j_{perm}}{j_{in,0}} = \frac{\sigma_{rou,l} k_{rec,l} c_H^2}{\sigma_{rou,l} k_{rec,l} c_H^2 + \sigma_{rou,0} k_{rec,0} c_H^2}\xi \tag{2.8}$$

which, by using eq. (2.4), turns to

$$\chi = \frac{\sigma_{rou,l}\alpha_{m,l}}{\sigma_{rou,l}\alpha_{m,l} + \sigma_{rou,0}\alpha_{m,0}}\xi \tag{2.9}$$

or by expansion with ε_f

$$\chi = \frac{\sigma_{rou,l} k_{rec,l}}{\sigma_{rou,l} k_{rec,l} + \sigma_{rou,l} k_{rec,l}\varepsilon_f}\xi = \frac{1}{1+\varepsilon_f}\xi \tag{2.10}$$

which shows a direct correlation of surface asymmetry and permeation probability for the case of surface limited permeation. Assuming perfectly symmetrical surfaces, ε_f becomes unity and the permeation probability is half the absorption probability ξ.

Thus, the condition of the surfaces has a tremendous impact on the permeation process. Eq. 2.10 shows the potential of manipulating the surface barriers towards high upstream and low downstream barriers. However, such a change in the surface condition is not straight forward. The upstream barrier should not hinder the absorption of hydrogen atoms, which might not be fulfilled with any upstream surface condition. An increase in the downstream recombination factor by one-sided coating with Pd has shown promising results but led to the two material's interdiffusion [64]. The group of T. Fuerst investigates the introduction of nanolayers between the metal foil and the Pd coating to prevent this diffusion while still enabling the hydrogen to pass through [65]. Nonetheless, active surface manipulation is out of the scope of this work, which restricts itself to the investigation of plasma and plasma-surface phenomena and the design of a MFP based on the findings with readily available pure metal materials.

3 Plasma in plasma-driven permeation applications

The performance of a MFP is linked to the efficiency of suprathermal particle production with a suitable amount of energy to overcome the non-metallic impurity monolayer on the foil surface but, also, to not damage this layer. The characterization of the MFP plasma is essential to the description of the superpermeation process and to the quantification of the performance of a MFP. It builds on the principle physics of rarefied gases, which ties into the description of cold plasma, for which a focus on collisions and energy distribution functions is essential. In order to implement cold plasma physics into a simulation model, the interactions between energetic particles in the gas phase but also surface reactions are described in a general way. A review of plasma source technologies possibly applicable in a MFP focuses on the description of a linearly extended microwave plasma source, for which the physics of power transfer from the electromagnetic wave into the gas phase is explained. The chapter closes with the description of effects arising in such a plasma with a superimposed magnetic field, allowing for a critical analysis of the operation of the MFP.

The term plasma was first coined by Langmuir in 1928 [66] and is also commonly referred to as the 4th state of matter [67]. While, technically speaking, this is not an appropriate description of the plasma-state, it can help understanding how plasma forms. Any element can be present in solid state and when increasing the temperature further and further, it first becomes liquid and then gaseous. The transition of those states is accompanied by a change in the enthalpy of the matter. In this way, an isobaric phase transition is always linked to an exchange of heat. Delivering energy to gas at constant pressure leads to an increase in temperature, i.e., an increase in the velocity of the gas particles. They can collide elastically or inelasically in the gas phase, depending on the energy of their collision. The key to plasma is the presence of inelastic collisions. Those collisions are powerful enough to strip the atoms or molecules (in the following also considered as “heavy species”) in the gas of their electrons and create a state of ionization. An important characteristic of the plasma emerges as the degree of ionization y_{ion}, which can be expressed by the ratio of the ion density n_{ion} to the heavy species density, which is composed of of the neutral particle density of the background gas n_g and the ion density as stated in equation 3.1 [68]

$$y_{ion} = \frac{n_{ion}}{n_g + n_{ion}} = \frac{n_e}{1} \cdot \frac{p}{RT_g} N_A, \tag{3.1}$$

in which p is the pressure, R is the universal gas constant and T_g is the gas temperature in K. On macroscopic scales, plasmas exhibit charge neutrality.

In plasma, the temperature T of particles is described by equivalent energies in electronvolts (eV). The conversion between eV and Joule comes from the idea that an elementary charge, i.e. an electron, can be accelerated by a specified potential, obtaining kinetic energy equivalent to its charge number and the voltage V. In this way, 1 eV is equal to 1 J over the elementary charge e (=1.602 · 10^{-19} C). Multiplication of the temperature in K by Boltzmann’s constant k_B (=1.381 · 10^{-23} J K^{-1}) yields an energy, which is then divided by the elementary charge e according to equation 3.2 to obtain the temperature in eV.

$$T_e(in\ eV) = T(in\ K)\frac{k_B\left(in\frac{J}{K}\right)}{e(in\ C)} \approx \frac{T\ (in\ K)}{11600}. \tag{3.2}$$

Generally, the temperatures of the electrons T_e, ions T_{ion} and neutral gas particles T_g are distinguished. In many industrial plasma sources, the power is applied via acceleration of the electrons, which are subsequently much faster than ions or neutral background gas particles. Such plasmas are also commonly termed non-thermal plasmas or cold plasma because the heavy species are not in thermal equilibrium with the electrons. In thermal plasmas, however, heavy species possess a temperature

comparable to that of the electrons. An example of such a plasma is the magnetically confined fusion plasma. Showing a broad variety of characteristics, cosmic plasmas do not only exist as nebulas or stellar remnants like white dwarfs but also in form of active stars like the sun. Some examples of cosmic and technical application plasmas are classified in the illustration in Figure 3.1 according to their electron temperature and density. The industrially available plasma sources that are interesting for application in the MFP will rank on the bottom left of the graph as the electron energies are typically below the range of a few eV at the given pressures and the electron densities below 10^{18} m^{-3}. Thus, they are also considered weakly ionized plasma as the electron density is orders of magnitude below the neutral density and electron-neutral collisions play an important role within the plasma [68]. Some examples for such plasma sources are given in section 3.4.

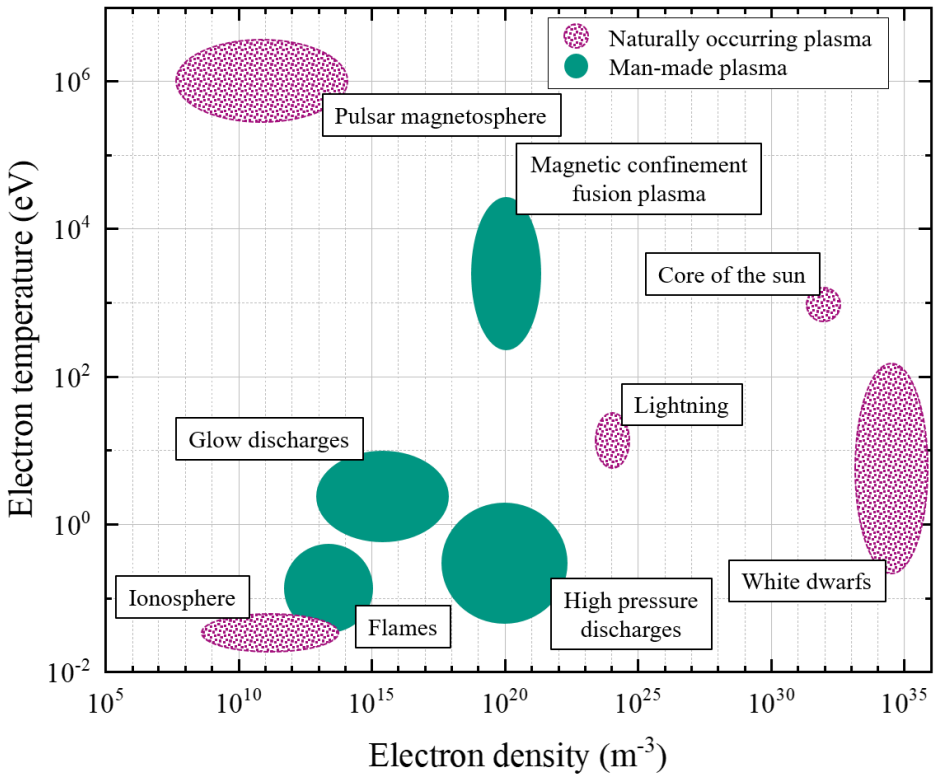

Figure 3.1: Different types of naturally occurring and man-made plasma and their respective electron densities and temperatures [68] [69].

3.1 Description of particle transport in vacuum

While there are approaches to describe single particle behavior, its common practice to use statistical thermodynamics and the kinetic gas theory to describe the macroscopic plasma behavior. In a gas, not all particles have equal velocity but a velocity distribution function, which describes the position $\vec{x}$ and the velocity $\vec{v}$ at the time t. The Maxwell-Boltzmann distribution f_M poses a commonly used, idealized example to describe the velocity distribution as it assumes thermodynamic equilibrium among a particle ensemble. Assuming that the velocity distributions in the different directions in space are isotropic and independent, one can express the Maxwell-Boltzmann distribution as [70]

$$f_M(m,T,v) = 4\pi n v^2 \left(\frac{m}{2\pi k_B T}\right)^{1.5} \exp\left(-\frac{mv^2}{2k_B T}\right). \tag{3.3}$$

Here, n denotes the number density and v the scalar amount of the velocity vector, which is composed of the velocities in the three dimensions of space $v = (v_x^2 + v_y^2 + v_z^2)^{0.5}$. One can exchange the

term $\frac{v^2 m}{2}$ for the kinetic energy E_{kin} to express the Maxwell-Boltzmann distribution as an energy distribution in the way:

$$f_M(T, E_{kin}) = \left(\frac{4E_{kin}}{\pi k_B^3 T^3}\right)^{0.5} \exp\left(-\frac{E_{kin}}{k_B T}\right), \tag{3.4}$$

which causes vanishing of the particle mass. Hence, a system with particles of different mass can, in global equilibrium be described by a single energy distribution. Using eq. (3.3), one can derive the mean velocity $\bar{v}$ of a particle of a given distribution f_M, or in other words the thermal velocity, by integrating from 0 to infinity over the product of velocity and probability density

$$\bar{v} = \int_0^\infty v f_M(m, T, v) dv = \left(\frac{8k_B T}{\pi m}\right)^{0.5} or \left(\frac{8RT}{\pi M}\right)^{0.5}, \tag{3.5}$$

where M is the molar mass. Another important variable in vacuum as well as plasma applications is the flux of particles through an imagined plane caused by their random motion. This can, for example, be the opening of a channel or a solid surface like a reactor wall. In this case, the flux is also called impingement flux. It is obtained by integration over the product of probability density and the particle number density n [71], which leads, after simplification, to

$$\dot{n}_{imp} = \frac{\bar{v}}{4} \cdot n = \sqrt{\frac{8k_B T}{\pi m}} \cdot \frac{p}{4RT} = \frac{p}{N_A} (2\pi m k_B T)^{0.5}, \tag{3.6}$$

in particles m^{-2} s^{-1}. In vacuum technology, the $p\dot{V}$-flow is frequently used and it is easily derived from the molar flow $\dot{N}$ by using the ideal gas law or from the bulk flow velocity u of a gas flowing through a channel with the cross-section A at a pressure p according to

$$p\dot{V} = J = \dot{N}RT \equiv u \cdot A \cdot p. \tag{3.7}$$

In correspondence, volumetric flow pumped by a vacuum pump is also referred to as pumping speed S, which is composed of an ideal pumping speed S_{id} and a capture coefficient ψ according to

$$S = S_{id}\psi = \frac{\bar{v}}{4} \cdot A\psi. \tag{3.8}$$

The ideal pumping speed describes the amount of gas evacuated by a pump with an opening cross-section A per unit time in case that all arriving particles with the thermal velocity $\bar{v}$ are being pumped. For a real vacuum pump, the pumping speed S is smaller than S_{id} by the capture coefficient pre-factor (which assumes a value between 0 and 1), which considers the reflection of a certain fraction of the incoming particles. Often, the conductance C in the channel in front of a pump has to be considered as it can be compromised by small cross-sections for the flow, which leads to the formation of a pressure profile in the channel according to

$$\Delta p = \frac{J}{C}, \tag{3.9}$$

where J can be expressed through the pumping speed and the pressure at which the flow is pumped. The conductance of pipes and orifices depends on the flow regime and can be assessed using analytical formulas. Different flow regimes and how they are distinguished is introduced below.

Arriving at thermodynamic equilibrium requires the exchange of energy between particles by collisions. In plasma, one has to differentiate between “normal” and Coulomb collisions. The latter occur between electric charges, which interact over larger distances than the particles in a neutral-neutral or neutral-charge collision. The stronger the degree of ionization in a plasma, the more important charge collisions

become. The kinetic gas theory describes the distance, which neutral species can travel before they, on average, collide with another moving particle as the mean free path λ_{mfp}. It can be calculated by

$$\lambda_{mfp} = \frac{k_B T_G}{\sqrt{2}\pi d_{kin}^2 p}, \tag{3.10}$$

where d_{kin} is the diameter of the collision cross-section, which is often taken as the kinetic diameter of an atom (or molecule, respectively) if it collides with an atom of the same element.

The assumption of thermal equilibrium is not always fulfilled in gases or plasma. A more accurate description of non-equilibrium systems is given by the Boltzmann equation. It describes a distribution of particles in six-dimensional phase space, composing of the particles' position $\vec{x}$ and velocity $\vec{v}$ at a certain time t and independence of $\vec{x}$ and $\vec{v}$ from each other [68]. Over time, the distribution can change due to movement and due to external forces $\vec{F}$. As such, gravity is often neglected but, in the case of charges for example, electric and magnetic fields can be of importance [72]. While there are collisionless forms of the Boltzmann equation, it is reasonable to consider a collision term that takes into account changes in the distribution function due to particle interactions with each other [68]

$$\frac{df}{dt} = \frac{\partial f(\vec{x},\vec{v},t)}{\partial t} + \vec{v}\frac{\partial f(\vec{x},\vec{v},t)}{\partial \vec{x}} + \frac{\vec{F}}{m}\frac{\partial f(\vec{x},\vec{v},t)}{\partial \vec{v}} = \left(\frac{\partial f(\vec{x},\vec{v},t}{\partial t}\right)_{coll}. \tag{3.11}$$

The Boltzmann equation restricts itself, however, to only consider binary collisions and assume molecular chaos, which means that intermolecular interaction times are much larger than the time of free motion. Three-body collisions have a much smaller likelihood than two-body collisions and, thus, can often be neglected for low pressure systems. The importance of the collision term can be evaluated using the Knudsen (*Kn*) number. It is a dimensionless number that is determined by the ratio of the mean free path within a gas to the characteristic length l_c, of the gas confining domain according to

$$Kn = \frac{\lambda_{mfp}}{l_c} = \frac{k_B T_G}{\sqrt{2}\pi d_{kin}^2 p l_c}. \tag{3.12}$$

Depending on the value of Kn, several different flow regimes are distinguished. For computational reasons, calculations rarely use an exact description by solving the Boltzmann equation but instead rely on simplifications, accounting for the flow regime of the problem. For simple geometries, analytical equations with empirical correction factors [73] can be used to describe the flow in the whole range of rarefaction. For high *Kn* (> 10), free molecular flow is assumed. This means that scattering between particles is neglected and wall collisions are predominant. The Test Particle Monte Carlo (TPMC) method represents an option for numerical simulation of more complex models in the case of collisionless flows. As Monte Carlo method, it produces a statistically averaged result by repeating the same simulation with random sampling. In the case of a gas flow, the random sampling is respected in form of interaction probabilities of the gas particles with specified surfaces. Flows with any Kn number < 0.01 are considered as continuum flow, in which interactions among the particles are dominant and the velocity at the wall is assumed as 0. They are described with the Navier-Stokes equation. Values of $0.01 > Kn \geq 10$ are classified as transition regime and neither continuum, nor free molecular flow simplifications can be utilized. Instead, calculation of transition flows necessitates a kinetic approach, which means obtaining a direct solution of the Boltzmann equation.

To reduce computational expenses, applying simplifications to the Boltzmann equation is common practice as with the Bhatnagar-Gross-Krook (BGK) model [74] in the case of isothermal flows, which introduces kinetic equations to describe the collision integral. The probabilistic Direct Simulation Monte Carlo (DSMC) method employs the same strategy to avoid solving the Boltzmann equation directly, but it is still a rather complex and computationally expensive approach to model vacuum flows. Another

approach uses moments of the Boltzmann equation to express macroscopic quantities such as particle densities, mean velocities and energy densities by averaging over the velocity coordinates of the Boltzmann equation, which allows describing the distribution as a function of space and time [75]. For the description of plasma, the collision integral and collisions in general are of paramount importance and discussed in the following.

3.2 Description of collisions in cold plasma

Ionization of gas is the prerequisite to create plasma. It happens, when the energy exchange in a particle collision is sufficient to knock electrons out of the gas particle's electron shell. Such inelastic collisions can, for a collision between two heavy particles, also result in fusion but also in recombination, dissociation, electronic, vibrational or rotational excitation of molecules or electronic excitation of atoms. For each collision of two particles in plasma, there is a certain occurrence probability depending on the collision partners, the incident angle and, most importantly, the collision energy, i.e. the relative collision velocity. The most important inelastic collisions in cold plasmas are electron-neutral collisions. Their probability is usually given by a collisional cross-section $\sigma_{en}(\epsilon)$ as a function of the electron's energy ϵ. Heavy species chemical reactions are described using Arrhenius' law or with rate constants that take into account the particle densities and the gas temperature. For some collisions, additional particles present nearby can participate in the collision or contribute via stabilization of one of the reaction partners due to absorption of excess reaction energy [68]. Collisions can also be elastic and superelastic. The former means that only a transfer of momentum (or kinetic energy) and not of potential energy of the particles take place and the latter means that one collision partner gains kinetic energy from the potential energy of the other collision partner. Hence, the total kinetic energy of the particles increases in superelastic collisions. In cold plasma, fusion reactions can be neglected due to the low kinetic energies of the heavy species, however, so-called quench reactions, in which heavy species de-excite one another, can sometimes play important roles. Some excitation processes can also produce long-lived meta-stables, the participation of which in further reactions can be significant.

To describe the probability for the result of a single collision, it is sufficient to know the collision partner, the energy and the incident angle of the electron [76]. However, to make predictions on the reaction rates of collisions in a plasma volume, one has to consider that not all electrons in the plasma possess the same energy. Instead, the energy of single electrons in a plasma can have very different values, sometimes ranging over orders of magnitude. Conventionally, the population of electrons is described with an electron energy distribution function (EEDF), which can be based on very different assumptions that lead to simplifications of the Boltzmann equation. Such an EEDF f_e is generally an approximation of reality and used as such in modelling to describe a fluid of electrons, as it is computationally excessive to simulate individual particle's energies and trajectories. The EEDF is a function of the electron energy ϵ. EEDFs with high mean energies ε have a larger fraction of high energy electrons. The high energy tail of the EEDF determines the incidence of high energy collisions such as ionization. Electron energy loss channels, i.e., vibrational excitation of molecules, typically affect the shape of the EEDF significantly, leading to gas-characteristic shapes of the EEDF. EEDFs are usually plotted as the fraction of electrons with a certain energy over the respective electron energy ϵ, meaning the integral of the curve is 1.

The most commonly used type of EEDF is a Maxwellian, coming from the Maxwell-Boltzmann distribution, which assumes thermodynamic equilibrium among all electrons due to high collisionality between them. This assumption is less valid at lower ionization degrees. In a plasma with Maxwellian EEDF, there is no drop in the high-energy tail of the population, which can arise in a real plasma due to consumption of the electron energy by inelastic collisions. A Druyvesteyn EEDF, on the other hand, is usually used to describe plasmas with great differences between electron and gas temperature. It drops off more rapidly at higher energies. A generalized approach that combines the Maxwellian' and the

Druyvesteyn' EEDF with a power factor g that assumes a value between 1 and 2, where 1 yields the Maxwellian and 2 the Druyvesteyn distribution, then reads [72]

$$f_e(\epsilon) = g \cdot b_1 \cdot \varepsilon^{-1.5} \exp\left(-\left(\frac{\epsilon \cdot b_2}{\varepsilon}\right)^g\right), \tag{3.13}$$

with $b_1 = \Gamma \cdot (2.5/a)^{1.5} \cdot \Gamma \cdot (1.5/a)^{-2.5}$ and $b_2 = \Gamma \cdot (2.5/a) \cdot \Gamma \cdot (1.5/a)^{-1}$ and the incomplete gamma function $\Gamma(s) = \int_0^\infty v_e^{s-1} \exp(-v_e)\, dv_e$ with s being a complex number [77] [78]. Under certain conditions, one can describe the EEDF more precisely by approximating a solution of the Boltzmann equation. Assuming spherical symmetry of the EEDF, which presumes spatial homogeneity of the electric field (which is considered in the force-term of eq. (3.4)) and of the collision probabilities for collisions considered in the collision term, one can write the Boltzmann equation in spherical coordinates in velocity space and expand it in spherical harmonics such as [79]

$$f(v, \cos(\tau), z, t) = f_0(v, z, t) + f_1(v, z, t)\cos(\tau) \tag{3.14}$$

when truncating at the 2nd term, which is why this solution is also called two-term approximation. Here, f_0 is the isotropic part of f, f_1 is an anisotropic perturbation, τ is the angle between velocity and the field direction and z is the position along this direction. Still, solving the two-term approximation is computationally very demanding. In Figure 3.2, the different types of EEDFs are shown for a typical industrially used hydrogen plasma with a mean electron energy ε of 3 eV and 4 eV, respectively. The axes are truncated at 100 eV and 10^{-15} $eV^{-1.5}$, respectively, as the corresponding populations beyond those values are already very low and barely contribute to the integral reaction rates of inelastic collisions relevant in laboratory plasmas. The solution of the two-term approximation of the Boltzmann equation uses the assumptions of n_e = 10^{17} m^{-3}, y_{ion} = $3 \cdot 10^{-5}$ and T = 500 K. The Maxwellian EEDF with higher mean energy drops off less quickly with electron energy than the one with lower mean energy. Still, for the majority of the displayed electron energies, the Maxwellian EEDF with 3 eV mean energy assumes larger populations of high energy electrons than the other EEDFs. Up to 30 eV, the Boltzmann solution is in good agreement with the EEDF of the generalized approach using a power factor of 1.5. This generalized approach lies, as to be expected, in between the Maxwellian and the Druyvesteyn EEDF.

Integrating the product of the EEDF (ϵ) of a certain electron mean energy ε with the collisional cross-section $\sigma_i(\epsilon)$ and electron energy ϵ yields the reaction rate $k_{r,i}$ (in $m^3\ s^{-1}$) of a reaction i according to

$$k_{r,i} = \left(\frac{2}{m_e}\right)^{0.5} \int_0^\infty f_e(\epsilon)\sigma_i(\epsilon)\epsilon d\epsilon, \tag{3.15}$$

where m_e is the electron mass. Due to being negligibly small in population at high energies and because of low collisional cross-sections, the EEDF is often truncated at 100 to 1000 eV for cold plasma. Taking into account the densities of the electron and the particle participating in the reaction n_i, one can compute the total reaction rate $k_{R,i}$ in a given volume in $m^{-3}s^{-1}$:

$$k_{R,i} = k_{r,i} \cdot n_e \cdot n_i. \tag{3.16}$$

This equation is crucial to determine the source and loss terms of individual species in a plasma. Reaction rates for quenching of heavy species are described using the collisional cross-section σ_{ij} of the two species i and j and their relative velocity according to

$$k_{r,i} = \sigma_{ij} \cdot \frac{\bar{v}_i + \bar{v}_j}{2}, \tag{3.17}$$

where $\bar{v}_{i,j}$ are the thermal velocities of the gas species.

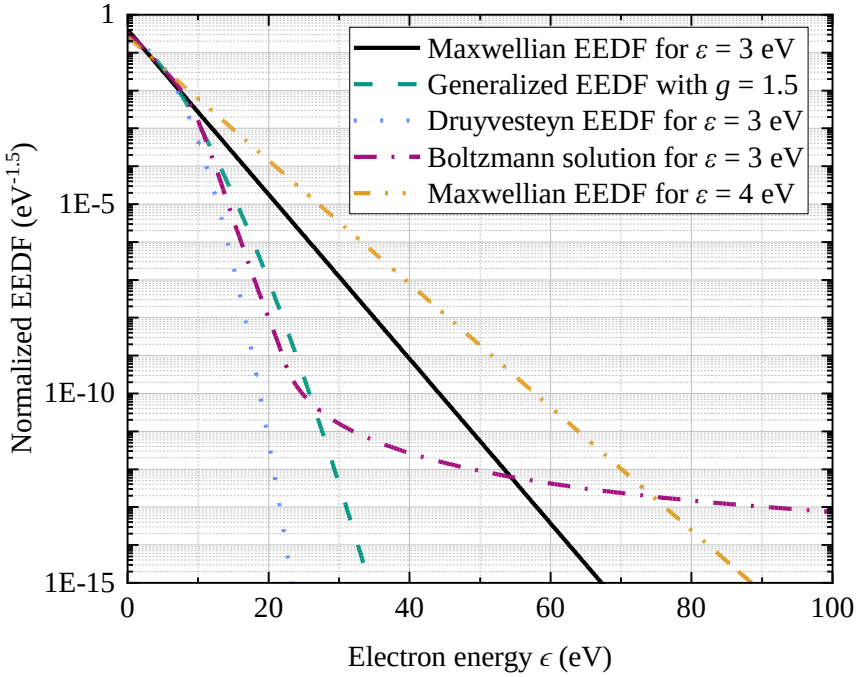

Figure 3.2: Examples of different types of EEDFs in a typical industrial hydrogen plasma for the case of electron mean energies ε of 3 and 4 eV. The solution of the two-term approximation of the Boltzmann equation uses n_e = 10^{17} m^{-3}, y_i = $3 \cdot 10^{-5}$ and T = 500 K; power g = 1.5.

The variety of excited states produced by inelastic collisions differ for atomic and molecular gases, with the former being significantly more simple to describe. Atomic gases, such as the noble gases feature a fully occupied valence electron shell and, hence, are reluctant to chemically bond with other gas-particles by sharing one of their electrons. This is typically done by gases with incomplete valence shells, such as hydrogen (H_2) or oxygen (O_2). Upon impact of a fast electron onto a ground-state atom, an inelastic collision can lead to (i) the electronic excitation of the atom, (ii) ionization of the atom, producing a positive ion and (iii) electron attachment to the atom, resulting in a negative ion. The latter, however, is an unlikely event in the plasmas of interest and, thus not discussed further. Figure 3.3 shows a schematic presentation of the different energy levels an atom or molecule can assume based on electronic, vibrational or rotational excitation.

In electronic excitation, a part of the incoming electron's energy is absorbed by the electron shell of the atom collision partner to lift a valence electron into a higher energy level as shown on the left side of the scheme. For each different atomic species, there are specific energy levels, which the valence electrons can assume. Electronic excitation requires energy exchanges in the range of a few eV up to the ionization threshold (13.6 eV for H), at which the electron is completely detached from the shell. De-excitation of the excited state can occur via radiative emission or further collision-induced reactions like quenching reactions between two heavy species. As in excitation, radiative emission only happens in discrete energy portions corresponding to the energy difference between the levels a valence electron can take. The energy of the photon can be calculated with the Planck relation $E = h\nu$, with h being Planck's constant and ν the frequency of the wave, which is obtained from the wavelength λ according to $\nu = c/\lambda$. An emitted photon carries the energy away from the particle and can be spectroscopically detected. Each atom features characteristic emission lines according to the different energy levels the shell electron can assume. This provides an experimental way to monitor such processes. Given the right energy portion to yield allowed transitions, photons can also be re-absorbed to yield electronic excitation. This effect is also termed self-absorption and it finds consideration in the evaluation of spectroscopic data.

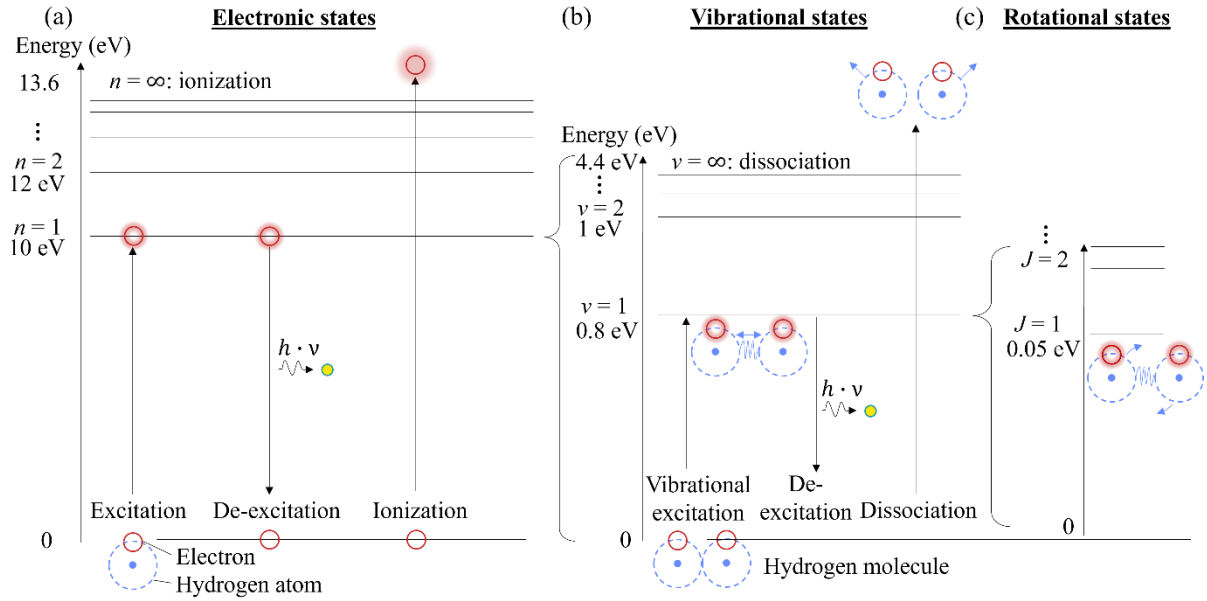

Figure 3.3: Schematic representation of electronic excitation (a) of the hydrogen atom and vibrational (b) and rotational (c) excitation of the hydrogen molecule.

Electronic excitation and ionization can also occur in molecules. However, molecules can also be (iv) rotationally and (v) vibrationally excited, which is possible simultaneously to electronic excitation, increasing the amount of energy levels an electron can take in the shell of a molecule exponentially. The upper threshold for vibrational excitation is the (vi) dissociation energy. Typically, changes in the vibrational state of a molecule are accompanied by energy exchanges of a few tenths of an eV and in rotational state by a few hundreds of an eV. As in electronic excitation, vibrational and rotational states can be spontaneously depopulated by emission of a photon. In some cases, like molecular hydrogen for example, this huge variety of possible energy levels of emitted photons generates quasi-continuous spectra. Emission lines in the visual spectrum (400 – 780 nm) give plasmas of different gases their characteristic glow. Despite the impressive visual effect, the gas temperature in such laboratory plasmas is often in the range of the room temperature and only the electrons are hot. Electrons transfer their energy to the gas molecules or atoms in inelastic collisions but momentum exchange is usually poor in low pressure applications. Thus, a majority of the energy is transferred to the walls, which causes their temperature to increase and indirectly contribute to the heating of the heavy species. Plasma-surface interaction features various phenomena dependent on plasma type, wall material and, thus demands a more detailed description.

3.3 Plasma surface interactions in cold plasma

Industrial plasmas, as in a MFP, are contained within closed vessels leading to plasma-surface interactions. This holds especially for low pressure plasmas, in which volume recombination rarely occurs. There are different types of surface interactions. The simplest reaction is the diffuse reflection of the particle on the wall, which typically happens for slow particles. For particle energies below the range of a few 10 eV, the repulsion from the interaction potential dominates and there are high probabilities of back-scattering. Faster heavy species often deposit on the surface or implant in the solid in a certain implantation depth, which increases with the kinetic energy of the particle [72]. Fast heavy particles can also cause physical sputtering, the removal of surface-atoms of the target material. In this way or by fast electron impact, secondary electrons can be emitted. Particles in excited states can be reflected as ground-state particles or stay excited after the reflection. A naturally forming plasma sheath at the plasma-surface interface is responsible for the acceleration of ions towards the surface, which is exploited in industrial surface processing as it intensifies the interaction of plasma and surface.

Plasma sheaths are characterized by a potential drop over a small distance and explained on the basis of the schematic description in Figure 3.4. As electrons from cold plasmas have much higher thermal velocities than ions, they are lost at higher rates to surrounding walls and charge the surface with a negative potential relative to the plasma. This leads to repelling of negative charges and an acceleration of positive charges towards the surface by an electric field $\vec{\boldsymbol{E}}$. The electron density n_e drops off more steeply towards the surface than the ion density, creating a small volume, in which the quasi-neutrality of plasma is not fulfilled. The sheath thickness is typically in the range of a few Debye-lengths λ_D [68], which is the distance, in which charge gradients in plasma can exist without being shielded by other charges. It can be computed with eq. (3.18), in which ε_0 is the permittivity of free space

$$\lambda_D = \left(\frac{\varepsilon_0 \cdot T_e}{e \cdot n_e}\right)^{0.5}. \tag{3.18}$$

Assuming a grounded plasma facing surface at U = 0 V and a cold plasma at U_p, introduction of an insulated probe into the plasma allows for some peculiar observations. If a negative bias is applied to the probe and the voltage increased, electron and ion currents balance each other at a voltage called floating potential U_f. Further increasing the negative bias until running into the saturation of collected ion current yields the plasma potential. In order to confine most of the electrons within the plasma, the plasma potential reaches values of some V, a few times higher than the electron energy in eV [68]. Langmuir used this experiment to study the U-I-characteristic of plasmas and derive electron density and temperature from it [80]. To date, this is used as a simple experimental diagnostic for determination of these parameters but often finds its limitations in the destruction of the probes by the plasma.

There are different models available to describe the interaction of impinging particles and surfaces. One approach for classical trajectory collisions is formulated in the binary collision model. It considers only binary collisions of an incoming particle and individual surface atoms in a single impact. The impact itself can be treated as classical, quantum mechanical or with a semi-classical approximation [72], while the former suffices for most laboratory plasmas. Then, the scattering is not only a function of the impact parameter but also depends on the interaction potential between the two collision partners and is obtained from energy and momentum conservation. Another approach to describe the surface impact is based on a molecular dynamics ansatz, which computes the movement of the surface atoms and their interaction with each other over time.

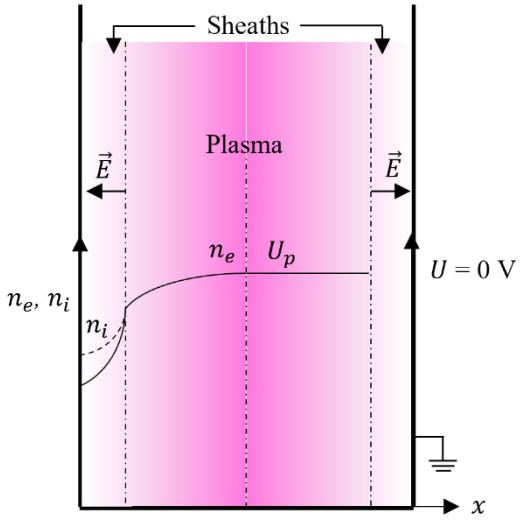

Figure 3.4: Schematic depiction of plasma and its sheath forming at the wall interfaces, where electron density drops. The size of the sheath thickness is increased dramatically for illustration purposes.

Electron-surface interactions such as reflection, electron loss from the plasma or creation of secondary electrons are often described with fixed parameters. But for discharges that rely on secondary electron emission or in plasma with a low volume to surface-ratio, a higher degree of resolution of those processes is necessary. In most cases, a reasonable requirement for the emission of a considerable amount of secondary electrons are primary energies of tens to hundreds of eV. The secondary yield increases with primary electron energy [81]. In the range of 10 eV, there is a threshold to secondary electron emission [82]. Both, the threshold as well as the secondary particle yield heavily depend on wall material and are unique to each experimental setup as minor changes such as surface processing and exposure history matter. For metal-oxides, one typically finds electron yields of 1 per impacting electron around a few tens of eV, while for metals, the required energy for this yield is around 80 eV [83]. With a peak in their energy distribution at ~ 2 eV, secondary electrons always have less energy than the primary electron. There have been several approaches to describe secondary electron emission on electron impact. While the model of [84] captures the yield at higher energies relatively accurately, it does not show good consistency with data at low electron energies close to the threshold. For lower primary electron energies, [83] provides a better analytical fit formula. Their experiments also demonstrate that reflection of the primary electrons without secondary emission happens predominantly for lower energies of the primary and for energies exceeding 50 eV, the main contribution of detected electrons comes from the secondaries.

For some of the heavy species, namely ions, there is not only the kinetic emission but also a potential emission, which is based on the potential energy carried by the impinging particle. Potential emission requires kinetic energies of the impinging ion of at least two times the work function of the target material [81]. However, the electron yield of kinetic emission scales with the kinetic energy of the impinging ion or neutral [85] and becomes dominant for energies in the range of hundreds of eV. Thus, a significant increase in the electron emission yield only occurs at the corresponding energies. The electron yield also increases with the mass of the incoming particle. Similar to electron impact, wall material, condition and experimental history play an essential role for the result of individual collisions. An important parameter describing the heavy particle wall collisions is the thermal accommodation coefficient, which can take values between 0 and 1. At 0, the particle maintains its kinetic energy throughout the collision and it assumes the kinetic energy in equilibrium with the wall temperature at 1.

The majority of surface interaction data available in literature has been obtained from experiments. However, this data only covers a small fraction of the potential interaction scenarios and even for generic cases like ground-state atomic hydrogen recombination coefficients on stainless steel, the values recorded in literature can vary significantly [0.03 – 0.2] [86-88]. Assuming certain values in modeling, thus, is associated with large uncertainties, caused by different surface finishings, oxidation states or operational history [89]. The concentration of a species adsorbed on the surface of a material also affects the interaction of incoming atoms of the same species. Recombination of a gas-phase atom with a surface adsorbed atom by the Eley-Rideal (ER) mechanism is particularly important at high pressures of the atom in the gas phase. The Langmuir-Hinshelwood (LH) mechanism, describing the recombination of two surface-adsorbed atoms and their release into the gas phase, becomes more significant at higher surface temperatures and surface concentrations.

When fully describing the system of a bounded plasma, not only the material and temperature but also the geometry of the plasma vessel can have major impact on the plasma behavior. This stresses the importance of surface characterization and accuracy of data in modelling of plasma. However, the type of plasma source usually defines the design of the plasma vessel, the heating mechanism and a typical range of power densities, which are crucial keystones in the design of a MFP.

3.4 Plasma source technologies for superpermeation

The choice of the MFP plasma source has to match operational requirements given by pressure levels between 0.1 Pa and 10 Pa and, if possible, at 0.5 mPa without external magnetic field. it can be regarded as beneficial if operation at 0.5 mPa is possible without external magnetic field. The MFP is positioned in a domain with a strong, gradient magnetic field of 1.2 T to 0.4 T. The process gases include noble gases and the three hydrogen isotopes, of which tritium requires special treatment, which prevents use of organic hydrocarbon components such as oil or viton gaskets as structural or functional MFP materials. As the main performance driver of the MFP, a high dissociation rate in the plasma is appreciated, which translates to high power densities – while still facilitating the sensitive metal foil surface condition. The plasma source of choice should profit from industrial availability and scalability to reach the desired throughputs by use of the available pump duct space.

None of the plasma sources used in publications on PDP is industrially available and scalable, unlike microwave discharges, which represent an attractive plasma source type with a wide variety of applications. They operate with electromagnetic waves with frequencies above 300 MHz [76], most commonly 2.45 GHz and compose of a magnetron, a dummyload for protection of the magnetron from reflected power, a standing wave ratio meter, matching circuit, a microwave-to-plasma applicator and the plasma chamber [90]. Their design and the plasma they produce can take lots of different shapes like in resonant cavities [91], slot antenna type plasma sources [92], planar microwave plasma [93], electrode discharges [94], volume wave sustained discharges [95] and surface wave sustained discharges [96], to name only a few. The latter are the most commonly used and best researched types of discharges with a wide application range of mPa to several atm and reliable in reproducibility of discharge conditions with stable plasma densities. Surface wave sustained discharges introduce a microwave through a dielectric window along the wave propagation direction. Electrons are displaced by the electric field leading to an oscillation within the plasma, the frequency of which is based on the electron density. This frequency is called the plasma frequency

$$\omega_{pe} = \sqrt{\frac{n_e e^2}{m_e \varepsilon_0}}, \tag{3.19}$$

and the electron density, which produces a plasma frequency equal to the microwave frequency ω is called the critical electron density $n_{e,c}$. Usually, the microwave cannot penetrate into regions, where $n_e \geq n_{e,c}$ because it is reflected by the quickly arranging electrons. External magnetic fields are used to produce plasma with higher electron densities or to extend the operational pressure range to lower values. The plasma source of the MFP should not use permanent magnets or operate with its own magnetic field due to the high external magnetic flux density of ~ 1 T present in the pump duct of a fusion reactor. Microwave plasma sources feature dissociation degrees far higher than ionization rates [97], which is a favourable condition in view of the metal foil's impurity layer maintenance. Using such plasma for the MFP process, atomic hydrogen is the species with the largest contribution to PDP.

An industrially used surface wave sustained plasma source with promising characteristics is the Duo-Plasmaline produced by *Muegge GmbH* [98] [99]. The peculiarity of this plasma source is that the plasma is not ignited within the dielectric but outside of it as shown in the sketch in Figure 3.5. It consists of a waveguide system that supplies a linearly extended coaxial line with microwaves of either 2.45 GHz or 0.915 GHz. The larger the frequency, the higher typically is the power density [76]. The microwave is guided along the coaxial line to the vacuum chamber, which it can enter through a dielectric, commonly made of quartz. Upon entering vacuum, the surface wave radially decays and plasma forms outside of the dielectric. It can take on the role of an outer conductor for further axial transmission of the microwave by reaching the critical electron density to reflect the electromagnetic wave. The two-sided feed system allows for reaching axial homogeneity with electron temperatures of

a few eV and electron densities of up to several 10^{17} m^{-3}, resulting in rather high power densities and dissociation rates of molecular gases. It has been built in length of up to 3 m or in arrays with parallel installation [90], demonstrating scalability.

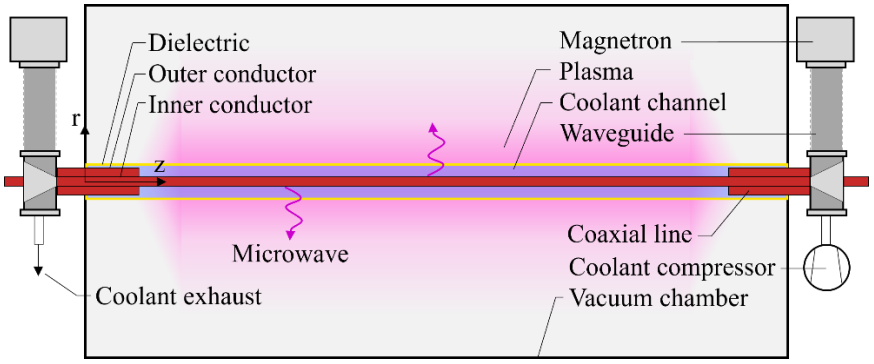

Figure 3.5: Scheme of the linearly extended Duo-Plasmaline with two-sided microwave feed.

3.5 Power transfer in microwave discharges

Here, the plasma physics is described, which is used to simulate a discharge, starting from the energy transfer from the electromagnetic wave to the gas. A microwave plasma is sustained when the available electrons absorb a sufficient amount of power from a microwave in the active zone of a plasma and transfer it to the gas to produce ions and balance charge losses to surrounding walls.

In a microwave plasma, a harmonic electric field with a sinusoidal function in time *t* acts on free charges. Assuming no external magnetic field, the plasma can be considered isotropic and the electromagnetic fields can be described using Maxwell's equations [79]

$$\nabla \times \vec{\boldsymbol{E}} = -\frac{\partial}{\partial t}\vec{\boldsymbol{B}}, \tag{3.20}$$

$$\nabla \times \vec{\boldsymbol{H}} = \overrightarrow{\boldsymbol{J}_p} + \frac{\partial}{\partial t}\vec{\boldsymbol{D}}, \tag{3.21}$$

where ∇ is the nabla operator, which represents the partial derivatives for the three dimensions of space x, y, z, $\vec{\boldsymbol{E}}$ is the electric field in V/m, $\vec{\boldsymbol{B}}$ is the magnetic flux density in T, $\vec{\boldsymbol{H}}$ is the magnetic field in A/m, $\overrightarrow{\boldsymbol{J}_p}$ is the plasma current density in A/m² and $\vec{\boldsymbol{D}}$ is the electrical displacement in C/m². Bold letters indicate the variation with time corresponding to the frequency $f = \omega/(2\pi)$. Another expression for the plasma current density can be derived from the movement of a bulk of plasma with mean electron velocity in the given bulk as a function of time $\vec{\boldsymbol{u}}_e$, electron density n_e and elementary charge e via

$$\overrightarrow{\boldsymbol{J}_p} = -e n_e \vec{\boldsymbol{u}}_e. \tag{3.22}$$

A simplification in the description of the motion of a single electron in an electromagnetic field neglects its thermal motion and the force exerted by the magnetic field. The latter is reasonable if the velocity of the particle is orders of magnitude smaller than the vacuum speed of light *c* [76]. Due to their large mass and the high frequency of the wave, ions remain practically motionless, which allows consideration of solely a fluid of electrons reacting to the electric field for the hydrodynamic description of the plasma. Within a specified region of the plasma, the electron movement can be described with an average velocity $\vec{v}_e$. Furthermore, the electron density is assumed as constant on the microwave timescale since λ_D is much smaller than the scale of the microwave interaction with the plasma [100]. The electron motion can then be expressed by a momentum equation as

$$m_e \frac{d\vec{\boldsymbol{u}}_e}{dt} = -e\vec{\boldsymbol{E}} - m_e \vec{\boldsymbol{u}}_e \nu_m, \tag{3.23}$$

where ν_m is the electron-neutral collision frequency for momentrum transfer. The two terms on the right hand side can be interpreted as force terms caused by the electric field ($-e\vec{\boldsymbol{E}}$) and by friction due to collisions with the heavy species in the gas ($-m_e\vec{\boldsymbol{u}}_e\nu_m$). Because the steady-state solution of eq. (3.23) is a sinusoidal function of time, using phasors allows solving it with $\vec{\boldsymbol{u}}_e$ = Re($\mathrm{u}_e \exp\, j\omega t$), with the upright letter indicating the complex amplitude of the variable, in this case the velocity u_e [76]. The derivative d/dt of the phasor u_e can be substituted by the pre-factor $j\omega$, yielding eq. (3.24), in which $\vec{\mathrm{E}}$ is the complex amplitude of the electric field and $j = \sqrt{-1}$ is the imaginary unit of a complex number:

$$j\omega m_e \mathrm{u}_e + m_e \mathrm{u}_e \nu_m = -e\vec{\mathrm{E}}. \tag{3.24}$$

Multiplication of eq. (3.24) by $-\,e \cdot n_e / m_e$ gives

$$-j\omega e n_e \mathrm{u}_e - e n_e \mathrm{u}_e \nu_m = e^2 \frac{n_e}{m_e}\vec{\mathrm{E}}, \tag{3.25}$$

which can be summarized to

$$-e n_e \mathrm{u}_e = e^2 \frac{n_e}{m_e}\frac{\vec{\mathrm{E}}}{(j\omega + \nu_m)} \; or \; \overrightarrow{\mathrm{J}_p} = \sigma_p \vec{\mathrm{E}}, \tag{3.26}$$

with the important parameter of specific electric plasma conductivity

$$\sigma_p = \frac{e^2 n_e}{m_e(j\omega + \nu_m)}. \tag{3.27}$$

Solving eq. (3.24) for the electron kinetic energy during the oscillation caused by the electric field yields

$$\mathrm{u}_e = -\frac{e\vec{\mathrm{E}}}{m_e}\frac{1}{(j\omega + \nu_m)}, \tag{3.28}$$

which can be translated into the true time-dependent velocity $\boldsymbol{v}_e(t)$ by taking the real part of the phasor $\mathrm{u}_e \cdot \exp(j\omega t)$

$$\boldsymbol{v}_e(t) = -\frac{e}{m_e} Re\left(\frac{\vec{E}}{(j\omega + \nu_m)} \exp(j\omega t)\right). \tag{3.29}$$

To obtain the kinetic energy of an electron in three-dimensional space, the velocity component parallel to a single axis x caused by the electric field aligned to this axis, E_x, can be written as

$$\boldsymbol{v}_x(t) = \frac{e}{m_e}\frac{E_x}{(\nu_m^2 + \omega^2)^{0.5}} \cdot \cos(\omega t + \psi_x), \tag{3.30}$$

where ψ_x is the phase angle. The kinetic energy $E_{kin,x} = m_e v_x^2(t)/2$ follows as

$$\begin{aligned} E_{kin,x}(t) &= \frac{e^2}{2m_e}\frac{E_x^2}{\nu_m^2 + \omega^2}\cos^2(\omega t + \psi_x), \\ &= \frac{e^2}{4m_e}\frac{E_x^2}{\nu_m^2 + \omega^2}(1 + \cos(2\omega t + 2\psi_x). \end{aligned} \tag{3.31}$$

Averaging over one period of the sinusoidal function yields

$$E_{kin,x} = \frac{e^2}{4m_e}\frac{E_x^2}{\nu^2 + \omega^2}. \tag{3.32}$$

All three dimensions of space are considered by summarizing the squared field intensities and substituting E_x for E. Evaluating the case for a microwave plasma like that created by the Duo-Plasmaline, the mean kinetic energy E_{kin} of an electron obtained during one oscillation of the electric field is too low to cause ionization. The displacement length is also considerably smaller than the plasma

vessel dimensions [76]. If the plasma is collisional, the electron continuously picks up momentum in other dimensions of space than that of the oscillating electric field in collisions with the background gas. At some point, its kinetic energy is sufficient to cause inelastic collisions, in which it will lose a part of the energy and the acceleration process starts from new. The impact of the electron-neutral collision frequency for momentrum transfer on the power transfer from the electromagnetic wave to the electron fluid can be found by considering the force on a single electron $-e\vec{\boldsymbol{E}}(t)$ and multiplying it with the mean electron velocity during the oscillation. Averaging over one oscillation, one obtains for the power transfer to the electron fluid [101]

$$P_e = \frac{e^2 E^2}{2m_e} \frac{\nu_m}{\nu_m^2 + \omega^2}, \tag{3.33}$$

where E is the maximum amplitude of the electric field. The total power transfer from the microwave to the plasma can be described through the plasma's conductivity and collisionality. Taking eq. (3.20) and the time derivative of (3.22), the wave equation can be expressed as

$$\nabla \times \mu_r^{-1}\left(\nabla \times \vec{E}\right) - k_0^2 \left(\varepsilon_r - \frac{j\sigma_p}{\varepsilon_0 \omega}\right)\vec{E} = 0, \tag{3.34}$$

where μ_r is the relative permeability of the medium, through which the wave propagates (i.e. plasma), ε_r the relative permittivity, and k_0 is the wave number. The expression in brackets in the second term can be rearranged by taking the complex conductivity σ_p according to eq. (3.27) and the plasma frequency ω_{pe} according to eq. (3.19) with the assumption of $\varepsilon_r = 1$ to

$$\varepsilon_r - \frac{j\sigma_p}{\varepsilon_0 \omega} = 1 - \frac{\omega_{pe}^2}{\omega\left(1 - j\frac{\nu_m}{\omega}\right)}. \tag{3.35}$$

Assuming $\varepsilon_r = 1$ is a common approach to solve for the total power transfer P_e to an electron fluid in a certain volume V as it enables computation of the total current density J_p through the conductivity. In a Drude model, J is the electron current as given by eq. (3.26). The absorbed power can be described as in the direct current case $P_e = U \cdot I = U^2/R_\Omega = U^2\sigma_{DC}$, which translates to the volume specific power absorption caused by the electric field,

$$\frac{P_e}{V} = 0.5Re\left(\overrightarrow{J_p} \cdot \vec{E}\right) = 0.5Re\left(\sigma_p \cdot \vec{E}^2\right), \tag{3.36}$$

where Re considers the real part of the product of current density and complex amplitude of $\vec{E}$. The correlation of complex and direct current plasma conductivity is explained in more detail in Appendix 1. Taking the conductivity from eq. (3.27), the absorbed power then reads to:

$$\frac{P_e}{V} = \frac{n_e e^2}{2m_e \nu_m} E^2 \frac{\nu_m^2}{\nu_m^2 + \omega^2} \tag{3.37}$$

in absence of magnetic fields [92]. In reality, the electric field in the plasma is not constant but, for the case of the Duo-Plasmaline, radially decaying. In typically two resonance zones, one close to the dielectric and one at a second, larger radius, in which $n_e = n_{e,c}$, the plasma oscillation leads to locally increased electric fields, in which a major part of the microwave power is absorbed. While the microwave can propagate into the volume beyond the first resonance zone, it vanishes beyond the second one. Thus, the plasma also serves as containment for the microwave. Higher electron-neutral collision frequencies, i.e., higher pressures, disturb the plasma oscillation and reduce the resulting electric field in the plasma [99].

In Figure 3.6, the power absorption per volume is plotted over the ratio of electron-neutral collisions for momentum transfer ν_m to microwave frequency ω for several different electron densities with the

assumption of a constant electric field of 50 V/m. The power absorption per volume spikes for all electron densities when the two frequencies are of the same magnitude and drop off quickly with frequency ratios diverging from 1. Thus, the best conditions for power transfer are met when the electron undergoes one collision per displacement by the electric field. This can also be shown through eq. (3.33), in which the term $\nu_m/(\nu_m^2 + \omega^2)$ is maximized for the case of $\nu_m = \omega$. The figure also shows, the higher the electron density, the more power can be absorbed. In other words, a sufficiently high electron density or electric field strength is required to sustain the discharge. Especially at low pressures, when $\nu_m \ll \omega$, the electron mean free path becomes too large to enable buildup of kinetic energy and power transfer to the gas. For microwave plasmas operating at 2.45 GHz, this is the case around pressures of ca. 1 Pa [102]. The superposition of a magnetic field can extend the pressure range, in which a microwave discharge can be operated.

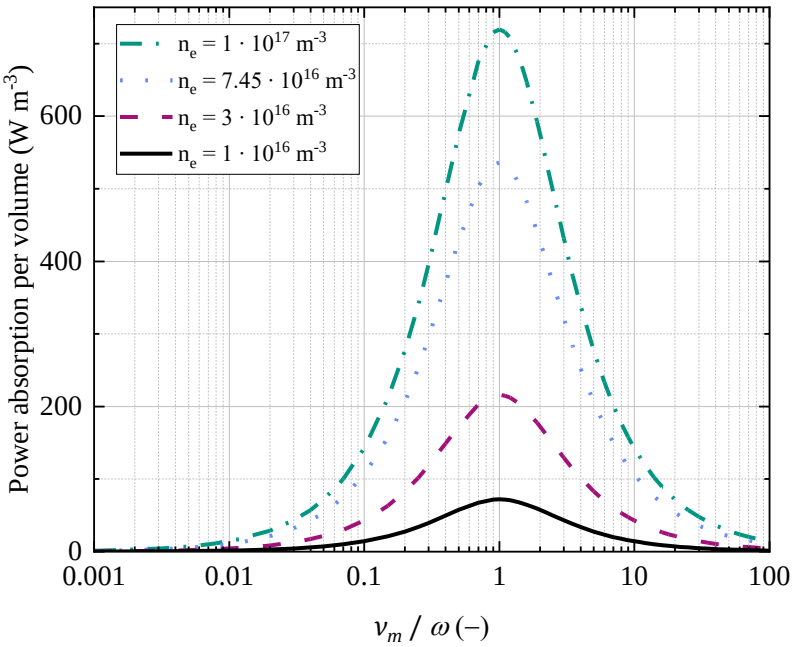

Figure 3.6: Absorbed power density in plasma over varying ratios of electron-neutral collision to microwave frequency for a range of electron densities with an average electric field of E = 50 V / m.

3.6 Microwave plasma with imposed magnetic fields

Magnetic fields can impact plasma shape by Lorentz forces, which cause charges to experience different drift types, possibly simultaneously. Magnetic fields generally assist plasma maintenance by reducing charge losses as charged particle motion perpendicular to magnetic field lines are suppressed. As a result, the plasma exhibits an anisotropic behavior and the electric conductivity has to be expressed as a tensor.

An electron or ion moving parallel to the magnetic field line without experiencing collisions or electric fields is not affected by the magnetic field. However, in practice magnetic field gradients appear or the charged particle has some velocity component perpendicular to the magnetic field. If the latter is the case, the left (or right in the case of positive ions) hand rule applies and the particle experiences a Lorentz force that puts it on a helical path, the center of which is guided by the magnetic field line. The charge maintains its velocity parallel to the magnetic field and does not gain kinetic energy in absence of electric fields. The circular motion, also called gyration, depends on the magnetic field strength and its frequency ω_g can be obtained by force balance of the centripetal force $\vec{F}_C$ and the Lorentz force $\vec{F}_L$

$$F_C = F_L \rightarrow \frac{m{v_\perp}^2}{r} = qBv_\perp, \tag{3.38}$$

with $v_\perp$ as the velocity perpendicular to the magnetic field with flux density B, which is also the gyration velocity that can be described with $v_\perp = \omega \cdot r$ to give

$$\frac{m\omega r}{r} = qB \rightarrow \omega_g = \frac{qB}{m}. \tag{3.39}$$

The radius of the gyration increases with the velocity but the frequency does not. This allows exploitation of the cyclotron-resonance effect, also used as plasma heating principle in fusion devices, by superimposing a time-varying electric field with frequency $\omega = \omega_g$. In the case of an electron with the mass m_e that is accelerated by microwaves of ω = 2.45 GHz, a magnetic flux density of B = 87.5 mT is required to match gyration with microwave frequency. No matter if the electric field is linearly or circularly polarized, the electron continuously experiences acceleration and gains kinetic energy, even in absence of collisions. A plasma with such an electron heating mechanism is also called electron-cyclotron-resonance (ECR) plasma. The same effect can be applied for ions in ion-cyclotron-resonance, which requires significantly stronger magnetic fields or lower electric field frequencies due to the ions larger mass. For ions, gyration happens in the opposite direction. Even without matching the resonance, power absorption can be amplified by magnetic field application but generally suffers when the magnetic field is too strong, leading to high gyro-frequencies, at which the accelerating, time-varying electric field can appear as constant in time over several gyrations.

Acceleration of an electron by a static electric field perpendicular to a homogeneous magnetic field causes a $\vec{E}x\vec{B}$ drift as illustrated in Figure 3.7. The Figure shows the electron's movement through two-dimensional space and time. Let $\vec{E}$ be an unidirectional electric field E_y of 5000 V/m and $\vec{B}$ be an unidirectional magnetic field B_z of 250 mT, both perpendicular to each other and homogeneous in space and time. An electron initialized with an energy of 1 eV and the corresponding velocity v_y at the position (x, y) = (0, 0) experiences a Lorentz force perpendicular to v_y and B_z which puts it on a helical path as the velocity component v_y is transformed into v_x and vice versa in the absence of collisions. One can see in the projections of the electron position over time that the guiding center of the electron does not move in direction of $\vec{E}$ or $\vec{B}$. It only drifts perpendicular to both fields, namely in x-direction.

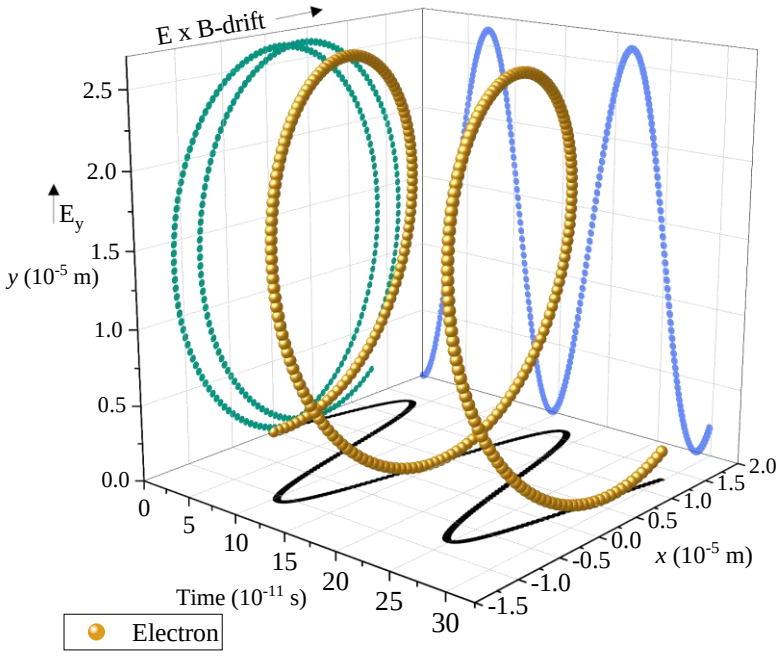

Figure 3.7: Electron gyromotion in 2D-space over time in perpendicular and homogeneous, static electric and magnetic fields with B_z = 250 mT, E_y = 5000 V/m and initial electron velocity $v_{y,0}$ = 5.934 · 10^5 m / s. The electron drifts perpendicular to both fields.

Taking the time derivative of the position equations allows determination of the velocity components during the gyration and subsequent calculation of the kinetic energy, see in Appendix 2. Surprisingly, the total kinetic energy of the electron never exceeds the initial kinetic energy at t = 0, meaning the electric field cannot perform work on the electron. However, the situation changes if the electric field becomes variable in time as in the case of a microwave for example. The absorbed power P_e then considers the gyrofrequency ω_g and changes to [72]

$$\frac{P_e}{V} = \frac{n_e e^2}{4 m_e \nu_m} \left(\frac{\nu_m^2}{\nu_m^2 + (\omega - \omega_g)^2} + \frac{\nu_m^2}{\nu_m^2 + (\omega + \omega_g)^2} \right) E^2. \tag{3.40}$$

The electron movement becomes an interplay between the microwave frequency, the gyrofrequency and the electron-neutral collision frequency for momentum transfer, which offers cross-field mitigation. One can plot the power absorption per volume over the ratio of the electron-neutral collision frequency to microwave frequency for several different magnetic field strengths as illustrated in Figure 3.8 to observe a change in behavior around the electron-cyclotron-resonance condition. At 87.5 mT and 2.45 GHz microwaves, the ECR condition is reached and the power absorption per volume becomes infinite without collisions. In ECR plasmas in practice, electrons absorb a lot of energy from the microwave at low pressures but collide with the plasma vessel walls before distributing their energy in the gas to produce more free electrons. Thus, the plasma does not ignite when the order of magnitude of the mean free path is larger than that of the vessel.

The further away from the resonance condition at 87.5 mT, the lower the power absorption in the shown plot. At 20 mT, it is approximately the same as in the case without magnetic field and with an electron density of 10^{17} m^{-3}. Furthermore, the peak in power absorption shifts towards larger electron-neutral collision frequencies with increasing magnetic flux density as collisions become the main channel enabling cross-field motion of the electron. This helps avoiding the problem depicted in Figure 3.7, in which the electric field cannot perform work on the electron.

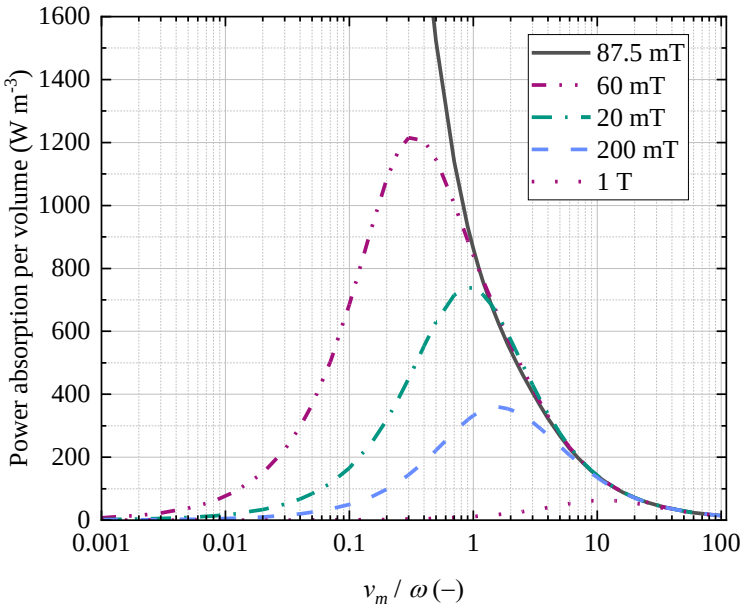

Figure 3.8: Absorbed power density in a plasma with a magnetic field perpendicular to an oscillating electric field over the ratio of electron-neutral collision to microwave frequency for several different magnetic field flux densities at $n_e = 10^{17}$ m^{-3} and an average electric field E = 50 V/m.

The shown graph considers perpendicular E to B fields only. The ratio of gyro- to collision frequency, however, allows making qualitative statements on the cross-B-field mobility and cross-B-field energy diffusivity in any E to B field configuration and, thus, to estimate whether a species of particles in a plasma with superimposed magnetic field is “magnetized” or not. One has to differentiate

for electrons and ions to determine their respective degree of magnetization. The collisions that can cause disturbance of the gyromotion are both, Coulomb collisions and those with neutrals. Here, the latter is denoted as ν_{en} for electron-neutral and ν_{in} for ion-neutral collisions. The degree of magnetization $\varsigma_{mag,e}$; $\varsigma_{mag,i}$ is determined by:

$$\varsigma_{mag,e} = \frac{\omega_g}{\nu_{e,C} + \nu_{en}} \; or \; \varsigma_{mag,i} = \frac{\omega_{g,i}}{\nu_{i,C} + \nu_{in}} \tag{3.41}$$

with the fundamental electron and ion collision frequencies [103]

$$\nu_{e,C} = \frac{5 \cdot 10^{-11} n_e Z_i \ln(\Lambda)}{17 \cdot [T_e(ev)]^{1.5}} \; and \; \nu_{i,C} = \left(\frac{m_e}{m_i}\right)^{0.5} \left(\frac{T_e}{T_i}\right)^{1.5} \frac{Z_i^2}{\sqrt{2}} \cdot \nu_{e,C} \tag{3.42}$$

where Z_i is the charge number and the Coulomb logarithm, which represents all Coulomb collisions within a sphere of a radius of the Debye-length λ_D, is

$$ln(\Lambda) = \frac{\ln(\lambda_D)}{b_{min}}, b_{min} = \max\{b_{min}^{cl} | b_{min}^{qm}\}, \tag{3.43}$$

where b_{min} is the minimum impact parameter, which is chosen as the larger one; either the classical b_{min}^{cl} or quantum-mechanical b_{min}^{qm} approach, formulations given in [103]. The electron-neutral collision frequency is derived by summing the reaction rates of a reduced set of electron-neutral collision reactions. In a typical microwave excited hydrogen plasma with $T_e = 2$ eV, $n_e = 10^{17}$ m^{-3} and $p = 20$ Pa, ν_{en} can be in the range of 10^6 s^{-1}. At this degree of ionization, the Coulomb collision rate for electrons is typically about 1 order of magnitude smaller. Due to their much larger gyrofrequency, electrons are confined by magnetic fields significantly stronger than ions, which means that cross-B-field energy transport has to predominantly occur through neutrals and ions in strong magnetic fields.

General forces, such as the gravitational force, cause a $\vec{F} \times \vec{B}$ drift, like the $\vec{E} \times \vec{B}$ drift, but in opposite directions for ions and electrons. Gravity, however, can be neglected in plasmas. If the magnetic field is non-homogeneous and features a curvature as in most laboratory applications, charges that move along the magnetic field lines experience an additional drift. The curvature drift occurs perpendicular to the magnetic field and is caused by a centrifugal force on a particle that moves along a bend magnetic field line. This is often accompanied by a gradient drift, which can, in theory, also be present on its own. A particle gyrating in space can on one side of its gyration experience larger magnetic flux densities than on the other. This causes the contraction of the particle's gyroradius on the gyromotion's side of larger magnetic field strength. Therefore, it is perpendicular to the magnetic field gradient and points in opposite directions for electrons and ions. The curvature and the gradient drift often occur together and produce macroscopic currents and electric fields, which is one of the major problems in fusion devices as it is responsible for most of the ion drifts towards the wall. In a magnetic field perpendicular to a time-varying electric field, a charge experiences an inertia drift in direction of the electric field due to the initial gain in velocity perpendicular to the magnetic field before experiencing a Lorentz force. This drift is also commonly called polarization drift and tends towards 0 with ω / ω_g [104].

It becomes clear that the description of charged particle motion in magnetic fields is far from trivial even without accounting for any of the numerous plasma instabilities that can occur. The introduction given to this matter should suffice as a foundation for a first evaluation of the risks associated with the operation of plasma in a complex inhomogeneous magnetic field. The information presented on vacuum and plasma physics, along with the phenomenological description of superpermeation in the previous section, allows setting up a development plan for a MFP.

4 Verification & validation strategy towards a closed MFP design

The main objective of this work is the development of a metal foil pump for operation in DEMO as an advancement of [31]. One focus is the development of a validated modeling tool, that allows predicting the performance of the MFP as a pump and as a separator based on variable, realistic input parameters. The latter depend on the fuel cycle as well as the plasma scenario. Engineering a simulation strategy requires an analysis of the plasma-driven permeation process. As illustrated in Figure 4.1, it is composed of individual steps a single particle undergoes to fulfil the pump's purpose. The process is initiated by the energization of the particle, in this case the dissociation of the hydrogen molecule, by the plasma. In energized state, meaning in atomic form for most of the particles, it moves through the gas-phase (step 2) until it reaches the foil, where the third step is taken: the interaction with the upstream surface, which results in the absorption of the particle. The fourth step can be described by diffusive transport through the bulk of the metal foil, leading to the final step, the interaction with the downstream surface, where the particle recombines with another hydrogen atom and is released into the gas phase.

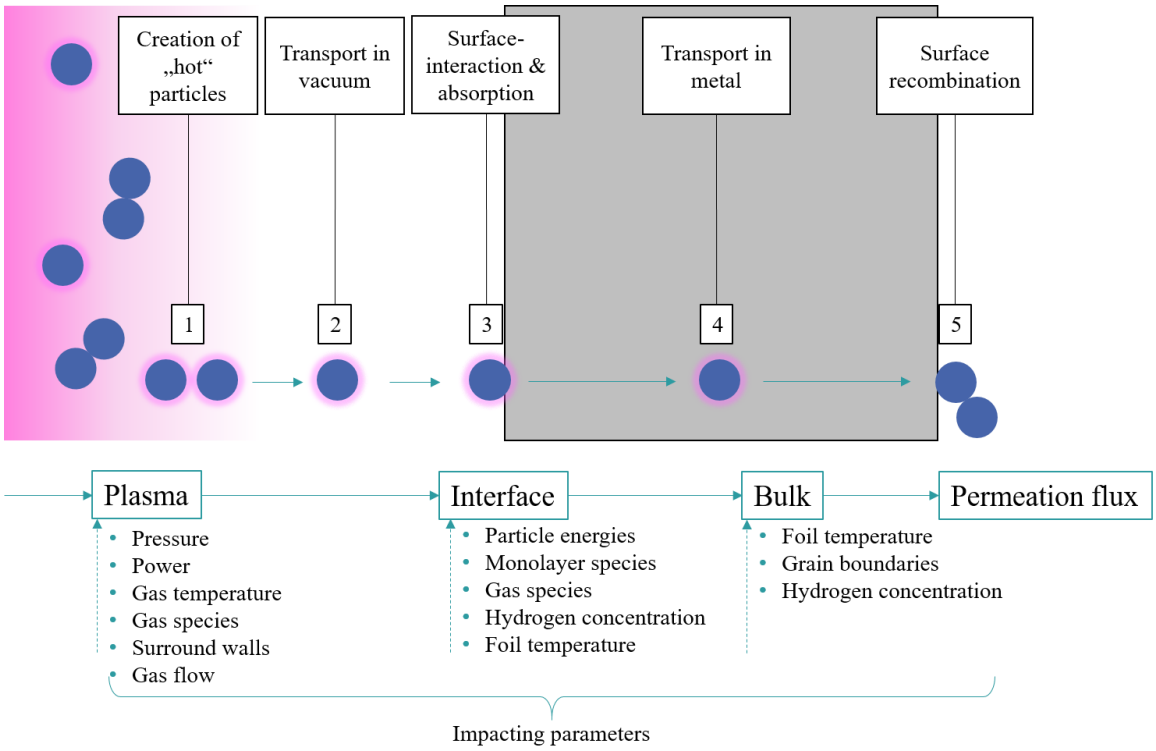

Figure 4.1: Schematic description of a particle evolution during the plasma-driven permeation process.

The energization in the plasma, i.e., the production rate of suprathermal particles, heavily depends on the EEDF, which develops as a function of an array of different variables, but mainly the given pressure, gas temperature, absorbed power density and gas. Those process parameters can be considered in a multiphysics plasma simulation. The simulation software COMSOL offers a microwave plasma module, which uses a fluid approximation with a high degree of flexibility in the model creation. The fluid approximation holds down to a pressure of 1 Pa [77], which is sufficiently low for the MFP plasma. By solving the electromagnetic wave function and its interaction with the electron fluid in the simulation domain, the simulation achieves self-consistency. Setting up such a simulation with multiple different gas species increases the required collisional cross-section database and complicates the computational effort significantly. Instead, the simulation is set up with pure hydrogen and a detailed workaround is introduced further below to account for the integral effect of other gas species' presence on the permeation fluxes. Given the finite volume of the plasma, wall interactions play a significant role and require an accurate model of the plasma vessel. An experimental validation of the plasma simulation is necessary and conducted in the HERMES*plus* setup at KIT [105].

One essential parameter for the validation is the atomic hydrogen concentration, which is experimentally accessible via residual gas analysis [106] and several spectroscopic experimental methods such as vacuum ultraviolet absorption spectroscopy (VUVAS) [107], coherent anti-Stokes Raman scattering (CARS) [108], resonance-enhanced multiphoton ionization (REMPI) [109], two-photon absorption laser induced fluorescence (TALIF) [110] and optical emission spectroscopy (OES) [111]. TALIF yields the most accurate measurement of the dissociation degree but requires expensive hardware and a tedious experimental setup. REMPI cannot be used in microwave discharges as it requires electrode immersion into the plasma. The OES approach is based on the actinometry principle and can only be used if a certain set of conditions is fulfilled in the discharge. Actinometry is broadly used and allows a limited spatial resolution of the atomic hydrogen concentration. Here, OES is chosen for the determination of the atomic hydrogen concentration measurement.

The transport through vacuum depends on the collisionality of the plasma, gas density and temperature, transport domain geometry and the presence of a bulk flow. Any MFP design published so far used incandescent filaments with a surrounding metal foil. However, there has been no proof that such cylindrical configuration is superior but, instead, a large degree of freedom is given to imagine MFP designs, which fulfil the requirements and can be fit into the pump duct. The vacuum flow simulation model has to account for such a variety of designs and be capable of predicting the MFP performance parameters pumping speed and separation ratio. The TPMC method is chosen as it allows for modelling of complex geometries at low computational cost. The surfaces to consider in an exemplary MFP model are support structures (steel), the metal foil material and the plasma source.

Calculation of the Knudsen number (see eq. 3.12) is useful for a first estimation of the flow regime to guide a decision for the modelling approach. To this end, the characteristic length l_c of a cylindrical MFP is estimated. It corresponds to the diameter of a MFP module D_{mfp}, for which a value of 0.4 m is assumed. The gas temperature in the MFP approximately takes on that of the foil, for which steady-state operation at 900 K is experimentally demonstrated. While some of the hydrogen molecules will be dissociated in the plasma, their kinetic diameter does not differ substantially from that of atoms. The gas mixture in the MFP additionally features noble gases, for the composition of which a conservative assumption is given together with the respective diameters of the particles involved [112] [113] in Appendix 3. This yields $Kn \approx 0.1$, which represents the transition regime. The assumption of free molecular flow is conservative for the transport through the channel, i.e. the pumping speed [73]. Neglecting bulk gas flow might artificially increase the residence time of a single particle in the pump and does not consider reduced flow velocities at the boundaries of the channel and, therefore, overestimate the number of surface interactions before ejection. However, given the order of magnitude difference between the thermal velocity and any realistic bulk velocity, this effect is felt to be negligible.

The use of TPMC facilitates that the particle interactions with the surface are simplified to events characterized by probabilities. Those depend on the particle's velocity and the condition of the surface, i.e., the impurity present on the surface and its thickness. The implantation depth of thermal atoms, which are by far the most abundant species contributing to PDP, is 0. However, since the foil is considered as a boundary with zero thickness, on which particles either spontaneously permeate or not, no implantation depth is considered in the TPMC model. More energetic particles, such as ions accelerated in the sheath, can cause sputtering. To simplify the complex behavior of the foil surface in plasma environment with various gases, it is assumed that the surface layer does not change in time but remains at a coverage of one monolayer. This is supported by experimental demonstration of steady-state operation of PDP. Due to lack of data and to simplify the simulation approach, it is assumed that the different possible surface orientations of the material show the same behavior during PDP. The viable non-metallic impurities differ in their energy absorption diagrams, which is reflected in differences in molecular and atomic absorption probabilities. As the best researched and most promising impurity candidate, O is chosen as the reference here. Usually, the metal foil's temperature affects the

kinetics of the surface interactions as well as the hydrogen concentration in the surface, which has strong implications on the sticking and recombination of impinging hydrogen atoms. However, the foil is operated at the lowest temperature that facilitates steady-state PDP as obtained from experiments and fixed in the TPMC model. As single particles are injected into the model one after another, the model is re-initialized each time and test particles do not accumulate on the foil boundary. Hence, the model does not consider a species concentration on the surface.

In order to achieve an integral description of the single particle evolution, the plasma simulation is coupled with the TPMC simulation. The information of suprathermal particle production is condensed into particle-boundary collision interaction probabilities for use in the TPMC simulation. To this end, the plasma source boundary is imagined as a solid plasma surface, on which excitation or de-excitation of the particles occurs. Before the interaction probabilities are derived, the considered species in the TPMC model are defined. Particles with low and high permeation probabilities, i.e. ground-state and suprathermal particles, are distinguished. The former are represented by ground-state hydrogen molecules and the latter are summarized into ground-state hydrogen atoms as they constitute the majority of suprathermal particles in the cold plasma. The particles enter the simulation domain as ground-state molecules. Their excitation probability on the plasma boundary cannot directly be extracted from the plasma simulation. However, by modelling a simplified version of the plasma simulation with only two species and no volume but only surface interactions, such an excitation probability on the plasma boundary can be used to obtain excited particle compositions in the simulation domain. The corresponding volume averaged excited particle concentration is then compared to the atomic hydrogen concentration in the plasma simulation to find a match between plasma source operation and excitation probability. Further particle interactions with the plasma boundary are discussed in section 7.

The foil boundary offers a loss channel of particles through permeation. Once permeated, a particle is removed from the model. Permeation probabilities of hydrogen atoms and molecules differ by orders of magnitude for the metal foil in the assumed condition. With symmetric metal foil surfaces, the permeation probability is half the sticking probability, which varies from 0.1 to 0.3 [38] [40] [49] [114] for atomic hydrogen on Nb and V with most data pointing towards 0.25 at foil temperatures above 400 K. By knowledge of the atomic hydrogen concentration in the experimental setup HERMES*plus*, an impingement flux is evaluated and a corresponding permeation probability obtained from the measured permeation flux. This procedure is used to probe the foil condition in HERMES*plus* and support a parameter selection for the permeation probability of atoms assumed in the model.

The presence of noble gases in the torus exhaust affects the plasma behavior and has to be considered in the model. In noble gas plasma, no energy of electrons is lost to molecular excitations or dissociation, which is why the EEDF in noble gas plasma can considerably differ from that in molecular gases such as hydrogen. As they make up some percent of the volumetric flow in the duct, their presence also reduces the partial pressure of hydrogen. The amount of noble gases for radiative seeding of the burning plasma in DEMO is given by the plasma scenario. According to current, conservative estimates, their concentration at the inlet of the MFP can at maximum make up about 5 % of the total flow [115]. As hydrogen is lost through permeation, the percentage of noble gases in the MFP increases towards its outlet. The relative change in PDP fluxes along the MFP axis is quantified experimentally in HERMES*plus* by admixing noble gas concentrations specific to the axial position of the MFP at constant pressure and measuring the reduction of the PDP flux compared to the pure hydrogen case. Considering that some excited particles in the TPMC simulation are noble gas particles that do not contribute to permeation, a permeation probability that accounts for the relative change in the permeation flux caused by noble gas seeding can be evaluated. The presented workflow includes a shortcoming. The lowest pressure at which ignition of hydrogen plasma with the Duo-Plasmaline in HERMES*plus* is possible, is about 15 Pa. This lower limit of plasma ignition fits to the inability to reach convergence in the microwave plasma simulation but does not accurately represent the pressure in the pump duct, which is

one order of magnitude lower. There, the plasma might still ignite due to the supporting effect of the magnetic field as observed in a dedicated experimental setup, which investigates the plasmaline behavior in a homogeneous magnetic field of up to 250 mT [116]. While the magnetic field applied in this reference does not accurately represent the pump duct of EU-DEMO, it offers means of extrapolation. The hardware for the ignition of the Duo-Plasmaline at this low pressure, in form of assisting magnetic field coils, is not available to this work. However, the behavior of the plasma at the low pressure expected in the duct (1 – 5 Pa) is approximated with the results from the plasma simulation by extrapolation of the volume-averaged atomic hydrogen concentration towards low pressures. Generally, lower pressures benefit the production of suprathermal particles as they feature larger electron energies. A secondary effect is that obtaining the same dissociation degree requires significantly less energy at lower pressures because the amount of hydrogen to dissociate is lower. Taking suprathermal particle production rates from the 20 Pa operation is on the conservative side. In the analysis with the TPMC simulation, suprathermal particle production rates for both pressure regimes, ~ 20 and 2 Pa, are analyzed.

A workflow that incorporates all the above derived steps is shown in Figure 4.2. The microwave plasma simulation is validated with OES on the basis of atomic hydrogen density measurements. Those measurements simultaneously allow calculation of the impingement flux of atomic hydrogen onto the foil, from which a permeation probability for the given setup can be computed by knowledge of the permeation flux. The choice of the tested parameter range of the permeation probability for the two material candidates, Nb and V, is made based on data from literature. The experimentally determined effect of the noble gases present in the torus exhaust on the PDP flux finds consideration in the permeation probability as well. The validated plasma simulation is used to quantify the suprathermal particle production in the operational range of the MFP. In an intermediate step, the same quantity of suprathermal particles are produced with a simplified version of this simulation using a single excitation parameter. From this comparison, an excitation probability on the plasma boundary is found. All data, including foil temperature values, for which steady-state PDP can be demonstrated, are fed into the TPMC simulation to test different designs for their performance in terms of pumping speed and separation efficiency.

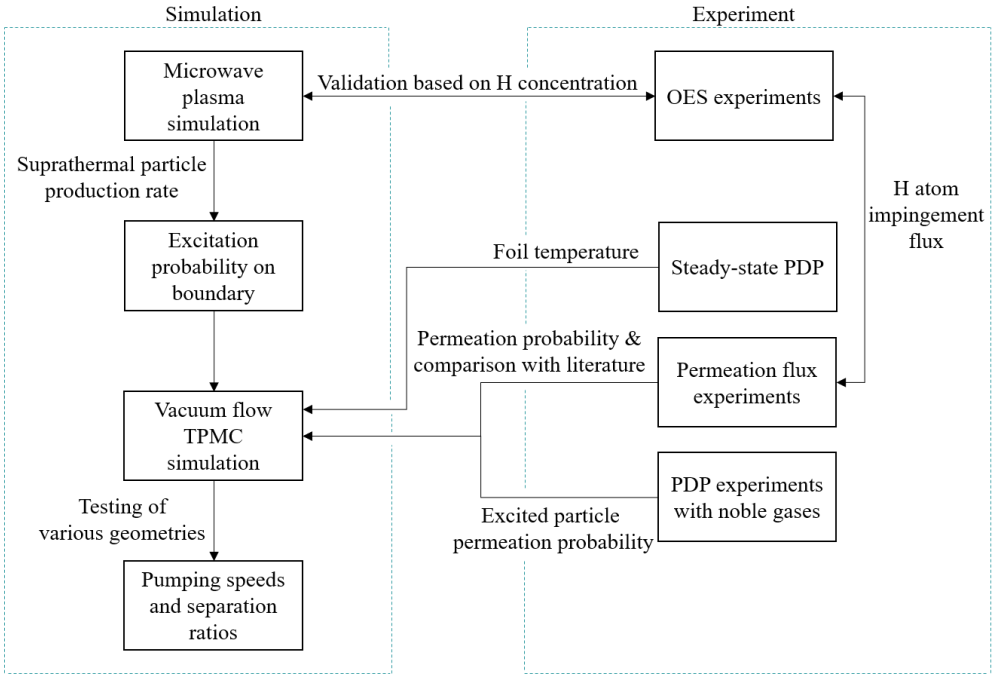

Figure 4.2: Workflow towards a predictive modeling tool using an experimentally validated plasma simulation and a TPMC approach for modeling of the vacuum flow.

5 Simulation of microwave generated hydrogen plasma in a MFP

The simulation model reflects the characteristics of the experimental setup HERMES*plus* in terms of geometry, materials and plasma source, which is a Duo-Plasmaline with a 2-side microwave feed. The electromagnetic waves produced in the magnetrons at 2.45 GHz are guided to the vessel in two rectangular waveguides. A perpendicularly fixed aluminum cone couples the wave into the coaxial line that consists of an inner conductor made from copper and an Al_2O_3 dielectric. At the insertion into this coaxial line, the wave is guided some distance by an outer copper conductor before reaching the axial position for entering the vacuum through the dielectric. The model considers the boundary, at which the electromagnetic wave enters the coaxial line, a port for injection of the electromagnetic wave as illustrated in Figure 5.1. The transmission in the waveguide of ~ 0.4 m has negligible power losses. Thus, it is reasonable to assume the port for feeding the microwave at the position, where the microwave is coupled into the coaxial line. Power losses within the coaxial line are also negligible if a metal with high conductivity is used as is the case with Cu. The input electromagnetic wave power can be specified without active feedback, meaning that the reflection of some part of the input power is possible. Thus, the power absorbed by the plasma through resistive heating is be monitored in the simulation to compare it with the microwave power absorbed in the experiment.

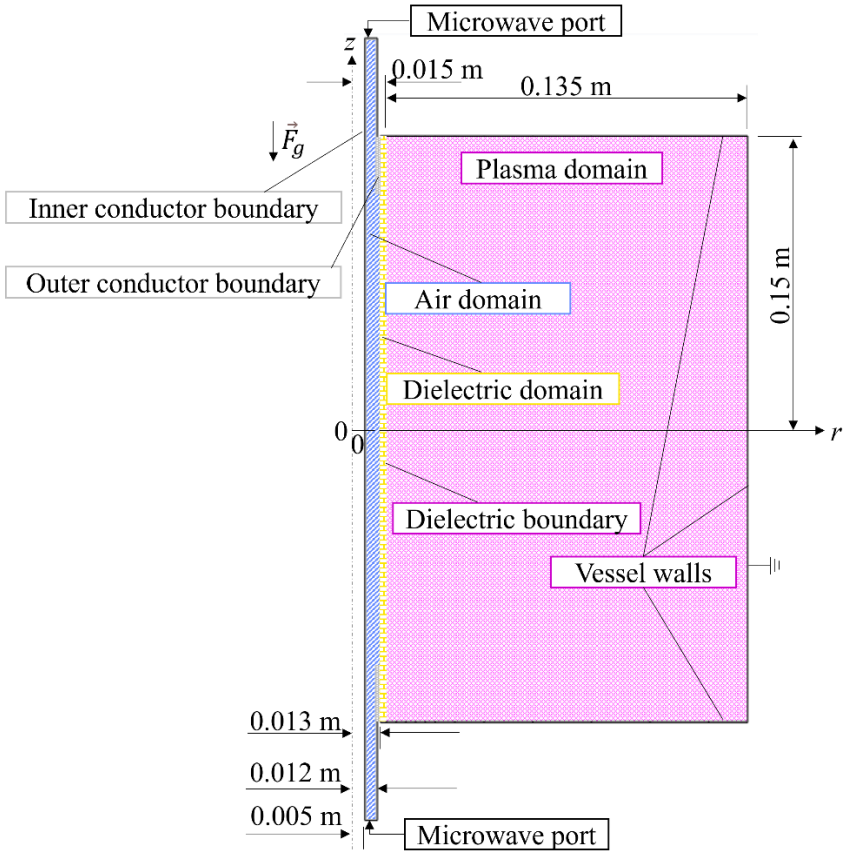

Figure 5.1: Hydrogen plasma simulation model as based on the experimental vessel of HERMES*plus*.

Upon entering the vacuum through the dielectric, the microwave accelerates a small population of electrons. In reality, free electrons are constantly produced by cosmic background radiation but in the simulation, an initial density of electrons $n_{e,0}$ is assumed. The interaction between the electromagnetic wave and the electrons is described by solving the electromagnetic wave function and considering the electric field's action on the plasma through its conductivity. The electrons absorb power from the microwave until they can collide inelastically with the heavy gas species according to the assigned plasma chemistry. The plasma reactions are carefully chosen to find a compromise between computational cost and accuracy and the reaction set is of major importance to guide the simulation

towards agreement with experiments. The inelastic collisions feature ionization processes, which contribute to a buildup of electron density. The main channels of de-excitation of the particles are wall collisions and, for some species, chemical reactions with specified rates in the gas volume. The output of the simulation are plasma characteristics like electron density and temperature as well as gas composition for a specified set of input parameters. The goal is matching those output characteristics as closely as possible to reality to provide the justification of their use for the simulation of the MFP performance.

5.1 Physics model description of the electron fluid

The modelling of the hydrogen plasma is done on the basis of the COMSOL Multiphysics platform using the interfaces of *Microwave Plasma* and *Electromagnetic Waves*. The electromagnetic wave eq. (3.34) is solved in the *Frequency Domain*. The electric field acts on an assumed initial density of electrons. The resulting electron fluid movement represents a current density which is mathematically accessible using the conductivity of the plasma. By using eq. (3.37), a resistive heating in the plasma is computed, which denotes the power density of microwave power transferred to the electron fluid.

A peculiarity of the modelling approach is the fluid approximation of the electrons. Although it simplifies the computational demand, it becomes inaccurate at too low pressures. The simulation software discourages use of the fluid approximation for problems with pressues below 1 Pa [77], which is more than one order of magnitude below the pressures modelled here. The fluid approximation facilitates using macroscopic quantities such as electron density, mean electron energy and mean electron momentum to describe the electrons with conservation equations. The equations are obtained by taking a moment of the Boltzmann equation (3.11) and averaging it over velocity space so that the resulting distribution functions are only dependent on space and time. As for the lowest moment of the Boltzmann equation, the integration over velocity space yields the continuity equation [68]

$$\frac{\partial n_e}{\partial t} + \nabla \cdot \Gamma_e = G_e - L_e, \tag{5.1}$$

which is an electron balance equation, in which Γ_e is the electron flux, G_e the source term of all electrons through ionization reactions and L_e the loss term. Volume recombinations of electrons can be neglected in low pressure discharges. The left-hand side of eq. (5.1) describes the number of electrons either created (or destroyed) within a volume cell or crossing the boundaries of an assumed volume element by transport.

The mean electron velocity u_e is obtained by averaging the Boltzmann distribution over velocity space after multiplication with the electron velocity v_e. In analogy, the energy conservation equation is derived by multiplication with the kinetic energy before integration over velocity space, more details in [68]. Consequently, the electron momentum can be expressed as a function of time and space [117] by:

$$\frac{\partial}{\partial t}(n_e m_e u_e) + \nabla \cdot (n_e m_e u_e u_e) = -(\nabla \cdot p_e) + q n_e E - n_e m_e u_e \nu_m, \tag{5.2}$$

and, correspondingly, the electron energy density

$$\frac{\partial n_\varepsilon}{\partial t} + \nabla \cdot \Gamma_\varepsilon + E \cdot \Gamma_e = S_{en} \tag{5.3}$$

where p_e is the electron pressure tensor in Pa, Γ_ε is the electron energy flux and S_{en} is the loss or gain of energy caused by ineleastic collisions in [V m^{-3}]. Several assumptions for the plasma simplify the handling of these equations. In weakly ionized plasma above a certain pressure, one can assume that the momentum exchange frequency is much larger than the electromagnetic wave frequency, the ionization frequency or the frequency of collisions with attachment reactions. This allows neglecting the first term

in eq. (5.2). Similarly, the second term can be neglected if the thermal velocity of the electrons is much larger than their drift velocity. Assuming a Maxwellian' EEDF, the pressure tensor is expressed through

$$p_e = n_e k_B T_e I_M \tag{5.4}$$

with I_M being the identity matrix. This allows rewriting eq. (5.2) to obtain the electron drift velocity u_e with

$$u_e = \frac{q}{m_e \nu_m} - \frac{k_B}{m_e \nu_m} \nabla T_e - \frac{k_B T_e}{n_e m_e \nu_m} \nabla n_e, \tag{5.5}$$

which is then used to express the electron flux by:

$$\Gamma_e = u_e n_e = -n_e(\mu_e E) - \nabla(D_e n_e). \tag{5.6}$$

The symbol μ_e is also referred to as the electron mobility in ($m^2\ V^{-1}\ s^{-1}$), which depends on the charge, mass and collision frequency of the electrons for momentum transfer according to

$$\mu_e = \frac{e}{\nu_m m_e}, \tag{5.7}$$

and, similarly, the electron diffusivity D_e in ($m^2\ s^{-1}$) increases with the electron temperature and reduces with the momentum transfer frequency corresponding to

$$D_e = \frac{k_B T_e}{\nu_m m_e}. \tag{5.8}$$

Eq. (5.1) is expanded by taking into account the flow of background gas, which introduces a directed motion of the electron bulk. However, this is not foreseen for the simulation since the given feed flows in the experiment produce negligible bulk flow velocities through the plasma vessel of < 1 m s^{-1}. Eq. (5.3) for the electron energy density is extended considering the absorbed power in the given volume caused by external heating Q (as obtained from a generally assigned power deposition Q_g and the enthalpy of transported background gas through the domain according to

$$\frac{\partial n_\varepsilon}{\partial t} + \nabla \cdot \Gamma_\varepsilon + E\Gamma_e = S_{en} + \left(\frac{Q + Q_g}{q}\right) - (u \cdot \nabla) n_\varepsilon. \tag{5.9}$$

The electron energy flux Γ_ε formulates, in analogy to eq. (5.6), as

$$\Gamma_\varepsilon = -n_\varepsilon(\mu_\varepsilon E) - \nabla(D_\varepsilon n_\varepsilon), \tag{5.10}$$

with the electron energy density n_ε in (V / m^3), the electron energy mobility μ_ε in (m^2 / (V s)) and the electron energy diffusivity D_ε in (m^2 / s). The electron energy density in a given volume allows computation of an electron mean energy ε_V in (V) through the simple relation

$$\varepsilon_V = \frac{n_\varepsilon}{n_e}, \tag{5.11}$$

which allows computation of the electron temperature T_e in (eV) which is by definition 2/3 ε_V. In the plasma sheath region, a charge separation, induced by differences in electron and ion mobilities, produces large electric fields and density gradients that can cause numerical instabilities. The simulation software supplies a method to stabilize the solution by solving for the logarithm of electron density and electron energy density, for details see [77].

The applied plasma chemistry yields the electron source term G_e as well as the electron energy loss S_e in a given volume. The electron source term only considers electrons produced in ionizing collision reactions considered by the model. The reaction rates of ionizing reactions are obtained in analogy to eq. (3.16) and summed up according to

$$G_e = \sum_{i=1}^{n} y_i n_g n_e k_{r,i}, \tag{5.12}$$

for a total of n ionizing reactions. Another source of electrons is considered due to secondary electron emission on the walls. The walls also act as a primary sink for electrons. The different boundary conditions that are assumed for the walls are described in more detail in section 5.3. In the plasma domain, the balance equations require consideration of an electron energy loss term based on the collisional energy loss from all assigned reactions. Electron energy losses arise from inelastic collisions and elastic collisions with momentum transfer. For a given volume element, the energy loss is obtained through the relation

$$S_e = \sum_{i=1}^{m} y_i n_g n_e k_{r,i} \Delta\varepsilon_i, \tag{5.13}$$

for m reactions with the respective electron energy loss $\Delta\varepsilon_i$ at the rate $k_{r,i}$ in collision i.

5.2 Transport and reactions of the heavy species

The background gas consists of several hydrogenic species formed by plasma collision reactions. The main species is the neutral ground-state hydrogen molecule. A description of the diffusion of a species i in a multicomponent fluid is given by the Maxwell-Stefan equation

$$\frac{y_i}{RT}\nabla\mu_i = -\sum_{j\neq 1}^{m} \frac{x_j J_{M,i} - x_i J_{M,j}}{c_{tot} D_{ij}} \; for\; i = 1 \dots n, \tag{5.14}$$

which is based on the assumption of a local equilibrium of the thermodynamical driving force (term on the left hand side) of a species and the total friction force this species experiences (term on the right hand side) [118]. The thermodynamic driving force depends on the molar fraction y_i and the chemical potential μ_i of species i while the friction force is a function of the diffusive molar fluxes $J_{M,i}$ or $J_{M,j}$ of the different species and the binary Maxwell-Stefan diffusivity D_{ij}. Depending on the number of species in the multicomponent system, the Maxwell-Stefan diffusivity is formulated as a matrix. With the number of components in a fluid rising, this formulation becomes excessively complex to solve. Thus, a simplification can be employed using a mixture-averaged approach that is based on a mixture-averaged diffusion coefficient $D_{i,m}$ for a species i that can be expressed through the mass fraction w_i of the respective species i according to

$$D_{i,m} = \frac{1 - w_i}{\sum_{j\neq i}^{Q} \frac{y_j}{D_{ij}}}, \tag{5.15}$$

with the binary diffusion coefficient D_{ij} for a system with Q total species. Using this mixture-average diffusion coefficient, the diffusive flux vector

$$j_i = \rho w_i V_{D,i}, \tag{5.16}$$

can be described with the multicomponent diffusion velocity

$$V_{D,i} = D_{i,m}\frac{\nabla w_i}{w_i} + D_{i,m}\frac{\nabla M_m}{M_m} + D_{i,T}\frac{\nabla T}{T} - z_i \mu_{i,m}\vec{E} + \sum_j \frac{M_j}{M_m} D_{j,m}\nabla x_j, \tag{5.17}$$

where M_m is the mixture's mean molar mass and $D_{i,T}$ is the thermal diffusion coefficient. The 4th term on the right hand side describes the diffusion of ionic species in superimposed electric fields $\vec{E}$ with the mixture averaged mobility of the ion $\mu_{i,m}$. The 5th term on the right-hand side introduces a mixture

diffusion correction, which becomes increasingly relevant for species with different molar masses and is, thus, considered in the model, which features a maximum mass difference of the gas species of factor ~ 3. A single species' balance equation for a volume element can then be formulated using the mixture-average approach according to its mass fraction

$$\rho \frac{\partial}{\partial t}(w_i) + \rho(u \cdot \nabla)w_i = \nabla \cdot j_i + R_i, \tag{5.18}$$

where the first term describes the temporal change in mass fraction of component i, the second term expresses the change of the components mass fraction in a given volume due to mass transport through the mass averaged fluid velocity described by the vector u and R_i is the reaction term for species i in (kg m^{-3} s^{-1}). The reaction term is obtained from the plasma chemistry in analogy to eq. (5.12). The mean molar mass of the mixture M_m is obtained by simply adding the weighted individual components' molar masses M_i according to

$$M_m^{-1} = \sum_{i=1}^{Q} \frac{w_i}{M_i}. \tag{5.19}$$

At last, Einstein's relation yields the mixture-averaged mobility $\mu_{i,m}$ by

$$\mu_{i,m} = \frac{q}{k_B T} D_{i,m}, \tag{5.20}$$

with the unit charge q in C.

Four different types of collisions between electrons and heavy species are considered in the electron-impact reactions: Elastic, attachment, excitation and ionization. Only the latter three provide a means of energy transfer between electrons and background gas. All electron-impact reactions share the commonality that their rate depends on the electron mean energy. Most of the reactions are described using tabular data for the collisional cross-section $\sigma(\epsilon)$ and some of them using analytic expressions. Deriving a solution for the rate constant of a reaction requires knowledge of the given electron mean temperature and density and the type of EEDF according to eq. (3.15) and (3.16). A Maxwellian' EEDF as well as an initial gas composition close to the expected result in steady state are assumed. Additional knowledge of spatially resolved plasma parameters allows solving for the exact EEDF in the respective location and, consequently, for the reaction terms. Assuming plasma parameters and gas concentrations close to the expected outcome in steady-state yield faster convergence.

Next to electron-impact reactions, a variety of volume reactions can be assigned to the plasma domain, such as radiative decay or quenching reactions. Radiative decay reactions are of first order, while two- and three-body reactions are of second and third order, respectively. Plasma reactions as well as wall reactions are crucial in the determination of the steady-state composition of the gas. In elastic collisions, the mass ratio of the electron and the heavy particle determines the momentum transfer and the energy loss of the electron. Those collisions cause the electron temperature to become more isotropic and not strictly aimed in the direction of the radial electric field of the microwave. This has strong implications on the EEDF as it allows assuming a spherically symmetric energy distribution, which simplifies finding a solution to the Boltzmann equation. However, the elastic collisions are not associated with a gain of kinetic energy of the heavy species in this simulation, but instead, the background gas temperature T_G remains the same throughout the whole simulation time. It is given with a radial profile, peaking at some radial distance of ~ 5 cm from the central axis in the volume of the plasma and dropping off towards the inner and outer wall, which are both cooled by forced convection. The radial temperature profile is assigned with a weak dependency on the microwave input power and the profile shifts upward with this power. The change with power is based on experimental observations, in which the vessel wall temperature increases with supplied microwave power. The fit function for the gas temperature is derived from arbitrarily chosen gas temperatures in the plasma, which are close to

the experimentally described values [97] [99] [119] [120] and exhibit good agreement with the experimental data. The gas temperature usually decreases with pressure as the frequency for momentum transfer between electrons and background gas declines. As significantly less power input is required to reach the desired total power absorbed at lower pressures, the power dependent fit function for the radial temperature profile carries this temperature change with pressure.

In Table 5.1, an excerpt of the most important reactions used in the plasma simulation is given. The exhaustive list of all reactions, including electron-impact, chemical reactions, radiative decay reactions and wall reactions, is extracted from [83] [86] [97] [111] [121-139] and given in Appendix 4. Reactions 5.1 and 5.2 describe the two elastic collisional cross-sections for momentum transfer between electrons and hydrogen molecules or atoms. Secondly, the two electron-impact ionization reactions that supply the plasma with electrons are given by reactions 5.3 & 5.4. The choice of cross-section for those reactions are important as they strongly influence the electron population. Special attention is paid to accurately represent the relevant processes to create hydrogen atoms. The most dominant of which is typically direct electron-impact excitation to the repulsive H_2 $b^3\sum_u^+$ hydrogen triplet state that dissociates immediately on plasma time-scales. This reaction has particularly high cross-sections at low electron energies < 20 eV.

Table 5.1: Some of the most important electron-neutral collisions and wall reactions considered in the hydrogen plasma model.

Nr.	Reaction	Type	Given as	Reference
5.1	$e + H_2 \rightarrow e + H_2$	Elastic	Table	[121]
5.2	$e + H \rightarrow e + H$	Elastic	Table	[122]
5.3	$e + H \rightarrow e + H^+$	Ionization	Table	[123]
5.4	$e + H_2 \rightarrow e + H_2^+$	Ionization	Table	[122]
5.5	$e + H_2 \rightarrow e + 2\ H$	Excitation	Table	[124]
5.6	$e + H_2(v1) \rightarrow e + 2\ H$	Excitation	Table	[125]
5.7	$e + H_2(v2) \rightarrow e + 2\ H$	Excitation	Table	[125]
5.8	$e + H_2(v3) \rightarrow e + 2\ H$	Excitation	Table	[125]
5.9	$e + H \rightarrow e + H(n=3)$	Excitation	Table	[122]
5.10	$e + H(2s) \rightarrow e + H(n=3)$	Excitation	Table	[126-129]
5.11	$e + H(2p) \rightarrow e + H(n=3)$	Excitation	Table	[126-129]
5.12	$H \rightarrow 0.5\ H_2$	Wall (metal)	0.1	[86]
5.13	$H \rightarrow 0.5\ H_2$	Wall (ceramic)	0.02	[97] [130]
5.14	$e + H_2 \rightarrow e + H + H(n=3)$	Excitation	Table	[122]

The term triplet comes from the splitting of a molecule's spectral lines into triplets, which is caused by the presence of two unpaired electrons in the electronic configuration of the molecule. A singlet, on the other hand, has no unpaired electrons and does not show this splitting of the spectral lines. Other H_2 triplet states have a high chance to dissociate through radiative decay down to the H_2 $b^3\sum_u^+$ state [123] [140]. Dissociation through excitation to singlet states is less relevant at low electron impact energies because of a lower dissociation probability since there is no low energy repulsive state as it is the case for the triplet states. In [124], an approach is made to determine an integral dissociation cross-section for the formation of neutral fragments with the single center convergent close-coupling method. The approach summarizes the dissociation through excitation to a set of the first eight triplet as well as eleven singlet states of the hydrogen molecule and finds good agreement with experimental data [141]. The list of the considered states is not exhaustive but covers the most relevant species. Using the integral collision cross-section for the dissociation into neutral fragments allows reducing the complexity and accelerating the computation of the simulation by avoiding consideration of all the individual electronically excited hydrogen molecular states. The corresponding collision is given by reaction 5.5. Though this reaction incorporates the dissociation through reaction 5.14 already, the rate of the latter is

evaluated to proof the validity of actinometry. Thus, reaction 5.14 is not considered individually in the plasma simulation.

In molecular plasmas, a significant amount of the electron energy is consumed by vibrational or rotational excitations. Hence, a considerable fraction of the particles is in the respective excited states. Especially the vibrationally excited states can present important intermediate steps to the dissociation of the molecule. Therefore, three vibrationally excited states with the highest excitation cross-sections are considered in the model. Of the reactions that produce the vibrationally excited states, only the second step in the dissociation process, the electron impact on the vibrationally excited states v = 1 to 3 is considered in Table 5.1, listed by reactions 5.6 to 5.8 and its cross-section is taken from a fit of the data from [125]. The reference differentiates between the processes that lead to the formation of the repulsive H_2 $b^3\sum_u^+$ state and that lead to dissociation through the excitation to singlets. Both cross-sections are extrapolated to higher electron energies up to 500 eV and added to yield total dissociation cross-sections for the vibrationally excited states.

The spectral line at 656.2 nm in the hydrogen spectrum is of special interest for the validation of the simulation by actinometry. It occurs when a hydrogen atom with the main quantum number n = 3 de-excites to the n = 2 level. The line associated with this transition is also called Balmer-α line. To prove the validity of the actinometry principle, one has to make sure that the direct electron impact on the ground-state hydrogen atom (according to reaction 5.9) is the dominant reaction to produce the H(n=3) state and not reaction 5.14 in Table 5.1 or the cascade reactions 5.10 and 5.11 through the H(n=2) intermediate state. For the excitation of some of the species, for which a significant concentration is expected, such as the rotationally and vibrationally excited hydrogen molecules, the cross-section data for the reverse reaction are calculated according to the principle of detailed balance [68].

Except for the recombination of atomic hydrogen, the wall reactions of dielectric and vessel wall are considered identical. Surface recombination of hydrogen atoms play a significant role in the low pressure discharge – especially due to the importance of the dissociation degree for the chosen modelling approach and the experimental validation method. There are different ways to describe the recombination of hydrogen on walls. Phenomenologically, the recombination occurs through the LH- or the ER-mechanism but always starts with the adsorption of an H atom on the surface. In the ER-mechanism, the reaction is of first order with respect to the gas species density and this reaction path gains importance with increase in dissociation degree. The activation energy is lower than in the LH-mechanism, which is, therefore, more relevant at higher temperatures [142]. One can avoid implementation of a surface-adsorbed species into the model by consideration of a recombination factor as described in [86]. This factor measures the amount of H-H recombinations to heat a plate exposed to plasma over the incident rate of atoms. Therefore, it is comparable to a “removal rate” or sticking coefficient of H according to the reaction $H \rightarrow 0.5\ H_2$, in which a hydrogen atom is substituted for half a hydrogen molecule. A lot of different values have been reported in literature for this factor, not only based on different experimental measurements but certainly also due to variation in material, wall temperature, discharge characteristics such as pressure, power and discharge mechanism, processing history of the surface and so on. A lot of the reports in literature feature silica-based wall materials, which generally show lower recombination factors [97]. The reported values for stainless steel range from 0.1 to 0.2. In [87], it is shown that achieving a steady-state condition of the plasma-exposed surface, on which the recombination takes place, is crucial and requires some time of waiting before measurements are taken. Here, a constant coefficient for the recombination on the two different walls according to reactions 5.12 and 5.13 is applied for each simulation and a parametric study of the recombination coefficient on the steel wall performed in section 5.5.3.

5.3 Boundary conditions of the simulation model

The 2D model assumes axisymmetric geometry and represents the experimental setup HERMES*plus*. The three different domains considered in the physics are the cooling air channel, the dielectric and the plasma as sketched in Figure 5.1. Equivalent portions of microwave power are injected into the central coaxial line from top and bottom, travelling between inner and outer conductor in the first few cm and then penetrating through the dielectric into the plasma domain. Inner and outer conductor, as well as the vessel walls, are assumed as ideal electrical conductors. The cooling air channel is modelled as an air domain with its respective physical properties, of which the relative permeability and relative permittivity are that of free vacuum, 1, and the electrical conductivity is 0. The dielectric is considered with material properties of alumina with an electrical conductivity of 10^{-14} S m^{-1} and a relative permittivity of 10.

The boundary conditions of the surfaces within the plasma domain are dielectric for the alumina dielectric and ground for the vessel walls. The dielectric boundary condition assumes an accumulation of charges on the surface, which is physically described by a differential equation that expresses the surface charges' σ_s change in time with the normal components of ion and electron current densities on the wall, J_{ion} and J_e according to [77]

$$\frac{d\sigma_s}{dt} = \boldsymbol{n} \cdot J_{ion} + \boldsymbol{n} \cdot J_e. \tag{5.21}$$

The normal component of the electric displacement field *D*, which is caused by the presence of charge separation in the dielectric, is a function of the surface charge density through

$$\sigma_s = -\boldsymbol{n} \cdot \left(D_{d,1} - D_{d,2}\right). \tag{5.22}$$

The ground boundary condition of the vessel walls means that the potential of the wall is V = 0. All of the four plasma-facing walls are potentially sources of electrons through secondary emission. Two mechanisms of secondary emission are differentiated: Electron impact and heavy species impact. Electron emissions from the latter are handled in the individual wall reactions for the different species. The respective reaction's secondary emission probability is given in the complete list (Appendix 4). The mean energy of the secondary electrons from heavy species impingement is assumed as 2 eV [85].

Secondary electron emission caused by electron impact is fundamentally different due to the lower mass of the impinging particle. There is a large variation in data on secondary electron yield (SEY) from primary electron impingement. The dominant influencing factors are the primary electron energy, the material [143], the surface temperature [144], the incident angle [145] and the condition of the surface, which can be subjected to specific treatments to influence the SEY. Generally, the SEY drops to lower energies but the average energy of the secondary electron increases with lower primary energy [83]. In [144], the data for iron is shown down to energies of 33 eV, but in most references, extrapolation is necessary to obtain data for lower energies. The energy of impacting electrons on the plasma vessel walls of HERMES*plus* depends on the EEDF of the plasma. For a plasma of the given pressure and power density, it has been assumed that the majority of the electrons in the plasma bulk have mean energies of a few eV. Those electrons escape the electric field oscillation from the plasma bulk by collision promoted migration but are mostly rejected from the walls due to the electric field that forms cause of the charge density gradient as they move from the quasineutral plasma region into the non-neutral space charge sheath in front of the wall. Only the electrons of the high energy tail of the energy distribution are able to overcome the potential and reach the wall. The energy of the median of this population is in the range of a few eV after deceleration by the sheath. Extrapolating the data in [144] leads to a secondary emission coefficient of ~ 0.2 at the corresponding electron energy of 10 eV. A similar value can be read from Figure 5 in [83] for 20 eV primary electrons.

The observed energy range of secondary electrons from metals is quite broad. While in [144], measurements of the energy distribution of secondary electrons from impact on tungsten show that the majority of secondary electrons posseses < 0.5 eV, in [83], the median for secondary energies from stainless steel impact is ~ 3 eV. This value is derived from 100 eV primary electrons. However, the change in the energy of secondaries with primary energy observed by this group was very small, and only increased with lower primary energies. Thus, secondary electrons are assumed with 3 eV, which is considered conservative. The electrons impinging on the wall despite the presence of a plasma sheath can also be reflected with a certain probability γ_e. Those reflected electrons contribute to the current density aimed away from the wall just as the electrons from secondary electron emission. The probability of secondary emission of single primary electron impact is given as γ_b. Another source of electrons at the wall is caused by thermionic emission, which includes all electron emissions cause by wall reactions of heavy species impact. Taking the thermionic electron emission flux Γ_t, the balance equation for the normal component of the electron flux towards the wall can be described as [77]

$$\vec{\boldsymbol{n}} \cdot \Gamma_e = \frac{1-\gamma_e}{1+\gamma_e}\left(\frac{1}{2}\bar{v}_e n_e\right) - \left(\sum_i \gamma_i(\Gamma_i \cdot \boldsymbol{n}) + \Gamma_t \cdot \boldsymbol{n}\right), \tag{5.23}$$

where $\vec{\boldsymbol{n}}$ is the outward normal unit vector. Similar to the electron density, the balance equation for the electron energy density at the wall is fulfilled for

$$\vec{\boldsymbol{n}} \cdot \Gamma_\varepsilon = \frac{1-\gamma_e}{1+\gamma_e}\left(\frac{5}{6}\bar{v}_e n_\varepsilon\right) - \left(\sum_i \gamma_i \varepsilon_{s,i}(\Gamma_i \cdot \boldsymbol{n}) + \varepsilon_t \Gamma_t \cdot \boldsymbol{n}\right), \tag{5.24}$$

where $\varepsilon_{s,i}$ is the mean energy of secondary electrons emitted by impingement of species *i* and ε_t is the mean energy of electrons created in thermal emission. For all thermoionic emission reactions, individual electron energies have to be specified and are, as such, considered in the total energy flux at the boundary.

Surface reactions can be specified using a sticking coefficient γ_s that can be implemented with Arrhenius' law or a constant value. For all considered surface reactions, the latter approach is chosen with a single reactant participating in the reaction. In this case, the reaction is of first order and its rate in (mol m^{-2} s^{-1})) can be expressed as [77]

$$k_{surf} = \delta_i \left[c_{m,i}\gamma_s \frac{1}{4}\sqrt{\frac{8RT}{\pi M_i}} + \Gamma_{mig} \right], \tag{5.25}$$

where the concentration $c_{m,i}$ in (mol m^{-3}) of species i in front of the wall can be obtained with the mixture-averaged approach through the relation

$$c_i = \frac{w_i \rho}{M_i}. \tag{5.26}$$

The stoichiometric factor δ_i depends on the stoichiometry of the reaction according to the correlation

$$\delta_i = \delta_i^b - \delta_i^f, \tag{5.27}$$

where the notation b stands for backward and f for forward reaction, meaning the factor becomes negative for the species that is consumed in the reaction. Γ_{mig} is a migration flux that only assumes non-zero values in the case of charge migration. It is described with the mixture-average mobility of ionic species i according to

$$\Gamma_{mig} = M_i \mu_{i,m} c_{m,i} z_i (\boldsymbol{n} \cdot E). \tag{5.28}$$

5.4 Sensitivity analysis of the plasma simulation on H-atom yield

As the most important characteristic of a MFP plasma source, the yield of atomic hydrogen serves as the basis of comparison for the validation and is fed into the MFP performance simulation through a performance key parameter. Its variation with the plasma parameters electron density and temperature are of outstanding interest in this work, but also its variation with generally accessible operation parameters, such as pressure, plasma input power and wall recombination.

The coupling of electromagnetic wave physics in the frequency domain and plasma physics in the time domain necessitates a transient simulation. A reasonable simulation time to achieve steady-state discharge conditions is obtained by evaluating the volume-averaged atomic hydrogen molar fraction over the simulation time. This is done for the baseline simulation, which considers 20 Pa, 2.4 kW plasma power and 0.1 as a constant recombination coefficient of atomic hydrogen on the stainless steel vessel walls. Figure 5.2 shows the change in the atomic hydrogen molar fraction y_H over the logarithmic simulation time for this parameter configuration. The value of y_H saturates after several tens of ms. Beyond the 10 ms value, the simulation converges quickly. Therefore, 1 s is chosen as a standard for the simulation real-time.

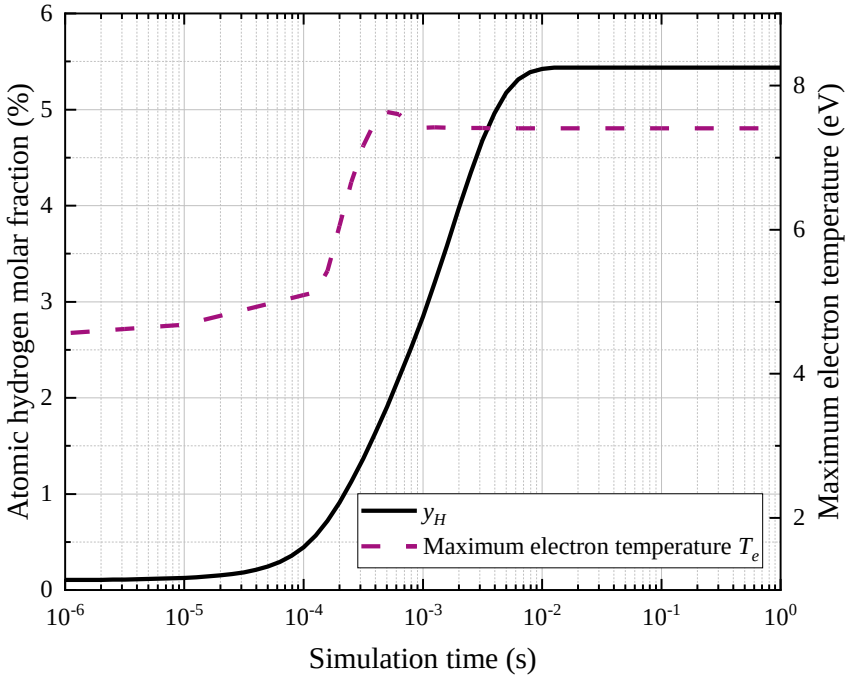

Figure 5.2: Atomic hydrogen molar fraction over time at the simulation parameters of 20 Pa, 2.4 kW plasma power and 0.1 atomic recombination coefficient.

5.4.1 Pressure sensitivity

For the baseline configuration, the computed distribution of the electron temperature and electron density is depicted in Figure 5.3. The x- and y-axes indicate the location within the plasma domain and the color code is representative of the magnitude of the electron temperature or density, respectively. The former, shown in Figure 5.3 a) ranges from ~ 0.2 eV to 7.4 eV and is highest close to the dielectric. The same observation is made in [98]. However, the axial homogeneity observed in experiments using argon as discharge gas in [98] cannot be seen in the simulation with hydrogen but instead, the electron temperature peaks close to the microwave insertion ports. An explanation for this difference is that there are significantly fewer channels for power absorption in cold plasma of atomic gases, leading to smoother power density profiles along the axis of the plasmaline as the gas' ability to absorb power saturates more quickly. Close to the dielectric, the simulation shows peak electron temperatures of 7.4

eV with a drop to about 2.5 eV in the middle of the plasmaline. The electron temperature in the bulk of the plasma is ~ 2 eV, dropping of to ~ 0.2 eV close to the walls. The electron density, given in Figure 5.3 b), shows a similar distribution inside the plasma chamber with peaks close to the ends of the dielectric. However, the simulation shows that the electrons themselves diffuse through the vessel way easier than the electron energy, yielding a smooth density profile with ~ 10^{17} m^{-3} in the bulk of the plasma. At the walls, the electron density quickly drops off before reaching values close to 0 in the plasma sheath.

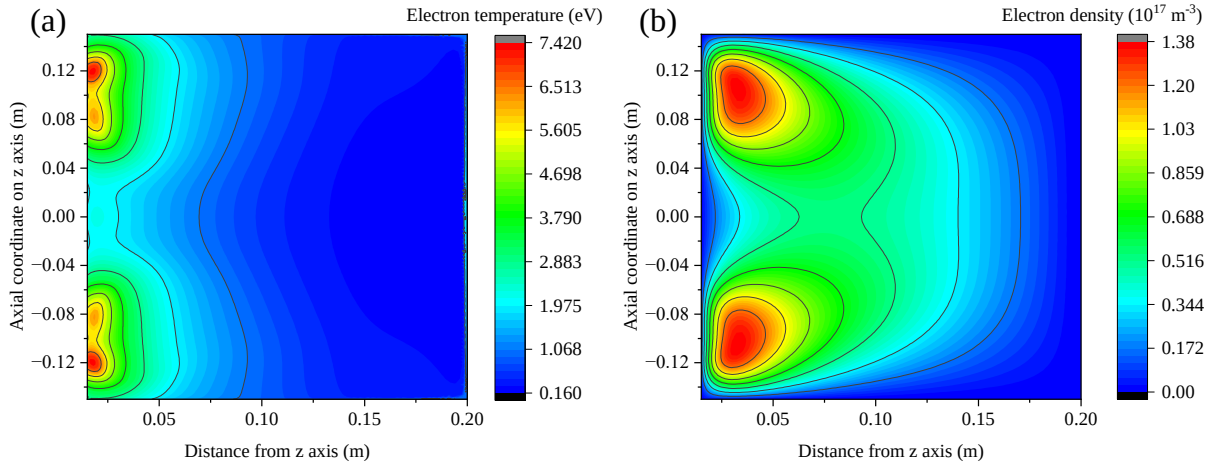

Figure 5.3: Computed spatial distribution of electron temperature (a) and electron density (b) for the simulated plasma vessel at 20 Pa, 2.4 kW plasma power and 0.1 atomic recombination coefficient. Data previously published by the author in [146].

Figure 5.4 shows a calculated spatial distribution of the local atomic hydrogen concentration in the plasma vessel with the baseline parameter configuration. The values of y_H are highest close to the dielectric at the end points of the plasma source. Throughout the plasma bulk, atomic hydrogen makes up > 10 % of the total gas species, peaking at about 27 %. The distribution shows a strong correlation with the electron temperature heatmap. Most of the atomic hydrogen is produced close to the dielectric, especially at the two ends of the plasmaline, where electron temperatures are highest. The vessel walls act as the main sink for atomic hydrogen, leading to a sharp decline in y_H towards the outer walls.

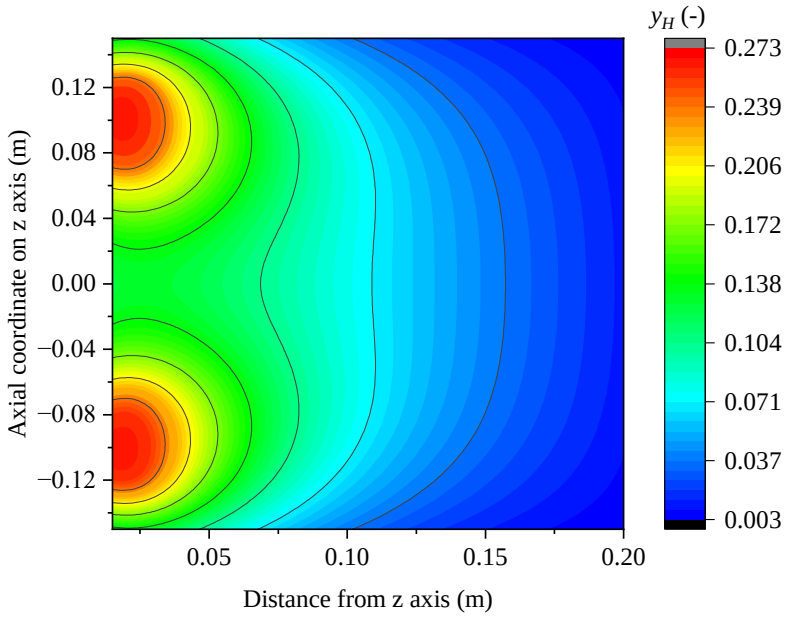

Figure 5.4: Atomic hydrogen molar fraction in the plasma domain for a simulation with 20 Pa, 2.4 kW plasma power and 0.1 atomic recombination coefficient.

The simulated radial distribution of the electron temperature and the atomic hydrogen molar fraction is shown in Figure 5.5 a) and b), respectively, as an average for the r-coordinate. The plasma vessel wall recombination coefficient of atomich hydrogen is 0.1 and the plasma power ~ 2.4 kW with a maximum offset to 2385.1 W (~ 0.62 %). Calculations for several different pressures from 10 Pa to 30 Pa are performed. The electron temperature decreases with distance from the plasma source. The maximum and overall values of the electron temperature increase towards lower pressures from about 4.1 eV at 30 Pa to 4.8 eV at 10 Pa. The electron temperature in the bulk of the plasma, however, increases more significantly, producing a flatter profile for T_e at lower pressures. This matches well the experimentally observed expansion of the high intensity glow region of the plasma towards lower pressures [116]. Thus, reduction of the pressure is beneficial to the production rate of suprathermal particles, since high electron temperatures allow for more inelastic collisions. Further support for this is found in the results of the computed atomic hydrogen molar fraction shown in Figure 5.5 b). It exhibits a similar behavior as the electron temperature, producing an only slightly elevated peak of molar fractions at 10 Pa of about 22.1 % as compared to 19.4 % at 30 Pa. However, at lower pressures, more atomic hydrogen is produced in the volume further away from the plasma source, leading to significantly increased concentrations at the outer walls.

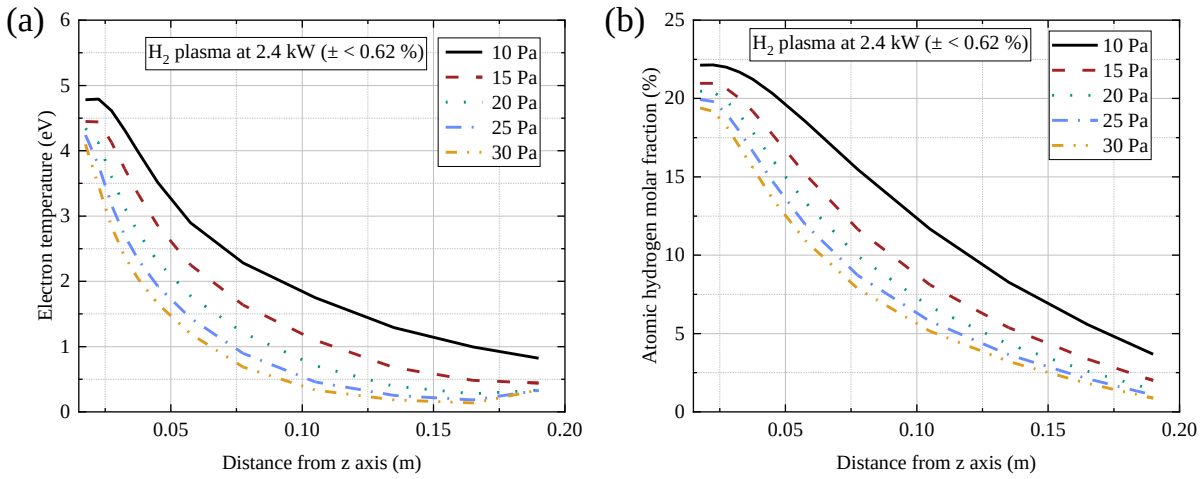

Figure 5.5: Simulated, height-averaged radial electron temperature (in a) and atomic hydrogen molar fraction (in b) for different pressures. The plasma power is 2.4 kW ($\pm < 0.62$ %) in all simulations.

When averaging the atomic hydrogen molar fraction over the whole volume, one can see that the overall atomic hydrogen molar fraction increases towards lower pressures in a non-linear fashion, as shown in Figure 5.6. The Figure shows y_H over pressure for a constant plasma power of 2.4 kW and an atomic hydrogen recombination coefficient on the plasma vessel walls of 0.1. It is noted, that the polynomial extrapolation is only an approximation and no claim for the accuracy of this approach can be made since the ignition of the plasma at pressures below 10 Pa facilitates the presence of magnetic fields. Magnetic fields can significantly impact the behavior of plasma and extrapolating plasma characteristics from the power density of the plasma without magnetic field assistance neglects this. Nonetheless, it is a useful and simple method to predict the performance of the MFP until experimental data more representative of the actual plasma in the MFP environment are available. The pressure expected at the MFP location in the DEMO pump duct is ~ 3 Pa.

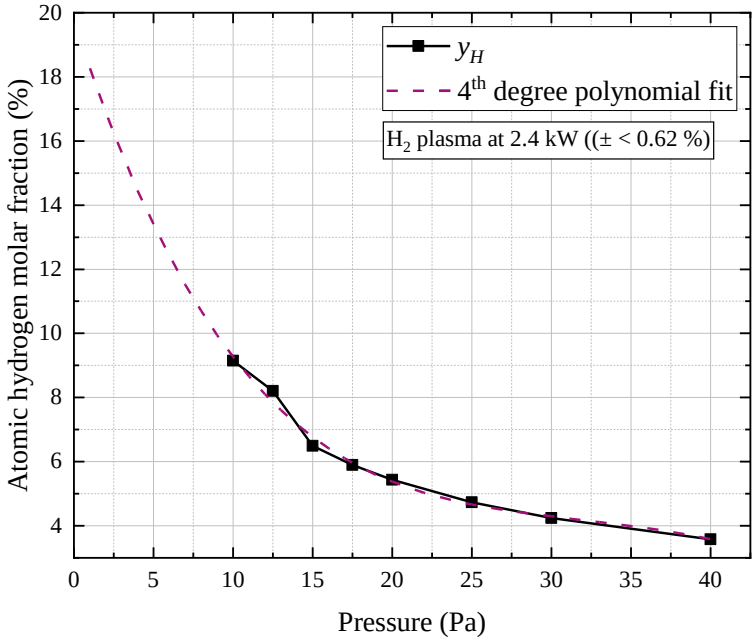

Figure 5.6: Change of atomic hydrogen molar fraction y_H according to simulations with pressures between 40 Pa and 10 Pa. The plasma power is 2.4 kW ($\pm < 0.62$ %) in all simulations. A 4th degree polynom fits best the observed behavior in y_H and is used to extrapolate to lower pressures.

5.4.2 Relevance of plasma input power

The microwave input power regulates the performance of the MFP. Based on the resistive heating capability of the plasma, a fraction of the input power is absorbed by the electron fluid and deposited in the gas. Thus, it directly influences the production of suprathermal particles. For plasma powers from 1 to 3 kW, Figure 5.7 a) and b) show the computed radial profiles of electron temperature and atomic hydrogen molar fraction, respectively, as obtained from volume-averaging along the z-axis. The pressure is 20 Pa in all of the simulation results. The electron temperature rises with plasma power and drops with radial distance from the plasma source. Especially the peak electron temperature close to the dielectric increases with power while the difference in the plasma bulk is almost unaffected. At ~ 3 kW plasma power, the electron temperature reaches almost 5 eV close to the dielectric and, as a comparison, only 3 eV at ~ 1 kW plasma power. Close to the wall, there is a slight increase in electron temperatures, possibly caused by secondary emission. There, the electron temperature is ~ 0.3 eV for all cases.

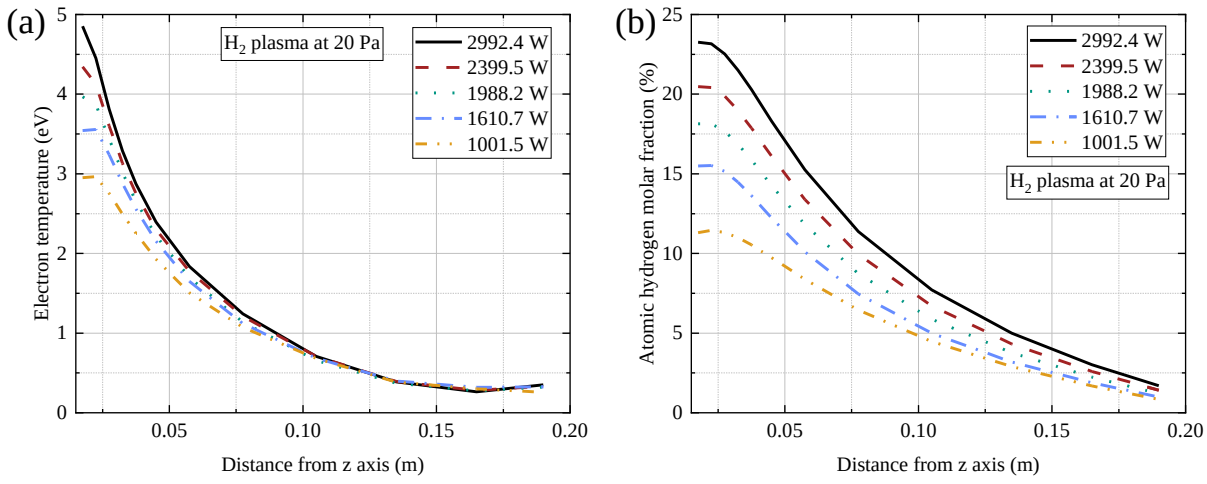

Figure 5.7: Simulated, height-averaged radial profile of electron temperature (a) and atomic hydrogen molar fraction (b) for hydrogen plasma at 20 Pa and varying power inputs.

It seems as if most of the power is absorbed close to the plasma source in all simulated cases and, in opposition to the results obtained by a reduction of pressure, the fraction of absorbed power further in the plasma does not increase significantly with plasma power.

The calculated atomic hydrogen molar fraction is plotted in Figure 5.7 b). There is a significant increase in the peak values of y_H close to the plasma source with power. The differences in y_H for varying powers decrease with distance from the central axis, almost collapsing at the outer wall. At maximum, y_H reaches 23.3 % for ~ 3 kW plasma power. The simulated values for y_H, volume-averaged for the whole plasma domain, as function of the power allow investigation of the integral effect of power increase on the suprathermal particle production. This is illustrated in Figure 5.8 for a constant pressure of 20 Pa. The y_H values increase with power, following an inverse quadratic correlation. At the lowest displayed plasma power of 1222 W, y_H reaches ~ 3.13 % and increases to ~ 6.25 % at 2992 W.

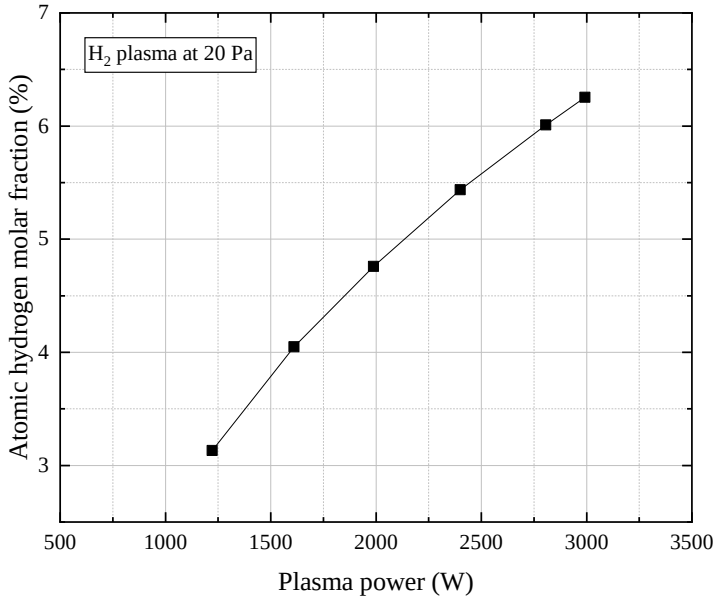

Figure 5.8: Calculated change in y_H with plasma power in hydrogen plasma at 20 Pa.

5.4.3 Impact of different wall recombination coefficients

The atomic hydrogen recombination coefficient on plasma facing surfaces strongly influences atomic hydrogen densities in plasma and large spreads in the recombination coefficient for the same wall materials exist [86-88] [142]. The value for the walls of the plasma vessel of HERMES*plus* is approximated to produce a best match between simulation and experiment, though it is not measured directly. The parameter is varied in a parametric study within the range of the literature data to develop an understanding of how much the atomic hydrogen concentration in the plasma may change due to material variation. Changes may occur during the experiments as, e.g., the case of surface roughening by plasma exposure, deposition of impurities or even temperature changes. However, the recombination coefficient is not a quantity that directly affects the production of suprathermal particles, since this is considered exclusively a property of the plasma bulk.

Changes in the heavy species population affect the electron fluid through the reaction term that determines the energy transfer from electrons to heavy species and, thus, a variation of the recombination coefficient also affects the plasma parameters. Figure 5.9 shows the calculated change in y_H with the plasma vessel wall recombination coefficient for pressures from 20 to 10 Pa at a constant plasma power of 2.4 kW. The atomic hydrogen molar fraction increases dramatically towards low recombination coefficients. As the latter approaches 0, the only channels for destruction of atomic hydrogen that remain are recombination on the dielectric or volume recombination. The dielectric

surface has significantly lower impact on the process because its area is much smaller than the outer wall surface area and rates of three-body volume reactions, necessary to recombine the hydrogen atom, are negligibly low at the given densities. This leads to a sharp increase of the atomic hydrogen molar fraction towards low recombination coefficients and the confirmation that recombination on the vessel wall is the predominant mechanism for recombination of atomic hydrogen. While a reduction in pressure is accompanied by an increase in the atomic hydrogen molar fraction anyway, the increase towards low recombination coefficients is stronger for the lower pressure cases. This is due to the surface recombination being even more important as compared to the high pressure case because of lower volume recombination rates.

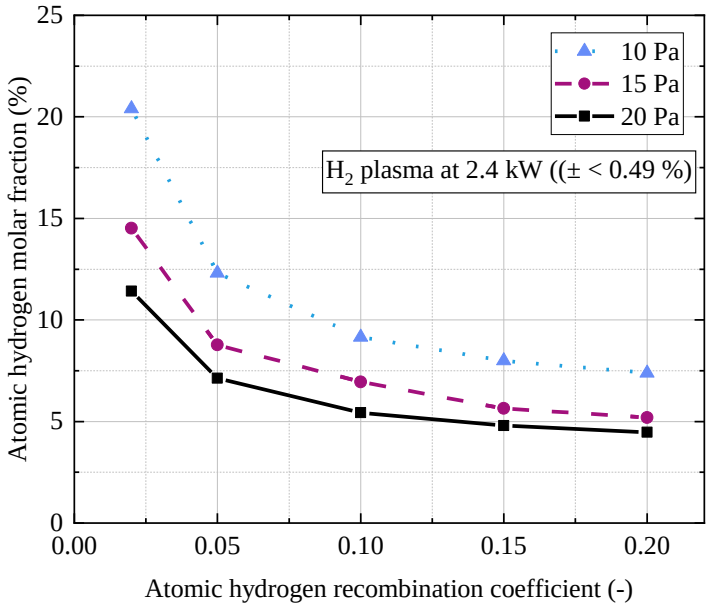

Figure 5.9: Simulated change in the atomic hydrogen molar fraction in the plasma based on variation of the recombination coefficient on the outer stainless steel walls for different pressures. The covered range of recombination coefficients represents all values assumed in literature for this material.

5.5 Evaluation of necessary parameters

The plasma simulation provides information on the supply of suprathermal particles, which drive plasma-driven permeation in a MFP, through the calculation of the atomic hydrogen density. Different operations of the plasma lead to respective volume-averaged atomic hydrogen densities in the plasma vessel. To implement the plasma performance in view of this quantity into the metal foil pump vacuum simulation with the TPMC approach, it has to be broken down into a single probability for the excitation of a particle impinging on the plasma surface.

To this end, the plasma domain described above is reconstructed in a dedicated simulation that uses the Heavy species transport interface of the simulation software COMSOL. This simulation is termed excitation simulation. The physics that determine the movement of the modelled particles is described in section 5.2. The model only considers surface interactions and a total of two different species, *A* and *B*. Species *A* represents the ground-state particles (ground-state hydrogen molecules in the real application) and species *B* the excited particles (hydrogen atoms in reality). Since the TPMC simulation only considers a single particle moving through the domain at a time, the excitation and de-excitation of ground-state or, respectively, excited particles does not introduce new particles into the domain. Thus, it does not account for mass conservation in the transformation process from species *A* to *B*. Instead, a single particle with the mass of a hydrogen atom turns into a single particle with the mass of a hydrogen molecule in the de-excitation and vice versa in the excitation process.

The three surfaces assigned as vessel walls are modeled analogous to the plasma simulation and prescribed with recombination probabilities for the excited particles of 0.1 [86]. On the plasma source surface, placed at the inner radius at 1.5 cm, excited particles can also recombine at a lower probability of 0.02 [97] [130]. Ground-state particle excitation only occurs upon collision with this plasma source surface with the probability φ. Depending on the value of φ, a volume-averaged excited particle concentration is achieved in steady state. This value is regarded as representative of a certain plasma source operation. Thus, this model represents a bridge from the plasma to the TPMC simulation.

The idea behind the excitation simulation is to simplify the plasma simulation and its physics, while describing the particle behavior as accurately as possible except for the creation of the excited species. This also means that the boundary conditions and the transport physics have to mimic those of the plasma simulation. If this is fulfilled, the electromagnetic wave excitation and the excitation on the boundary remain the only major model characteristics that are not matching between the two simulations – which is exactly the aim of this exercise, as they need to be swapped for each other to achieve the same outcome in terms of excited particle densities.

The calculated change of the excited particle molar fraction with the excitation probability on the plasma source φ is illustrated in Figure 5.10. The outer radius and height of the simplified model correspond to the plasma simulation model and measure 0.2 and 0.3 m, respectively. For the temperature in the model domain, the same radial profile as in the plasma simulation is used. The pressure is set to a given value, 20 Pa as a default, except for the case, in which excitation parameters are obtained that should reflect the operation at the low pressures in the sub-divertor area (1 to 5 Pa). In those cases, the exact pressures are used that correspond to the computed excited particle concentration of the simulation results for the atomic hydrogen molar fraction at a plasma power of 2.4 kW. The inner radius of the model is set to 0.015 m, corresponding to the plasma simulation dimension and the HERMES*plus* plasma source and 0.025 m, to simulate a larger plasma source diameter.

The excited particle molar fraction rises quite dramatically with the excitation probability up to a value of φ = 0.1. In this range, it already reaches ~ 6.6 % for a plasma source with 0.015 m radius. This is shown by the black line. In a MFP, the employed plasma source is expected to transport more power, requiring larger annular gaps between inner and outer conductor, more conductor surface area and more cross-section in the annular gap for cooling, leading to 0.025 m as plasma source radius. Excitation on a plasma source of this radius corresponds to the pink dotted line, which includes a correction factor. This comes from the reduction of the vessel volume that is associated with the increase of the plasma source diameter. However, for consistency, the power density must stay the same, which necessitates the correction factor that multiplies the excited particle concentration with the ratio of reduced to original volume. With this, a linear correlation of excited particle molar fraction and power density is assumed. However, the difference between the values for the excited particle concentration with and without correction of the volume is very small.

Finally, the extrapolation to lower pressures is also employed using results from the plasma simulation. The exact y_H values corresponding to certain operation conditions in terms of plasma power and pressure are used as input to the y-value of the fit formula displayed in Figure 5.10 to obtain the corresponding φ-value, which yields the same excited particle concentration. Table 5.2 summarizes the received numbers.

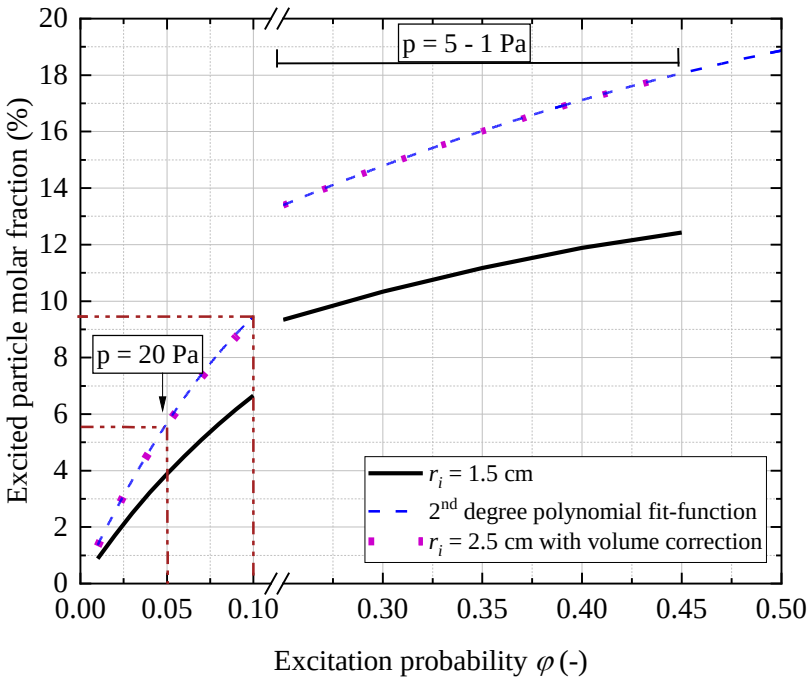

Figure 5.10: Calculated excited particle molar fraction as function of the excitation probability φ for a simplified excitation simulation. Molar fractions are obtained for simulations with 2 different plasma source boundary radii of 1.5 and 2.5 cm. Required values for φ to achieve molar fractions corresponding to the findings in the plasma simulation are on the conservative side for the simulations performed at 20 Pa and an extrapolation is used to account for pressures below 10 Pa. Data previously published by the author in [146].

An important characteristic of the approach to use the excitation probability on the plasma source is its applicability to various geometries. For consistency, the variation of the outer radius has to have the same effect on the integral excited particle molar fraction in both simulation types. Figure 5.11 shows the change in the atomic hydrogen molar fraction, or, in other words, the excited particle molar fraction, with the radius of the outer wall for the excitation simulation for several excitation probabilities φ and the comparison with a plasma simulation at 20 Pa, which uses 2.4 kW plasma power ($\pm < 0.15$ % uncertainty bound). The plots are parallel for the two simulaitons, providing the evidence that the use of the excitation parameter is consistent for varying sizes of the simulation domain.

Table 5.2: Volume-averaged atomic hydrogen molar fractions as obtained in the plasma simulation and the required values for the excitation probability φ to achieve the same excited particle molar fractions in the excitation simulation.

p (Pa)	P (W)	y_H (%)	r_i (cm)	φ (-)
20	1221.8	0.03131	2.5	0.025082
	1610.7	0.04047		0.03355
	1988.2	0.04759		0.04049
	2399.5	0.05436		0.047415
	2806.7	0.0601		0.053588
	2992.4	0.06253		0.056294
5	2400	0.13399		0.250073
4	2400	0.1447		0.288219
3	2400	0.1563		0.333466
2	2400	0.169		0.389472
1	2400	0.1827		0.461881

The value for the atomic hydrogen molar fraction increases quadratically to lower radii, which goes along with a quadratic increase in power density due to change in volume with r^2. At the lowest radius tested, 0.15 m, y_H increases up to ~ 7 % in the plasma simulation, which lies short of the value obtained by using φ = 0.05, in agreement with the table above.

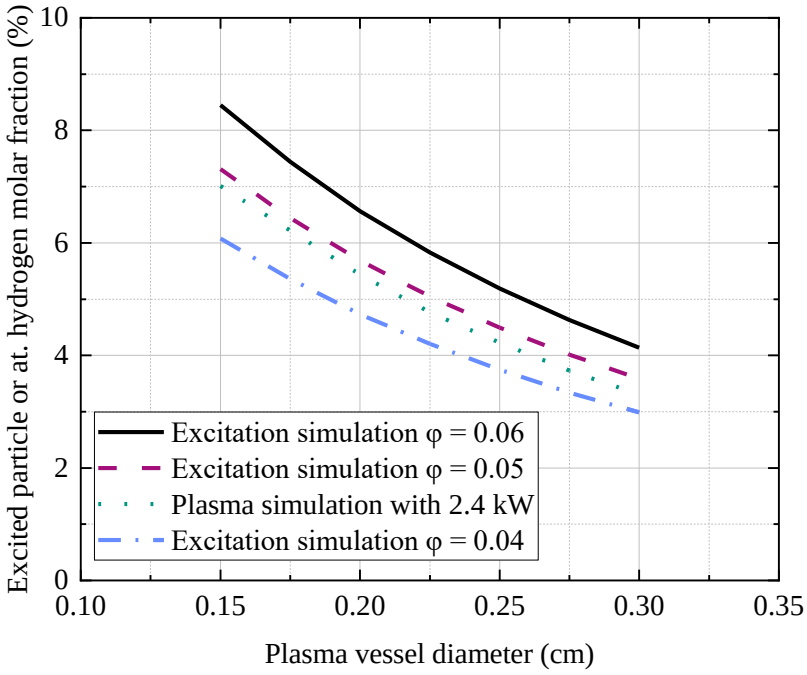

Figure 5.11: Calculated change in the atomic hydrogen, i.e., excited particle, molar fraction for varying plasma vessel radii and excitation probabilities of the simulation model. The variation of the radius has the same effect in both simulations, indicating that using the simplification of the excitation parameter is applicable to different geometries of the simulation model.

6 Hydrogen plasma experiment and diagnostics

The following chapter explains the experimental setup HERMES*plus* and the applied experimental methods for determination of the permeation flux and measurement of the atomic hydrogen density via optical emission spectroscopy.

6.1 Experimental setup HERMESplus

In this work, the experimental setup HERMES*plus*, as sketched in Figure 6.1, is used to investigate the PDP process. An approximately 300 mm high cylindrical vessel with two CF DN 400 end flanges serves as the plasma chamber for an axisymmetrical, linearly extended microwave plasma source, which is installed in the center of the cylinder. To improve readability, some images of the experimental setup are given in Appendix 5. The plasma source is customized from the Duo-Plasmaline product by the company *Muegge GmbH*. The coaxial line consists of a copper inner conductor, which is surrounded by a dielectric along the vacuum boundary and two copper outer conductors at the ends of the plasma source (Figure 3.5). The dielectric materials used consist of quartz SiO_2 and alumina Al_2O_3. The microwave is transported to the vacuum via waveguides installed at the top and bottom of the apparatus, which are connected to magnetrons. Upon entering the vacuum, the microwave ignites a plasma in the center of the vessel surrounding the dielectric. The magnetrons are protected by a circulator with dummy load and the reflected microwave power is measured and recorded. A stub-tuner system within each waveguide offers impedance tuning to reduce microwave reflection. In this way, the power reflection can be reduced to 0 during most of the experiments.

Approximately 145 mm in radial distance of the vessel center, a membrane module is installed on a CF DN 63 flange. This module consists of several parts, of which the most important one is a tubular metal foil of roughly 100 mm height, 10 mm diameter and 0.1 mm thickness. Two different membrane modules are tested, featuring a niobium and a vanadium metal foil. The current leads for the resistive heating are spot-welded to the bottom and top of the tube. For the current lead material, the metal foil material is used as well as molybdenum at the ends towards the vacuum feedthrough due to its high temperature resistance. At the top of the tube, its cylindrical end is electron-beam welded to a transition part made of stainless steel, which attaches to the main upstream body of the membrane module. For homogeneous temperature distribution, another resistive heating current lead, which is attached to the transition part, can be used. The connection of the membrane module to the vessel is equipped with a ceramic break to isolate the vessel electric potential from the metal foil. The vessel is electrically grounded and the metal foil is connected to the transformers, which apply a voltage to drive a current for heating. Hence, also all vacuum feedthroughs for the current leads are equipped with ceramic breaks. The metal foil heating circuit can be biased against the vessel using an external power supply.

The inside of the tubular metal foil marks the bottom part of the downstream chamber, which extends towards the top of the membrane module and is connected to several measurement devices as well as the downstream pumping train. The downstream chamber is also connected to the upstream chamber via a bypass that can be closed with valves during operation. From this bypass, another pipe is routed towards the third chamber of the setup, a residual gas analysis (RGA) system. The upstream chamber has three windows, of which one is used to monitor the plasma with an optical emission spectroscope (OES). The upstream chamber is connected to a DN 100 turbomolecular pump through a metal handvalve, which can be manually adjusted to regulate the upstream pumping speed.

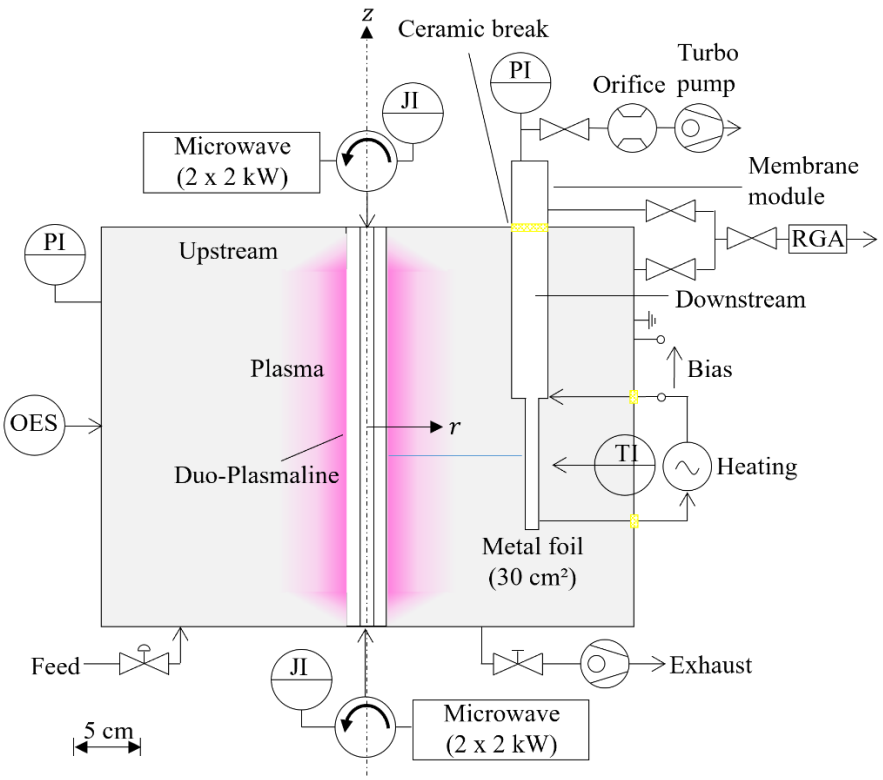

Figure 6.1: Experimental setup HERMES*plus* for investigation of the PDP process.

6.1.1 Measurement devices and infrastructure

During most of the experiments, the upstream chamber of HERMES*plus* as well as the downstream chamber are equipped with 5 pressure gauges each, which cover the whole operational range. A list of the gauges, their respective installation chamber and measurement method as well as name of the manufacturer, designation in the P&ID (see Appendix 6), pressure range and accuracy is given in Table 6.1. Temperature coefficients of the Baratron type gauges are not listed in the table as the gauges are all equipped with an internal temperature control and a constant temperature is assumed during operation. Therefore, uncertainty in the measurement due to temperature variations is not considered in the uncertainty estimation of the measurement.

The downstream chamber is pumped by a *Pfeiffer* DN63 turbomolecular pump HiPace 80 with an *Edwards* nXDS10i scroll pump as rough pump. During plasma operation, the throughput of the upstream chamber is significantly higher. Hence, the upstream connected *Pfeiffer* DN100 turbomolecular pump TPU 180H is backed by two *Leybold* ECODRY 25 plus roots pumps in parallel operation. The RGA chamber is equipped with another *Pfeiffer* HiPace 80 and an *Edwards* nXDSi 6 scroll as backing pump. A list of the pumps is given in Table 6.2. The OES is a *PLASUS* EMICON 2SA with a measurement range of 200 – 1100 nm and 1.5 nm spectral resolution. The upstream vessel wall temperature is continuously being monitored by several thermocouples. The metal foil temperature is measured with the *Sensortherm* ratio pyrometer Metis M322, which points at the foil inner surface from a window at the top of the downstream chamber. The RGA is equipped with 2 *MKS Instruments* MicroVision 2 quadrupole mass spectrometer units: one for high resolution of masses between 1 to 6 amu and another one for masses between 1 to 300 amu. The turbomolecular pumps as well as the plasma source power supply and magnetron are connected to a water cooling circuit that is powered by an *Aermec* ANL 020 continuous flow chiller with 5.65 kW cooling power. The setup features a multitude of feedlines with individual mass flow controllers (MFCs) to carry out experiments with gas mixtures, which is crucial to evaluate the effect of noble gases on PDP. However, most of the experiments are performed using only

H_2 or D_2. Hydrogen is fed through a 100 sccm *MKS* 1179B MFC, which can be connected to a computer through ethernet to change the calibration to different gases.

Table 6.1: Pressure gauges and their respective pressure range and error.

Chamber	P&ID designation	Measurement method	Name	Pressure range (Torr)	Error
Upstream	PI07	Baratron	*Mks* 690A	$10^3 – 3 \cdot 10^{-5}$	+/- 0.12 % of reading
	PI02	Cold cathode Pirani	*Mks* 972b	$10^{-3} – 10^{-8}$ 1 atm	+/- 30 % of reading +/- 5 % of reading
	PI08	Baratron	*Mks* 690A	$10 – 3 \cdot 10^{-5}$	+/- 0.12 % of reading
	PI01	Baratron	*Leybold* Capacitron CMH1	< 1	0.1 % + 0.01 % of max. value
	PI11	Hot cathode	*Mks* 355	$5 \cdot 10^{-2}$ - 10^{-9}	
Downstream	PI04	Cold cathode/Pirani	*Mks* 972b	$10^{-3} – 10^{-8}$ 1 atm	+/- 30 % of reading +/- 5 % of reading
	PI09	Baratron	*Mks* 690A	$10 – 3 \cdot 10^{-5}$	+/- 0.12 % of reading
	PI03	Baratron	*Mks* 627d	$0.02 – 10^{-5}$	+/- 0.25 % of reading
	PI14	Baratron	*Mks* AA02A	$0.1 – 5 \cdot 10^{-5}$	+/- 0.12 % of reading
	PI12	Hot cathode	*Mks* 355	$5 \cdot 10^{-2}$ - 10^{-9}	
RGA	PI10	Micro-Ion	*Mks* 354	$5 \cdot 10^{-2}$ - 10^{-9}	
Exhaust	PI05/PI06	Pirani	*APG*-M-NW16	$10^3 – 10^{-4}$	-
	PI13/PI14	Pirani	*Instrutech* 211 Stinger	$10^3 – 10^{-4}$	< +/- 10 % of reading

Table 6.2: List of pumps and the respective chamber, they are attached to as well as the maximum H_2 pumping speed.

Chamber	P&ID designation	Pump type	Name	H_2 pumping speed (l/s)
Upstream	P2	Turbomolecular	DN100 *Pfeiffer* TPU 180H	140
	P10/P11	Roots	*Leybold* ECODRY 25 plus	6.9
Downstream	P1	Turbomolecular	DN63 *Pfeiffer* HiPace 80	48
	P8	Scroll	*Edwards* nXDS10i	3.2
RGA	P6	Turbomolecular	DN63 *Pfeiffer* HiPace 80	48
	P4	Scroll	*Edwards* nXDS6i	1.7
Feedline	P5	Diaphragm	*Vacuubrand* MD4 NT	2
Plasma source	P7	Side channel blower	*Elektror* SD42	47

The calibration of the mass flow controllers (MFCs) is supplied by the manufacturer of the MFC based on experimentally validated 3D FEM multiphysics simulations that take into account the flow sensor structure, the sensor drive circuit and effects due to different gas properties. The same type of MFC is used to feed helium. Argon is fed through either a 10 sccm MFC of the type 1259CJ from *MKS Instruments* or a 0.5 sccm *Analyt* of the MTC 358 series. The latter can also be used to admit xenon.

6.1.2 Permeation flux measurement

The permeation flux through the tubular metal foil is determined via the pressure difference method. With the bypass closed and the downstream gate valve opened, the downstream chamber is continuously being evacuated by a turbomolecular pump with a specified pumping speed. The conductance of this pump duct is dominated by the flow through a precision-drilled orifice in front of the pump. The diameter of the orifice is measured as 4.2 mm with an uncertainty of $\pm$ 0.05 mm. The orifice size is chosen as such to obtain free molecular flow (FMF) through the opening at the normal operation pressure in the downstream chamber. Using eq. (6.1) and the assumption of FMF, the throughput through the orifice J_{ori} can be calculated, which is the same as the permeation flow J_{perm}, or the difference between the re-emission flow J_{emiss} and absorption flow J_{abs} of the metal foil:

$$J_{ori} = J_{perm} = J_{emiss} - J_{abs} = (p_d - p_t) \cdot S_{eff}. \tag{6.1}$$

Here, p_d is the downstream pressure and p_t the pressure behind the turbomolecular pump, which is negligible compared to p_d. S_{eff} is the effective conductance, which is determined from the turbomolecular pump's pumping speed for the gas species i $S_{p,i}$ and the black hole pumping speed of the orifice C_{ori}. The latter is obtained from eq. (3.8) according to

$$S_{eff} = \frac{1}{\frac{1}{S_{p,i}} + \frac{16}{\eta \cdot \pi \cdot d_{ori}^2 \cdot \left(\frac{8RT_d}{\pi M_i}\right)^{0.5}}}. \tag{6.2}$$

The uncertainty in the pumping speed of the pump is assumed as 5 % of the nominal value. The transmission probability η can be evaluated from the dimensions of the orifice using [148]. However, this value of η only holds for FMF. To be more accurate, experimental data from [73] are used to obtain a transmission probability, which requires knowledge of the Kn number in the orifice. The uncertainty in η is given with $\pm$ 2 %. The temperature in the downstream chamber at the position of the orifice T_d is assumed as 20 °C (with an uncertainty of +/- 2 K) as it is located within the stream of the air conditioner and rather far away from the only relevant heat source in the downstream chamber, the metal foil. This is supported by random measurements throughout the experimental campaigns. For the used orifice, the transmission probability is calculated to be η = 0.677, so that the effective conductance of the pump arrangement results as S_{eff} = 4 l · s^{-1}.

To obtain the permeation flux, the flow J_{perm} has to be divided by the metal foil surface area, which is roughly 30 cm² with an estimated uncertainty of $\pm$ 10 %. The absolute uncertainty of the calculated permeation flux is derived according to the estimation of the systemic combined standard uncertainty of uncorrelated input quantities in the guide to the expression of uncertainty in measurement [148].

6.1.3 Optical emission spectroscopy: Approach and setup of optics

An OES colllimatoroptic is used to obtain data for the experimental validation of a hydrogen plasma simulation. It is pointing in a 90° angle at the cylindrical plasma. A measurement method is developed to measure the atomic hydrogen density while accounting for the radial inhomogeneity of the plasma composition. As illustrated in Figure 6.2, a measurement of a specific optic angle shows the result of the integral along the measurement line and cannot resolve the particle density at a certain location within the plasma or at a certain radial distance from the plasma source. A common approach to this problem is using Abel's transformation to obtain a radial profile of the intensity readings [149]. However, in the given experimental apparatus, the parallel shifting of the optic to the circular system is not possible as the window of the plasma vessel is too small. Instead, the cylindrical plasma is imagined as separated into 12 concentric rings, which are subjected to the assumption of axisymmetry and homogeneity of the plasma parameters and gas compositions within each ring at the axial position z.

The ring numbers count from j = 1 to 12 from the center to the outside with each rings' respective species i density $n_{i,j}$, electron temperature $T_{e,j}$ and electron density $n_{e,j}$ for a certain axial position z. One measurement at the position z, delivering an integral atomic hydrogen density along the line of sight n_H, can also be expressed as the sum of products of the individual ring's length l_j fraction of the total measurement line l_{tot} times the respective atom density in this ring $n_{H,j}$ as expressed through

$$n_H = \sum_{j=1}^{12} \frac{l_j}{l_{tot}} \cdot n_{H,j}. \tag{6.3}$$

With 12 measurements at different optic angles, i.e., with different contributions of the individual rings to the total radiance, a linear equation system (LES) can be created that equates the measured atomic hydrogen concentration for each measurement to the sum of the weighted individual rings' concentrations. However, this LES does not have a reasonable physical solution because the assumption of homogeneous n_H within one ring is inaccurate. Increasing the number of rings to a value, at which a constant atom density for one ring is reached, is experimentally unfeasible without introducing uncertainties that prohibit correctly solving the LES. Instead, an expected atomic hydrogen concentration for each measurement is calculated from the simulation data based on the different optic angles. For each measurement, this value is compared to the experimentally obtained integral atomic hydrogen concentration along the line of sight to evaluate the level of agreement between the two.

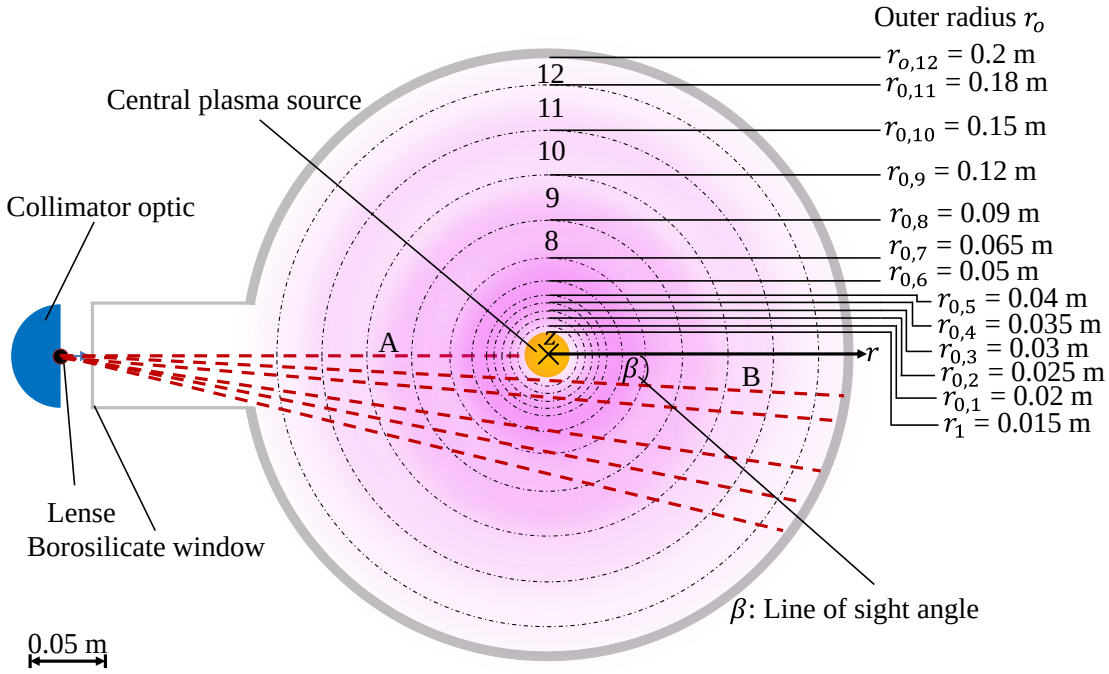

Figure 6.2: Bird view of the plasma vessel with the lines of sight of different optic alignments highlighted in red and the central plasma source in yellow.

The employed experimental method requires knowledge about some plasma parameters and reaction rates of the volume, from which the emission lines are measured. Following the same procedure, those parameters and reaction rates are averaged according to the fraction of the individual ring length of the total line of sight. The optic fibre is attached to a collimator optic, which is mounted on a customized steel plate screwed to a DN40 window flange. The setup is shown in Figure 6.3 with the optic fibre pointing at the center of a hydrogen plasma. The angle is adjusted manually and tightened with a wing screw. The uncertainty in the angle is given with +/- 1°.

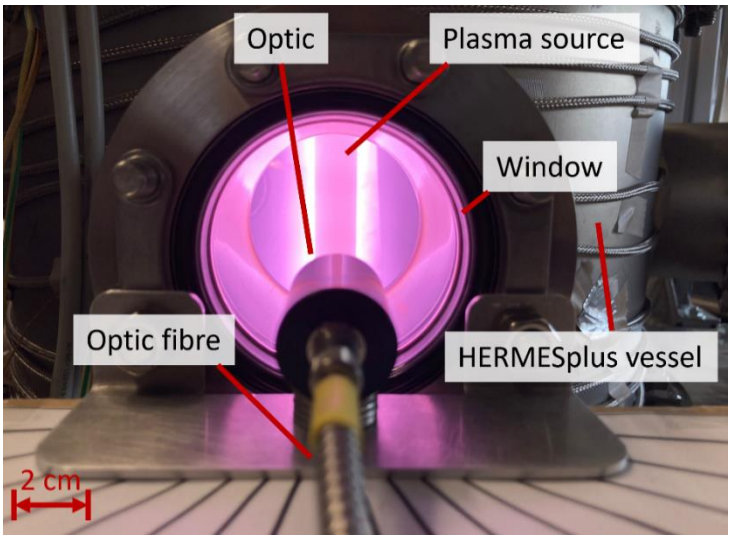

Figure 6.3: OES optic aligned in a 0° angle looking directly at the plasma source.

6.2 Validation of plasma model by spectroscopic measurements

Here, the experimental method applied to validate the simulation, actinometry, is introduced. The required data to perform the calculation are derived. Application of actinometry only yields reasonably accurate results if a certain set of conditions is fulfilled. This applicability of actinometry is evaluated before presentation of the measured atomic hydrogen molar fractions.

6.2.1 Actinometry calculation and comparison with literature

The atomic hydrogen concentration or atomic hydrogen molar fraction y_H in the plasma is used to validate the simulation. It is measured using actinometry, employing optical emission spectroscopy. A description of the actinometry method is given in [150]. Its assumes that the known density of a ground-state atom of element *A* is related to the de-excitation of a specified excited state of this atom in the same way as the ground-state density of element *B* to a respective specified excited state of *B* according to

$$\frac{n_A}{I_A} = k\frac{n_B}{I_B}, \tag{6.4}$$

where $I_{A/B}$ is the line emission intensity of a specified spectral line of the respective element, *A* or *B*, and k is a correction factor. The choice of spectral lines, from which the line intensities are taken, is linked to one of three conditions, that have to be met for the actinometry principle to be applicable.

- The first condition requires that the excitations to the excited states of elements *A* and *B*, which emit the specific lines, have similar excitation thresholds and cross-section shapes. In this way, the production of the excitated states changes in the same way with density and energy of the electron population.
- Secondly, the excited states have to be predominantly produced from electron impact reactions on the ground-state of the atom and not through multiple step excitation processes.
- Thirdly, the de-excitation of the excited state should mainly happen through radiative decay, which leads to the specified line emission, and not through quenching reactions or others.

Thus, introducing an atomic gas (*B*) at known concentration without disturbing the discharge gives a baseline to determine the concentration of the ground-state atom density of element *A*. Here, the discharge gas hydrogen is compatible with the actinometer argon [111] [151]. The electronic transitions

that fulfil the requirements mentioned above are, in Paschen notation, given as reactions 6.1 and 6.7 in Table 6.3. Their corresponding radiative decay reactions, which yield the lines observed with OES, are given by reactions 6.2 and 6.8.

Table 6.3: Ground-state excitation reactions that yield the excited states and their corresponding radiative emission reactions, which are observed via optical emission spectroscopy, as well as all considered quenching reactions.

Nr.	Reaction	Type	Threshold (eV)	Given as	Ref.
6.1	$e + H \rightarrow e + H(n=3)$	Excitation	12.11	$\sigma(\epsilon)$ [m²]	[122]
6.2	$H(n=3) \rightarrow H(n=2) + h\nu$ (656.2 nm)	Rad. decay	-	$4.41 \cdot 10^7$ s^{-1}	[137]
6.3	$H(n=3) + H \rightarrow 2\ H$	Quenching	-	$\sigma(\epsilon)$ [m²]	[135]
6.4	$H(n=3) + H_2 \rightarrow H + H_2$	Quenching	-	$\sigma(\epsilon)$ [m²]	[152]
6.5	$H(n=3) + Ar \rightarrow H + Ar$	Quenching	-	$\sigma(\epsilon)$ [m²]	[153]
6.6	$H(n=4) \rightarrow H(n=3) + h\nu$	Rad. decay		$8.986 \cdot 10^6$ s^{-1}	[137]
6.7	$e + Ar \rightarrow e + Ar(^2p_1)$	Excitation	13.48	$\sigma(\epsilon)$ [m²]	[121]
6.8	$Ar(^2p_1) \rightarrow Ar(^1s_2) + h\nu$ (750.3 nm)	Rad. decay	-	$4.45 \cdot 10^7$ s^{-1}	[154]
6.9	$Ar(^2p_1) + H \rightarrow Ar + H$	Quenching	-	$\sigma(\epsilon)$ [m²]	[153]
6.10	$Ar(^2p_1) + H_2 \rightarrow Ar + H_2$	Quenching	-	$\sigma(\epsilon)$ [m²]	[153]
6.11	$Ar(^2p_1) + Ar \rightarrow 2\ Ar$	Quenching	-	$\sigma(\epsilon)$ [m²]	[155]
6.12	$e + Ar(^1s_3) \rightarrow e + Ar(^2p_1)$	Excitation	1.87	$\sigma(\epsilon)$ [m²]	[156]
6.13	$e + Ar(^1s_5) \rightarrow e + Ar(^2p_1)$	Excitation	2.05	$\sigma(\epsilon)$ [m²]	[156]

By knowledge of the two gases, eq. (6.4) can be rewritten as

$$n_H = n_{Ar} \frac{I_{H(656.2)}}{I_{Ar(750.3)}} k. \tag{6.5}$$

The factor k is a variable that accounts for the details of the process, plasma and setup. It introduces corrections terms for the optical emission F_{opt}, for quenching de-excitation of the excited states investigated Q_r and, most importantly, for the actual reaction rates of reactions (6.1) $k_{r,H}$ and (6.7) $k_{r,Ar}$ according to

$$k = F_{opt} Q_r \frac{k_{r,Ar}}{k_{r,H}}. \tag{6.6}$$

The optical correction factor F_{opt} takes into account that a fraction of the excited hydrogen at H(n=3) radiatively decays to the H ground-state with an Einstein coefficient $A_{31} = 5.575 \cdot 10^7$ s^{-1} and the rest decays (according to reaction (6.2) in Table 6.3) with an Einstein coefficient A_{32} [137]. The term F_{opt} also considers the wavelength-specific optical device responses $K_{656.2}$ and $K_{750.3}$ according to [111]

$$F = \frac{K_{750.3} k_{rad,Ar} \lambda_{656.2} / A_{2p1}}{K_{656.2} A_{32} \lambda_{750.3} / (A_{32} + A_{31})} \tag{6.7}$$

where $k_{rad,Ar}$ is the radiative decay rate of the excited Ar(^{2}p$_1$) state, which is the same as the Einstein coefficient for the total radiative decay of the ^{2}p$_1$ state A_{2p1} and $\lambda_{656.2}$ and $\lambda_{750.3}$ are the respective wavelengths of the two observed emission lines. The quenching correction term Q_r considers de-excitation of the excited species through heavy species collisions with H, Ar and H_2. Here, reactions with other heavy species are neglected due to low concentrations and vanishing contributions to the total quenching reaction rate. The corresponding quenching reactions of interest are given as reactions 6.5 to 6.10 in Table 6.3.

The reaction rates depend on the collisional cross-sections and the relative velocities of the species towards each other, see eq. (3.17). The quenching reaction term then introduces a correction factor to

the measured atomic hydrogen concentration by forming the ratio of the reaction rates for quenched atomic hydrogen to quenched argon corresponding to [111]

$$Q = \frac{1 + \left(\frac{pN_A}{T_G R (A_{32} + A_{31})} \left(\bar{v}_{32} \sigma_{32} y_{H_2} + \bar{v}_{31} \sigma_{31} y_H \right) \right)}{1 + \left(\frac{pN_A}{T_G R \left(k_{rad,Ar} \right)} \left(\bar{v}_{34} \sigma_{34} y_{H_2} + \bar{v}_{33} \sigma_{33} y_H \right) \right)}, \tag{6.8}$$

where $\bar{v}_{ij}$ is the relative collision velocity of species i and j as obtained from their thermal velocities. For the molar fractions of atomic hydrogen y_H and molecular hydrogen y_{H2}, a first value is taken from the results of the simulation, followed by an iterative approximation. At last, the reaction rates of the two excitation reactions 6.1 and 6.3 are obtained from eq. (3.16).

To obtain a first solution for the EEDF, all considered plasma reactions are implemented into a 0D model of the *Boltzmann Equation* as provided by the simulation software COMSOL. The software allows variation of the assumptions for the EEDF and choice of the EEDF type between Druyvesteyn', Maxwellian', Boltzmann and a generalized approach. The latter is chosen for this application with the power law being a function of the electron temperature in the plasma. The model includes a reaction set of argon plasma reactions, which is listed in Appendix 7 as the presence of Ar influences the EEDF and the reaction rate of reaction 6.3 also must be computed to evaluate the measurement. The data to calculate the reaction rates are obtained from [121] [122] [154] [156-161]. This necessitates knowing the actual Ar concentration in the plasma vessel during the experiment. It can be derived from the reading of the respective, calibrated mass flow controllers. The feedlines of the H and Ar bottle are both evacuated, as is the vessel. A constant flow of H_2 is admitted with open bypass and the metal foil at ~ 500 °C to prevent hydride formation. Pumping through the downstream chamber and the RGA chamber is stopped by closing the connections to the main vessel with valves.

Thus, pumping only occurs through the upstream pumping channel. The handvalve in front of this pumping channel is put in a position, which allows feeding of a H_2 flow in similar magnitude as planned for the actinometry experiment. The flow $\dot{F}$ is adjusted so that a constant pressure of 20 Pa is maintained in the plasma vessel and the flow value is noted. Subsequently, the vessel is evacuated through downstream by opening the valve to the downstream pump again and the initial procedure is repeated with Ar as feed gas. A lower feed is required to sustain the same 20 Pa upstream pressure due to the lower pumping speed of Ar. The ratio of the two feeds in the given valve position, g, is calculated at a value close to the ratio of the thermal velocities of the two gases, indicative of close to free molecular flow through the small opening in the upstream pumping channel. The Ar molar fraction can be obtained from the ratio of the feed flows of the two gases and the corrected ratio of the two pumping speeds, which considers that a fraction of the hydrogen is dissociated in the plasma. An approximation of the atomic hydrogen molar fraction can be taken from simulation. In FMF, hydrogen atoms are pumped at larger rates than the molecules, necessitating the correction factor according to

$$x_{Ar} = \frac{1}{\frac{\dot{F}_{H2}}{\dot{F}_{Ar}} \cdot g} = \frac{1}{\frac{\dot{F}_{H2}}{\dot{F}_{Ar}} \cdot \left(y_H \frac{\bar{v}_{Ar}}{\bar{v}_H} + (1 - y_H) \frac{\bar{v}_{Ar}}{\bar{v}_{H2}} \right)}. \tag{6.9}$$

The dissociation of H_2 also leads to the dilution of Ar in the plasma, which can be taken into account by factoring in the assumed atomic hydrogen molar fraction y_H

$$y_{Ar,dil} = \frac{y_{Ar}}{\frac{1}{y_{H2} + 0.5 y_H}} = \frac{y_{Ar}}{\frac{1}{(1 - y_H) + 0.5 y_H}}. \tag{6.10}$$

Using the ideal gas law, the temperature assumed in each ring according to the chosen temperature profile and the weighing factors for each ring, an average particle density is computed for each line of sight. By multiplication with y_{Ar}, which is assumed as homogeneous throughout the whole vessel, the particle density of Ar in ground-state is calculated. Analogously, the molar fraction of atomic hydrogen is determined by dividing the computed atomic hydrogen particle density n_H as calculated through eq. (6.5) by the average particle density along one line of sight. To obtain the reaction rates and finish the calculation, the gas composition and the electron mean energy must be known. Obtaining this data is not straightforward but iterative and requires some additional explanation at first.

A first set of data for the gas composition can be taken from a first solution of the hydrogen plasma simulation. Simultaneously, using the same model as described in 5.3, an Ar plasma simulation that uses the same chemistry as listed in Appendix 7 is created to derive the molar fractions and plasma parameters of an Ar plasma. To get a solution for the EEDF, a data-set for the gas composition and plasma parameters that considers both, the results of the hydrogen plasma and of the argon plasma simulation, with their respective fractions of the total particle density, is obtained by weighting the individual plasma parameters and gas compositions with the corresponding molar fractions of the gases hydrogen and argon based on the calculated argon concentration in the plasma vessel. In this way, the mean electron energy, for example, used to solve the EEDF is computed via

$$\varepsilon = \varepsilon_H(1 - y_{Ar}) + \varepsilon_{Ar} y_{Ar}, \tag{6.11}$$

with ε_H being the respective value for the mean electron energy in the hydrogen plasma simulation and ε_{Ar} the analogous value in the argon plasma simulation in the respective ring. The individual hydrogen species molar fractions to consider in the EEDF calculation are computed by substracting the total argon molar fraction from each. The Ar molar fractions to consider for the EEDF calculation, on the other hand, are derived by multiplying the total Ar molar fraction with the gas composition from the Ar plasma simulation.

With all the above values in place, eq. (6.6) is solved and the measured line intensities are translated into an atomic hydrogen species density. The optical response measured in the experiment represents the integral line intensity along the line of sight of the optic. Hence, in the cylindrical plasma, there are different intensity contributions at different radii with their plasma parameters and emission intensities. If one assumes the plasma vessel as divided into several different rings, one can derive the optical length l_j each measurement has through one ring and, subsequently, can compute weighing factors for the individual rings by dividing through the total optical length l_{tot}. Assuming homogenous plasma parameters and gas composition within one ring allows to determine an average atomic hydrogen particle concentration expected for one measurement n_H according to eq. (6.3) for an axisymmetric plasma with j = 1 to 12 rings, each with individual volume-averaged atomic hydrogen concentrations $n_{H,j}$ within the axial position z = -2.5 to 2.5 cm (see Figure 6.1 and 6.2). Those expectation values for different optic angles, obtained from the simulation, can then be compared to the measured values for the atomic hydrogen particle density as computed by eq. (6.6) to evaluate the matching of simulation and experiment. The weighting of the different ring contributions is also crucial to evaluate the measurents.

Solving the simulation with the assigned plasma chemistry, radial gas temperature profile at 20 Pa and ~ 2.4 kW plasma power (2399.5 W resistive heating power in plasma) yields electron mean energies and atomic hydrogen fractions as a function of the radius as shown in Figure 6.4. The values are based on averaging of the parameters within one ring for z = -2.5 to 2.5 cm. Electron temperature and atomic hydrogen molar fraction decrease similarly over the radius of the plasma vessel. Close to the wall, the electron temperature rises due to secondary emission. However, y_H decreases monotonically due to dominant wall recombination.

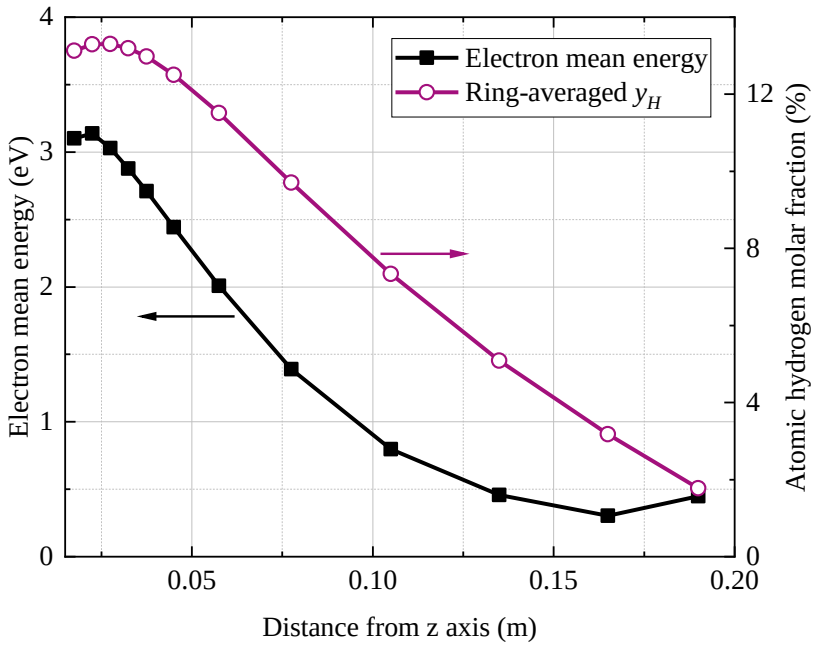

Figure 6.4: Computed radial profiles of electron mean energy and atomic hydrogen molar fraction as average values within the 12 rings at 20 Pa and 2.4 kW plasma power for the volume within the axial position of z = -2.5 to 2.5 cm.

The y_H values obtained from averaging withing the rings allow computation of the expected y_H value in the corresponding line of sight. This is done for a series of different plasma powers from 1.2 to 2.4 kW, upon which the validation is based. The computed atomic hydrogen molar fractions are shown in Figure 6.5 as a function of the angle, at which the virtual optic is aimed at the plasma. The expected atomic hydrogen molar fraction increases first when rotating the optic away from the β = 0° angle. At larger angles, the expected values for y_H drop in a similar manner for all the investigated powers. The larger the plasma power, the larger the expected atomic hydrogen concentration. For a plasma power of 2.4 kW, the highest expected value for y_H is roughly 8 % at a 3° angle, dropping down to ~ 6 % at an angle of β = 15 °. The decline towards large angles is less drastic than the actual radial decline since even at a 15 ° angle, a large portion of the line of sight considers regions of plasma with significant atomic hydrogen concentrations and y_H only drops off quickly close to the outer wall. For the lowest absorbed plasma power in the simulation shown, which is 1.2 kW, the expected value for y_H is ~ 4 % for the straight line of sight and drops to a little above 3 % at a 15 ° angle. The experiments enabling a comparison to the computed atomic hydrogen concentration along the line of sight are presented in section 6.2.4.

In [88], the authors compare their experimental measurements obtained using methods based on OES to those achieved with a 0D kinetic model. They use a DC plasma source within a metallic vessel of similar dimensions as HERMES*plus* but achieve slightly higher power densities. At the pressure of about ~ 10 Pa, [88] observe an atomic hydrogen molar fraction of 10 % being in accordance with this work. The electron temperatures measured with a Langmuir probe (max. 8 eV) match well with the values obtained in this work. They also observe an increase in the atomic molar fraction towards lower pressures. However, the atomic hydrogen recombination coefficient on the vessel walls is only 0.03 in their model because choosing higher values led to an underestimation of the atomic hydrogen concentration, not matching their experimental findings, according to the authors.

In [162], a 2.45 GHz microwave plasma source similar to the Duo-Plasmaline is investigated experimentally and in simulation using a fluid model approach for hydrogen plasma. A bit smaller in size than HERMES*plus*, their setup features ~ 1.2 to 2 kW plasma powers, yielding similar power densities. At 25 Pa, they report atomic hydrogen concentrations of ~ 40 % near the plasma source,

quickly dropping of with radial distance to values of ~ 2 % at the walls. This is in good agreement with the results presented here, which show ~ 27 % atomic hydrogen concentrations close to the plasma source (see Figure 5.4). The slightly higher peak atomic hydrogen concentration in [161] can be explained by their use of a lower recombination coefficient of $\gamma = 10^{-3}$ on the dielectric wall as well as the smaller overall outer vessel surface.

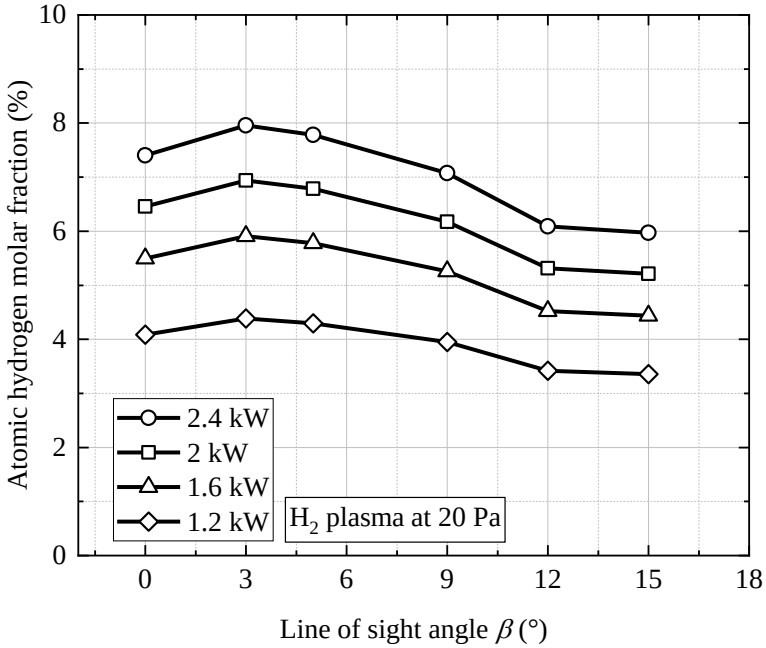

Figure 6.5: Calculated y_H values for different lines of sight through the plasma according to results obtained in simulation for powers between 1.2 and 2.4 kW. The pressure is fixed at 20 Pa and the volume considered is within the axial position of z = -2.5 to 2.5 cm.

6.2.2 Determination of collisional reaction rates of interest

The axisymmetric hydrogen plasma simulation is used to obtain a first set of plasma parameters and hydrogen species molar fractions for each of the 12 rings, which allows derivation of an EEDF and the reaction rates of reactions 6.1 and 6.7 for each ring. In analogy, the quenching reaction rates are computed for each ring and summed according to eq. (6.3) to obtain an integral quenching term correction factor for each measurement. Due to the radial variation of the gas temperature, the simulation also features a radial density gradient, which is considered in the calculation of each ring's corresponding argon particle concentration. The contribution of the inner rings to the total emission intensity is dominant as long as those are part of the line of sight in the measurement because there, electron temperatures and reaction rates are significantly higher than at larger radial distance. This is the reason for the closer spacing of the inner rings as compared to the outer ones. Figure 6.6 shows the radial change of the reaction rates (for z = -2.5 to +2.5 cm) of reactions 6.1 and 6.3 based on the values for the 12 different rings and the corresponding change in electron mean energy as taken from the plasma simulation for a case of 2.4 kW microwave power. Over the radius of the plasma vessel, the electron mean energy declines with radial distance from the z axis from about 3 to 0.5 eV. Close to the wall, it increases to a small extent due to secondary electron emission. The reaction rates of reactions 6.1 and 6.7 decline order of magnitude with the electron mean energy and show a small increase at the outer wall as well. The reaction rates span almost 9 orders of magnitude over the simulated domain. Thus, the importance of the contribution of the inner rings, with substantially higher reactions rates than the outer rings, to the line-of-sight averaged reaction rate of single measurements is noted.

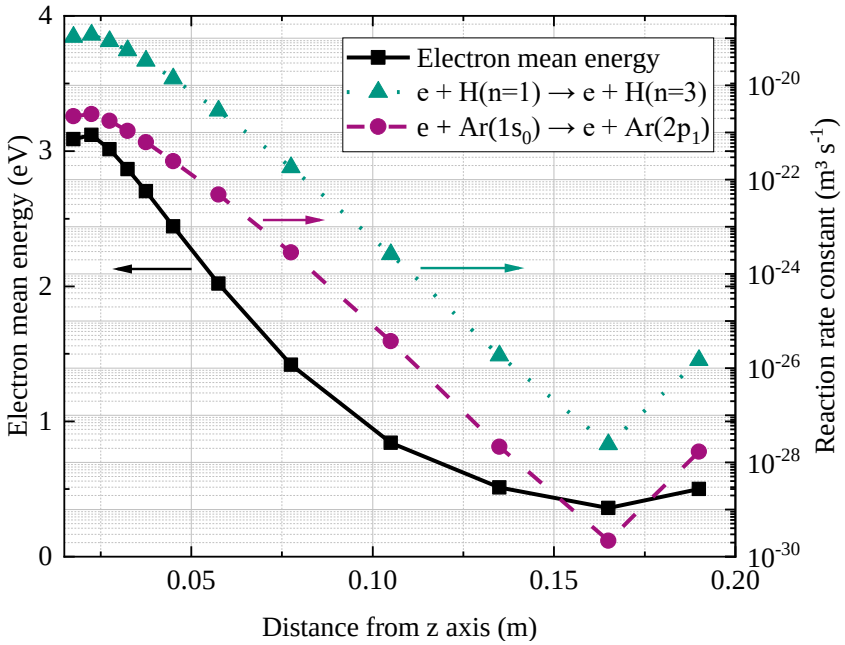

Figure 6.6: Ring-averaged electron mean energy and reaction rates for the axial locations z = -2.5 to 2.5 cm for 2.4 kW plasma power at 20 Pa. The reaction rates are obtained iteratively using a first solution of the plasma simulation to solve for the EEDF with a generalized approach.

6.2.3 Validity of the application of actinometry

The actinometry principle requires similar excitation thresholds of the two electron-impact reactions, which produce the emitting states. The choice of de-excitation reactions, i.e., the characteristic emission lines, accounts for this. The 656.2 nm Balmer-α line has most commonly been compared to the 750.3 nm characteristic Ar line to measure atomic hydrogen densities in the last decades [97] [111] [162]. The tresholds of the reactions are 12.11 and 13.48 eV, which is considered similar enough to be used for the experimental method. Figure 6.7 shows the collisional cross-sections as function of the electron energy. While the reaction rates differ in magnitude, their change with electron temperature is very similar, fulfilling the requirement of actinometry. Furthermore, two-step excitation processes should not compete with the ground-state electron-impact excitation. In the case of the creation of the H(n=3) state, there are three other relevant reactions, namely reactions 5.10, 5.11 and 5.14 in Table 5.1.

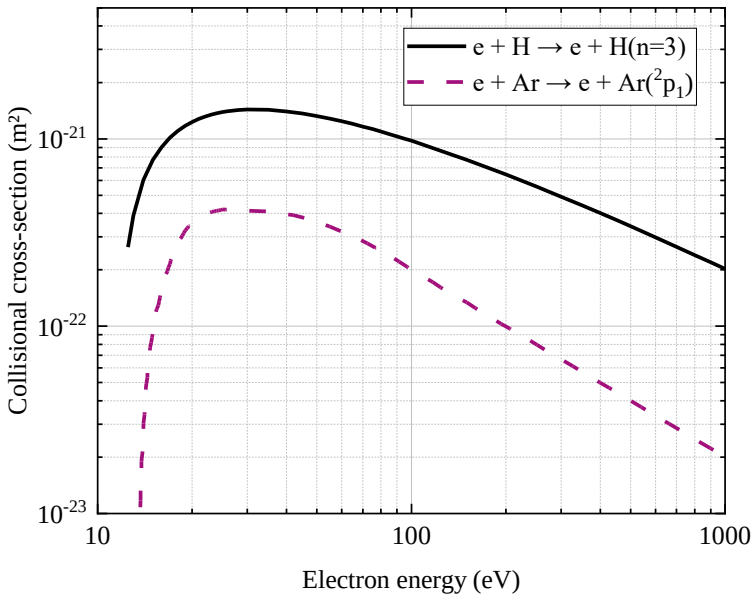

Figure 6.7: Collisional cross-sections by ground-state excitation electron impact.

The atomic hydrogen density measurement for a single line of sight considers the conditions in multiple of the assumed rings with different radii around the plasma source. If the ground-state excitation is larger than any of the other three reactions in all single rings, then actinometry can be used in the given case. It is noted that the correlation in the inner rings is especially important since the reaction rates in those rings are orders of magnitude larger than in the outer rings and, thus, this volume of the plasma is responsible for almost all the considered reactions in the measurements that probe the center of the plasma vessel. In Figure 6.8, the reaction rates of the four reactions are plotted over the radial distance from the central z axis of the plasma vessel for the case of 2.4 kW plasma power, 20 Pa and 0.1 atomic recombination coefficient on the vessel walls.

The reaction rates peak close to the central z axis and quickly drop off with distance to the plasma source. They reach a minimum before increasing close the outer wall again. However, there the reaction rates are ~ 8 orders of magnitude smaller than close to the plasma source. The ground-state excitation has the highest reaction rates for almost all evaluated radial distances. It is clearly dominant over the other reactions by two orders of magnitude, except for the radial distance of 0.165 m corresponding to the 11th ring close to the outer wall. However, emission intensity's contribution in this radial distance to the total measured intensity is negligible in all measurements at any line of sight angle and power.

The metastable H(2s) can achieve quite high concentrations in some hydrogen plasmas, but the presence of strong electric fields, such as the microwave in the plasma vessel, leads to its destruction through collisional mixing with the H(2p) state, which decays radiatively at high rates [138]. Thus, the total rate of the two-step excitation through the H(2s) state cannot compete with the ground-state excitation. Neither can the two-step excitation through the H(2p) state, which builds on even lower number densities of the H(2p) excited state. The dissociative excitation through the hydrogen molecule does not achieve as high production rates of the H(n=3) state because of the high threshold of the reaction of 16.57 eV, ultimately yielding the lowest reaction rates in all 12 rings.

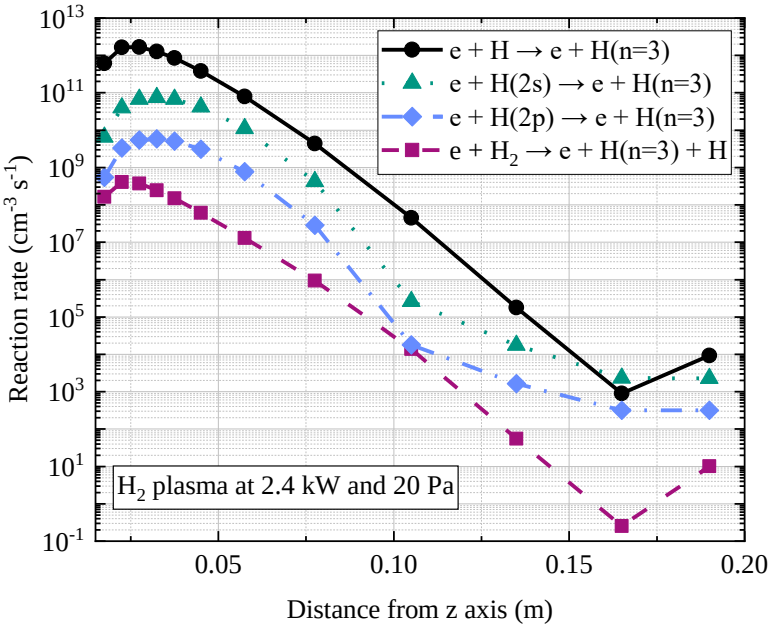

Figure 6.8: Calculated radial profiles of the relevant reaction rates that produce the H(n=3) state, which emits the 656.2 nm line. For each point, the plasma parameters and gas composition to solve the EEDF are taken from a solution of the simulation at 2.4 kW and 20 Pa.

Figure 6.9 shows the radial profile of the ratio of ground-state excitation to the three other considered reactions, which compete with the ground-state excitation in the total production of the H(n=3) state. One can see that for any of the rings' integral values at all powers, the ground-state excitation is clearly dominant with values of the ratio $\gg 1$, the only two exceptions being the 11th ring at 2.4 kW plasma

power and 2 kW plasma power. However, in all of the measurements, the impact of the reaction rate in this ring on the overall computed reaction rates of all single measurements is negligible, supporting that the application of actinometry is valid in the given plasma.

In the case of Ar, two-step excitation occurs through the two metastable states Ar($^1s_3$) and Ar($^1s_5$) according to reactions 6.12 and 6.13 in Table 6.3. While the rates for the given reactions can become quite high with a low threshold energy, the density of the Ar metastables is low in the hydrogen plasma. Just like the hydrogen metastable H(2s), they are lost to collisional mixing by the microwave electric field and are efficiently quenched in hydrogen plasma by collisions with H and H_2 [111] [164-166].

The only relevant species that can contribute to H(n=3) production through radiative cascade, is the H(n=4) state [111]. Taking the molar fraction of the H(n=4) state as calculcated in the simulation is not regarded as an accurate approach to determine a value for the rate of reaction 6.6 in Table 6.3 because of the low density of the H(n=4) species and the uncertainty in the species density calculation that comes with it. Instead, the production rate of the H(n=4) state through the ground-state is compared to that of the H(n=3) state based on the collision cross-sections of the two reactions. It appears, that the cross-section for production of the H(n=4) state is significantly smaller [122]. Furthermore, most H(n=4) atoms radiatively decay to the ground-state and a large fraction also decays to the H(n=2) state [137]. Thus, the production of H(n=3) through radiative decay of H(n=4) is negligible.

The reaction rate of the quenching reactions is obtained from the relation

$$k_R = n_i n_j \sigma_{ij} v_{ij}, \tag{6.12}$$

with n_i and n_j being the respective species number densities, σ_{ij} the collisional cross-section for quenching and v_{ij} the relative collision velocity in (m s^{-1}). The most important quenching reactions are collisions with species with high number density in the plasma, such as hydrogen molecules, atoms and argon atoms (reactions 6.3 to 6.5 and 6.9 to 6.11 in Table 6.3).

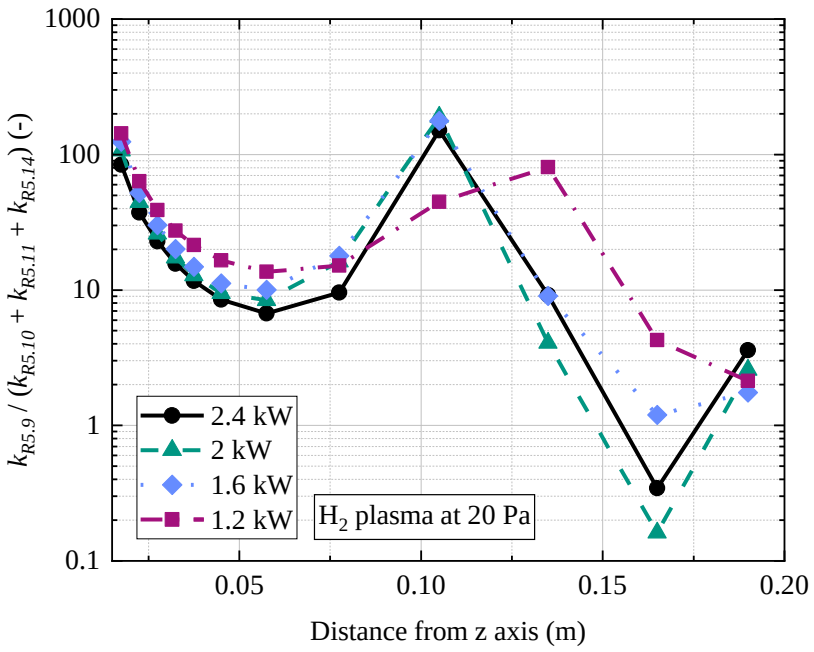

Figure 6.9: Calculated radial profile of the ratio of ground-state excitation reaction rate to the three competing reactions that produce the H(n=3) state for plasma powers from 2.4 to 1.2 kW. Plasma parameters and gas composition are taken from a first solution of the simulation.

Plotting the reaction rates in (cm^{-3} s^{-1}) over the radial distance from the central axis for the investigated volume between z = -2.5 to 2.5 cm yields the result shown in Figure 6.10. The data assumes a hydrogen plasma at 2.4 kW plasma power and 20 Pa. All reaction rates peak close to the central z axis

and drop off with radial distance by several orders of magnitude. At more than 0.1 m radius, the radial profiles flatten. Clearly, radiative decay of the H(n=3) state to H(n=2) state has significantly higher rates than the three quenching reactions for all calculated conditions.

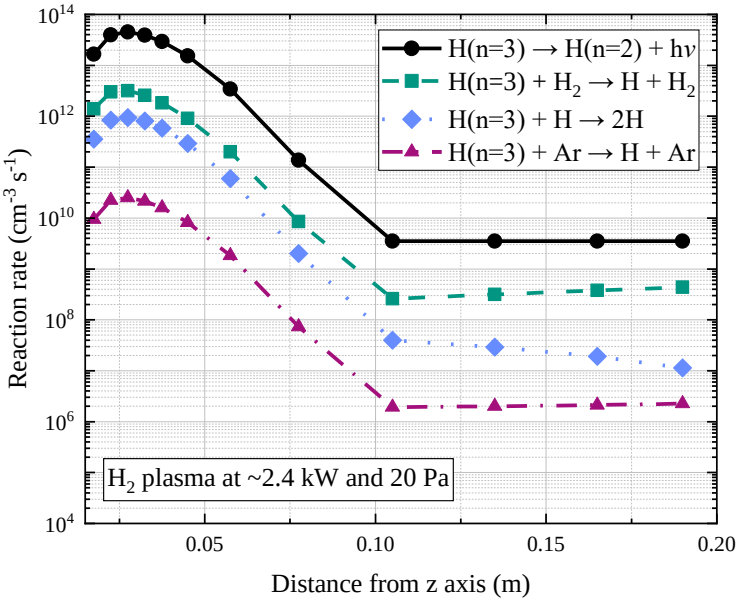

Figure 6.10: Calculated radial profiles of the reactions that depopulate the H(n=3) state in a hydrogen plasma at 2.4 kW and 20 Pa. The gas composition is taken from the hydrogen and argon plasma simulations for the axial positions z = -2.5 to 2.5 cm.

In Figure 6.11, the radial profiles of the reaction rates for the depopulation of the Ar(^{2}p$_1$) excited atom through radiative decay and quenching are given. The radial profiles have a maximum close to the plasma source and monotonically decline towards the outer wall. They are flatter than those of the corresponding hydrogen reactions, only decreasing about 1 order of magnitude towards the vessel walls. This is due to the larger electron densities calculated in the argon plasma simulation, leading to flat radial profiles of excited species. The radiative decay rate for the Ar(^{2}p$_1$) state is significantly larger than the quenching reaction rates, confirming the validity of the actinometry method in the given conditions.

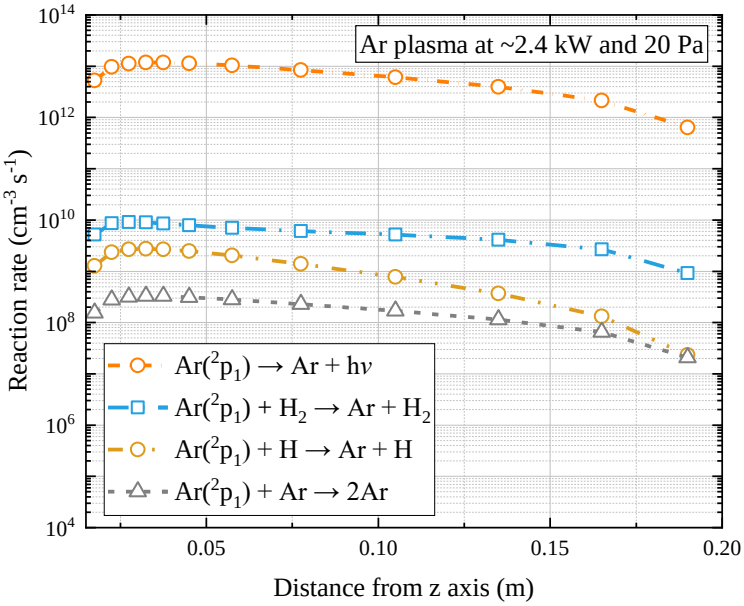

Figure 6.11: Calculated radial profiles of the reactions rates that depopulate the Ar(^{2}p$_1$) state in Ar plasma at 2.4 kW and 20 Pa. The gas composition is taken from the hydrogen and argon plasma simulations for the axial positions z = -2.5 to 2.5 cm.

An analysis of the ratio of the radiative decay rate to the sum of the three quenching reactions is performed for all powers investigated spectroscopically and for H and Ar individually. Figure 6.12 shows the radial profiles of this ratio. In Figure 6.12 (a), the results are shown for H and Ar at 2 kW and 1.2 kW plasma power and in Figure 6.12 (b), the results are shown for H and Ar at 2.4 kW and 1.6 kW plasma power. One can see that in the case of argon, the rate for radiative decay is three orders of magnitude larger than the quenching rates. For hydrogen, the difference is a factor of ~ 10, which is sufficient for the validity of actinometry in this experiment. Thus, the radiative de-excitation of the two excited states H(n=3) and Ar($^2p_1$) dominates over depopulation due to quenching reactions in all investigated conditions.

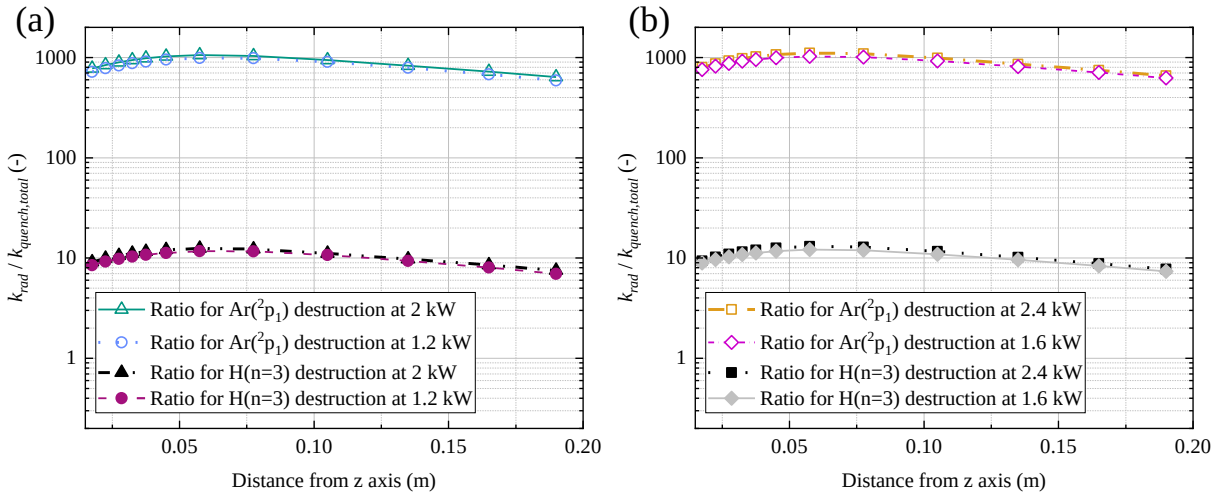

Figure 6.12: Calculated radial profile of the ratio of the radiative decay reaction rate to the sum of all quenching reactions for the excited states of H(n=3) and Ar($^2p_1$) at various powers.

7 Parametric studies of plasma and metal foil operation

The experimentally accessible operational parameters that potentially influence the PDP flux are the atomic hydrogen density, pressure, plasma power, metal foil temperature and noble gas concentration. The atomic hydrogen density also serves as the variable that is compared with the simulation for its validation. Here, the experimental results of the spectroscopic atomic hydrogen density measurements as well as parametric studies within the scope of the experimentally accessible variables are presented.

7.1 Atomic hydrogen density measurements in cold plasma

The atomic hydrogen density measurements obtained from the actinometry experiment are shown in Figure 7.1 (a) and (b) as atomic hydrogen molar fractions over the line of sight of different angles for powers from 1.2 to 2.4 kW and compared to the values from simulation. The uncertainty in the measurement value originates from the evaluation of the statistical error in the data of the spectroscope and is given as a 2σ-confidence. Initially, the measured and computed atomic hydrogen molar fraction increases with the β angle, peaking at 3° or 5° and then decreasing towards larger angles. At the highest evaluated input power of 2.4 kW, the highest atomic hydrogen molar fraction is measured at a 5 ° angle at ~ 8.5 %, dropping off to 6.3 % at 15 °. At the lowest input power of 1.2 kW, the highest molar fraction is determined at the same angle at 4.9 % before dropping off to 4.3 % for larger angles.

There is good agreement between simulation and experiment in the display of the increase in y_H for small angles and in the decrease towards large angles. The absolute values of the molar fractions are also in good agreement but the difference between simulation and experiment increases for smaller powers and larger angles. This can be caused by the increasing consideration of plasma regions with large radial distance from the central z axis. There, the uncertainty in the electron mean energy has a large impact on the ratio of the reaction rates, which changes more dramatically at low electron energies than at high electron energies as they are given close to the central axis. Towards lower plasma powers, the simulation underestimates the atomic hydrogen molar fraction. This may originate from an actual variation of the recombination coefficient, which is not accounted for in the model. With higher H atom concentration in the plasma, the ER recombination mechanism gains importance and increased plasma powers can cause more surface roughness, leading to an overall increased recombination probability of atomic hydrogen on the outer walls and a reduction in the atomic hydrogen molar fraction in the gas. Therefore, a recombination coefficient of 0.1 as assumed in the model represents a conservative value and it is probably lower at lower power inputs and atomic H concentrations.

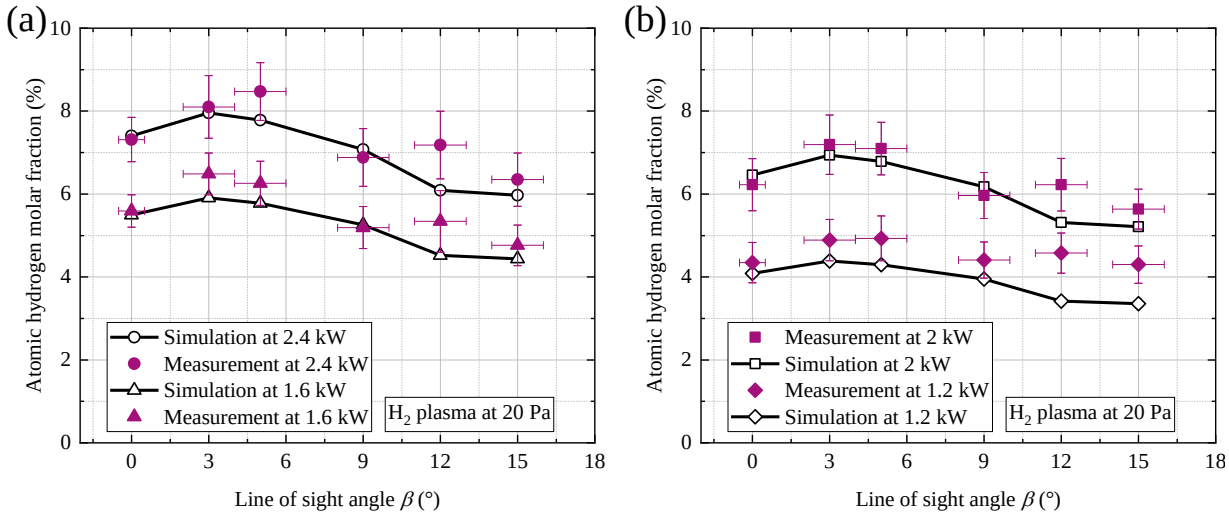

Figure 7.1: Comparison of measured and calculated values of the atomic hydrogen molar fraction along several line-of-sight angles through the plasma at 2.4 kW to 1.2 kW plasma power and 20 Pa. Data previously published by the author in [146].

7.2 Sensitivity to operational parameters of MFP

There are several PDP process parameters, which can be directly measured and controlled in the experimental setup HERMES*plus*. These are the pressure in the plasma vessel, the microwave power, the metal foil temperature and the bias applied to the metal foil. Within certain limits, these can also be controlled in a MFP during operation and by the knowledge of their impact on the permeation fluxes, allow important optimization of the MFP design and operation. PDP enables to deliver fluxes being largely independent of temperature over a broad range [38]. This behavior is linked to a condition of the metal foil enabling superpermeability. Thus, demonstration of temperature independence under incidence of a flux of suprathermal particles is considered as proof of superpermeability, adversely inability to achieve temperature independence is an evidence to the foil's imperfect condition. From a design perspective, temperature control of the foil in a MFP is essential and serves the purpose of reaching a temperature at which operational expenses are at a minimum while facilitating steady-state fluxes at a desirable magnitude. Thus, the lower the minimum temperature at which no more change in PDP flux is observed, the better it is for the operation of a MFP.

A major part of the experiments conducted has been focused on achieving high flux steady-state operation during plasma. This has constituted a major challenge as the measured PDP flux often decreased over time of plasma exposure. Several theories to explain the flux decrease during plasma are brought forward, tested and discussed. It is noted that consideration of the experimental history of the metal foil with the identification of possible contaminants and the treatments to clean the foil from them is extremely important when analyzing the findings. To put the results shown in this work into perspective, a summary of the experimental history of the foils is given. The metal foil surface condition represents a variable that is not accessible in the given experimental setup but has to be accepted and, hence, understood well, as it impacts the measured permeation flux considerably. A careful treatment of the obtained data points is required and experiments only exhibit proper comparability when conducted in close succession.

In total, two metal foils have been installed in the course of the experiments presented:

- a niobium and
- a vanadium foil.

The Nb foil lasted for ~ 3 years and the V foil for ~ 9 months before failing due to severe embrittlement. Post-mortem Auger Electron Spectroscopy (AES) as well as Scanning Electron Microscopy (SEM) and X-Ray Diffraction (XRD) spectroscopy helped identifying large amounts of oxygen in the materials, which is eventually seen as root cause for the breaking. The oxygen is assumed to have entered the vessel through (a posteriori) confirmed air leaks in the feedlines of the experimental setup, which led to an accumulation of O in the heated foil over time. Additionally, small amounts of oxygen have been admitted to the vessel during high temperature carbon desorption to assist the removal of C in the sub-surface of the foil, which is a treatment described in [36]. However, exposure to too large amounts of oxygen was not the only uncontrolled variable that potentially affected PDP fluxes for the shown measurements as discussed in more detail next.

7.2.1 Relation between surface cleanliness and steady-state PDP

The initial design of the microwave plasma source featured outer conductors made from an AlMg alloy [31]. However, proof of the deposition of Al and Mg of the outer conductor on other surfaces in the vessel was found on a plasma immersed plate using energy dispersive X-ray spectroscopy (EDX) and XRD. To still allow for repeatability of the experiments, a pre-heating treatment was necessary. The treatment consisted of keeping the foil at 1050 °C for one hour. Within certain timeframes, this allowed achieving the same PDP fluxes in terms of peak value and decrease rate. The permeation fluxes

presented in the parametric studies of pressure, power and foil temperature were obtained using this experimental procedure and the peak value of permeation in the experiments with the Nb foil. Finally, to avoid any supposed liberation of sputtered material into the plasma and the subsequent deposition on the membrane, the plasma source design was re-visited and new outer conductors made from copper manufactured. Those are shown on the right-hand side of Figure 7.2 (b), next to the old design in (a).

In one of the experimental campaigns, quartz was used as dielectric of the plasma source. Two interesting observations were made during the experimental campaign. The quartz, initially transmissive, developed a milky coloration over the time of exposure to hydrogen plasma as is displayed in Figure 7.2 (c), while, simultaneously, permeation fluxes increased with each experiment. Hydrogen plasma is known to chemically react with the SiO_2, liberating oxygen and silane [168]. The deposition of impurities on walls is known to affect recombination rates [168] on stainless steel and other metal walls. Quartz has particularly low recombination coefficients for hydrogen [97]. X-ray fluorescence (XRF) spectroscopy measurements confirmed the presence of Si on the vessel walls after operation of hydrogen plasma with the quartz tube, which supports the hypothesis of reduced hydrogen recombination rates on the walls and larger dissociation degree in the plasma, leading to higher permeation rates over time. The Si concentration ranged from ~ 3 to 9 weight-% in several different surfaces tested with XRF directly after the experimental campaign with the quartz tube but decreased in the months following. Thus, the reduction of the recombination coefficient seems to be a temporary effect.

The fact that the pre-heating treatment enabled repeatability of the experiments and “healed” the damage done during plasma exposure points to three different mechanisms that could be responsible for the decrease during plasma. These are

- removal of oxygen from the foil surface monolayer,
- deposition of unknown impurities, which are either evaporated or absorbed into the bulk during the pre-heating treatment, restoring a surface condition more fit for superpermeation or
- plasma irradiation causing strong porosity in the surface, increasing the effective surface area, yielding a high density of active centers for recombination as described in [55].

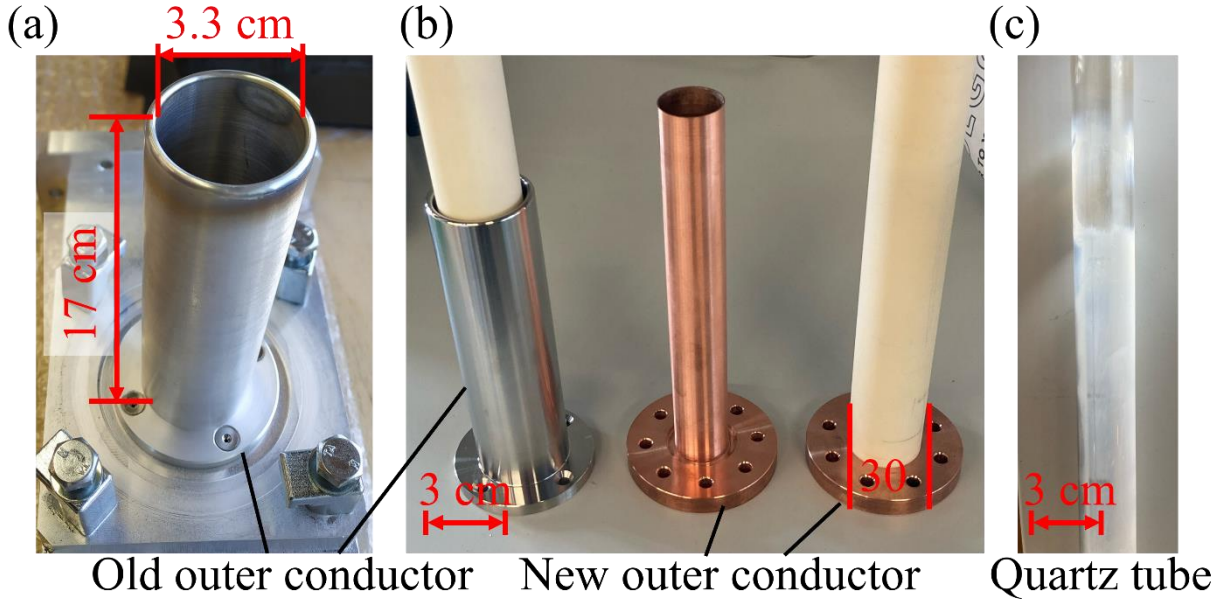

Figure 7.2: Old plasma source outer conductor made from AlMg in (a), new, out-of-vacuum outer conductor in (b) and quartz dielectric after exposure to hydrogen plasma in (c).

To investigate further if the impingement of fast ions helps the removal of a potential impurity deposition and, thereby, improves permeation conditions or contributes to the destruction of the O monolayer, a bias sweep is performed.

Over the years of operation, the bias application experiment has been repeated several times. A representative experimental finding of permeation flux change with bias application is depicted in Figure 7.3. The plot shows the magnitude of the permeation flux through the Nb foil with the quartz dielectric and the outer conductors removed from vacuum. The plasma is operated at 20 Pa and 2 kW power, while the metal foil is kept at 900 °C. The variation of bias is indicated by the dashed line. At minute 50, the bias is reduced from +35 to 0 V, allowing positive ions to reach the membrane. After a short duration, in which the foil temperature stabilizes after the heating by the electron current drawn from plasma is replaced by the resistive heating, the decrease of the flux continues slightly accelerated as compared to before the bias removal. The behavior indicates that positive ions accelerated in the sheath in front of the membrane are responsible to some extent for the reduction of the permeation flux during plasma. At minute 62, the bias is put to -64 V, accelerating positive ions from the plasma towards the foil. The rate of PDP flux decrease accelerates which fits with the hypothesis of oxygen poverty in the surface monolayer being responsible for the decrease. This observation is repeated using the V foil as shown in Figure 7.4.

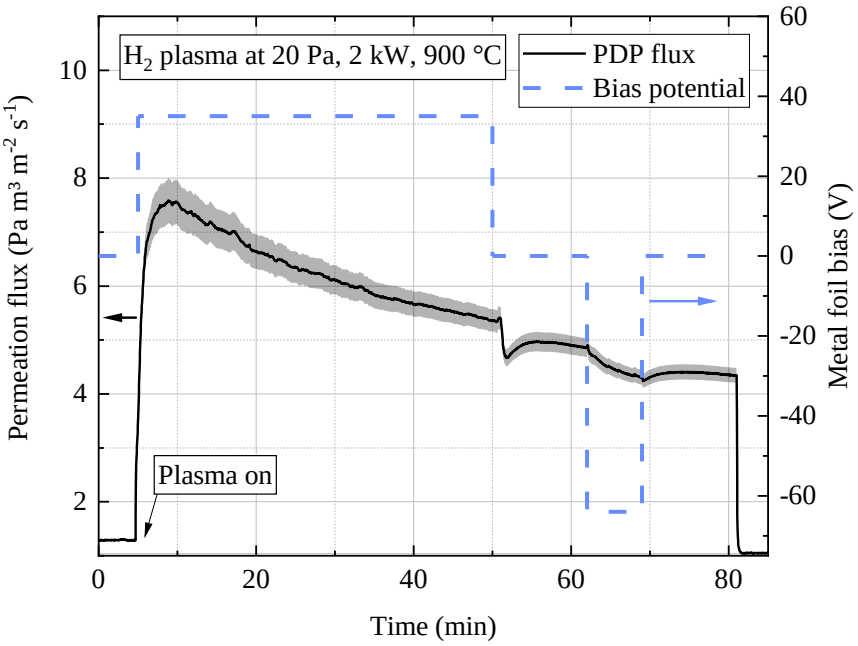

Figure 7.3: Measured PDP flux during an experiment with bias variation. The plasma is operated at 20 Pa, 2 kW power and the foil is kept at 900 °C. The quartz dielectric is installed. Uncertainties in the flux estimation are given by the shaded area enveloping the curve.

It is noted that the absolute values of the permeation flux achieved in this experiment are substantially lower, which is not attributed to the foil material V in general but mainly because the V foil has not been conditioned with the pre-heating treatment. However, Figure 7.4 shows that the achievable steady-state PDP flux with V is improved by applying a positive bias. The bias' magnitude of ~ +15 V appears to be especially beneficial to PDP. On the other hand, application of negative bias immediately leads to the decrease of the flux. The results indicate neutral particles with sufficient energy appear, causing damage to the metal foil surface as the decrease cannot be totally stopped with high positive bias unless the permeation flux is already low. The excitation of H_2 to the dissociative H_2 $b^3 \sum_u^+$ state by electron impact can produce hydrogen atoms of several eV kinetic energy [134], which is sufficiently large to cause chemical sputtering of the oxygen in the monolayer [37].

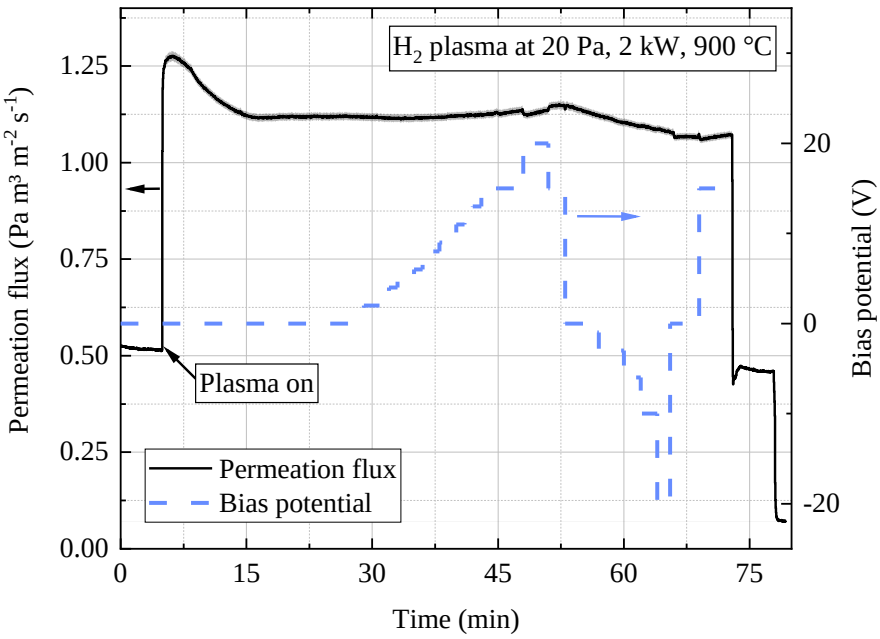

Figure 7.4: Measured PDP flux with bias variation and V foil without pre-heating treatments. The plasma is operated at 20 Pa and 2 kW power. The foil is kept at 900 °C. Positive bias shows to be beneficial to the PDP flux, opposite to negative bias.

However, removal of the sub-surface carbon as CO by high temperature de-carbonization should enable sputter resistance of the foil, compensating the negative effect of fast neutral particles.

A first CO desorption was performed at a very early stage during the commissioning of the experimental facility. As the inhibition of O replenishment in the surface has continued to be an issue, more CO desorption experiments have been carried out. Figure 7.5 shows the permeation flux over time as compared to before and after de-carbonization for a plasma operation at 20 Pa, 2 kW plasma power and a metal foil temperature of 900 °C. The plasma is switched on at ~ 5 minutes, leading to a large increase in the measured permeation flux. Before de-carbonization, PDP drops to ~ 1/6 of the peak value within 10 minutes. After the carbon outgassing, the PDP flux increases for about 15 minutes of plasma operation and then slowly declines to a value ~ 10 % lower than the peak over 30 minutes later. Thus, the CO desorption shows a positive effect on the PDP behavior, providing proof for the role of carbon in the inhibition of oxygen diffusion towards the surface.

The CO desorption consists of heating the foil to 1450 °C for 4 hours. During this process, the RGA is connected to the main vessel to observe the presence of carbon compounds and monitor their change over time to evaluate the rate of outgassing of C compounds. The reduction of observed C, CO and CO_2 peaks during this treatment happens significantly slower than in other publications [37] and a reduction of the CO peak of 1 order of magnitude only is observed after ~ 4 hours. The permeation flux is calculated based on measurements of the hot cathode PI12, yielding larger uncertainties as compared to permeation fluxes shown above. While the magnitude of the maximum achieved PDP fluxes does not increase by a lot, it appears to decrease at significantly lower rates. This can be interpreted as proof for the presence of C in the subsurface of the metal foil, inhibiting oxygen replenishment. However, no true steady state has been achieved at this point in time and the foil has continued to show degradation over time and experiments. The treatment has been repeated several times in the case of Nb due to a steepening decrease during PDP experiments. Repetition of the de-carbonization has always shown that carbon-associated peaks (12, 28, 44 amu) observed with the RGA increased in the meantime, leading to the conclusion that a continuos carbon contamination of the foil occurs.

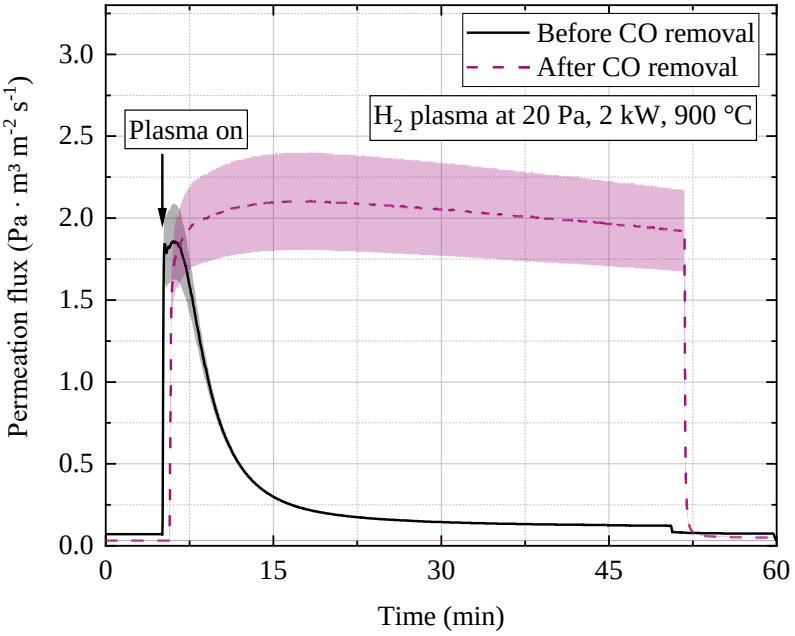

Figure 7.5: Measured PDP fluxes over time before and after de-carbonization (6 hours at 1500 °C) of the Nb foil, kept at 900 °C, with plasma operated at 20 Pa and 2 kW plasma power.

However, not only the plasma negatively affects the permeability of the membrane but also exposition of the foil to vacuum. Without performing pre-heating treatments inbetween, observed fluxes drastically reduce as a function of time as shown in Figure 7.6. The PDP flux magnitude decreases significantly over several days without operation. Several cathodes were removed from the vessel as their filament material is known to sometimes feature residual carbon from the production process, which improved the situation but could not resolve the decrease during plasma altogether.

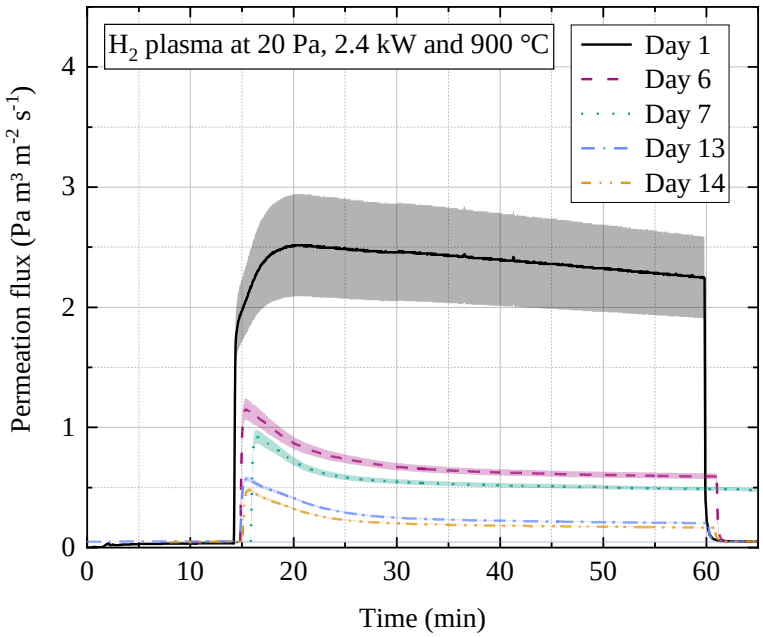

Figure 7.6: Measured PDP flux degradation over time without pre-heating treatments. The plasma is operated at 20 Pa, 2.4 kW plasma power and the Nb metal foil kept at 900 °C.

Similarly to Nb, the permeation fluxes measured with V show a strong decrease over time of plasma exposure before CO desorption campaigns. Figure 7.7 shows the first PDP experiments performed with the V foil after its commissioning, for 20 Pa and 2.8 kW plasma power. The foil temperature varies throughout the experiment and the first plasma is switched on at ~ 15 minutes with the foil temperature

of 700 °C. The permeation flux reaches a value of almost 12 Pa m^3 m^{-2} s^{-1} but quickly declines to a fraction of this within minutes. For ~ 40 minutes, the foil is kept at 900 °C and the plasma ignited a 2nd time at the same conditions, showing a less dramatic but still significant decline. Before the 3rd plasma ignition, the hydrogen remaining in the foil is outgassed to avoid hydrogen embrittlement and the foil is then cooled down. After ~ 40 minutes, the foil is heated to 900 °C again and plasma switched on. The measured PDP flux peak is at a similar level as the final value during the previous PDP experiment, as indicated by the dotted line. This emphasizes, the necessity of pre-heating treatments to achieve repeatability of the experiments, in both Nb and V.

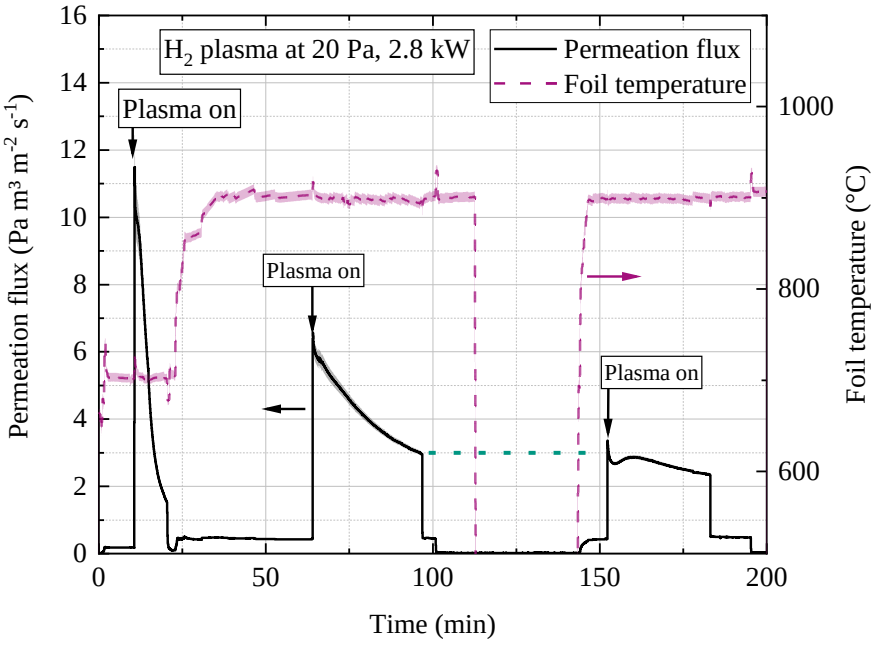

Figure 7.7: Measured permeation flux value and metal foil temperature in first PDP experiment performed with V foil before CO desorption. The plasma is operated at 20 Pa and 2.8 kW. Recovery of the PDP flux magnitude shows a dependence on the foil temperature in between plasma pulses.

Further proof for the hypothesis of fast neutral damage to the oxygen monolayer of the foil being responsible for the observed decrease has been found analyzing the behavior with pressure variation. The lower the pressure, the higher the electron energies and yields of fast neutrals from the electron impact dissociation. The foil's contamination with C has been a permanent issue that could not fully be resolved, which is why the foil has never achieved sputter-resistance reliably over the course of several experiments. Even with bias application, fast neutrals originating from the dissociation of the H_2 triplet state sputter oxygen in the monolayer on the foil. Combining those two characteristics fully explains the issues in achieving high flux steady-state PDP. The foil's routine de-carbonization initially improves the situation but has to be repeated several times in case of both foil materials as the decrease during PDP experiments steepen again. Post-mortem surface analyses of the foil materials and plasma immersed witnesses show a strong increase of surface roughness. Thus, the surface roughness factor, introduced in eq. (2.3), increases on the upstream surface, leading to a decrease of permeation fluxes over time. Additionally, Auger Electron Spectroscopy (AES) and EDX investigation of the upstream surfaces of both, the Nb and the V foil, exhibit a growth of oxide layers.

Repeatable experiments performed with varying operation parameters have been these experiments with preceeding pre-heating treatment of 1050 °C for one hour. They show a characteristic initial peak when switching on the plasma, followed by a monotonous flux decline. To isolate metal foil surface effects (which originate from the integral history of the foil under plasma and vacuum exposure) from those of operational parameters of pressure, plasma power and foil temperature, only the PDP peak values of the corresponding experiments are compared with each other subsequently.

7.2.2 Effect of pressure on plasma-driven permeation

Using the pressure-difference method, the PDP flux is calculated based on the downstream chamber pressure reading for a series of different upstream, i.e, plasma vessel pressures. The pressure readings in both chambers are recorded with the identical Baratron capacitance manometers PI08 and PI09. The metal foil made of Nb has been exposed to several hundred hours of plasma operation before the measurements have been conducted. For the results shown in Figure 7.8, the plasma source still features the AlMg outer conductors and has experienced only a short duration of CO desorption upon commissioning. The permeation flux values represent the PDP peak values before the characteristic decline. Before each peak value, the standard pre-heating treatment at 1050 °C is performed for 1 hour and the experiments are carried out in succession of each other to yield as comparable metal foil surface conditions as possible. When switching on the plasma, a peak value is obtained within minutes and the permeation flux reduces before plasma is shut down. The metal foil temperature during the PDP peak values varies a few degrees since steady state is not always obtained at that point yet but is at ~ 900 °C. Plasma power is set to 2 kW. The uncertainty in the upstream pressure is too low to show in the Figure.

Figure 7.8 shows that PDP fluxes decrease with increasing pressure. This is in good agreement with the increase in the atomic hydrogen molar fraction towards lower pressures in the model (section 5.4.1). This pressure behavior can be explained by the increased frequency of momentum exchange between electrons and heavy particles at higher pressures, causing lower electron energies and higher gas temperatures. High electron energy collisions are required to dissociate hydrogen in inelastic collisions and produce atomic species capable of superpermeation. Thus, despite the higher number density of hydrogen at higher pressures, PDP fluxes reduce. The highest permeation fluxes attained for the given conditions of 2 kW plasma power and ~ 900 °C foil temperature have been ~ 6 Pa m^3 m^{-2} s^{-1}.

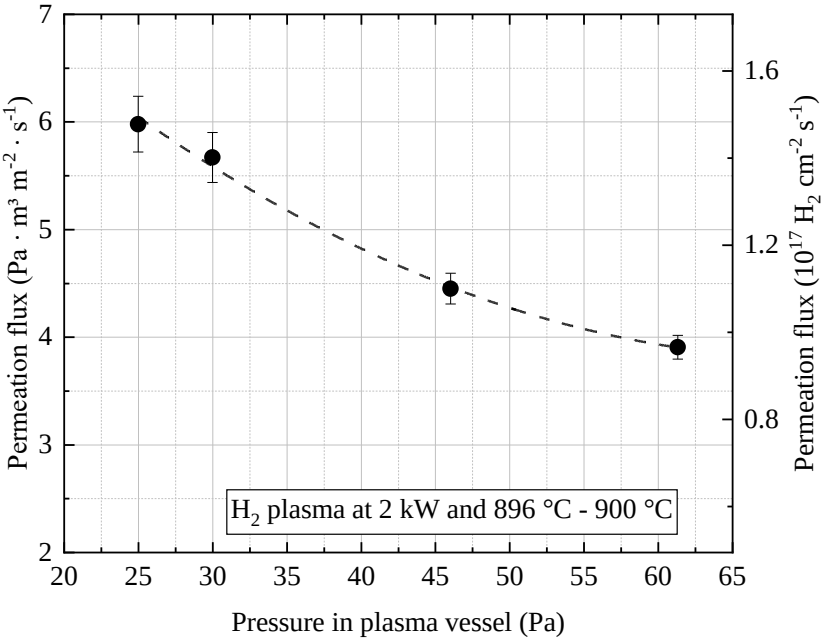

Figure 7.8: Measured permeation flux value as a function of pressure in the plasma vessel for a plasma power of 2 kW and a Nb metal foil temperature of ~ 900 °C.

At a later point in time, a similar experimental campaign is carried out with an upstream pressure varying from 15 to 60 Pa, employing the pre-heating treatment but with the Cu plasma source outer conductors. Downstream pressure is measured with the hot cathode PI12. The absolute achievable fluxes are lower and no additional CO desorption treatments have been carried out yet. Figure 7.9 shows the corresponding permeation fluxes as a function of time for the pressures from 15 to 60 Pa at a plasma power of 2 kW with a 900 °C Nb foil. Larger GDP flux values can be seen for the high pressure operations before switching on the plasma at ~ 10 minutes. With ignition of plasma, the measured PDP

flux spikes and immediately enters a sharp decrease. The observed PDP flux peak value increases with pressure but so does the slope of the ensuing decrease. As in Figure 7.8, the relationship between peak PDP flux and pressure is close to inversely quadratic. However, already within several minutes after plasma ignition, the flux for the low pressure operation decreases to values lower than that of high pressure operation. This is consistent in all shown experimental results.

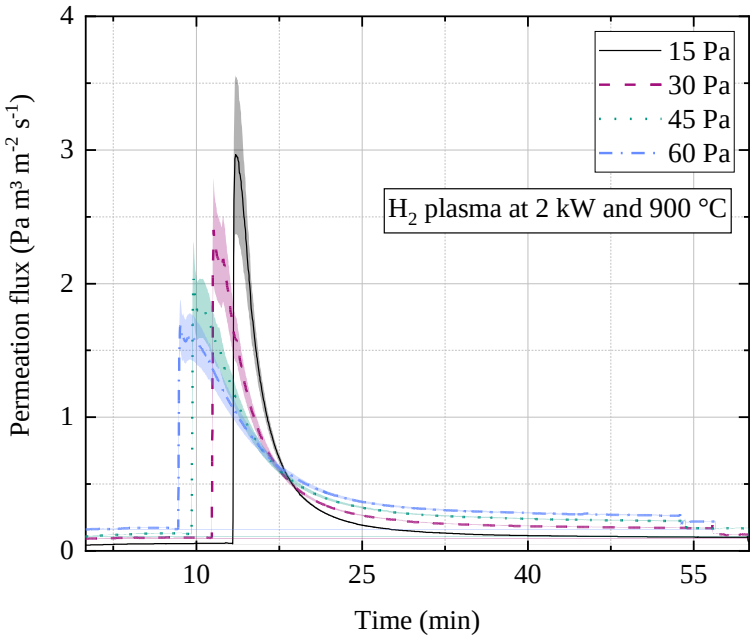

Figure 7.9: Measured permeation flux over time for different upstream pressures. The hydrogen plasma was operated at 2 kW power and the Nb foil kept at 900 °C. The peak PDP flux increases towards lower pressures, but it also decreases faster with time.

The observed increase of peak PDP fluxes towards lower pressures matches with the calculated increase in atomic hydrogen concentrations and indicates that working with the baseline of atomic hydrogen production at 20 Pa is conservative.

7.2.3 Impact of plasma input power

In theory, the increase in plasma input power leads to a larger suprathermal particle yield and hence, to larger permeation fluxes. However, similar to the pressure, the change in power density in the plasma is linked to a change in degradation of the metal foil surface condition for PDP. A sensitivity study is performed using the Nb foil with the pre-heating treatment of keeping the foil at 1050 °C for 1 hour before every single plasma experiment. The plasma is, then, operated for 45 minutes before the foil is desorbed from hydrogen and the experiment is repeated. The peak values of the observed PDP flux are used as representation of the maximum achievable PDP flux at the given pressure as depicted in Figure 7.10. At the time when the peak value is taken, the foil temperature varies between 893 and 905 °C. The upstream pressure is manually adjusted to 25 Pa at the time of the PDP peak value.

The permeation flux changes linearly with power as indicated by the dashed line. However, some measurements are outliers and cannot be fitted with a linear fit within their uncertainty. This is due to variations in the metal foil surface condition in the shown experiments and their impact being significantly larger than the measurement error. The highest fluxes have been obtained at the highest plasma power at around 2750 W, leading to a permeation flux slightly exceeding 6 Pa · m^3 m^{-2} s^{-1}. With the given pressure of 25 Pa and the experimental setup, there is a saturation for the absorbed microwave power around 3 kW and increasing the power only caused more reflection.

Experimental investigation has shown, that for a hydrogen plasma operated at 20 Pa, the absorbed power in a 0.3 m plasmaline saturates at ~ 3 kW. The 0.3 m is the dimension from main flange to main flange. The plasma, however, spreads a couple of cm into the large bore hole in the flange in both sides, which is why a total length of 0.35 m of the plasma is assumed. Most of the microwave power injected at more than 3 kW is reflected by the plasma in this operation.

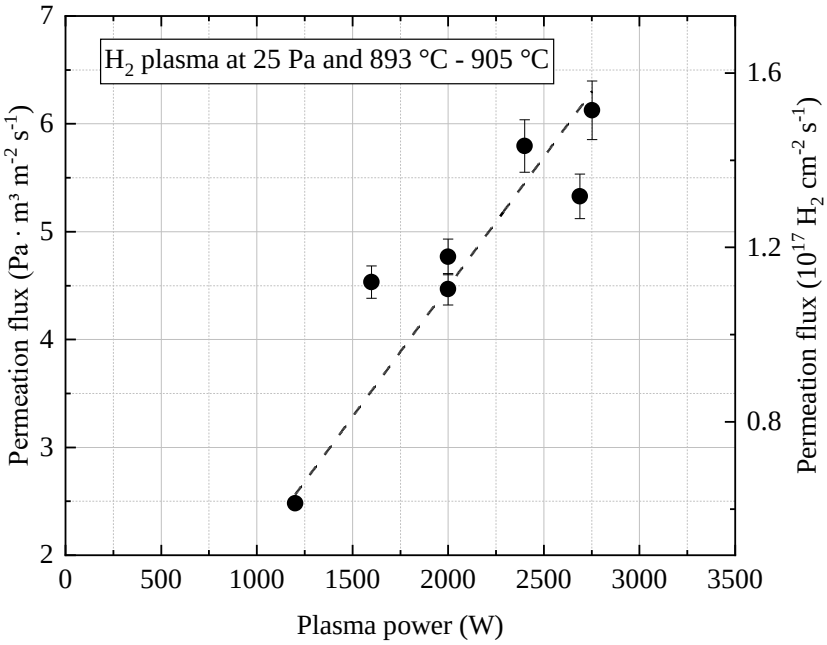

Figure 7.10: Measured permeation flux as a function of applied plasma power for a pressure of ~ 25 Pa and a Nb or V metal foil at ~ 900 °C.

7.2.4 Evaluation of metal foil temperature and isotopic selectivity effects

Using the same approach here, the variation of metal foil temperature on the PDP flux is measured using the standard pre-heating treatment to obtain as comparable foil surface conditions as possible. After heating the foil at 1050 °C for 1 hour, the vessel is filled with hydrogen to 20 Pa and a first value of GDP is measured. Then, plasma is switched on, leading to a spike in the measured PDP flux and a decrease over the duration of plasma exposure of 45 minutes. The PDP flux values obtained in the peak, are given for a series of temperatures between 600 and 900 °C. The same procedure is applied using deuterium as gas. Figure 7.11 shows the measured GDP and PDP peak values for both, protium and deuterium, plotted over the inverse metal foil temperature. Downstream pressures for the evaluation of the PDP fluxes are taken using the baratron capacitance manometer PI09 and those for the calculation of the GDP fluxes are based on measurements with the cold cathode PI04.

The measured GDP values for the two hydrogen isotopes differ significantly with protium showing higher values than deuterium by about one order of magnitude. GDP fluxes of both gases increase with temperature, indicative of the typical Arrhenius-behavior of GDP. Plasma-driven permeation (PDP) fluxes are several orders of magnitude larger; the difference being especially large at the lower temperatures investigated. A large difference between GDP and PDP fluxes is beneficial for reaching large compression ratios. This, as well as power efficiency and lifetime considerations, motivate using as low foil temperatures as possible in a MFP. At the given plasma operation of 2 kW plasma power and 19.9 to 20.9 Pa upstream pressure, PDP fluxes of protium vary between 3.9 to 4.5 Pa m^3 m^{-2} s^{-1} within the given temperature range of 600 to 900 °C and those of deuterium between 3.8 and 4.5 Pa m^3 m^{-2} s^{-1}. No temperature dependence is observed and variations in the measured permeation flux are probably due to variation in the foil surface condition. Only when reducing the temperature to 500 °C or increasing it to 1000 °C, a slight decrease in the fluxes is observed, for both, protium and deuterium.

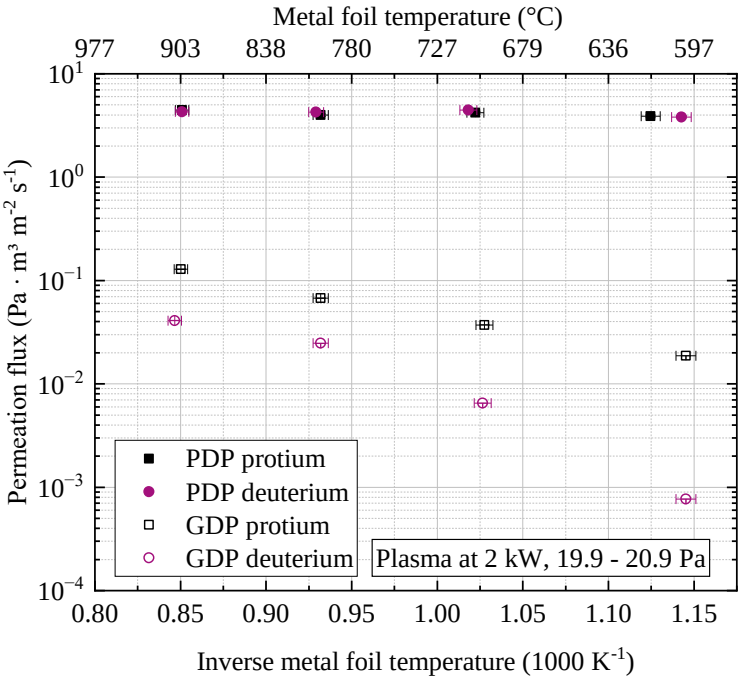

Figure 7.11: Temperature dependence of GDP and PDP fluxes of protium and deuterium. While GDP fluxes show an isotopic effect and temperature dependence, PDP fluxes exhibit neither and are several orders of magntiudes larger.

The shown results are considered as proof that PDP allows separating protium and deuterium at equimolar rates from a given torus exhaust composition. Using this as a baseline for the extrapolation to tritium, the MFP can deliver the same mass ratio of D/T as permeate as given in the torus exhaust. As the particles cross the foil as atoms, they can recombine as isotopologues DT, HD or HT on the downstream side of the foil.

7.2.5 Influence of noble gas impurities on performance

Capturing any effects that noble gases, such as He, Ar and Xe, may have on the process of the MFP, is an important aspect of the MFPs performance. This work aims at introducing a factor that correlates PDP fluxes with specified concentrations of the noble gases to those achieved with pure hydrogen in the same operation conditions. This factor is applied in the MFP performance assessment as a function of the expected gas composition. Considering a DIR-ratio of 80 % and a “worst-case” scenario that assumes the maximum concentration of impurity gases in the torus exhaust as lined out in the requirements table 1.1, the gas composition at the outlet of the MFP is computed. Table 7.1 shows the local gas compositions at several different axial positions along a cylindrical 2.27 m long MFP, if one linearly interpolates the gas compositions based on the values at the outlet.

Quantifying the effect of the noble gases on PDP is not straight forward. Two effects are assumed to potentially affect PDP fluxes:

- First, an immediate effect on the EEDF due to the different ionization characteristics of the noble gases leading to a change in the suprathermal particle production rate.
- Second, alternation of the metal foil surface sputtering yield by the heavier noble gas atoms or by a different rate of fast H neutral production. The damage to the foil surface monolayer is a cumulative effect, and thus, not recognizable in a PDP peak flux rightaway after switching on plasma with noble gas admission.

Table 7.1: Assumed gas composition at different axial positions along a 2.27 m long, cylindrical MFP as obtained by linear interpolation when considering a separation ratio of 0.8.

Pos. [m]	0	0.227	0.454	0.681	0.908	1.135	1.362	1.589	1.816	2.043	2.27
	[mol.-%]										
H	92.45	91.85	91.14	90.30	89.28	88.02	86.43	84.35	81.51	77.42	71.01
He	5.00	5.40	5.87	6.43	7.10	7.93	8.99	10.37	12.25	14.95	19.20
Ar	2.50	2.70	2.93	3.21	3.55	3.97	4.49	5.18	6.12	7.48	9.60
Xe	0.05	0.05	0.06	0.06	0.07	0.08	0.09	0.10	0.12	0.15	0.19

In this work, the evaluation of the integral effect of noble gases is conducted based on the baseline comparison with pure hydrogen PDP. The MFCs are calibrated to account for high accuracy of the gas composition. A constant flux of hydrogen is noted, for which a pressure of 20 Pa is achieved with the valve to downstream pumping in a certain position, corresponding to a certain pumping speed. The feed is stopped and the vessel evacuated through bypass and downstream pumping before admission of one of the noble gases. The required feed flow to achieve the same pressure as with hydrogen is noted to determine the pumping speed ratio of the two gases at the given valve opening. Thus, the required feeds for both gases are computed to achieve the compositions given in Table 7.1. The required feed to reach the same pressure with the different gases matches the ratio of the thermal velocities of the gases, indicating that the valve is in a position that causes free molecular flow through the small opening.

Pure hydrogen plasma is ignited and the foil subjected to some hours of plasma exposure before achieving a PDP flux that does not decrease in time anymore. The remaining PDP flux is still significantly larger than the GDP flux at the same operation conditions. The three noble gases are fed and a relative decrease of the PDP flux is measured. Figure 7.12 shows the relative change in the permeation flux as compared to the pure hydrogen case as a function of the axial position in the MFP. A decrease, similar in scale to the reduction of the hydrogen partial pressure, is observed. At maximum dilution, the remaining 71 % of hydrogen still permeate at a rate of 62 % of that with pure hydrogen plasma. These results are promising but it is noted that further studies need to be carried out to investigate the effect of noble gases in a setup without the ongoing decrease during plasma exposure.

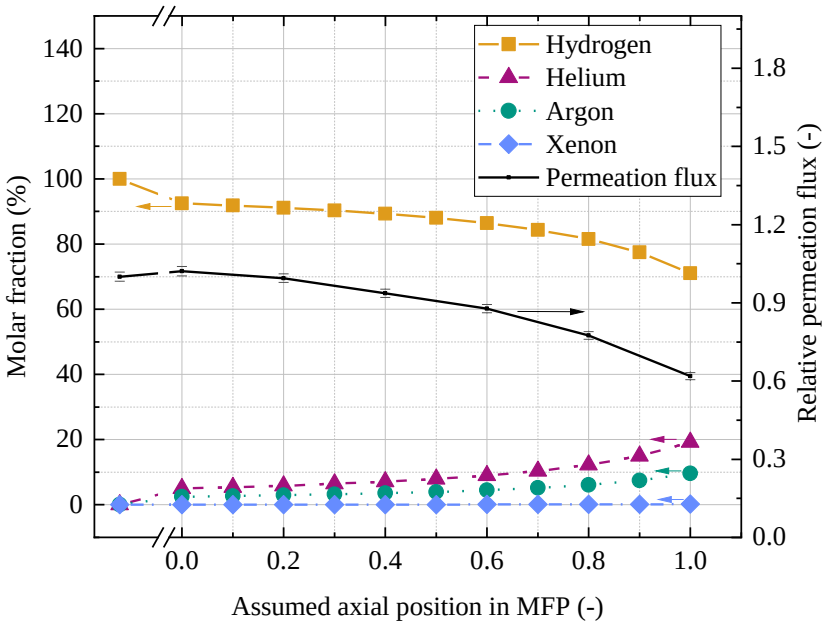

Figure 7.12: Relative change in measured PDP fluxes with varying gas compositions as a function of dimensionless pump length, corresponding to the torus exhaust composition. The uncertainties of the molar fractions of the four gases are no larger than 1.66 % for H, 27.9 % for He, 35.4 % for Ar and 25.8 % for Xe of the given values.

8 Integral performance assessment of a power plant MFP

The modelling of the MFP performance has a clear objective: To enable the evaluation of the performance of possible designs based on a pumping speed S and a separation ratio s. The latter is defined as the fraction of hydrogen pumped through the foil over the total amount of hydrogen pumped by the MFP and LDP through the foil and MFP outlet. The evaluation is performed in view of conductance maximization during dwell. At this point in time, it is not possible to quantify the throughput or pumping speed requirement during dwell as no reliable data is available to determine the outgassing rates of the plasma-facing first wall and divertor. However, the conductance of the system is evaluated by assuming a capture coefficient of 1 at the outlet of the MFP to obtain an idealized pumping speed for helium, for which no permeation through the foil is considered. The conductance optimization is prioritized in the first iteration and, subsequently, a corresponding design is tested for its ability to fulfil the requirements on fuel separation and hydrogen pumping speed during burn. At the current stage of the design, a separation ratio of 0.8 is pursued. The hydrogen pumping speed requirement for the MFP depends on the number of ducts used for fuel separation. Considering a baseline of 10 ducts and the current throughput window of 250 – 430 Pa m^3 m^{-2} s^{-1} at a currently assumed sub-divertor pressure range of 1 – 10 Pa [23], the effective hydrogen pumping speed through one duct can vary from 2.5 to 43 m^3 s^1.

The TPMC method (section 3.1) offers the option of modelling customized geometries and performing large parametric studies, covering a broad operational range in a reasonable amount of time. Although it allows a performance assessment of the MFP, the absence of treating particle interactions and assuming free molecular flow inside of the MFP challenge validity. During burn, the *Kn* number is ≈ 0.1 inside a baseline design that considers a cylindrical MFP with a linearly extended plasma source at its central axis. Neglecting particle interactions leads to an overestimation of residence time and surface interactions in the flow domain. Thus, the calculated pumping speed through the outlet of the MFP is a conservative estimate but the achievable separation ratio is potentially lower in an application with transitional flow. For dwell, free molecular flow is the expected regime inside of the MFP.

8.1 Introduction of three possible MFP designs

For the first time, three possible designs that imagine the plasma source-metal foil interaction in the pump duct are shown in this work in Figure 8.1. One of the guidelines to the dimensioning of the different designs is maximization of the conductance for the torus exhaust, i.e., maximization of the flow cross-section. The guideline of flow channel area maximization yields lower separation ratios because the number of surface interactions of the particles, necessary for permeation, is reduced. The shown designs consider a reasonable amount of installation space of the required components but, by now, no detailed design is available. The dimensions in Figure 8.1 are expressed with reserve as the optimization of the separation ratio succeeds a first estimate of the performance of the designs through a sensitivity study of the dimensions. Hence, the dimensions of one design are varied in a parametric study but performing the modelling with the degree of detail to each design as shown here is deemed as sufficient to provide an understanding of the strengths and weaknesses of each design.

In all designs, the foil is clamped in stainless steel segments, which are considered with 50 mm thickness. The plasma sources are fixed in a 100 mm width support structure at the inlet and outlet of the pump cask. Each design is equipped with 8 plasma sources. The non-permeated torus exhaust is pumped through the outlet of the MFP, which is connected via the pump duct closure plate to the downstream vacuum pumping system with baffle. The permeate, making up roughly 80 % of the throughput, is routed through the pump duct closure plate as well. This necessitates consideration of appropriately sized pipes on this flange, the cross-section of which reduces the flange surface for torus exhaust pumping. The individual designs are presented with solutions for this and a qualitative

comparison of the permeate pumping cross-section is performed. The larger this surface is, the lower is the requirement on the MFP to compress since a good conductance downstream improves the rough pumping of the DIR loop and reduces the pressure downstream the foil. The permeate is routed to the lower pipe chase through two DN 250 pipes [32]. The cross-section of the DIR loop pumping of each duct should be larger than that of the two DN 250 pipes to not create a bottleneck for the conductance of this channel.

Some part of either the inlet or outlet are intrinsically blocked by waveguide systems, which transmit the microwaves to the plasma sources. There are several different solutions for microwave distribution from a main power waveguide industrially available and marketed as waveguide couplers or magic tees. In the last decade, some different designs have spiked interest in research [169] [170]. However, microwave power distribution to the plasma sources in the pump duct is regarded as trivial with assistance of an industrial partner and all solutions look similar for the different MFP designs. Some part of the waveguides are imagined as hidden in the shadow of the 100 mm wide support structure of the plasma sources and, also due to the similarity for each design, the waveguide systems are not considered specifically in the simulation.

In the original idea to install the MFP, published in [105], an array of cylindrical MFP modules is fit in one duct. This design is called “Tube” design and shown in Figure 8.1 (b). Here, each MFP consists of a center cylindrical, linearly extended plasma source, encompassed by a cylindrical metal foil. The modules are mounted on three horizontal bars at the inlet and outlet of the pumps. The torus exhaust enters the MFP in the plasma volume and the permeate is evacuated downstream the foil, which is the volume in the shell radially outside the foil. In this area, thermal shielding, mounted on the outer wall of the MFP module, is foreseen. The outer wall has a backside cooling. Since the foil temperature is strongly affected by the performance regulating plasma power, additional foil cooling is necessary between the different modules, causing low energy efficiency. The permeate streams are collected through larger openings in the outer walls of the individual MFP modules and downstream pumping occurs through an opening in the duct wall.

The second configuration, termed “Sandwich” design, shown in Figure 8.1 (a), is based on the vertical installation of metal foil segments with several plasma sources in between. Just like the tube design, its front surface shows symmetry in both axes. The torus exhaust enters through two rectangular flow channels, in the middle of which 4 plasma sources are installed. At the inlet and outlet, the plasma sources are fixed on vertical support structures of 100 mm width that partially block the opening. The permeate from the center channel is pumped to the outer channels through two cylindrical connections of 200 mm width. On the duct walls, connection pipes can be installed to transport the permeate through the DIR loop. Inbetween the foils as well as towards the duct walls, some space for thermal shielding as well as wall cooling is considered, shrinking the space available for the torus exhaust.

The third solution is called “Halo” design and shown in Figure 8.1 (c) as it is composed of a large cylindrical arrangement that features a circular array of plasma sources in one volume inside of a large 1.8 m diameter metal foil with another smaller 0.5 m diameter foil in the center. Both foils, once again, are fixed in segments for structural stability. For the small central foil, an additional horizontal support is required, blocking the inlet and outlet to some extent. The 1.2 m diameter plasma source halo is supported by a 100 mm wide ring at inlet and outlet of the cask. The torus exhaust enters through the large annular gap where the plasma sources are installed. The permate is evacuated downstream the foil, which is the volume on the further outside of the duct and the volume in the center of the duct. The volume outside of the outer foil is rather large in the “Halo” design since thermal shielding and cooling of the foil should occur axisymmetrically and the installation space required limits the height of the foil cylinder, which is smaller than the width of the duct. With the foil being cylindrical but the duct rectangular, there is much unused space left and right in the duct and also in its corners.

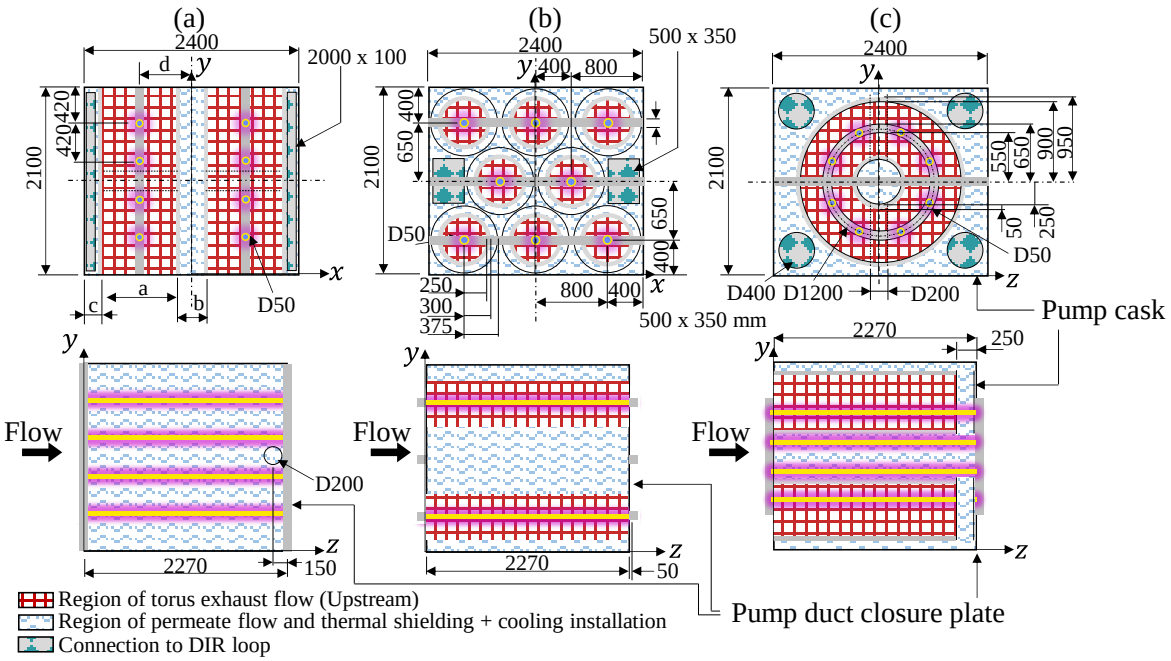

Figure 8.1: Sketches of the three considered MFP designs for EU-DEMO. Design (a) is referred to as "Sandwich" design, b) is the “Tube” design and c) the “Halo” design. Eight plasma sources are installed on support structures within the torus exhaust flow domain in each design. Downstream the foil, the DIR loop is connected through small openings channels in the pump duct closure plate. Planes of symmetry are the yz-plane and the xz-plane at y corresponding to half the height of the cask.

The outer and inner permeate flows are connected through a cross-pipe before the outlet and both are pumped by a connection on the duct wall. The inner foil requires internal cooling systems as it is exposed to high power densities from the plasma. Implementation of the inner foil reduces conductance but increases the separation ratio as it enhances the probability of surface interaction for the particles. Even without the inner foil, the cross-section for torus exhaust pumping is smaller than in the “Sandwich” design. However, the MFP with inner foil makes for a better comparison with the other two designs due to achieving similar separation ratios while the separated flux without inner foil is smaller. In all designs, the support structures at the in- and outlets represent surfaces with 0 depth.

Generally, conductance and separation ratio can be traded against each other in the different designs by variation of the dimensions or variation of the outlet sticking coefficient. In a first iteration, the designs are compared based on the helium pumping speed, D_2 pumping speed and separation ratio. For the most promising design, a variation of dimensions is performed within reasonable limits of the geometry to elaborate an understanding of the tradeoff and show possible operation points of the MFP. The sticking coefficient is varied to investigate the effect of throttling of the downstream linear diffusion pump’s (LDP) pumping speed on the separation ratio and the pumping of hydrogen.

8.2 Description of the Test Particle Monte Carlo approach

The Test Particle Monte Carlo approach used in this work considers a 3-dimensional flow domain, in which the movement of single particles is modelled, considering their mass, temperature and interactions with surfaces using the free molecular flow code ProVac3D [171]. A differentiation of the simulation of burn and dwell succeeds by considering D_2 particles during burn, which can interact with the plasma and foil, and helium particles during dwell. A large number of one species of particles is injected into the model one after another to exploit parallelization on multiple cores and achieve statistical averaging. The inlet of the model is the interface of the pump duct and the divertor (see Figure 1.5). The D_2 particles are injected as ground-state particles but can become excited upon interaction with the plasma surface. Thus, for the simulation of burn, a total of 2 particle species is considered. The

particles are injected obeying a Maxwellian' energy distribution function. The simulation does not strictly account for mass balance since the conversion of a ground-state to an excited particle is represented by the exchange of a D_2 molecule to a deuterium atom and vice versa.

Based on a 2-dimensional, axisymmetric sketch of the "Tube" design, the MFP simulation domain and the considered boundaries are explained in Figure 8.2. Before reaching the MFP, the particle has to pass through the duct and successfully enter through the MFP inlet. Figure 8.2 uses the schematic description of the superpermeation process introduced in section 4 with the 5 different steps as orientation. A deuterium particle is depicted, entering through the inlet at "0", undergoing excitation at "1" and permeation at "2" to "5". Upon collision with any wall, the particle assumes the corresponding wall's temperature. The trajectory, with which it is reflected from the walls, is determined according to a diffuse reflection boundary condition. The particle can enter and exit the MFP through its inlet B1. If the particle hits the pump duct inlet at the divertor, it is deleted. When hitting the outlet B4 of the MFP, a particle is "pumped" with a sticking coefficient c_{out}. The sticking coefficient depends on the performance parameters of the LDP and the cross-section of the pump duct closure plate. A conservative value for c_{out} can be estimated from [172] as 0.04. In this context, conservative means at the upper limit of the expectation since larger sticking coefficients lead to faster removal of hydrogen through the outlet and, thus, lower separation ratios.

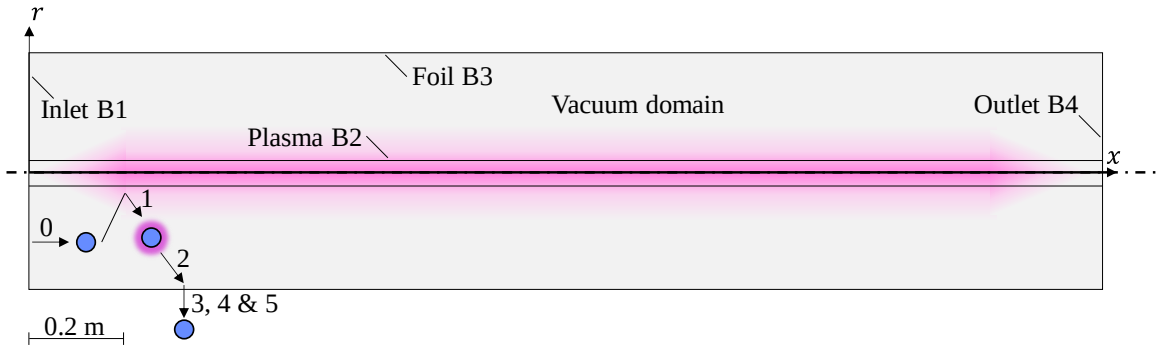

Figure 8.2: 2D sketch of the 3D model of a MFP module in the "Tube" design considered in the TPMC simulation. There are 4 different boundaries and two particle species considered for the simulation of burn. The point at 0 represents the ground-state deuterium, which can become excited upon collision with the plasma boundary to enable the particle's permeation through the foil boundary.

The two remaining boundaries are the plasma boundary B2 and the foil boundary B3. To successfully permeate, a particle injected in ground-state has to be excited on the plasma boundary with a certain probability c_{exc} and then permeate through the foil with a probability c_{perm}. Only excited particles are considered to permeate in the model. However, they can also "recombine" with certain probabilities on either of the boundaries as on the plasma boundary with $c_{rec,B2}$, the foil boundary with $c_{rec,B1}$ or the outlet with $c_{rec,B4}$. Recombination means de-excitation into ground-state, representing the atom-atom recombination. If no recombination takes place, the particle reflects with the probability $c_{ref,i} = 1 - c_{rec,i}$ on boundary i except for the foil boundary, on which also permeation is considered. There, reflection succeeds according to the probability $c_{ref,i} = 1 - 2 \cdot c_{perm}$ for symmetric surface barrier conditions. The permeation probability c_{perm} is multiplied with a factor f to consider the relative reduction in the permeation flux due to noble gases. A list of the different surface interaction probabilities for the two species is given in Table 8.1. The letter *g* refers to particles in the ground-state, while *e* refers to the excited state particles. For the two main parameters studied, the permeation and the excitation probability, ranges correspond to those in the simulation. In Appendix 8, a representative atomic hydrogen permeation probability in the experiments is calculated to be ~ 3 %, which is lower than most of literature reports for niobium and vanadium. Values for the permeation probability are, thus, taken from literature.

Table 8.1: Surface interaction probabilities assumed for the DEMO MFP designs.

Boundary	Description, Interaction	Variable	Probability	Ref.
Inlet	Deleting an incoming particle		1	
Plasma	Reflection of g as g	$c_{ref,B2,g}$	1 - c_{exc}	
	Exctiation of g to e	c_{exc}	0.03 – 0.45	(see Table 5.3)
	Reflection of e as e	$c_{ref,B2,e}$	1 - $c_{rec,B2}$	
	De-excitation of e to g	$c_{rec,B2}$	0.02	[97]
Foil	Reflection of g as g	$c_{ref,B3,g}$	1	
	Reflection of e as e	$c_{ref,B3,e}$	$1 - 2 \cdot c_{perm}$	
	De-excitation of e to g	c_{rec}	Same as c_{perm}	
	Permeation of e through B3	$f \cdot c_{perm}$	$f \cdot (0.05 - 0.2)$	[38] [40] [49] [114]
Outlet	Pumping through outlet	c_{out}	0.04	[172]

8.3 Sensitivity of performance to operational parameters

The first evaluation of the MFP inlet cross-section as documented in Table 8.2 shows that the "Sandwich" design has the largest transmission probability and, hence, the largest conductance. Nontheless, to be able to take the performance during burn into account, the hydrogen pumping speed and separation ratio during burn are studied for the three designs, varying the permeation and excitation probability.

Table 8.2: Inlet cross-sections (neglecting support structure) and transmission probabilities for the three different MFP designs.

	Sandwich (a = 850 mm)	Halo	Tube
Inlet cross-section (m²)	3.57	2.26	1.56
Transmission probability (-)	0.116	0.081	0.04

First, for the "Sandwich" design, Figure 8.3 shows the change in D_2 pumping speed during burn over the excitation probability on the plasma source for different permeation probabilities through the metal foil. The high values tested for the excitation probability represent a high power plasma operated at a pressure of 1 Pa.

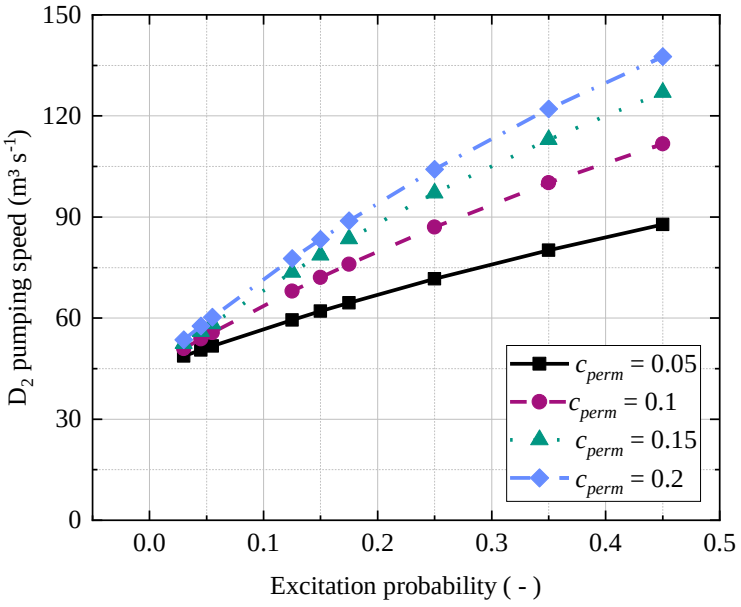

Figure 8.3: Calculated D_2 pumping speed of a MFP as a function of excitation probability on the plasma source and permeation probability through the metal foil in a single duct of EU-DEMO using the MFP "Sandwich" design.

The pumping speed increases with the excitation probability and with permeation probability as more suprathermal hydrogen is produced and permeates through the foil. Despite increase of the permeation probability c_{perm} by factor 4, the pumping speed only increases by about 50 % at most.

In Figure 8.4, the separation ratio s of the "Sandwich" design MFP is plotted as a function of the excitation probability for different permeation probabilities. Again, increase in the permeation probability leads to increasing separation ratios but at maximum to an increase of ~ 50 %. The excitation probability, on the other hand, more significantly impacts separation ratios and yields an increase from ~ 0.2 at an excitation probability of 0.03 to ~ 0.8 with a permeation probability of 0.2.

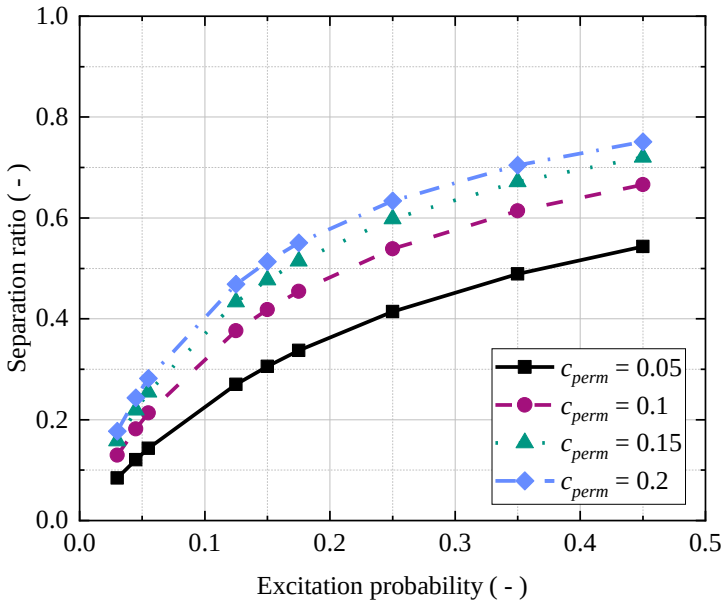

Figure 8.4: Calculated change in the separation ratio over the excitation probability for the MFP "Sandwich"-design assuming several different permeation probabilities.

The two other designs show a similar change of pumping speed and separation ratio with excitation and permeation probability. but have their individual benefits and weaknesses. The D_2 pumping speeds and separation ratios of all designs are given in Table 8.3 and 8.4. The pumping speed of the "Tube" design increases more significantly with the excitation probability than for the other designs. This is due to the larger number of surface interactions the particles undergo in this design, enabling larger permeation flows. This also results in larger separation ratios for the "Tube" design than for the other two designs.

Table 8.3: Calculated pumping speeds for three different MFP designs for EU-DEMO based on parametric sweeps of the plasma excitation probability and the foil permeation probability.

S ($m^3\ s^{-1}$)		Sandwich				Halo				Tube			
c_{exc}	c_{perm}	0.05	0.1	0.15	0.2	0.05	0.1	0.15	0.2	0.05	0.1	0.15	0.2
0.03		48.7	51.0	52.5	53.5	47.1	49.3	50.7	51.6	41.0	42.9	43.8	44.3
0.045		50.5	53.8	56.0	57.6	49.1	52.4	54.4	55.8	43.8	46.5	47.8	48.6
0.055		51.7	55.7	58.3	60.3	50.4	54.4	56.8	58.5	45.6	48.8	50.3	51.3
0.125		59.4	68.0	73.6	77.6	59.0	67.3	72.4	75.8	56.6	62.9	66.1	68.0
0.15		62.0	72.0	78.7	83.4	61.8	71.4	77.4	81.3	60.0	67.3	70.9	73.1
0.175		64.5	76.0	83.5	88.9	64.4	75.4	82.1	86.6	63.2	71.4	75.4	77.8
0.25		71.6	87.0	97.1	104.2	71.8	86.3	95.0	100.9	71.7	82.2	87.3	90.3
0.35		80.2	100.1	113.0	122.1	80.2	98.7	109.7	117.1	81.0	93.8	100.0	103.8
0.45		87.8	111.7	127.0	137.6	87.5	109.2	122.1	130.7	88.5	103.2	110.3	114.6

Despite having the largest permeation flows, however, the "Tube" design has lower total pumping speeds than the other two designs for the whole parameter range with the exception of a few cases with low permeation probabilities (c_{perm} = 0.05) and high excitation probabilities ($c_{exc} \geq 0.25$). Especially at low permeation probabilities, the "Tube" design outperforms the other two designs in terms of separation ratio. However, those operation conditions are not most relevant to the application in EU-DEMO since operation at low pressure and high power is the more likely scenario and considered by high excitation probabilities c_{exc} = 0.25 – 0.45. To account for the higher relevance of the high excitation probability scenarios and consider both, as figure of merit, the separation ratio and the pumping speed are multiplied with each other to yield the product *P* for every single parameter constellation. The results for *P* are given in Table 8.5.

Table 8.4: Calculated separation ratios for three different MFP designs for EU-DEMO based on parametric sweeps of the plasma excitation probability and the foil permeation probability.

s (-)		Sandwich				Halo				Tube			
c_{exc}	c_{perm}	0.05	0.1	0.15	0.2	0.05	0.1	0.15	0.2	0.05	0.1	0.15	0.2
0.03		0.08	0.13	0.16	0.18	0.10	0.15	0.18	0.20	0.18	0.22	0.24	0.26
0.045		0.12	0.18	0.22	0.24	0.15	0.21	0.25	0.27	0.24	0.30	0.33	0.34
0.055		0.14	0.21	0.25	0.28	0.17	0.24	0.28	0.31	0.28	0.34	0.37	0.39
0.125		0.27	0.38	0.43	0.47	0.31	0.42	0.47	0.50	0.47	0.54	0.58	0.59
0.15		0.31	0.42	0.48	0.51	0.35	0.46	0.51	0.54	0.51	0.59	0.62	0.64
0.175		0.34	0.45	0.51	0.55	0.39	0.50	0.55	0.58	0.55	0.63	0.66	0.67
0.25		0.41	0.54	0.60	0.63	0.46	0.58	0.63	0.66	0.63	0.70	0.73	0.75
0.35		0.49	0.61	0.67	0.70	0.54	0.65	0.70	0.73	0.70	0.77	0.80	0.81
0.45		0.54	0.67	0.72	0.75	0.59	0.70	0.75	0.77	0.74	0.81	0.83	0.85

For the combination of highest permeation and excitation probability, the "Sandwich" design reaches the largest *P* value. It also increases most with c_{perm} but yields lower values for *P* than the other two designs for permeation probabilities ≤ 0.1. The permeation probability is more relevant in the "Sandwich" design because of the larger distance between the foils and the lower number of particle collisions with the foil boundary. In the other two designs, the particles are more "saturated" with foil collisions, yielding a low likelihood for the case that a particle will not hit the foil after its excitation.

Despite its high separation capabilities, the "Tube" design performs poorly during dwell due its small inlet cross-section. All values for *P* are summed for the parameter combinations under study and listed in Table 8.6 to derive a design recommendation. By multiplication of P_{sum} with the total cross-section of the design, being the sum of torus exhaust and DIR loop pumping cross-section, a total evaluation score is obtained. Prioritizing the conductance maximization, the "Sandwich" design appears as the best candidate for EU-DEMO. This is reflected by the inlet cross-sections as calculcated when neglecting the 100 mm wide support beams in all designs. However, even when considering the D_2 pumping speed, separation ratio and the DIR loop pumping cross-section, the "Sandwich" design still outperforms the other two designs. Though not considered in this evaluation, this design features beneficial power efficiency due to better geometric factors for the cooling of the foil and the use of plasma for foil heating.

Table 8.5: Product of pumping speed and separation ratio for all MFP designs and parameter constellations.

P (m³ s⁻¹)		Sandwich				Halo				Tube			
c_{exc}	c_{perm}	0.05	0.1	0.15	0.2	0.05	0.1	0.15	0.2	0.05	0.1	0.15	0.2
0.03		4.1	6.6	8.3	9.5	4.9	7.5	9.1	10.1	7.3	9.6	10.7	11.4
0.045		6.1	9.8	12.3	14.0	7.2	11.0	13.3	14.9	10.7	14.0	15.6	16.6
0.055		7.4	11.9	14.9	17.0	8.7	13.3	16.1	18.0	12.9	16.8	18.8	20.0
0.125		16.1	25.6	31.9	36.4	18.6	28.1	33.9	37.9	26.4	34.2	38.1	40.4
0.15		19.0	30.1	37.5	42.8	21.8	32.9	39.7	44.3	30.6	39.6	44.0	46.7
0.175		21.8	34.6	43.0	48.9	24.8	37.5	45.1	50.3	34.6	44.6	49.5	52.5
0.25		29.7	46.9	58.1	66.0	33.3	49.9	60.0	66.7	45.0	57.8	64.0	67.7
0.35		39.2	61.5	75.9	86.0	43.0	64.2	76.8	85.3	56.4	72.0	79.6	84.1
0.45		47.7	74.4	91.5	103.4	51.3	76.2	91.0	100.9	65.6	83.4	92.0	97.2

Table 8.6: Torus exhaust and DIR loop cross-sections, which lead to the final evaluation score for each design by multiplication with the sum of all pumping speed x separation ratio products for each design.

	Sandwich	Halo	Tube
MFP inlet cross-section (m²)	3.57	2.26	1.56
DIR flow cross-section (m²)	0.4	0.5	0.35
Total cross-section (m²)	3.97	2.76	1.91
P_{sum}(m³ s⁻¹)	1290	1348	1510
Final evaluation score (-)	5121	3720	2884

Subsequently, the "Sandwich" design is further studied by variation of its internal subdimension (the channel width), the number of plasma sources and the sticking coefficient. The channel width is varied from 0.85 m to 0.45 m in 0.1 m steps. The results of this parametric study are plotted in Figure 8.5 as pumping speed over separation ratio. Towards higher separation ratios, the channel width decreases. A maximum in the pumping speed is reached at a channel width of 0.55 m and a separation ratio of ~ 67 %. The total D_2 pumping speed during burn benefits from the improved conditions for permeation with lower channel widths. Thus, if the only requirement is D_2 pumping speed optimization, the best channel width is 0.55 m.

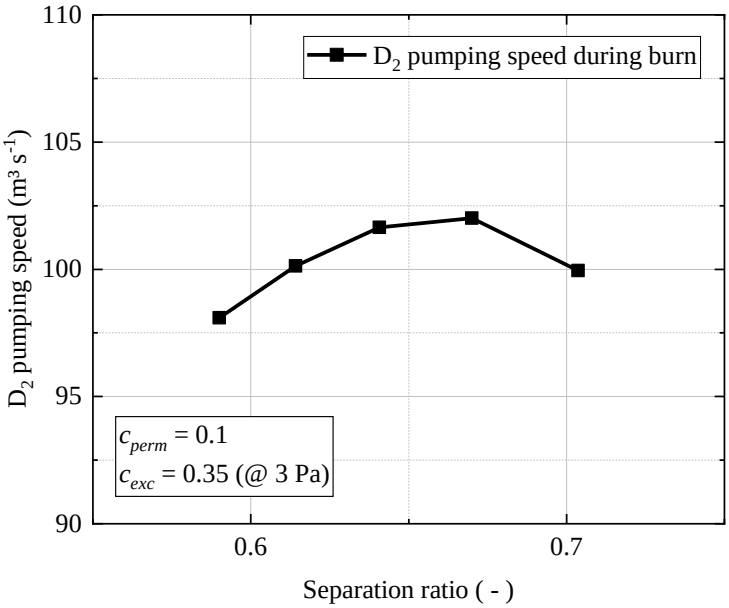

Figure 8.5: Calculated D_2 pumping speed over fuel separation ratio for the "Sandwich" design channel width varying from 0.85 to 0.45 m from left to right.

Further reduction increases the separation ratio but comes at the cost of decreasing conductance and reduced outlet pumping speeds. The latter is especially important to consider since permeation is selective for hydrogen and the impurities from the torus, such as noble gases and helium, are only removed through the MFP outlet. This effect is also relevant to the analysis of the impact of the sticking coefficient variation. A high separation ratio is always accompanied by high selective pumping speeds for the hydrogen fuels. Low pressures and good conductance in the MFP and pump duct favor propagation of an elevated partial pressure of noble gases towards the divertor. The extent of this and if it affects pumping at the divertor is unknown and requires a dedicated analysis of the transitional flow that prevails in the duct during burn, which is beyond the scope of this work.

Continuing with the assumption of possible LDP throttling to regulate the MFP outlet sticking coefficient, possible operation points of the MFP during burn can be analyzed. Therefore, the sticking coefficient is varied between 0.005 and 0.06, with 0.04 as benchmark. In Figure 8.6, the change of separation ratio with excitation probability is shown for different sticking coefficients. The lowest value for the excitation probability (= 0.1) represents a conservative lower limit, which is taken from the plasma operation at 10 Pa (see Figure 5.10). The difference in the separation ratio dramatically reduces for the varying plasma performances towards lower sticking coefficients. In the case of low sticking coefficients, the pumping through the outlet is increasingly suppressed, meaning that the particles are mainly removed through the foil. When pumping through the outlet approaches zero at low sticking coefficients, the separation ratio almost reaches unity, even for low excitation probabilities. The dashed line in the Figure indicates the separation ratio of 0.8. Any arbitrary combination of the outlet sticking coefficient (LDP throttling) and the plasma performance, that yields the separation ratio of 0.8 can be read from the plot. For example, assuming a sticking coefficient of 0.01 for the “Sandwich” design with 0.85 m wide channels, the required plasma excitation probability that yields 0.8 separation is ~ 0.26. The corresponding atomic hydrogen molar fraction of ~ 14 % can be extracted from Figure 5.10.

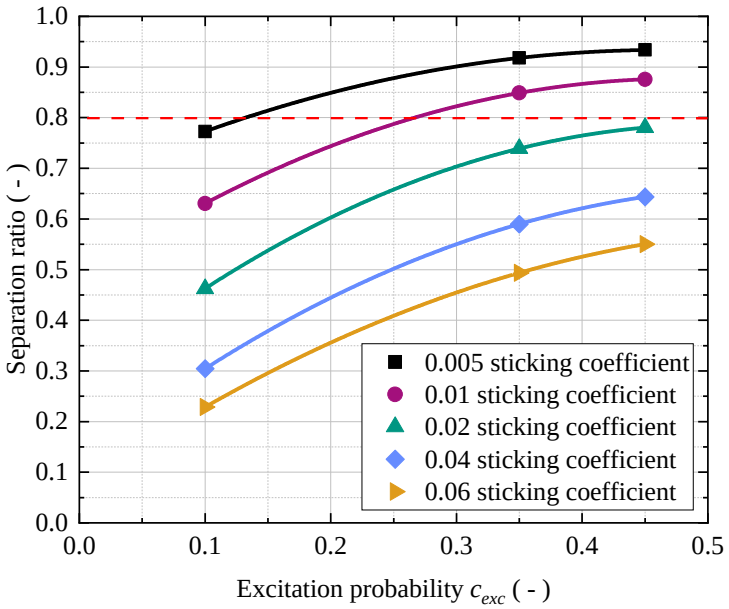

Figure 8.6: Calculated change of separation ratio with excitation probability for different outlet sticking coefficients c_{out} in the “Sandwich” MFP design with 0.85 m channel width. At very low c_{out} values, the separation ratio of 0.8 can be reached with almost any considered plasma performance.

Figure 8.7 shows the calculated D_2 pumping speed over the excitation probability for several different outlet sticking coefficients. The pumping speed increases with higher excitation probabilities and higher sticking coefficients. The excitation probability has an especially large impact on the total pumping speed at low sticking coefficients because most of the hydrogen is removed through the foil in this case.

Considering Figures 5.6, 5.10, 8.6 and 8.7, a possible operation point of the MFP is determined. The dashed red line in Figure 8.7 shows the D_2 pumping speed provided by this operation point, which is about 60 $m^3\ s^{-1}$. With a total DEMO throughput of 450 Pa $m^3\ m^{-2}\ s^{-1}$, of which 92.45 % is hydrogen (416 $Pam^3\ s^{-1}$), a total number of only 2 MFPs operating at full power is required to recycle the total throughput at 4 Pa in the MFP.

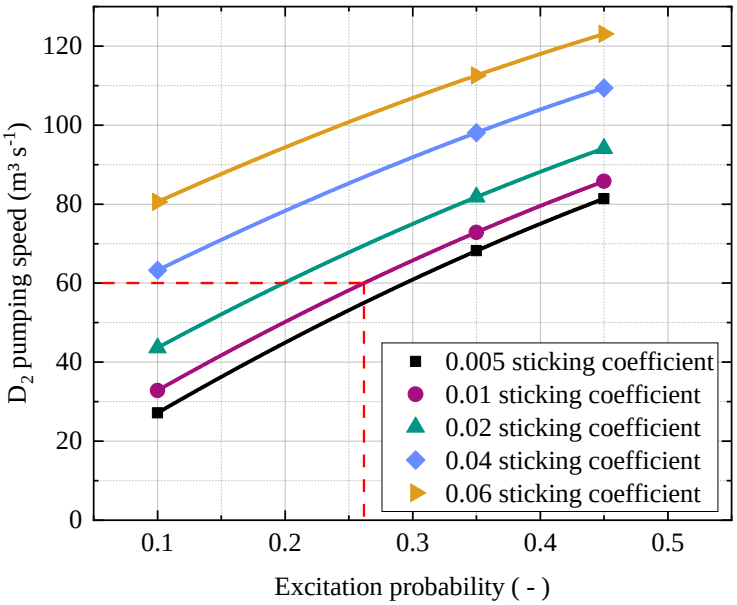

Figure 8.7: Calculated D_2 pumping speed of a single duct with "Sandwich" MFP for different outlet sticking coefficients and plasma excitation probabilities.

Figure 8.6 also shows that a separation ratio of 0.8 cannot be achieved with the baseline wide channel "Sandwich" design at a sticking coefficient value of 0.04 and no option of throttling of the LDP pumping speed. However, the number of plasma sources within one MFP channel can be increased. This is especially easy to do for the "Halo" and the "Sandwich" design. The effect of this on the separation ratio of the wide channel "Sandwich" design is illustrated in Figure 8.8.

To determine the maximum number of plasma sources in one channel, a lower limit for the distance between the center of two plasma sources is defined as 0.25 m to avoid that the microwave of one plasma penetrates into the plasma produced by the neighboring plasma source. The minimum distance to the wall is assumed as 0.15 m. Thus, a maximum of 8 plasma sources can be fit in one channel if no additional supporting beam is to be employed, which could hold additional plasma sources while still respecting the defined minimum distances. For the variation of the plasma source number, an excitation probability of 0.35 is assumed, representative of the full power plasma operation at ~ 3 Pa. The outlet sticking coefficient is 0.04, representing a fully opened channel to the LDP. As shown in Figure 8.8, pumping speed and separation ratio increase with the number of plasma sources. However, assuming this sticking coefficient, the design does not reach a separation ratio of 0.8 even with 8 plasma sources per channel (16 per duct). The separation ratio increases with the number of plasma sources, which linearly scales with the used power per duct, but the increase flattens towards high plasma source numbers and it requires increasingly more plasma power to obtain higher separation ratios.

The separation ratio and D_2 pumping speed for a "Sandwich" design with 3 channels, each with 0.52 m width, are also displayed in Figure 8.8. It provides significantly higher separation ratios and D_2 pumping speeds during burn than the 2 channel solution, but yields ~ 18 % lower He pumping speed during dwell due to the smaller inlet cross-section. For the case of 6 and 7 plasma sources per channel, the separation ratio of at least 0.8 is reached, delivering about 160 and 170 $m^3\ s^{-1}$ pumping speed. Theoretically, this is sufficiently high to only operate 1 MFP at 3 Pa to recycle the total hydrogenic

species throughput of 416 Pa m³ s^{-1}. However, it has to be noted that the free molecular flow assumption of the model overestimates the separation efficiency, and it represents only a rough estimate.

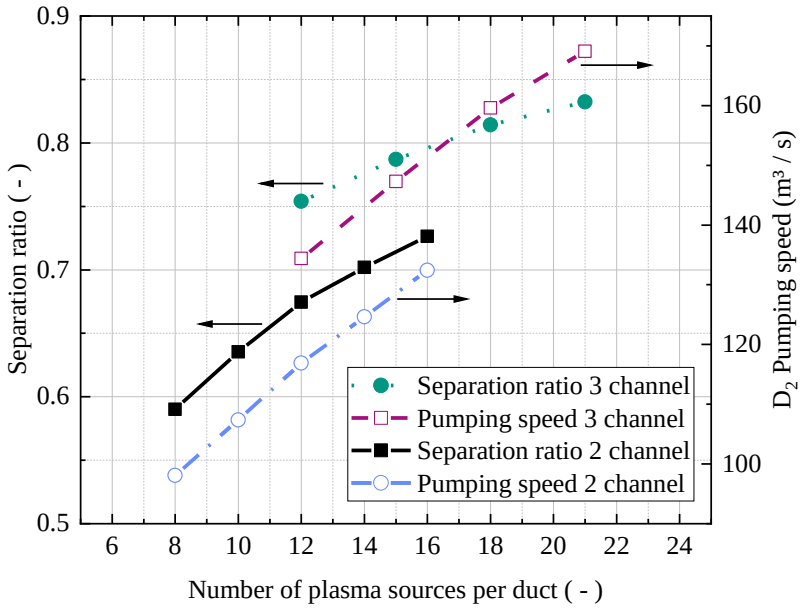

Figure 8.8: Calculated separation ratio and D_2 pumping speed during burn over the number of plasma sources within one duct for a "Sandwich" design with 3 and 2 torus exhaust channels. The excitation probability is assumed as 0.35, the outlet sticking coefficient as 0.04.

8.4 Development of a fusion power plant MFP design

It has been demonstrated that the "Sandwich" design, composing of vertically installed metal foil segments with a parallel array of linearly extended plasma sources in between two foils, is able to deliver the highest conductance. Large MFP inlet cross-sections provide large conductances but reduce the amount of surface interactions. This leads to lower separation ratios of unburnt fuel during burn as compared to using narrower channels. With a torus exhaust channel width of 0.85 m and the given performance of the LDP, a separation ratio of 0.8 can not be reached unless an installation is introduced that allows variation of the LDP pumping speed. The effect of this is reflected in the simulations presented here by variation of the sticking coefficient. Utilizing the regulation of the sticking coefficient, a large variety of operation points of the MFP are possible, all delivering a separation ratio of at least 0.8 while still providing sufficient pumping speeds. In one given example, the D_2 pumping speed of this configuration is sufficiently high to only require 2 MFPs to recycle the whole throughput of DEMO. It is noted, though, that, if a lower outlet sticking coefficient is assumed, the pumping speed of the MFP drops, resulting in the need of more MFPs for DEMO. Furthermore, the use of free molecular flow overestimates the amount of surface interactions and, thus, a safety margin has to be considered when analysing the results for the separation ratio. At the cost of dwell pumping speed, the "Sandwich" design with three channels delivers higher separation ratios than that with two channels, even with the same amount of plasma sources used. Installation of a high number of plasma sources, up to 16 in the two-channel "Sandwich" design, yields better results in terms of separation ratio but this effect is increasingly less cost-efficient in terms of additional power consumption.

A design option that allows for highest dwell pumping speed could foresee only a few of the ducts for fuel separation, leaving the rest without MFP for maximum conductance. However, this design requires the option of closing pumping of the ducts without MFP for example by installation of a valve instead of an MFP. The design respects the geometric boundary conditions imposed by the pump duct and facilitates installation of all essential components consisting of plasma sources, waveguides and microwave distribution system, segmented metal foils with resistive heating and a plasma gaseous

cooling circuit. The latter is commonly used with the plasmaline and fed through the center of the hollow inner conductor, which leads to the backflow between the annular gap of inner conductor and surrounding dielectric, directly cooling the dielectric. For this cooling, for example D_2 can be used due to its naturally good coolant properties in comparison to other gases and the lower damage to the MFP in case of accidents like rupture of a dielectric. Of all the designs, the "Sandwich" also appears to have the easiest way of moderating the temperatures within the system as the foil surfaces are best accessible. With ~ 19 m², it ranks second in terms of foil surface area with the "Tube" design having ~ 28 m² and the "Halo" design 16 m². More foil surface area translates to more resistive heating as well as active cooling installation necessary.

The pressure in the MFP is defined by the plasma scenario of the hot fusion plasma. Assuming the cold MFP plasma ignites, lower pressures (down to 1 Pa) have been shown to improve plasma performance of the MFP and, thus, increase the separation ratio and D_2 pumping speed. However, at lower pressure, the throughput is also reduced. The recommendation is given to perform experiments that investigate the ignitability of the plasma source in the magnetic field present in the pump duct. Should be found that the plasma cannot ignite under these conditions, the MFP can be positioned in larger radial distance from the torus until the magnetic flux density within the MFP is < 100 mT in all locations during burn. In this regime, the plasma is expected to ignite properly, given sufficient microwave power is used. Magnetic flux densities of this magnitude, and especially around the ECR condition at 87.5 mT, have been demonstrated to benefit the operation of the plasma down to pressures of 1 Pa. The requirement of dwell pumping speed ultimately depends on the not yet available data on outgassing rates of the reactor walls. Should the supplied dwell pumping speed be sufficient and the installation of the above-mentioned valve system be possible, the recommendation is given to use a total of only 5 ducts for fuel separation and another 5 without MFP. Then, the three channel "Sandwich" design is to be employed in the 5 ducts with MFP and a total of 7 plasma sources per torus exhaust channel installed. This translates into 21 plasma sources per duct, or a total of 105 plasma sources for DEMO, each equipped with a maximum microwave power of ~ 15 kW. This value comes from the extrapolation to low pressure operation of the plasma source operation benchmark in HERMES*plus* at 2.4 kW. The corresponding plasma length is 0.35 m. This yields about 15 kW microwave power when considering the length of the plasmaline in the MFP (2.27 m). This also represents the highest power 2.45 GHz magnetron currently industrially available. However, most of the installed plasma sources are the result of safety margin consideration.

Taking the example of the three-channel design with 7 plasma sources per channel in the section above, in which only one duct is required for fuel separation, a total microwave power of 21 times 15 kW is necessary to separate 83 % of hydrogenic species with a D_2 pumping speed of 160 $m^3\ s^{-1}$, which results in a throughput of 480 Pa $m^3\ s^{-1}$ if the MFP is operated at 3 Pa. The total microwave power in this case is ~ 315 kW. Additionally, resistive heating has to be supplied to the foils to keep them at a temperature that facilitates steady-state PDP. In some experiments, it has been possible to achieve this at 600 °C. It is expected that most of the power to reach this temperature is already supplied by the plasma and only little additional resistive heating power is required.

The recommendation is based on the assumption that sputtering-resistant foils can be produced and used as such in the MFP, since it has been demonstrated before that sputtering resistance of the foil material candidates is possible. However, should it not be possible to obtain sputtering resistant foils, the power density of the plasma needs to be lowered to stop the removal of oxygen from the surface monolayer and, thus, obtain reasonably high steady-state fluxes. To this end, the feasibility of using a 915 MHz plasma source has to be investigated. This plasma source typically features larger components such as waveguides due to the longer wavelength. It also produces larger plasma and can, using magnetic fields, also be operated down to pressures relevant for DEMO [173]. More commonly used in large processing facilities, higher power magnetrons are available for the production of 915 MHz microwaves.

9 Summary of results and future work

The operation of nuclear fusion reactors relies on the availability of sufficient amounts of tritium, which is not guaranteed with current prospects. The Direct Internal Recycling (DIR) concept proposes the separation of a majority of unburnt fuel from the torus exhaust close to the reactor to dramatically reduce the tritium inventory of a fusion power plant. While there are no established technologies available to separate large hydrogen throughputs at the given conditions, a metal foil pump (MFP) is a promising candidate. It employs a hydrogen-selective effect called superpermeation to separate hydrogen from other gases at large rates in vacuum. The key to this process is the generation of large quantities of atomic hydrogen in a plasma, which subsequently permeates through a metal foil.

This work is streamlined along the development of a modeling tool to predict the performance of a MFP in EU-DEMO. It is initiated by dividing the process a hydrogen particle undergoes in the MFP into five steps, which are summarized to (i) the production of suprathermal hydrogen with the potential to permeate through the foil and (ii) the transport and permeation of suprathermal hydrogen through the foil.

Step (i) is characterized using a 2D axisymmetric plasma fluid simulation, which represents the experimental setup HERMES*plus*. It is experimentally validated based on atomic hydrogen density measurements obtained with optical emission spectroscopy by application of the actinometry method in the setup. A novel technique is developed that assumes the plasma as separated into 12 rings with inidivdually homogeneous plasma parameters and gas composition. It allows evaluation of different angles of the optical line of sight to enable some degree of spatial resolution of the atomic hydrogen density. The validation covers plasma powers between 1.2 and 2.4 kW. The plasma simulation, especially the chemistry, is adapated until a good match between simulation and experiment is found. Parametric studies of pressure, power and the atomic hydrogen recombination coefficient are performed on the validated simulation. For the validated operational range, the volume-averaged atomic hydrogen molar fraction y_H varies between 3.13 % and 5.44 %. It increases strongly towards lower pressures, up to 9 % at 10 Pa. An extrapolation is performed to pressures below 10 Pa to obtain an estimate of the expected y_H value in the magnetic field-assisted plasma of the MFP in the EU-DEMO pump duct.

Step (ii) is considered using permeation probabilities of atomic hydrogen as given in literature and by accounting for the presence of noble gases in a vacuum simulation that employs a Test Particle Monte Carlo (TPMC) appraoch. The experimentally demonstrated temperature independence of permeation fluxes for the range of 600 °C to 900 °C supports the assumption of 600 °C as foil temperature in the performance simulation. Experiments with H_2 and D_2 are conducted to proof isotopic independence of the process.

In plasma-driven permeation (PDP) experiments, the measured change of the permeation flux with pressure and plasma power behaves in a similar manner as the simulation. Using quartz for the plasma source dielectric has led to the deposition of silicium on the vessel walls, which is accompanied by increasing permeation fluxes through reduction of the recombination coefficient. With the clean stainless-steel vessel, the highest permeation fluxes measured are ~ 6 Pa m^3 m^{-2} s^{-1}. Noble gases helium, argon and xenon have been added to the hydrogen plasma to measure the relative change in permeation fluxes with specified gas compositions. Those have been obtained through linear interpolation based on the assumption of separating 80 % of unburnt fuels by the outlet of the MFP. The results exhibit a decrease of the permeation flux not significantly stronger than the change of the hydrogen partial pressure in the plasma. The measured relative change of permeation with noble gas presence represents a conservative estimate.

By use of the actinometer argon, optical emission spectroscopy experiments evaluate the atomic hydrogen molar fraction for different lines of sight through the plasma at ~ 8.5 % to 6.2 %. Calculation

of the impingement flux of atomic hydrogen points towards strongly unfavorably asymmetric surface conditions of the metal foils employed in HERMES*plus* (niobium and vanadium), yielding low permeation probabilities (~ 3 %). This is likely caused by the destruction of the surface monolayer during operation by fast hydrogen neutrals from the plasma, which cannot be repelled by applying bias voltage on the foil. De-carbonization initially alleviated the issue by enabling oxygen replenishment from the bulk but a persistent contamination with carbon has prevailed, highlighting the importance of clean feedlines and low leak rates.

The performance of three different MFP designs is predicted in terms of separation ratio and pumping speed using the TPMC approach that assumes free molecular flow and simplified particle-wall interactions with probabilities. The most important interactions are described by the permeation probability through the foil and the excitation probability on the plasma source. The latter is obtained by approximating the results for the atomic or excited particle concentration from the validated plasma simulation to an excitation simulation. This uses the same model without volume, but only surface reactions and identical boundary conditions as the plasma simulation except for the plasma source surface, for which an excitation probability is swept. The operation conditions of the plasma are, thus, matched to a certain excitation probability, which is used in the TPMC simulation.

The three tested designs use the baseline of torus exhaust flow channel area maximization to optimize conductance while still allowing for the installation of 8 plasma sources and large, segmented metal foils. The largest conductance, most suitable for dwell pumping with reasonably good performance during burn is delivered by the “Sandwich” design. It consists of vertically installed metal foil segments, which reach from the duct bottom to the top. In between those segments, a vertical array of plasma sources is installed and fixed on beams at the ends of the MFP cask. A parameter study of the torus exhaust channel width, which is given by the distance between the foil segments, shows that a maximum D_2 pumping speed is reached with narrow channels due to improved hydrogen pumping through the foil, which also delivers higher separation ratios. Nonetheless, the recommendation is given to choose the largest possible opening of the channels of 0.85 m for maximum pumping during dwell. For this design, a parameter study of the outlet sticking coefficient is performed to consider the effect of throttling of the LDP pumping speed during burn. It is shown that this is necessary to achieve separation ratios of ≥ 0.8 with this explicit design and also opens a large possible range of operation. Reducing the outlet sticking coefficient allows to easily achieve the required separation ratios while still facilitating sufficiently high pumping speeds.

An exemplary operation point is described, at which only 2 MFPs are required to recycle the DEMO throughput of 450 Pa m^3 s^{-1} at 4 Pa, assuming a sticking coefficient of 0.01. This value is factor 4 smaller than the baseline with fully opened LDP pumping. A recommendation is made to use throttling of the LDP pumping speed for example by installation of valves behind the MFP. Some of the available pump ducts can also be equipped with such valves instead of MFPs to allow for routing of the exhaust during burn through only some ducts with MFPs. In this case, the ducts can be opened for dwell to achieve maximum pumping speed without conductance reduction in the given channels at the dispense of MFPs in those ducts. Increasing the number of plasma sources per torus exhaust channel yields higher separation ratios and D_2 pumping speeds. At the cost of conductance, the torus exhaust channels can be narrowed to fit a third channel with its respective foil segments and plasma sources in one duct. It is demonstrated that this three-channel design is able to achieve a separation ratio of 0.8 even with a sticking coefficient of 0.04 and, thus, no valve at the outlet of the MFP. This design even produces sufficiently high D_2 pumping speeds to recycle the whole throughput of DEMO through one duct at 3 Pa. The installed microwave power in this design is ~ 315 kW. It is not expected that a significant amount of resistive foil heating is required additionally. The separation ratios calculated in this work assume free molecular flow in the MFP, which overestimates surface interactions and, thus, the separation ratio and the permeated flux through the foil.

9.1 Outlook to further the development of a MFP

The critical analysis of operational risks is an important element in the development of a working MFP. Several of those risks cannot be addressed in the scope of this work as those require information, which is not available at the current state of development of EU-DEMO or require experimental hardware, which has not been available to this work. Still, such risks are pointed out for consideration at a later stage in the development.

Evaluation of the feasibility of cold plasma ignition in the pump duct environment is not trivial. The description of weakly ionized plasma in a strong and curved magnetic field with gradients and superimposed time-varying electric fields is an extremely complicated venture. The physical problem is very specific, and no publication has been found allowing to draw useful conclusions to the ignitability for a MFP type plasma. A similar topic in research and rich in literature is the simulation of thermonuclear fusion plasmas. However, due to their high temperature, full ionization and different magnetic configuration, those plasmas behave very differently from the MFP plasma. Yet, insights gained from this field disencourage modelling of the described problem due to excessive computational cost and little validity of the simulation without experimental backing.

The plasma source operation in strong magnetic fields, not exactly representing those in DEMO, has been tested experimentally with promising results. The accurate experimental consideration of the magnetic fields of DEMO, however, is strongly recommended. Such investigation has to focus on the plasma ignitability, microwave power absorption efficiency, heat flux distribution and potential damage to plasma-facing surfaces such as the metal foil. If the plasma can not be ignited at the given conditions, the MFP has to be moved to a larger radial distance of the Tokamak central axis.

The predictive modeling tool developed in this work uses extrapolation to pressures below 10 Pa to characterize the production of suprathermal particles at the respective conditions. More accurate values for the suprathermal hydrogen yield at the given conditions in the DEMO pump duct can, for example, be obtained by extending the pressure range, at which the plasma can be operated by use of magnetic fields. The HERMES*plus* facility receives a major upgrade and is equipped with two Helmholtz-coils close to the plasma vessel, which allow sustaining a magnetic field with maximum flux densities of ~ 100 mT in the bulk of the plasma.

It is crucial to demonstrate high flux steady state PDP operation in a reasonably clean environment with a plasma source that fulfils the requirements of a MFP. If the foil cannot attain sputter-resistance, a lower power density plasma source has to be considered. Once steady state PDP is achieved, more accurate input values for the simulation are accessible and the relative change of PDP fluxes with noble gas concentrations can be measured, as well as a low-as-possible metal foil temperature that facilitates steady state PDP determined. In the scope of this, the tolerable concentrations of impurities such as carbon and oxygen can be evaluated, which compromise steady state [36] and lifetime [50]. In the choice of the design and foil material, the aspects of remote maintenance and long-lived radioactive isotope creation by neutron damage must be considered. The requirement of the MFP to facilitate a certain duct conductance has to be quantified once the outgassing rates during dwell are known.

The feasibility of installing the foils in segments has to be tested in an experimental facility, which is currently being built at KIT. The foil is clamped in metal frames with an electrical insulation coating to allow for resistive heating of the foil. The clamped surface has to be leaktight to avoid leakage of significant amounts of the torus exhaust into the pure permeate stream. The coating process as well as the structure material are under study as well. An optimization of the segment design considers requirements on the mechanical stability to support the thin foils against rupture due to pressure gradients or induced forces due to the resistive heating current non-parallel to the superimposed

magnetic field. Additionally, the temperature distribution in the foil, thermal cycle fagitue and thermal elongation play important roles in the determination of the segment size.

Mockups of a MFP can be designed for tests in suitable testbeds. This is agreed for the Direct Internal Recycling Development Platform Karlsruhe (DIPAK) and proposed for the Divertor Tokamak Test (DTT) project in italiy, as well as for the UNITY test bed operated by *Kyoto Fusioneering* to gain more data on the operation of a large-scale interaction of plasma and foil and the behavior of the process under an external magnetic field.

References

[1] R. d. E. Atkinson, F. G. Houtermans, *Zur Frage der Aufbaumöglichkeit der Elemente in Sternen*, Zeitschrift für Physik 54 (1929) 656-665. doi: 10.1007/BF01341595

[2] A. Eddington, *The Internal Constitution of the Stars*, Cambridge University Press, 1926. doi: 10.1017/CBO9780511600005

[3] H. A. Bethe, *Energy Production in Stars**, Physical Review 55 (1939) 434-456, 1939. doi: 10.1103/PhysRev.55.434

[4] E. P. Gorbunov, K. A. Razumova, *The effect of a strong magnetic field on the magnetohydrodynamic stability of plasma and the containment of charged particles in the "Tokamak"*, Soviet Atomic Energy 15 (1963) 1105-1112. doi: 10.1007/BF01115931

[5] Global Carbon Project, *Supplemental data of Global Carbon Budget 2021 (Version 1.0)*, Global Carbon Project. doi: 10.18160/gcp-2021

[6] World Bank and International Energy Agency, *Sustainable Energy for All Database – Share of final energy consumption from renewable sources*, https://datacatalog.worldbank.org/search/dataset/0037712 (Accessed on 24th of January 2022).

[7] A. Einstein, *Ist die Trägheit eines Körpers von seinem Energieinhalt abhängig?*, Annalen der Physik 323, 13 (1905), 639-641. doi: 10.1002/andp.19053231314

[8] M. Wang et al., *The AME 2020 atomic mass evaluation (II). Tables, graphs and references*, Chinese Phys. C 45 (2021) 030003. doi: 10.1088/1674-1137/abddaf

[9] A. B. Balantekin, N. Takigawa, *Quantum tunneling in nuclear fusion*, Rev. Mod. Phys. 70 (1998) 77-100. doi: 10.1103/RevModPhys.70.77

[10] H. S. Bosch and G. M. Hale, *Improved formulas for fusion cross-sections and thermal reactivities*, Nuclear Fusion 32 (1992) 611-631. doi: 10.1088/0029-5515/32/4/I07

[11] G. H. Miley, H. Towner and N. Ivich, *Fusion cross sections and reactivities*, Report COO-2218-17, University of Illinois, 1974.

[12] M. Kikuchi, K. Lackner, M. Quang Tran, *Fusion Physics*, International Atomic Energy Agency, 2012. ISBN: 9789201304100.

[13] W. M. Nevins, R. Swain, *The thermonuclear fusion rate coefficient for p-^{11}B reactions*, Nuclear Fusion 40, 4 (2000) 865-872. doi: 10.1088/0029-5515/40/4/310

[14] G. R. Caughlan, W. A. Fowler, *Thermonuclear reaction rates V**, Atomic Data and Nuclear Data Tables 40 (1988) 283-334, 1988. doi: 10.1016/0092-640X(88)90009-5

[15] I. Friedman, *Deuterium content of natural waters and other substances*, Geochimica et Cosmochimica Acta 4, 1-2 (1953) 89-103. doi: 10.1016/0016-7037(53)90066-0

[16] W. F. Libby, *Atmospheric helium three and radiocarbon from cosmic radiation*, Phys. Rev. 69 (1946) 671-672. doi: 10.1103/PhysRev.69.671.2

[17] R. J. Pearson, A. B. Antoniazzi, W. J. Nuttall, *Tritium supply and use: a key issue for the development of nuclear fusion energy*, Fusion Engineering and Design 136 (2018) 1140-1148, 2018. doi: 10.1016/j.fusengdes.2018.04.090

[18] M. Movari, M. Coleman, I. Cristescu, R. Smith, *Tritium resources available for fusion reactors*, Nuclear Fusion 58 (2018) 026010. doi: 10.1088/1741-4326/aa9d25

[19] G. Federici, L. Boccacini, F. Cismondi, M. Gasparotto, Y. Poitevin, I. Ricapito., *An overview of the EU breeding blanket design strategy as an integral part of the DEMO design effort*, Fusion Engineering and Design 141 (2019) 30-42. doi: 10.1016/j.fusengdes.2019.01.141

[20] J. H. You et al., *Divertor of the European DEMO: Engineering and technologies for power exhaust*, Fusion Engineering and Design 175 (2022) 113010. doi: 10.1016/j.fusengdes.2022.113010

[21] T. Puetterich et al., *Determination of the tolerable impurity concentrations in a fusion reactor using a consistent set of cooling factors*, Nuclear Fusion 59 (2019) 056013. doi: 10.1088/1741-4326/ab0384

[22] B. Ploeckl et al., *Matter injection in EU-DEMO: The preconceptual design*, Fusion Science and Technology 77:4 (2021) 266-278. doi: 10.1080/15361055.2021.1903784

[23] C. Day et al., *The pre-concept design of the DEMO tritium, matter injection and vacuum systems*, Fusion Engineering and Design 179 (2022) 113139. doi: 10.1016/j.fusengdes.2022.113139

[24] T. Giegerich, C. Day, *The KALPUREX-process – A new vacuum pumping process for exhaust gases in fusion power plants*, Fusion Engineering and Design 89 (2014) 1476-1481. doi: 10.1016/j.fusengdes.2014.03.082

[25] B. J. Peters, S. Hanke, C. Day, *Metal foil pump performance aspects in view of the implementation of direct internal recycling for future fusion fuel cycles*, Fusion Engineering and Design 136 B (2018) 1467-1471. doi: 10.1016/j.fusengdes.2018.05.036

[26] C. Day, T. Giegerich, *The Direct Internal Recycling concept to simplify the fuel cycle of a fusion power plant*, Fusion Engineering and Design 88 (2013) 616-620. doi: 10.1016/j.fusengdes.2013.05.026

[27] M. Rubel, *Fusion Neutrons: Tritium breeding and impact on wall materials and components of diagnostic systems*, Journal of Fusion Energy 38 (2019) 315-329. doi: 10.1007/s10894-018-0182-1

[28] T. Tanabe, *Tritium: Fuel of fusion reactors*, Springer Japan, Fukuoka, Japan, 2017. ISBN 978-4-431-56458-4. doi: 10.1007/978-4-431-56460-7.

[29] M. Abdou et al., *Physics and technology considerations for the deuterium-tritium fuel cycle and conditions for tritium fuel sufficiency*, Nuclear Fusion 61 (2021) 013001. doi: 10.1088/1741-4326/abbf35

[30] J. Igitkhanov, T. Giegerich, C. Day, *Burn-up fraction in DEMO operation with the Direct Internal Recycling*, Poster contribution to IAEA Fusion Energy Conference, Poster-ID 2260, London, UK, 20th of October 2023.

[31] B. J. Peters, *Development of a hydrogen-selective vacuum pump on the basis of superpermeation*, PhD-Thesis, Karlsruher Institute für Technology, Fakultät für Maschinenbau, Karlsruhe, 2020. doi: 10.5445/IR/1000122305

[32] T. Giegerich et al., *Preliminary configuration of the torus vacuum pumping system installed in the DEMO lower port*, Fusion Engineering and Design 146 B (2019) 2180-2183. doi: 10.1016/j.fusengdes.2019.03.147

[33] T. Härtl, C. Day, T. Giegerich, S. Hanke, V. Hauer, Y. Kathage, J. Lilburne, W. Morris, S. Tosti., *Design and feasibility ofa pumping concept based on tritium direct recycling*, Fusion Engineering and Design 174 (2021) 112969. doi: 10.1016/j.fusengdes.2021.112969

[34] M. Bacal, F. E. Balghiti-Sube, A. I. Livshits, M. E. Notkin, D. Riz, M. N. Soloviev, T. Kuroda, M. Y. Tanaka, *Plasma driven superpermeation and its possible applications to ion sources and neutral beam injectors*, Review of Scientific Instruments 69 (1998) 935-937. doi: 10.1063/1.1148596

[35] A. I. Livshits, M. E. Notkin, M. Bacal, *Plasma driven superpermeation of hydrogen through group Va metals*, Journal of Applied Physics 84 (1998) 2558-2564. doi: 10.1063/1.368418

[36] A. I. Livshits, V. N. Alimov, M. E. Notkin, M. Bacal, *Hydrogen superpermeation resistant to ion sputtering*, Applied Physics A 80 (2005) 1661-1669. doi: 10.1007/s00339-004-2595-0

[37] M. Scannapiego, C. Day, *Experimental investigation on charcoal adsorption for cryogenic pump application*, IOP Conference Series: Materials Science and Engineering 278 (2017) 012160. doi: 10.1088/1757-899X/278/1/012160

[38] A. I. Livshits, A. Samartsev, M. E. Notkin, *Physico-chemical origin of superpermeability – Large-scale effects of surface chemistry on "hot" hydrogen permeation and absorption in metals*, Journal of Nuclear Materials 170 (1990) 79-94. doi: 10.1016/0022-3115(90)90329-L

[39] A. I. Livshits, M. E. Notkin, A. A. Samartsev, I. P. Grigoriadi, *Large-scale effects of H_2O and O_2 on the absorption and permeation in Nb of energetic hydrogen particles*, Journal of Nuclear Materials 178 (1991) 1-18. doi: 10.1016/0022-3115(91)90450-L

[40] Y. Hatano, K. Watanabe, A. I. Livshits, A. Busnyuk, V. Alimov, Y. Nakamura, K. Hashizume, *Effects of bulk impurity concentration on the reactivity of metal*

surface: Sticking of hydrogen molecules and atoms to polycrystalline Nb containing oxygen, The Journal of Chemical Physics 127 (2007) 204707. doi: 10.1063/1.2804874

[41] A. I. Livshits, M. E. Notkin, M. Bacal, *Anomalous isotope effect in the permeation, retention and reemission at interaction of energetic hydrogen with niobium*, Journal of Applied Physics 91 (2002) 4105-4109. doi: 10.1063/1.1455156

[42] A. I. Livshits, A. Samartsev, *Interaction of a deuterium atomic beam with a palladium membrane*, Sov. Phys. Tech. Phys. Lett. 21 (1976) 848-854.

[43] A. I. Livshits, *Superpermeability of solid membranes and gas evacuation*, Vacuum 29, 3 (1979) 103-112. doi: 10.1016/S0042-207X(79)80450-9

[44] J. Park, T. Bennett, J. Schwarzmann, S. A. Cohen, *Permeation of hydrogen through palladium*, Journal of Nuclear Materials 220 – 222 (1995) 827-831. doi: 10.1016/0022-3115(94)00591-5

[45] T. Tanabe, N. Saito, Y. Etoh, S. Imoto, *Permeation and reemission of deuterium implanted in first wall materials*, Journal of Nuclear Materials 103 (1981) 483-488. doi: 10.1016/0022-3115(82)90644-4

[46] A. I. Livshits, *Superpermeability in the atomic hydrogen-nickel system*, Sov. Tech. Phys. Lett. 3 (1977) 236 – 237.

[47] F. Waelbrock, I. Ali-Khan, K. J. Dietz, P. Wienhold, *Hydrogen solubilisation into and permeation through wall materials*, Journal of Nuclear Materials 85 -86 (1979) 345-349. doi: 10.1016/0022-3115(79)90514-2

[48] A. I. Livshits, *Superpermeability of atomic hydrogen in Armco iron*, Sov. Tech. Phys. Lett. 4 (1978) 848 – 854.

[49] Y. Nakamura, A. Busnyuk, H. Suzuki, Y. Nakahara, N. Ohyabu, A. I. Livshits, *Nb interaction with hydrogen plasma*, Journal of Applied Physics 89 (2001), 760-766. doi: 10.1063/1.1331075

[50] Y. Hatano, A. I. Livshits, Y. Nakamura, A. Busnyuk, V. Alimov, C. Hiromi, N. Ohyabu, K. Watanabe, *Influence of oxygen and carbon on performance of superpermeable membrane*, Fusion Engineering and Design 81 (2006) 771-776. doi: 10.1016/j.fusengdes.2005.06.368

[51] T. Otsuka, M. Ihara, H. Komiyama, *Hydrogen dissociation on hot tantalum and tungsten filaments under diamond deposition conditions*, Journal of Applied Physics 77 (1995) 893-898. doi: 10.1063/1.359015

[52] A. I. Livshits, M. E. Notkin, A. A. Samartsev, A. O. Busnyuk, A. Y. Doroshin, V. I. Pistunovich, *Superpermeability to fast and thermal hydrogen particles: Applications to the pumping and recycling of hydrogen isotopes*, Journal of Nuclear Materials 196-198 (1992) 159-163. Doi: 10.1016/S0022-3115(06)80023-1

[53] R. K. Musyaev, B. S. Lebedev, S. K. Grishechkin, A. A. Yukhimchuk, A. A. Busnyuk, M. E. Notkin, A. A. Samartsev, A. I. Livshits, *Tritium*

superpermeability: Experimental investigation and simulation of tritium recirculation in "Prometheus" Setup, Fusion Science and Technology 48, 1 (2005) 35-38, 2005. doi: 10.13182/FST05-A874

[54] A. I. Livshits, M. E. Notkin, V. I. Pistunovich, M. Bacal, A. O. Busnyuk, Superpermeability: *Critical points for applications in fusion*, Journal of Nuclear Materials 220-222 (1995) 259-263. doi: 10.1016/0022-3115(94)00424-2

[55] W. M. Shu, Y. Hayashi, K. Okuno, *Surface recombination of hydrogen in plasma-driven permeation*, Journal of Nuclear Materials 220-222 (1995) 497 – 500. doi: 10.1016/0022-3115(94)00511-7

[56] D. I. Cherkez, A. V. Spitsyn, A. V. Golubeva, V. M. Chernov, *Deuterium permeation through the low-activated V-4Cr-4Ti alloy under plasma irradiation*, Nuclear Materials and Energy 23 (2020) 100756. doi: 10.1016/j.nme.2020.100756

[57] A. A. Skovoroda, V. S. Svishchov, A. V. Spitsyn, V. L. Stolyarov, Y. M. Pustovoit, V. D. Borman, V. S. Kulikauskas, A. M. Shipilin, *Plasma-driven superpermeation of hydrogen through Nb membranes: bulk effects*, Journal of Nuclear Materials 306, 2-3 (2002) 232-240. doi: 10.1016/S0022-3115(02)01324-7

[58] R. A. Kerst, W. A. Swansiger, *Plasma driven permeation of tritium in fusion reactors*, Journal of Nuclear Materials 122-123 (1984) 1499-1510. doi: 10.1016/0022-3115(84)90292-7

[59] H. Wichmann, W. Weizel, *Report Der Einfluß einer Glimmentladung auf die Permeation von Gasen durch Metalle*, Forschungsberichte des Landes Nordrhein-Westfalen Nr. 1038 (in German), Westdeutscher Verlag, 1961. doi: 10.1007/978-3-322-98647-4

[60] F. Waelbrock, K. J. Dietz, P. Wienhold, J. Winter, I. Ali-Khan, H. Merkens, E. Rota, *Investigation of adsorption and absorption processes of hydrogen in plasma devices with SS or Ti-coated walls*, Journal of Nuclear Materials 93-94 (1980) 839-846. doi: 10.1016/0022-3115(80)90216-0

[61] K. L. Zheludkevich, A. G. Gusakov, A. G. Voropaev, E. N. Kozyrski, S. A. Raspopov, A. A. Vecher, *"Superpermeability" and "pumping" of atomic hydrogen through palladium membranes*, Journal of Membrane Science 320 (2008) 528-532. doi: 10.1016/j.memsci.2008.04.045

[62] I. Ali-Khan, K. J. Dietz, F. G. Waelbroeck, P. Wienhold, *The rate of hydrogen release out of clean metallic surfaces*, Journal of Nuclear Materials 76-77 (1978) 337-343. doi: 10.1016/0022-3115(78)90167-8

[63] A. Vazquez Cortes, C. Day, C. Stihl, P. Vladimirov, *Ab-initio simulations of atomic hydrogen interaction with Nb and V at clean and oxygen covered surfaces*, Nuclear Materials and Energy 38 (2024) 101600. doi: 10.1016/j.nme.2024.101600

[64] V. N. Alimov, Y. Hatano, A. O. Busnyuk, D. A. Livshits, M. E. Notkin, A. I. Livshits, *Hydrogen permeation through the Pd-Nb-Pd composite membrane: Surface effects and thermal degradation*, International Journal of Hydrogen Energy 36 (2011) 7737-7746. doi: 10.1016/j.ijhydenee.2011.04.016

[65] T. Fuerst et al., *Membrane material development for fuel cycle applications*, Poster contribution to the 32nd Symposium on Fusion Technology, Poster-ID P-2197, 18th of September 2022, Dubrovnik, Croatia.

[66] I. Langmuir, *Oscillations in ionized gases*, Proceedings of the National Academy of sciences of the United States of America 14, 8 (1928) 627-637. doi: 10.1073/pnas.14.8.627

[67] D. A. Frank-Kamenetskii, *Plasma – The Fourth State of Matter*, Springer US, New York, USA, 1972. ISBN: 9781468418965

[68] M. A. Lieberman, A. J. Lichtenberg, *Principles of Plasma Discharges and Materials Processing*, John Wiley & Sons, Hoboken, USA, 2005. Doi: 10.1002/0471724254

[69] M. Kaufmann, *Plasmaphysik und Fusionsforschung*, Springer Spektrum, Wiesbaden, Germany, 2013. doi: 10.1007/978-3-658-03239-5

[70] F. Sharipov, *Rarefied Gas Dynamics*, Fundamentals for Research and Practice, Wiley-VCH, Weinheim, Germany, 2016. ISBN: 978-3-527-41326-3

[71] K. Jousten, *Handbook of Vacuum Technology*, Wiley-VCH, Wiesbaden, Germany, 2016. doi: 10.1002/9783527688265

[72] R. Hippler, M. Schmidt, K. H. Schoenbach, S. Pfau, *Low Temperature Plasma Physics: Fundamental Aspects and Applications*, Wiley-VCH, Germany, 2001. ISBN: 3-527-28887-2

[73] T. Fujimoto, M. Usami, *Rarefied gas flow through a circular orifice and short tubes*, Journal of Fluids Engineering 106 (1984) 367-373. doi: 10.1115/1.3243132

[74] F. Sharipov, K. Jousten, *Analytical and numerical calculations of rarefied gas flows*, Handbook of vacuum technology 2nd edition, Wiley-VCH, Wiesbaden, Germany, 2016. doi: 10.1002/9783527688265.ch5

[75] H. Struchtrup, *Macroscopic Transport Equations for Rarefied Gas Flows*, Springer Berlin, Berlin, Germany, 2005. doi: 10.1007/3-540-32386-4

[76] M. Moisan, J. Pelletier, *Microwave excited plasmas*, Elsevier Science Publishers, Amsterdam, Netherlands, 1992. doi: 10.1002/ctpp.2150340111

[77] COMSOL, *COMSOL Plasma Module User's Guide*, https://doc.comsol.com/5.4/doc/com.comsol.help.plasma/PlasmaModuleUsersGuide.pdf (Accessed on 30th of May 2023).

[78] M. Abramowitz, I. A. Stegun, *Handbook of Mathematical Functions with Formulas, Graphs, and Mathematical Tables*, National Bureau of Standards Applied Mathematics Series 55 (1964). ISBN: 0-486-61272-4

[79] G. J. M. Hagelaar, L. C. Pitchford, Solving the Boltzmann equation to obtain electron transport coefficients and rate coefficients for fluid models, Plasma Sources Sci. Technol. 14 (2005) 722-733. Doi: 10.1088/0963-0252/14/4/011

[80] I. Langmuir, *The effect of space charge and initial velocities on the potential distribution and thermionic current between parallel plane electrodes*, Phys. Rev. 21 (1923) 419-435. doi: 10.1103/PhysRev.21.419

[81] R. Gueroult, G. Fubiani, L. Garrigues, *Pitfalls in modelling walls and neutrals physics in gas discharges using parallel partice-in-cell Monte Carlo collision algorithms*, Frontiers in Physics 6:128 (2018) 1-12. doi: 10.3389/fphy.2018.00128

[82] M. Radmilovic-Radjenovic, J. K. Lee, *Modeling of breakdown behaviour in radio-frequency argon discharges with improved secondary emission model*, Physics of Plasmas 12 (2005) 063501. doi: 10.1063/1.1922267

[83] J. J. Scholtz, D. Dijkamp, R. W. A. Schmitz, *Secondary electron emission properties*, Philips J. Res. 50 (1996) 375-389. Doi: 10.1016/S0165-5817(97)84681-5

[84] J. R. M. Vaughan, *A new formula for secondary emission yield*, IEEE Transactions on Electron Devices 36, 9 (1989) 1963-1967. doi: 10.1109/16.34278

[85] G. Lakits, H. Winter, *Electron emission from metal surfaces bombarded by slow neutral and ionized particles*, Nuclear Instruments and Methods in Physics Research 48 (1990) 597603. doi: 10.1016/0168-583X(90)90191-V

[86] M. Mozetic, M. Drobnic, A. Zalar, *Recombination of neutral hydrogen atoms on AISI 304 stainless steel surface*, Applied Surface Science 144-145 (1999) 399-403. doi: 10.1016/S0169-4332(98)00830-7

[87] P. Kae-Nune, J. Perrin, J. Jolly, J. Guillon, *Surface recombination probabilities of H on stainless steel, a-Si:H and oxidized silicon determined by threshold ionization mass spectrometry in H_2 RF discharges*, Surface Science 360 (1996) 1495-1498. doi: 10.1016/0039-6028(96)00732-7

[88] I. Mendez, F. J. Gordillo-Vazquez, V. J. Herrero, I. Tanarro, *Atom and ion chemistry in low pressure hydrogen DC plasmas*, J. Phys. Chem. A 110 (2006) 6060-6066. doi: 10.1021/jp057182+

[89] A. Rousseau, G. Cartry, X. Duten, *Surface recombination of hydrogen atoms studied by a pulsed plasma excitation technique*, Journal of Applied Physics 89 (2001) 2074-2078. doi: 10.1063/1.13250000

[90] Y. A. Lebedev, *Microwave discharges at low pressures and peculiarities of the processes in strongly non-uniform plasma*, Plasma Sources Sci. Technol. 24 (2015) 053001. doi: 10.1088/0963-0252/24/5/053001

[91] F.C. Fehsenfeld, K. M. Evenson, H. P. Broida, *Microwave discharge cavities operating at 2450 MHz*, Review of Scientific Instruments 36, 3 (1965) 294-298. doi: 10.1063/1.1719557

[92] D. Korzec, F. Werner, R. Winter, J. Engemann, *Scaling of microwave slot antenna (SLAN): a concept for efficient plasma generation*, Plasma Sources Sci. Technol. 5 (1996) 216-234. doi: 10.1088/0963-0252/5/015

[93] A. Ohl, *Fundamental and limitations of large area planar microwave discharges using slotted waveguides*, J. Phys. IV France 8, Pr7 (1998) 83-98. doi: 10.1051/jp4:1998707

[94] Y. A. Lebedev, I. L. Epstein, A. V. Tatarinov, V. A. Shakhatov, *Electrode microwave discharge and plasma self-organization*, J. Phys.: Conf. Ser. 44 (2006) 30-39. doi: 10.1088/1742-6596/44/1/004

[95] M. Nagatsu, K. Naito, A. Ogino, K. Ninomiya, *Characteristics of surface-wave and volume-wave plasmas produced with internally mounted large-area planar microwave launcher*, Applied Physics Letters 87 (2005) 161501. doi: 10.1063/1.2108119

[96] M. Moisan, Z. Zakrzewski, *Plasma sources based on the propagation of electromagnetic surface waves*, J. Phys. D: Appl. Phys 24 (1991) 1025-1048. doi: 10.1088/0022-3727/24/7/001

[97] L. St-Onge, M. Moisan, *Hydrogen atom yield in RF and microwave hydrogen discharges*, Plasma chemistry and plasma processing 14 (1994) 87-116, 1994. doi: 10.1007/BF01465741

[98] W. Petasch, E. Räuchle, H. Muegge, K. Muegge, *Duo-Plasmaline – a linearly extended homogeneous low pressure plasma source*, Surface and Coatings Technology 93 (1997) 112-118. Doi: 10.1016/S0257-8972(97)00015-7

[99] E. Räuchle, *Duo-Plasmaline, a surface wave sustained linearly extended discharge*, J. Phys. IV France 8, Pr7 (1998) 99-108. doi: 10.1051/jp4:1998708

[100] G. J. M. Hagelaar, K. Makasheva, L. Garrigues, J. P. Boeuf, *Modelling of a dipolar microwave plasma sustained by electron cyclotron resonance*, J. Phys. D: Appl. Phys 42 (2009) 194019. doi: 10.1088/0022-3727/42/19/194019

[101] L. Conde, *An Introduction to Plasma Physics and its Space Applications*, Volume 2, 4-10, IOP Publishing, 2020. doi: 10.1088/978-0-7503-3543-0

[102] J. Asmussen, *Electron cyclotron resonance microwave discharges for etching and thin-film deposition*, J. Vac. Sci. Technol. A 7 (1989) 883-893. doi: 10.1116/1.575815

[103] J. D. Callen, *Fundamentals of Plasma Physics*, University of Wisconsin, Madison, 2006. https://de.scribd.com/document/85976601/Fundamentals-of-Plasma-Physics-2006 (Accessed on 26th of October 2023)

[104] F. F. Chen, *Introduction to plasma physics and controlled fusion*, Springer Cham, Switzerland, 2015. doi: 10.1007/978-3-319-22309-4

[105] S. Hanke, C. Day, T. Giegerich, J. Igithkanov, Y. Kathage, X. Luo, S. Varoutis, A. Vazquez Cortes, *Progress of the R&D programme to develop a metal foil pump for DEMO*, Fusion Engineering and Design 161 (2020) 111890. doi: 10.1016/j.fusengdes.111890

[106] A. Cotter, A. Stowell, J. Carlson, J. R. Doyle, *Mass spectrometric method for estimating dissociation rates in hydrogen discharge plasmas*, J. Vac. Sci. Technol. A 36 (2018) 031304. doi: 10.1116/1.5020723

[107] S. Takashima, M. Hori, T. Goto, *Absolute concentration and loss kinetics of hydrogen atom in methane and hydrogen plasmas*, Journal of Applied Physics 90 (2001) 5497-5503. doi: 10.1063/1.1410327

[108] K. H. Chen, M. C. Chuang, C. Murray Penney, *Temperature and concentration distribution of H_2 and H atoms in hot-filament chemical-vapor deposition of diamond*, Journal of Applied Physics 71 (1992) 1485-1493, 1992. doi: 10.1063/1.351242

[109] F. G. Celii, J. E. Butler, *Hydrogen atom detection in the filament-assisted diamond deposition environment*, Appl. Phys. Lett. 54 (1998) 1031-1033. doi: 10.1063/1.100789

[110] J. Amorim, G. Baravian, J. Jolly, *Laser-induced resonance fluorescence as a diagnostic technique in non-thermal equilibrium plasmas*, Journal of Physics D: Applied Physics 33 (2000) R51-R65, 2000. doi: 10.1088/0022-3727/33/9/201

[111] A. Gicquel, M. Chenevier, K. Hassouni, A. Tserepi, M. Dubus, *Validation of actinometry for estimating relative hydrogen atom densities and electron energy evolution in plasma assisted diamong deposition reactors*, Journal of Applied Physics 83 (1998) 7504-7521. doi: 10.1063/1.367514

[112] P. N. Ekemezie, E. E. Enekwechi, S. C. Odinma, *Measurement of the viscosities of He, Ne and Ar for the determination of their gas-kinetic diameters*, American Journal of Engineering Research 4, 11 (2005) 57-62. E-ISSN: 2320-0847

[113] I. Cooley, L. Efford, E. Besley, *Computational predictions for effective separation of Xenon/Krypton gas mixtures in the MFM family of metal-organic frameworks*, J. Phys. Chem. C 126 (2022) 11475-11486. Doi: 10.1021/acs.jpcc.2c02237

[114] Y. Hatano, A. Busnyuk, A. I. Livshits, Y. Nakamura, M. Matsuyama, *Absorption of atomic hydrogen by vanadium*, Fusion Science and Technology 52 (2007) 613-617. doi: 10.13182/FST07-A1556

[115] C. Day et al., *A smart three-loop fuel cycle architecture for DEMO*, Fusion Engineering and Design 146 (2019) 2462-2468. doi: 10.1016/j.fusengdes.2019.04.019

[116] Y. Kathage, A. Vazquez Cortes, S. Merli, C. Day, T. Giegerich, S. Hanke, J. Igitkhanov, A. Schulz, M. Walker, *Experimental progress in the development of a Metal Foil Pump for DEMO*, Plasma 6, 4 (2023) 714-743. doi: 10.3390/plasma6040049

[117] E. Gogolides, H. H. Sawin, *Continuum modelling of radio-frequency glow discharges. Theory and results for electropositive and electronegative gases*, J. Appl. Phys. 72 (1992) 3971-3987. doi: 10.1063/1.352250

[118] D. Bothe, *On the Maxwell-Stefan Approach to Multicomponent Diffusion* in *Parabolic Problems*, Progress in Nonlinear Differential Equations and Their Applications 80, Springer Basel AG, 2011. doi: 10.1007/978-3-0348-0075-4

[119] C. M. Samuell, C. S. Corr, *Atomic and molecular hydrogen gas temperatures in a low-pressure helicon plasma*, Plasma Sources Sci. Technol. 24 (2015) 045003. doi: 10.1088/0963-0252/24/4/045003

[120] C. H. Chen, T. C. Wei, L. R. Collins, J. Phillips, *Modelling the discharge region of a microwave generated hydrogen plasma*, J. Phys. D: Appl. Phys. 32 (1999) 688-698, 1999. doi: 10.1088/0022-3727/32/6/015.

[121] S. F. Biagi, Plasma Data Exchange Project, *Fortran program, MAGBOLTZ v 8.97*, CERN, 2012. www.lxcat.net/Biagi (Accessed on 30th of May 2022)

[122] L. L. Alves, *The IST-Lisbon database on LXCat*, J. Phys. Conf. Series 565 (2014) 012007. Doi: 10.1088/1742-6596/565/1/012007

[123] R. K. Janev, D. Reiter, U. Samm, *Collision processes in low-temperature hydrogen plasmas*, Berichte des Forschungszentrums Jülich 4105, Institut für Plasmaphysik, 2003.

[124] L. H. Scarlett, J. K. Tapley, D. V. Fursa, M. C. Zammit, J. S. Savage, I. Bray, *Electron-impact dissociation of molecular hydrogen into neutral fragments*, Eur. Phys. J. D 72 (2018) 34, 1 – 8. doi: 10.1140/epjd/e2017-80649-8

[125] L. H. Scarlett, J. S. Savage, D. V. Fursa, M. C. Zammit, I. Bray, *Electron-impact dissociation of vibrationally-excited molecular hydrogen into neutral fragments*, Atoms 2019, 7 (3), 75, 2019. doi: 10.3390/atoms7030075

[126] I. Bray, A. T. Stelbovics, *Convergent close-coupling calculations of electron-hydrogen scattering*, Phys. Rev. A 46 (1992) 6995-7011. doi: 10.1103/PhysRevA.46.6995

[127] D. V. Fursa, I. Bray, *Calculation of electron-helium scattering*, Phys. Rev. A 52 (1995) 1279-1297. doi: 10.1103/PhysRevA.52.1279

[128] M. C. Zammit, D. V. Fursa, I. Bray, *Electron scattering from the molecular hydrogen ion and its isotopologues*, Phys. Rev. A 90 (2014) 022711. doi: 10.1103/PhysRevA.90.022711

[129] M. C. Zammit, J. S. Savage, D. V. Fursa, I. Bray, *Complete solution of electronic excitation and ionization in electron-hydrogen molecule scattering*, Phys. Rev. Lett. 116 (2016) 233201. doi: 10.1103/PhysRevLett.116.233201

[130] B. J. Wood, H. Wise, *The kinetics of hydrogen atom recombination on pyrex glass and fused quartz*, J. Phys. Chem. 66, 6 (1962) 1049-1053. doi: 10.1021/j100812a019

[131] Plasma Data Exchange Project, Morgan database, Kinema Research & Software, 236 Washingston St., St. Monument, CO 80132, USA www.lxcat.net/Morgan (Accessed on 30th of May 2022).

[132] K. Hassouni, T. A. Grotjohn, A. Gicquel, Self-consistent microwave field and plasma discharge simulations for a moderate pressure hydrogen discharge reactor, Journal of Applied Physics 86 (1999) 134-151. doi: 10.1063/1.370710

[133] C. D. Scott, Determining electron temperature and density in a hydrogen microwave plasma, Journal of Thermophysics and Heat Transfer 10, 3 (1996) 426-435. doi: 10.2514/3.807

[134] J. Geddes, R. W. McCullough, A. Donnelly, H. B. Gilbody, *Dissociation of hydrogen in high-frequency discharges*, Plasma Sources Science and Technology 2 (1993) 93-99. doi: 10.1088/0963-0252/2/2/004

[135] J. W. L. Lewis, W. D. Williams, *Collisional deactivation of atomic and molecular hydrogen*, J. Quant. Spectrosc. Radial. Transfer 16 (1976) 939-946. doi: 10.1016/0022-4073(76)90108-4.

[136] C. A. Slocomb, W. H. Miller, H. F. Schaefer, *Collisional quenching of metastable hydrogen atoms*, J. Chem. Phys. 55 (1971) 926-932. Doi: 10.1063/1.1676163

[137] W. L. Wiese, M. W. Smith, B. M. Glennon, *Atomic transition probabilities Volume 1 hydrogen through neon*, National Standard Reference Data Series National Bureau of Standards 4, Category 3 – Atomic and Molecular Properties, 1966.

[138] I. A. Sellin, *Experiments on the production and exctinction of the 2s state of the hydrogen atom*, Physical Review 136, 5A (1964) A1245-A1253. doi: 10.1103/PhysRev.136.A1245

[139] A. M. Karo, J. R. Hiskes, R. J. Hardy, *Vibrational relaxation in H_2 molecules by wall collisions: Applications to negative ion source processes*, Journal of Vacuum Science & Technology A 3 (1985) 1222-1228. doi: 10.1116/1.573068

[140] U. Fantz, D. Wünderlich, *Franck-Condon factors, transition probabilities and radiative lifetimes for hydrogen molecules and their isotopomeres*, Atomic Data and Nuclear Data Tables 92 (2006) 853-973. doi: 10.1016/j.adt.2006.05.001

[141] J. S. Yoon, M. Y. Song, J. M. Han, S. H. Hwang, W. S. Chang, B. Lee, *Cross sections for electron collisions with hydrogen molecules*, Journal of Physical and Chemical Reference Data 37, 2 (2008) 913-931. doi: 10.1063/1.2838023

[142] B. J. Wood, H. Wise, *Kinetics of hydrogen atom recombination on surfaces*, J. Phys. Chem. 11 (1961) 1976-1983. doi: 10.1021/j100828a015

[143] V. Baglin, Y. Bozhko, O. Grobner, B. Henrist, N. Hilleret, C. Scheuerlein, M. Taborelli, *The secondary electron yield of technical materials and its variation with surface treatments*, Contribution to 7th European Particle Accelerator Conference EPAC 2000, 217-221, 2000.

[144] L. R. G. Treloar, D. H. Landon, *Secondary-electron emission from nickel, cobalt and iron as a function of temperature*, Proc. Phys. Soc. 50, 5 (1938) 625-634. doi: 10.1088/0959-5309/50/5/301

[145] H. Y. Chang, A. Alvarado, J. Marian, *Calculation of secondary electron emission yields from low-energy electron deposition in tungsten surfaces*, Applied Surface Science 450 (2018) 190-199. doi: 10.1016/j.apsusc.2018.04.155

[146] Y. Kathage, S. Hanke, T. Giegerich, C. Day, *Atomic hydrogen production in a cold plasma for application in a metal foil pump*, Physics of Plasmas 31 (2024) 043503. doi: 10.1063/5.0190210

[147] A. S. Berman, Free molecule transmission probabilities, Journal of Applied Physics 36 (1965) 3356-3358. doi: 10.1063/1.1702984

[148] JCGM, JCGM 100:2008, *Evaluation of measurement data – Guide to the expression of uncertainty in measurement*, Joint Committee for Guides in Metrology, 2008. https://www.bipm.org/documents/20126/2071204/JCGM_100_2008_E.pdf/cb0ef43f-baa5-11cf-3f85-4dcd86f77bd6 (Accessed 20th of February 2023)

[149] K. Bockasten, *Transformation of observed radiances into radial distribution of the emission of a plasma*, Journal of the Optical Society of America 51, 9 (1961) 943-947. doi: 10.1364/JOSA.51.000943

[150] J. W. Coburn, M. Chen, *Optical emission spectroscopy of reactive plasmas: A method for correlating emission intensities to reactive particle density*, Journal of Applied Physics 51 (1980) 3134-3136. doi: 10.1063/1.328060

[151] A. Rousseau, A. Granier, G. Gousset, P. Leprince, *Microwave discharge in H_2: influence of H-atom density on the power balance*, J. Phys. D: Appl. Phys 27 (1994) 1412-1422. doi: 10.1088/0022-3727/27/7/012

[152] J. Bittner, K. Kohse-Höinghaus, U. Meier, T. Just, *Quenching of two-photon-excited H and O atoms by rare gases and small molecules*, Chemical Physics Letters 143, 6 (1988) 571-576. doi: 10.1016/0009-2614(88)87068-4

[153] A. Francis, U. Czarnetzki, H. F. Döbele, N. Sadeghi, *Quenching of the 750.4 nm argon actinometry line by H_2 and several hydrocarbon molecules*, Appl. Phys. Lett. 71 (1997) 37963798. doi: 10.1063/120555

[154] W. L. Wiese, J. W. Brault, K. Danzmann, V. Helbig, M. Kock, *Unified set of atomic transition probabilities for neutral argon*, Physical Review A 39, 5 (1989) 2461-2471. doi: 10.1103/PhysRevA.39.2461

[155] N. Sadeghi, D. W. Setser, A. Francis, U. Czarnetzki, H. F. Döbele, *Quenching rate constants for reactions of Ar atoms with 22 reagent gases*, J. Chem. Phys. 115 (2001) 3144-3154. doi: 10.1063/1.1388037

[156] O. Zatsarinny, K. Bartschat, *The B-spline R-matrix method for atomic processes: application to atomic structure, electron collisions and photoionization*, J. Phys. B: At. Mol. Opt. Phys. 46 (2013) 112001. Doi: 10.1088/0953-4075/46/11/112001

[157] A. Yanguas-Gil, J. Cotrino, L. L. Alves, *An update of argon inelastic cross sections for plasma discharges*, J. Phys. D: Appl. Phys 38 (2005) 1588-1598. doi: 10.1088/0022-3727/38/10/014

[158] A. P. Napartovich, N. A. Dyatko, I. V. Kochetov, A. G. Sukharev, *EEDF software package for calculations of electron energy distribution function*, The State Science Center Troitsk Institute for Innovation and Fusion Research, Russia, www.lxcat.net/TRINITI (Accessed on 30th of May 2022).

[159] O. Zatsarinny, Y. Wang, K. Bartschat, *Electron-impact excitation of argon at intermediate energies*, Physical Review A 89 (2014) 022706. doi: 10.1103/PhysRevA.89.022706

[160] O. Zatsarinny, *BSR: B-spline atomic R-matrix codes*, Comp. Phys. Commun. 174, 4 (2006) 273-356, doi: 10.1016/j.cpc.2005.10.006

[161] G. M. Grigorian, N. A. Dyatko, I. V. Kochetov, *Determination of the coefficient of reflection of metastable argon atoms from the discharge tube wall*, Plasma Physics Reports 41 (2015) 434-440. doi: 10.1134/S1063780X15050049

[162] A. Obrusnik, Z. Bonaventura, *Studying a low-pressure microwave coaxial discharge in hydrogen using a mixed 2D/3D fluid model*, J. Phys. D: Appl. Phys. 48 (2015) 065201. doi: 10.1088/0022-3727/48/6/065201

[163] Z.-C. Geng, Y. Xu, X.-F. Yang, W.-G. Wang, A.M. Zhu, *Atomic hydrogen determination in medium-pressure microwave discharge hydrogen plasmas via emission actinometry*, Plasma Sources Science and Technology 14, 1 (2005) 76-82. doi: 10.1088/0963-0252/14/1/010

[164] A. Bogaerts, R. Gijbels, *Effects of adding hydrogen to an argon glow discharge: overview of relevant processes and some qualitative explanations*, Journal of Analytical Atomic Spectrometry 15 (2000) 441-449. doi: 10.1039/A909779A

[165] N. Sadeghi, D. W. Setser, *Symmetry constraints in energy transfer between state-selected Ar($^3p_2$, $^3p_0$) metastable atoms and ground state H atoms*, Chemical Physics 95 (1985) 305-311. doi: 10.1016/0301-0104(85)80083-5

[166] L. G. Piper, J. E. Velazco, D. W. Setser, *Quenching cross sections for electronic energy transfer reactions between metastable argon atoms and noble gases and small molecules*, J. Chem. Phys. 59 (1973) 3323-3340. doi: 10.1063/1.1680477

[167] N. M. Johnson, J. Walker, C. M. Doland, K. Winer, R. A. Street., *Hydrogen incorporation in silicon thin films deposited with a remote hydrogen plasma*, Appl. Phys. Lett. 54 (1989) 1872-1874. doi: 10.1063/1.101264

[168] M. Yamawaki, K. Yamaguchi, S. Tanaka, *Effect of surface impurities on the hydrogen recombination coefficient of first-wall materials*, Journal of Nuclear Materials 162-164 (1989) 1071-1076. doi: 10.1016/0022-3115(89)90411-X

[169] L. T. Guo, C. Chang, W. H. Huang, Y. S. Liu, Y. B. Cao, C. L. Liu, J. Sun, *Compact high-power microwave divider and combiner*, Review of Scientific Instruments 87 (2016) 024702. doi: 10.1063/1.4941663

[170] J. Yang, H. Raza, *Empirical formulas for designing gap-waveguide hybrid ring coupler*, Microwave and Optical Technology Letters 55, 8 (2012) 1917-1920. doi: 10.1002/mop.27714

[171] X. Luo, C. Day, *3D Monte Carlo vacuum modelling of the neutral beam injection system of ITER*, Fusion Engineering and Design 85 (2010) 1446-1450. doi: 10.1016/j.fusengdes.2010.04.002

[172] T. Teichmann, X. Luo, T. Giegerich, C. Day, *Study of the effective torus exhaust high vacuum pumping system performance in the inner tritium plant loop of EU-DEMO*, Fusion Science & Technology. Doi: 10.1080/15361055.2023.2229679

[173] Y. Kwai, K. Uchino, H. Muta, T. Röwf, *Development of a 915 MHz ECR plasma source*, Vacuum 87 (2013) 123-127. doi: 10.1016/j.vacuum.2012.03.01

Appendix 1: Specific electric conductivity calculation in Drude model

Let J_p be the current density $J_p = e \cdot n_e \cdot v_e$ and the force $\vec{F}$ experienced by an electron in an electric field $\vec{E}$, i.e., $\vec{F} = \vec{E} \cdot e = m_e \cdot a_e$. The specific electric conductivity becomes

$$\sigma = \frac{J_p}{E} = \frac{e^2 n_e v_e}{m_e a_e}. \tag{0.1}$$

The acceleration of an electron a_e within the time interval of a single collision τ_e results in its velocity v_e through $v_e = \tau_e \cdot a_e$. Taking the reciprocal of the collision time, the collision frequency ν_e yields

$$\sigma = \frac{e^2 n_e \tau_e}{m_e} = \frac{e^2 n_e}{m_e \nu_e}. \tag{0.2}$$

The complex electric conductivity σ_p is obtained from the solution of the differential equation for the case with periodically changing electric field

$$m\dot{v}(t) + \frac{m}{\tau} v(t) = -eE(t). \tag{0.3}$$

with $\vec{E}(t) = \bar{E}(\omega) \cdot \exp(-j\omega t)$. Assuming the medium of propagation is isotropic, the velocity reads as

$$v(\omega) = -\frac{e\tau}{m_e} \bar{E}(t) \cdot \frac{1}{1 - j\omega\tau}, \tag{0.4}$$

which allows to express σ_p as

$$\sigma_p = \frac{e^2 n_e \tau_e}{m_e} \cdot \frac{1}{1 - j\omega\tau} = \frac{\sigma_{DC}}{1 - j\omega\tau}. \tag{0.5}$$

Appendix 2: Kinetic energy of charged particle in magnetic field

The position of an electron in terms of x and y coordinates moving through three-dimensional space-time with an initial velocity in y-direction $v_{y,0}$ and in an unidirectional electric field $\vec{E}_y$ = 5000 V/m with a superimposed perpendicular magnetic field of the field strength B_z = 250 mT as described by

$$x(t) = \frac{v_{y,0} - \frac{E_y}{B_z}}{\omega_g} \cdot \sin(\omega t) + \frac{E_y}{B_z} \cdot t, \tag{0.6}$$

$$y(t) = \frac{v_{y,0} - \frac{E_y}{B_z}}{\omega_g} \cdot (1 - \cos(\omega t)). \tag{0.7}$$

The velocities are obtained by forming the derivatives leading to

$$\dot{x}(t) = v_x(t) = \frac{\left(B_z \cdot v_{y,0} - E_y\right)\cos(\omega t)}{B_z}, \tag{0.8}$$

$$\dot{y}(t) = v_y(t) = v_{y,0} - \frac{E_y}{B_z} \cdot \sin(\omega t). \tag{0.9}$$

The kinetic energy is E_{kin} = 0.5 · m_e $(v_x^2 + v_y^2)^{0.5}$. If the kinetic energy and the velocity components are depicted as a function of time as shown in Figure A.1, one can see that the initial total velocity is not exceeded during the entire gyration and no work is performed on the particle.

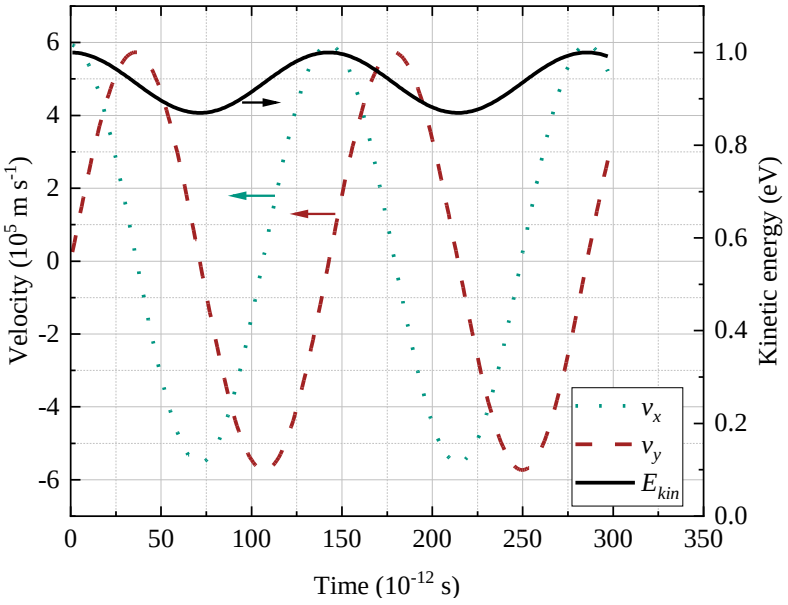

Figure A.1: Velocity and kinetic energy of electron during gyromotion drifting in E × B field.

Appendix 3: Calculation of the Knudsen number (Kn) in a MFP

Here, the *Kn* number for the flow of deuterium and small amounts of noble gases through an exemplary cylindrical MFP with a characteristic diameter of 0.4 m is computed. The gas composition is assumed according to Table A.1. The kinetic diameter of neon is additional supplement in case Ne is added to the plasma-enhancement gases in the future. The temperature of the gas is taken as in equilibrium with the surrounding 900 °C metal foil.

Table A.1: Assumed gas composition of the torus exhaust with respective gas species kinetic diameters.

Gas species	Molar fraction (%)	Kinetic diameter (pm)
Deuterium	92.45	289
Helium	5	190
Argon	2.5	330
Xenon	0.05	396
Neon	0	220

The Kn number is determined via

$$Kn = \frac{\lambda_{mfp}}{l_c} = \frac{k_B T_G}{\sqrt{2}\pi d_{kin}^2 p l_c}, \tag{0.10}$$

$$= \frac{1.38 \cdot 10^{-23}\,\frac{kg \cdot m^2 K}{s^2 \cdot K} \cdot 900\,K}{\sqrt{2}\pi \cdot \left(d_{kin} \cdot \sqrt{1 + \frac{273\,K}{900\,K}}\,m\right)^2 \cdot 1\,\frac{kg \cdot m}{s^2 \cdot m^2} \cdot 0.4\,m},$$

with the average kinetic diameter of the gas molecules

$$d_{kin} = (0.9245 \cdot 289 + 0.05 \cdot 190 + 0.025 \cdot 330 + 0.0005 \cdot 389)\,pm$$
$$= 285\,pm,$$

as

$$Kn = 0.066 \approx 0.1,$$

which is within the transitional flow regime.

Appendix 4: Hydrogen plasma chemistry

Table A.2 shows the plasma chemistry used in the hydrogen plasma simulation, consisting of electron-impact, heavy species and wall reactions. The reaction type specifies whether it is an elastic (El.), ionization (Ion.) or excitation reaction (Exc.), including rotational, vibrational, electronic excitation, dissociation (Diss.), de-excitation (De-exc.), attachment (Att.) or radiative decay reaction. The reverse reactions to some of the listed reactions are obtained through the principle of detailed balance [68]. Table A.3 shows the wall reactions.

Table A.2: Plasma chemistry used in the hydrogen plasma simulation.

Nr.	Reaction	Type	Given as	Reference
5.1	$e + H_2 \rightarrow e + H_2$	El.	Table	[121]
5.2	$e + H \rightarrow e + H$	El.	Table	[122]
5.3	$e + H \rightarrow e + H^+$	Ion.	Table	[123]
5.4	$e + H_2 \rightarrow e + H_2^+$	Ion.	Table	[122]
5.5	$e + H_2 \rightarrow e + 2\ H$	Exc.	Table	[124]
5.6	$e + H_2(v1) \rightarrow e + 2\ H$	Exc.	Table	[125]
5.7	$e + H_2(v2) \rightarrow e + 2\ H$	Exc.	Table	[125]
5.8	$e + H_2(v3) \rightarrow e + 2\ H$	Exc.	Table	[125]
5.9	$e + H \rightarrow e + H(n=3)$	Exc.	Table	[122]
5.10	$e + H(2s) \rightarrow e + H(n=3)$	Exc.	Table	[126-129]
5.11	$e + H(2p) \rightarrow e + H(n=3)$	Exc.	Table	[126-129]
5.12	$H \rightarrow 0.5\ H_2$	Wall	0.1	[86]
5.13	$H \rightarrow 0.5\ H_2$	Wall	0.02	[97] [130]
5.14	$e + H_2 \rightarrow e + H + H(n=3)$	Exc.	Table	[122]
0.1	$e + H_2\ (J = 0) \rightarrow e + H_2\ (J = 2)$	Exc.	Table	[131]
0.2	$e + H_2\ (J = 1) \rightarrow e + H_2\ (J = 3)$	Exc.	Table	[131]
0.3	$e + H_2\ (J = 2) \rightarrow e + H_2\ (J = 0)$	De-ex.	Table	
0.4	$e + H_2\ (J = 3) \rightarrow e + H_2\ (J = 1)$	De-ex.	Table	
0.5	$e + H_2 \rightarrow e + H_2(v1)$	Exc.	Table	[122]
0.6	$e + H_2 \rightarrow e + H_2(v2)$	Exc.	Table	[122]
0.7	$e + H_2 \rightarrow e + H_2(v3)$	Exc.	Table	[122]
0.8	$e + H_2(v1) \rightarrow e + H_2$	De-ex.	Table	
0.9	$e + H_2(v2) \rightarrow e + H_2$	De-ex.	Table	
0.10	$e + H_2(v3) \rightarrow e + H_2$	De-ex.	Table	
0.11	$e + H \rightarrow e + H(2s)$	Exc.	Table	[131]
0.12	$e + H(2s) \rightarrow e + H$	De-ex.	Table	
0.13	$e + H \rightarrow e + H(2p)$	Exc.	Table	[131]
0.14	$e + H \rightarrow e + H(n=3)$	Exc.	Table	[122]
0.15	$e + H \rightarrow e + H(n=4)$	Exc.	Table	[122]
0.16	$e + H \rightarrow e + H(n=5)$	Exc.	Table	[122]
0.17	$e + H(2s) \rightarrow e + H(2p)$	Exc.	$f(\epsilon)$	[123]
0.18	$e + H(2s) \rightarrow e + H(n=3)$	Exc.	Table	[126-129]
0.19	$e + H(2s) \rightarrow 2e + H^+$	Ion.	Table	[126-129]
0.20	$e + H(2p) \rightarrow 2e + H^+$	Ion.	Table	[126-129]
0.21	$e + H(2p) \rightarrow e + H(n=3)$	Exc.	Table	[126-129]
0.22	$e + H(n=3) \rightarrow e + H(n=4)$	Exc.	Table	[126-129]
0.23	$e + H(n=3) \rightarrow 2e + H^+$	Ion.	Table	[126-129]
0.24	$e + H(n=3) \rightarrow e + H(2p)$	De-ex.	Table	[126-129]
0.25	$e + H(n=3) \rightarrow e + H(2s)$	De-ex.	Table	[126-129]
0.26	$e + H(n=4) \rightarrow 2e + H^+$	Ion.	Table	[126-129]
0.27	$e + H(n=4) \rightarrow e + H(n=3)$	De-ex.	Table	[126-129]
0.28	$e + H(n=4) \rightarrow e + H(2s)$	De-ex.	Table	[126-129]
0.29	$e + H(n=4) \rightarrow e + H(2p)$	De-ex.	Table	[126-129]

0.30	$e + H_2^+ \rightarrow H + H(2s)$	Att.	$f(\epsilon)$	[123]
0.31	$e + H_2^+ \rightarrow H + H(2p)$	Att.	$f(\epsilon)$	[123]
0.32	$e + H_2^+ \rightarrow H + H(n=3)$	Att.	$f(\epsilon)$	[123]
0.33	$e + H_2^+ \rightarrow H + H(n=4)$	Att.	$f(\epsilon)$	[123]
0.34	$e + H_2^+ \rightarrow e + H + H^+$	Exc.	$f(\epsilon)$	[123]
0.35	$e + H_3^+ \rightarrow H + H_2$	Att.	$f(\epsilon)$	[123]
0.36	$e + H_3^+ \rightarrow 3\ H$	Att.	$f(\epsilon)$	[123]
0.37	$e + H_3^+ \rightarrow e + H^+ + H_2$	Exc.	$f(\epsilon)$	[123]
0.38	$e + H_3^+ \rightarrow e + H^+ + 2\ H$	Exc.	$f(\epsilon)$	[123]
0.39	$2\ H_2 + H^+ \rightarrow H_2 + H_3^+$		$1.95 \cdot 10^8\ T_g^{-0.5}$ $m^6\ s^{-1}\ mol^{-2}$	[132]
0.40	$H_2 + H_2 \rightarrow 2\ H + H_2$		$8.61 \cdot 10^{11}\ T_g^{-0.5} e^{\frac{-52530}{T_g}}$ $m^3\ s^{-1}\ mol^{-1}$	[133]
0.41	$2\ H + H_2 \rightarrow H_2 + H_2$		$1 \cdot 10^5\ T_g^{-0.6}$ $m^6\ s^{-1}\ mol^{-2}$	[133]
0.42	$H + H_2 \rightarrow 3\ H$		$2.7 \cdot 10^{10}\ T_g^{-0.1} e^{\frac{-52530}{T_g}}$ $m^3\ s^{-1}\ mol^{-1}$	[132]
0.43	$3\ H \rightarrow H + H_2$		$1.95 \cdot 10^3$ $m^6\ s^{-1}\ mol^{-2}$	[133]
0.44	$H(2s) + H_2 \rightarrow e + H_3^+$	Ion.	$1.68 \cdot 10^7\ T_g^{-0.5}$ $m^3\ s^{-1}\ mol^{-1}$	[132]
0.45	$H(2p) + H_2 \rightarrow 3\ H$	Diss.	$1.26 \cdot 10^7$ $m^3\ s^{-1}\ mol^{-1}$	[134]
0.46	$H(2s) + H_2 \rightarrow 3\ H$	Diss.	$1.26 \cdot 10^7$ $m^3\ s^{-1}\ mol^{-1}$	[134]
0.47	$H_2 + H_2^+ \rightarrow H + H_3^+$		$1.26 \cdot 10^9$ $m^3\ s^{-1}\ mol^{-1}$	[133]
0.48	$H + H_2^+ \rightarrow H_2 + H^+$		$3.895 \cdot 10^8$ $m^3\ s^{-1}\ mol^{-1}$	[132]
0.49	$H_2 + H^+ \rightarrow H + H_2^+$		$1.94 \cdot 10^8$ $m^3\ s^{-1}\ mol^{-1}$	[132]
0.50	$H(n=3) + H_2 \rightarrow H + H_2$		$1.083 \cdot 10^9$ $m^3\ s^{-1}\ mol^{-1}$	[111]
0.51	$H(n=3) + H_2 \rightarrow e + H_3^+$	Ion.	$1.68 \cdot 10^7\ T_g^{0.5}$ $m^3\ s^{-1}\ mol^{-1}$	[132]
0.52	$H(n=3) + H \rightarrow 2\ H$		$1.48 \cdot 10^9$ $m^3\ s^{-1}\ mol^{-1}$	[135]
0.53	$H(2s) + H_2 \rightarrow H + H_2$		$1.049 \cdot 10^9$ $m^3\ s^{-1}\ mol^{-1}$	[136]
0.54	$H(2s) + H \rightarrow 2\ H$		$6.3 \cdot 10^9$ $m^3\ s^{-1}\ mol^{-1}$	[136]
0.55	$H(2p) \rightarrow H$	Rad.	$6.2649 \cdot 10^8\ s^{-1}$	[137]
0.56	$H(2s) \rightarrow H$	Rad.	$1 \cdot 10^7\ s^{-1}$	[134] [138]
0.57	$H(n=3) \rightarrow H$	Rad.	$5.575 \cdot 10^7\ s^{-1}$	[137]
0.58	$H(n=3) \rightarrow H(2s)$	Rad.	$2.21 \cdot 10^7\ s^{-1}$	[137]
0.59	$H(n=3) \rightarrow H(2p)$	Rad.	$2.21 \cdot 10^7\ s^{-1}$	[137]
0.60	$H(n=4) \rightarrow H$	Rad.	$1.278 \cdot 10^7\ s^{-1}$	[137]
0.61	$H(n=4) \rightarrow H(2s)$	Rad.	$1.47 \cdot 10^7\ s^{-1}$	[137]
0.62	$H(n=4) \rightarrow H(2p)$	Rad.	$1.47 \cdot 10^7\ s^{-1}$	[137]
0.63	$H(n=4) \rightarrow H(n=3)$	Rad.	$8.986 \cdot 10^7\ s^{-1}$	[137]
0.64	$H(n=5) \rightarrow H(2p)$	Rad.	$0.64 \cdot 10^7\ s^{-1}$	[137]
0.65	$H(n=5) \rightarrow H(2s)$	Rad.	$0.64 \cdot 10^7\ s^{-1}$	[137]

Table A.3: Heavy species wall impact reactions.

Nr.	Reaction	Sticking coefficient	Secondary emission probability	Secondary electron mean energy	Reference
0.66	$H^+ \rightarrow H$	0.3	0.05	2	[83] [85]
0.67	$H_2^+ \rightarrow H_2$	0	0.05	2	[83] [85]
0.68	$H_2^+ \rightarrow 2\ H$	1	0.05	2	[83] [85]
0.69	$H_3^+ \rightarrow 3\ H$	1	0.05	2	[83] [85]
0.70	$H_2\ (J = 2) \rightarrow H_2$	0.7	0	0	[83] [85]
0.71	$H_2\ (J = 3) \rightarrow H_2$	0.7	0	0	[83] [85]
0.72	$H_2(v=1) \rightarrow H_2$	0.5	0	0	[83] [85] [139]
0.73	$H_2(v=2) \rightarrow H_2$	0.5	0	0	[83] [85] [139]
0.74	$H_2(v=4) \rightarrow H_2$	0.5	0	0	[83] [85] [139]
0.75	$H(2s) \rightarrow H$	0.7	0.1	2	[83] [85]
0.76	$H(2p) \rightarrow H$	0.7	0.1	2	[83] [85]
0.77	$H(n=3) \rightarrow H$	0.7	0.1	2	[83] [85]
0.78	$H(n=4) \rightarrow H$	0.7	0.1	2	[83] [85]
0.79	$H(n=5) \rightarrow H$	0.7	0.1	2	[83] [85]

Appendix 5: Images of the experimental facility HERMES*plus*

To improve the readability of the experimental section and the description of the experimental setup, several images of the experimental setup, the plasma source design and the plasma during operation are given here.

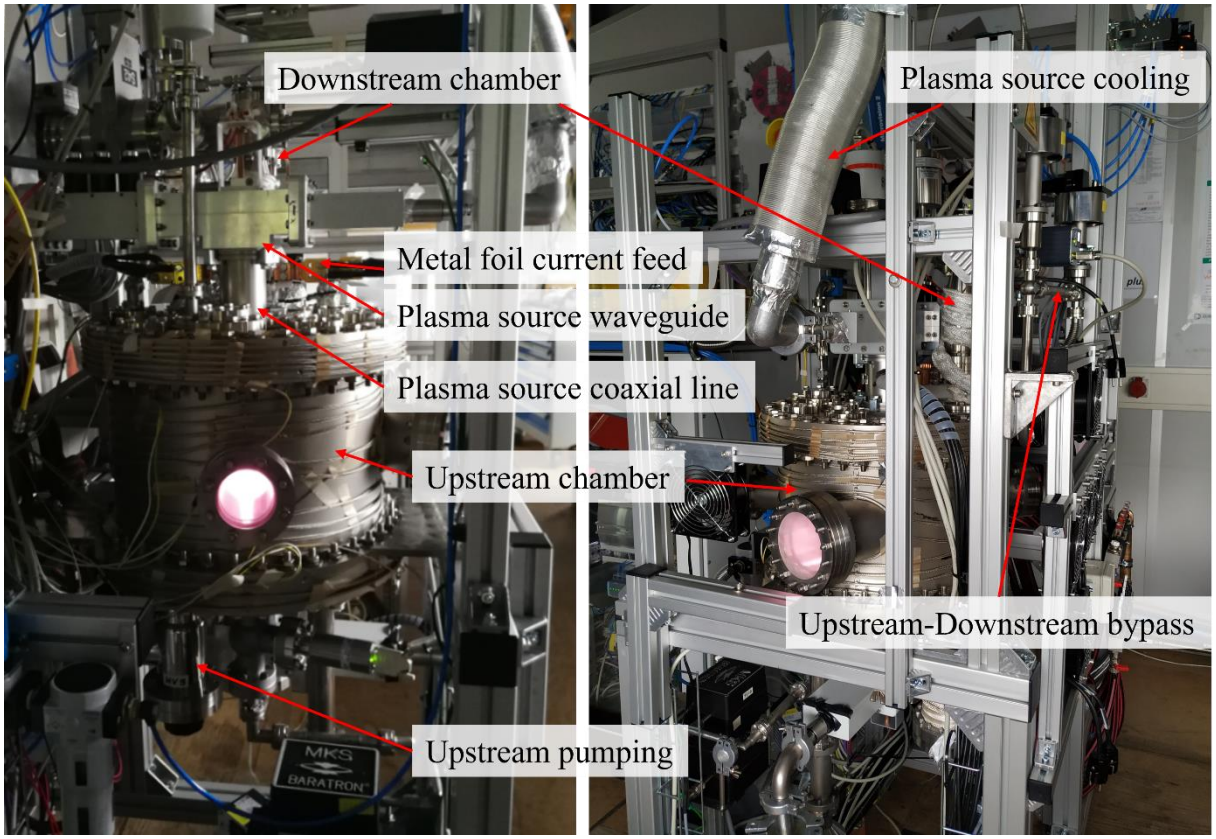

Figure A.2: Images of the vessel and infrastructure of the experimental setup HERMES*plus*.

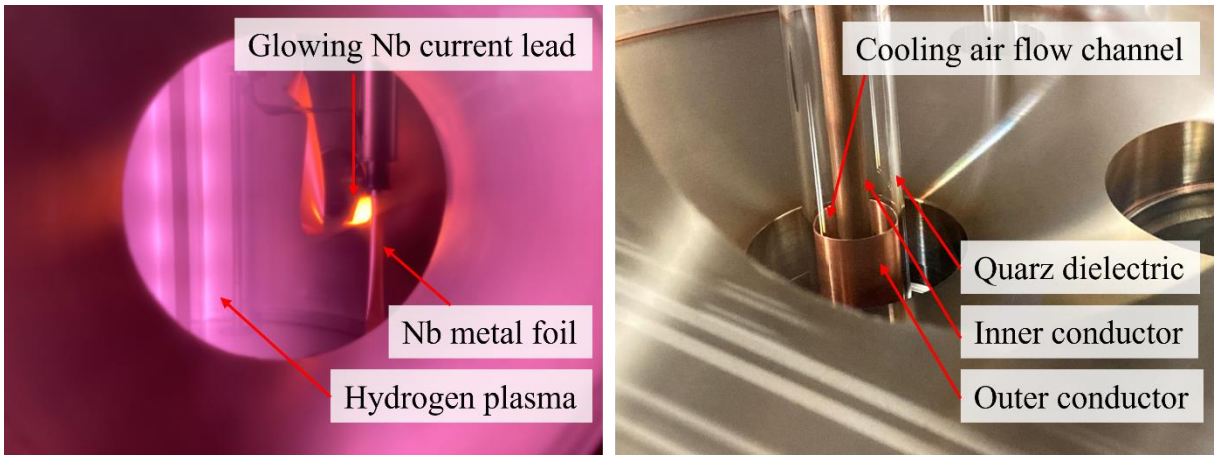

Figure A.3: Image of the plasma source with a quarz dielectric during operation on the left-hand side and switched off on the right-hand side.

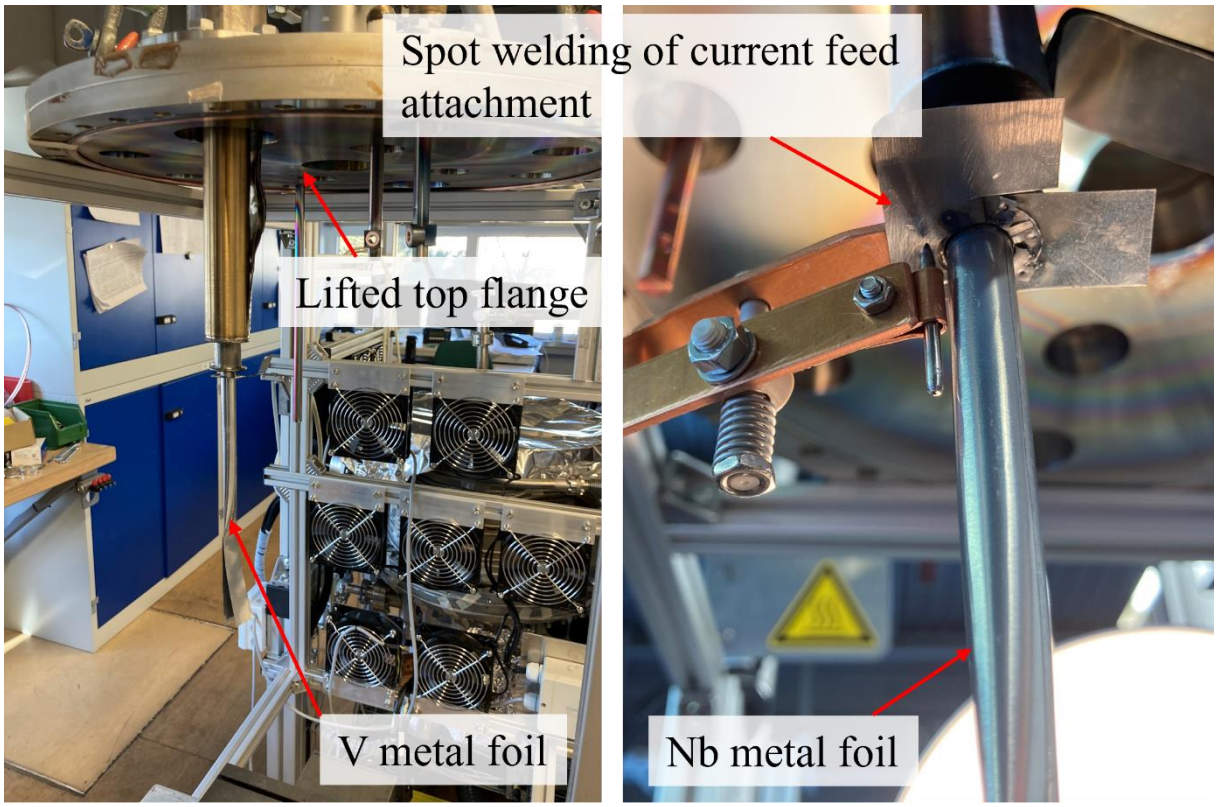

Figure A.4: Image of the metal foil modules mounted on the hanging top flange. The image on the left-hand side features a vanadium foil and the image on the right-hand side shows a Nb foil, which is being attached to resistive heating current leads via spot-welding.

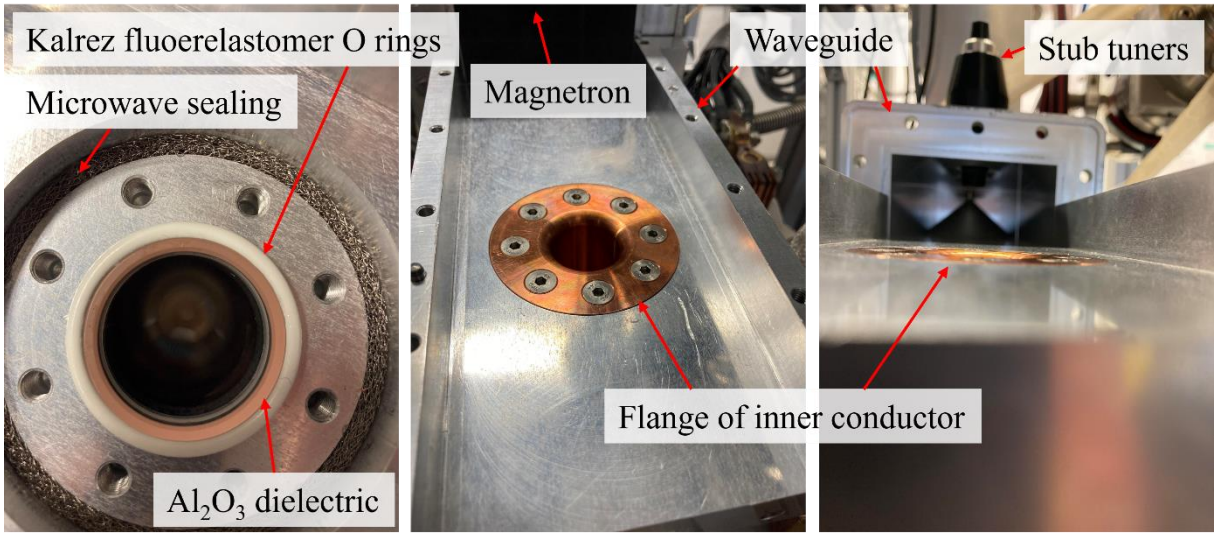

Figure A.5: Images of the plasma source. The coaxial line is rectangularly mounted into the waveguide. An aluminum cone, not visible here, couples the microwave into the coaxial line.

Appendix 6: HERMES*plus* P&ID

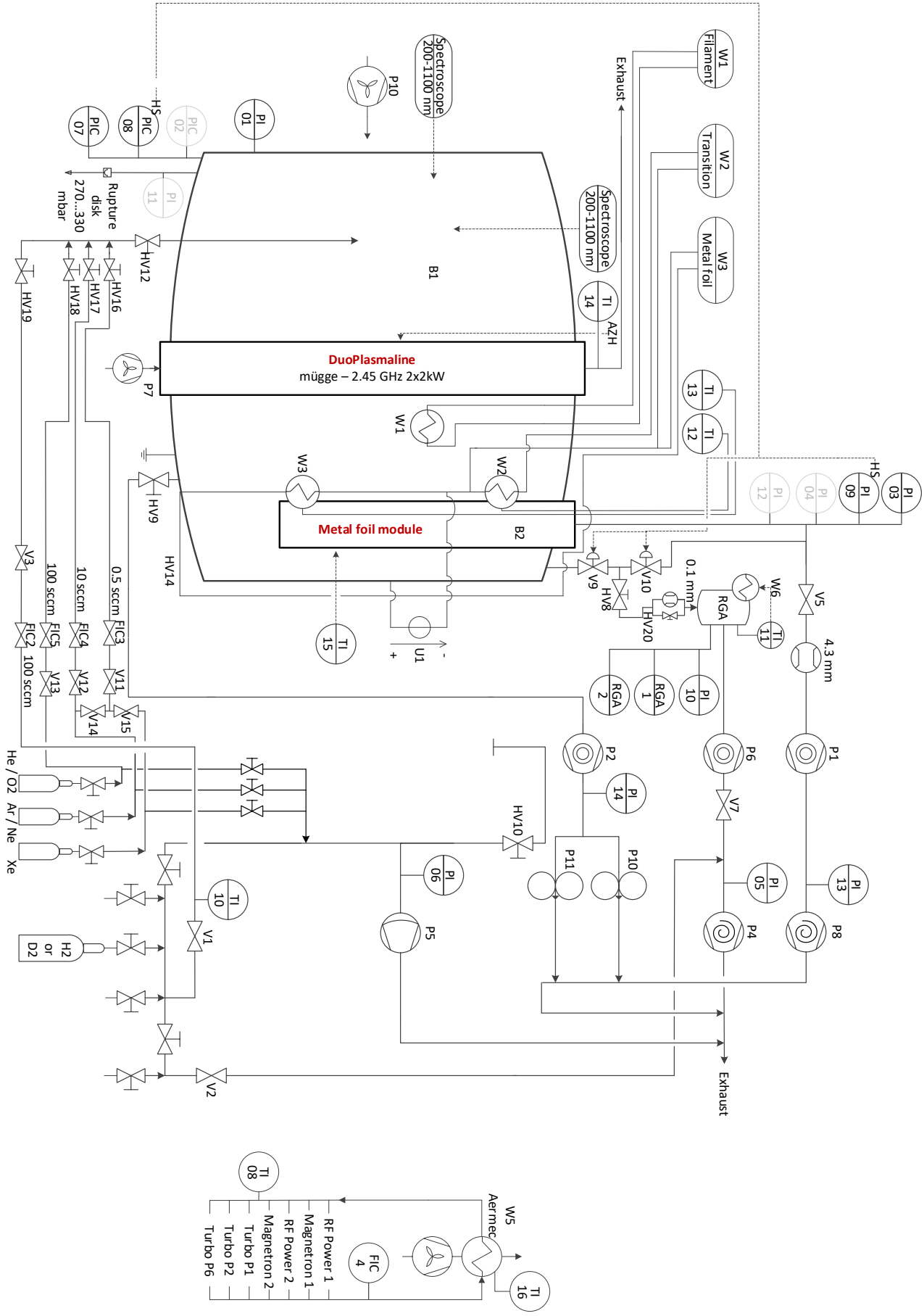

Figure A.6: HERMES*plus* piping and instrumentation diagram.

Appendix 7: Argon plasma chemistry

This Appendix features the plasma chemistry applied to the argon plasma simulation including electron-impact, radiative decay and wall reactions.

Table A.4: Plasma chemistry applied to the argon plasma simulation.

Nr.	Reaction	Type	Given as	Reference
6.3	$e + Ar \rightarrow e + Ar(^2p_1)$	Exc.	Table	[121]
6.4	$Ar(^2p_1) \rightarrow Ar(^1s_2) + h\nu$ (750.3 nm)	Rad.	Table	[154]
6.12	$e + Ar(^1s_3) \rightarrow e + Ar(^2p_1)$	Exc.	Table	[155]
6.13	$e + Ar(^1s_5) \rightarrow e + Ar(^2p_1)$	Exc.	Table	[155]
0.66	$e + Ar \rightarrow e + Ar$	Elastic	Table	[122]
0.67	$e + Ar \rightarrow e + Ar^+$	Ion.	Table	[122] [157]
0.68	$e + Ar \rightarrow e + Ar(^1s_5)$	Exc.	Table	[121] [156]
0.69	$e + Ar \rightarrow e + Ar(^1s_4)$	Exc.	Table	[121] [156]
0.70	$e + Ar \rightarrow e + Ar(^1s_3)$	Exc.	Table	[121] [156]
0.71	$e + Ar \rightarrow e + Ar(^1s_2)$	Exc.	Table	[121] [156]
0.72	$e + Ar \rightarrow e + Ar(^2p_{10})$	Exc.	Table	[121] [156]
0.73	$e + Ar \rightarrow e + Ar(^2p_9)$	Exc.	Table	
0.74	$e + Ar \rightarrow e + Ar(^2p_1)$	Exc.	Table	
0.75	$e + Ar \rightarrow e + Ar(^1s_5)$	Exc.	Table	
0.76	$e + Ar(^1s_5) \rightarrow e + Ar$	De-exc.	Table	[68]
0.77	$e + Ar(^1s_3) \rightarrow e + Ar$	De-exc.	Table	[68]
0.78	$e + Ar(^1s_5) \rightarrow 2e + Ar^+$	Ion.	Table	[158]
0.79	$e + Ar(^1s_3) \rightarrow 2e + Ar^+$	Ion.	Table	[158]
0.80	$e + Ar(^1s_5) \rightarrow e + Ar(^1s_4)$	Exc.	Table	[156] [159] [160]
0.82	$e + Ar(^1s_5) \rightarrow e + Ar(^1s_3)$	Exc.	Table	[156] [159] [160]
0.83	$e + Ar(^1s_5) \rightarrow e + Ar(^1s_2)$	Exc.	Table	[156] [159] [160]
0.84	$e + Ar(^1s_5) \rightarrow e + Ar(^2p_{10})$	Exc.	Table	[156] [159] [160]
0.85	$e + Ar(^1s_5) \rightarrow e + Ar(^2p_9)$	Exc.	Table	[156] [159] [160]
0.86	$e + Ar(^1s_5) \rightarrow e + Ar(^2p_1)$	Exc.	Table	[156] [159] [160]
0.87	$e + Ar(^1s_4) \rightarrow e + Ar(^1s_3)$	Exc.	Table	[156] [159] [160]
0.88	$e + Ar(^1s_4) \rightarrow e + Ar(^1s_2)$	Exc.	Table	[156] [159] [160]
0.89	$e + Ar(^1s_4) \rightarrow e + Ar(^2p_{10})$	Exc.	Table	[156] [159] [160]
0.90	$e + Ar(^1s_4) \rightarrow e + Ar(^2p_9)$	Exc.	Table	[156] [159] [160]
0.91	$e + Ar(^1s_4) \rightarrow e + Ar(^2p_1)$	Exc.	Table	[156] [159] [160]
0.92	$e + Ar(^1s_3) \rightarrow e + Ar(^1s_2)$	Exc.	Table	[156] [159] [160]
0.93	$e + Ar(^1s_3) \rightarrow e + Ar(^2p_{10})$	Exc.	Table	[156] [159] [160]
0.94	$e + Ar(^1s_3) \rightarrow e + Ar(^2p_9)$	Exc.	Table	[156] [159] [160]
0.95	$e + Ar(^1s_3) \rightarrow e + Ar(^2p_1)$	Exc.	Table	[156] [159] [160]
0.96	$e + Ar(^1s_2) \rightarrow e + Ar(^2p_{10})$	Exc.	Table	[156] [159] [160]
0.97	$e + Ar(^1s_2) \rightarrow e + Ar(^2p_9)$	Exc.	Table	[156] [159] [160]
0.98	$e + Ar(^1s_2) \rightarrow e + Ar(^2p_1)$	Exc.	Table	[156] [159] [160]
0.99	$e + Ar(^2p_{10}) \rightarrow e + Ar(^2p_9)$	Exc.	Table	
0.100	$e + Ar(^2p_{10}) \rightarrow e + Ar(^2p_1)$	Exc.	Table	
0.101	$e + Ar(^2p_9) \rightarrow e + Ar(^2p_1)$	Exc.	Table	
0.102	$Ar(^1s_4) \rightarrow Ar$	Rad.	$1.19 \cdot 10^8\ s^{-1}$	[154]
0.103	$Ar(^1s_2) \rightarrow Ar$	Rad.	$5.1 \cdot 10^8\ s^{-1}$	[154]
0.104	$Ar(^2p_{10}) \rightarrow Ar$	Rad.	$2.47 \cdot 10^7\ s^{-1}$	[154]
0.105	$Ar(^2p_9) \rightarrow Ar$	Rad.	$3.26 \cdot 10^7\ s^{-1}$	[154]
0.106	$Ar(^2p_1) \rightarrow Ar$	Rad.	$4.61 \cdot 10^7\ s^{-1}$	[154]
0.107	$Ar(^2p_9) \rightarrow Ar(^1s_5)$	Rad.	$3.31 \cdot 10^7\ s^{-1}$	[154]
0.108	$Ar(^2p_1) \rightarrow Ar(^1s_4)$	Rad.	$2..36 \cdot 10^7\ s^{-}$	[154]

0.109	$Ar(^2p_1) \rightarrow Ar(^1s_2)$	Rad.	$4.45 \cdot 10^7$ s$^-$	[154]
0.110	$Ar(^2p_1) \rightarrow Ar(^1s_4)$	Rad.	$2.36 \cdot 10^5$ s$^-$	[154]
0.111	$Ar(^2p_{10}) \rightarrow Ar(^1s_2)$	Rad.	$1.9 \cdot 10^5$ s^{-1}	[154]
0.112	$Ar(^2p_{10}) \rightarrow Ar(^1s_3)$	Rad.	$9.8 \cdot 10^5$ s^{-1}	[154]
0.113	$Ar(^2p_{10}) \rightarrow Ar(^1s_4)$	Rad.	$5.43 \cdot 10^6$ s^{-1}	[154]
0.114	$Ar(^2p_{10}) \rightarrow Ar(^1s_5)$	Rad.	$1.89 \cdot 10^7$ s^{-1}	[154]
0.115	$Ar(^1s_3) \rightarrow Ar$	Rad.	$1.59 \cdot 10^5$ s^{-1}	[138]
0.116	$Ar(^1s_5) \rightarrow Ar$	Rad.	$1.9 \cdot 10^5$ s^{-1}	[138]

Table A.5: Wall reactions considered in argon plasma simulation.

Nr.	Reaction	Sticking coefficient	Secondary emission probability	Secondary electron mean energy	Reference
0.117	$Ar(^1s_5) \xrightarrow{metal} Ar$	0.84	0.1	2	[83] [85] [161]
0.118	$Ar(^1s_4) \xrightarrow{metal} Ar$	0.8	0.1	2	[83] [85] [161]
0.119	$Ar(^1s_3) \xrightarrow{metal} Ar$	0.88	0.1	2	[83] [85] [161]
0.120	$Ar(^1s_2) \xrightarrow{metal} Ar$	0.8	0.1	2	[83] [85] [161]
0.121	$Ar(^2p_{10}) \xrightarrow{metal} Ar$	0.8	0.1	2	[83] [85] [161]
0.122	$Ar(^2p_9) \xrightarrow{metal} Ar$	0.8	0.1	2	[83] [85] [161]
0.123	$Ar(^2p_1) \xrightarrow{metal} Ar$	0.8	0.1	2	[83] [85] [161]
0.124	$Ar^+ \rightarrow Ar$	1	0.1	2	[83] [85] [161]
0.125	$Ar(^1s_5) \xrightarrow{dielectric} Ar$	0.74	0.1	2	[83] [85] [161]
0.126	$Ar(^1s_4) \xrightarrow{dielectric} Ar$	0.6	0.1	2	[83] [85] [161]
0.127	$Ar(^1s_3) \xrightarrow{dielectric} Ar$	0.76	0.1	2	[83] [85] [161]
0.128	$Ar(^1s_2) \xrightarrow{dielectric} Ar$	0.6	0.1	2	[83] [85] [161]
0.129	$Ar(^2p_{10}) \xrightarrow{dielectric} Ar$	0.6	0.1	2	[83] [85] [161]
0.130	$Ar(^2p_9) \xrightarrow{dielectric} Ar$	0.6	0.1	2	[83] [85] [161]
0.131	$Ar(^2p_1) \xrightarrow{dielectric} Ar$	0.6	0.1	2	[83] [85] [161]

Appendix 8: Permeation probability in HERMES*plus*

The permeation probability in an exemplary experiment is calculated using the pV-flow of molecular hydrogen through a precision-drilled orifice. At the experimental conditions of 2 kW plasma power, 25 Pa and ~ 900 °C foil temperature, a flux of ~ 6 Pa m³ m^{-2} s^{-1} has been reached. By use of the ideal gas law, a flux of permeating hydrogen molecules is calculated to be

$$\dot{n} = \dot{J}_{Perm}\frac{N_A}{RT} = 6\frac{Pa\cdot m^3}{m^2 s}\frac{6.022\cdot 10^{23}\ mol^{-1}}{8.314\ \frac{J}{mol\cdot K}\cdot 300\ K} \approx 1.45\cdot 10^{21}\frac{H_2}{m^2\cdot s}. \tag{0.11}$$

By knowledge of the number density of the impinging particles on the foil, a permeation probability is derived. This requires assuming a value for the gas temperature and for the atomic hydrogen density in the location of the metal foil which are taken from the simulation data leading to:

$$\begin{aligned}\chi = \frac{\dot{n}_{imp}}{\dot{n}_p} &= \frac{\sqrt{\frac{N_A}{2\pi M_{H2} k_B T_g}}\, p\cdot y_H}{1.45\cdot 10^{21}\frac{H_2}{m^2\cdot s}},\\ &= \frac{1.45\cdot 10^{21}\frac{H_2}{m^2\cdot s}}{\sqrt{\frac{6.022\cdot 10^{23}\ mol^{-1}}{2\pi\cdot 0.00216\ \frac{kg}{mol}\cdot 1.38\ \cdot 10^{-23}\ \frac{J}{K}\cdot 461\ K}}\cdot 20\ Pa\cdot 0.02955}.\\ &\approx 0.0294\end{aligned} \tag{0.12}$$

The corresponding permeation probability is close to 3 %, which is lower than stated in most reports in literature considering ideal symmetric surface conditions.